Discrimination of surface events with time resolved ionization channels in the EDELWEISS dark matter search

Zur Erlangung des akademischen Grades eines
DOKTORS DER NATURWISSENSCHAFTEN
von der Fakultät für Physik
des Karlsruher Instituts für Technologie

genehmigte

DISSERTATION

von

Dipl.-Phys.
Bernhard Siebenborn
aus Speicher

Tag der mündlichen Prüfung: 01.07.2016

Referent: Prof. Dr. Dr. h.c. Johannes Blümer
Korreferent: Prof. Dr. Marc Weber

Contents

Abstract

Only about 5% of our Universe is filled with baryonic matter, whereas 26% is expected to be a form of dark matter and 69% is dark energy. We know these numbers from precise measurements of the cosmic microwave background radiation with the Planck satellite [1] and from many other observations. Flat rotation curves of galaxies, the dynamics within galaxy clusters and the merging of these clusters give a strong evidence for the existence of a new particle with the generic name WIMP, **W**eakly **I**nteracting **M**assive **P**article. These particles have not been observed by an experiment to date. With their expected mass range of GeV/c^2 to TeV/c^2 and an expected WIMP-nucleon cross-section as small as 10^{-45} cm^2, a direct detection is challenging. Experiments directly looking for dark matter particles are also known as rare event searches, since the expected event rate is small, whereas the background event rate is high. A perfect understanding and identification of background events and their suppression in the experiment is mandatory.

The EDELWEISS experiment uses cryogenic (operational temperature $T = 18$ mK) mono-crystalline germanium detectors for the direct search of dark matter particles. The recoil of a Ge nucleus after elastic scattering of a WIMP can be identified by simultaneous measurement of a heat (phonon) and a charge (ionization) signal. The current EDELWEISS-III phase uses up to 36 detectors each with a mass of ~ 800 g and 6 channels, four for the charge signals and two for the heat measurement. All channels are digitized with 16 bit resolution and 100 kHz sampling rate. Within the work of this thesis, a new modular and scalable readout system was developed and successfully installed at the experimental site. Special features of the DAQ system are the direct inclusion of external detectors such as the muon veto system and a global time stamp for the whole experiment and its external detectors. The FPGA based acquisition system also enables a fast and precise trigger signal which is necessary for the event based readout of time resolved ionization channels. This trigger algorithm has to be sensitive to ionization pulses having the shape of a Heaviside step function, surrounded by a 500 Hz rectangular shaped cross talk pattern from the heat channels. This pattern has to be suppressed for a correct trigger decision which is achieved by a digital cascaded trapezoidal filter implemented in the FPGA software.

The physical ionization pulses have a rise time below the EDELWEISS sampling frequency of 100 kHz. Therefore, a prototype hardware with a sampling rate of 40 MHz is installed, to record time resolved ionization pulses on one of the EDELWEISS detectors. An analysis chain for the time resolved ionization channel is developed and presented here. The recorded signals are noisy and have to be filtered. Therefore, a staged filter is implemented in order to reduce the noise level. Afterwards, the pulse shape and the rise time can be analyzed on an event by event basis. A following statistical analysis demonstrates the potential of time resolved ionization data for surface event discrimination and shows the merit that rise time information as an additional channel can provide. It is shown that a simple cut on the rise time at 425 ns suppresses 95% of surface events while rejecting only 5.75% of fiducial events. However, the electronic noise limits this discrimination to event energies above 100 keV.

A comparison of the recorded time resolved data with an analysis of a simulated data set is presented in the last chapter. Therefore, a simulation code starts an event in form of electron-hole pairs in a small volume around a randomly selected impact coordinate. The simulation computes the residual electric field at the charge position and drifts the charges towards the detector electrodes. The Ramo theorem is applied to calculate the electric signal induced in the electrodes. Afterwards, the simulated events are folded with real noise and processed by the same algorithms as the experimental data. An excellent agreement validates the results of the time resolved data analysis. It shows that the rise time in the EDELWEISS detectors is correctly reproduced. A data set of simulated events with an optimistic low noise level, achievable with a new detector biasing and readout electronics, demonstrates the potential of a time resolved ionization channel for a next generation detector readout system. A future detector could be equipped with two sets of electrodes instead of four, using the rise time to reject surface events instead of veto electrodes.

During the implementation of the time resolved ionization channels and detailed work inside the analog part of the EDELWEISS readout electronics we found a way to increase the maximal detector biasing voltage from 20 V to 140 V by only minor changes of the hardware. The amount of energy that drifting charges dissipate into heat scales with the applied voltage. This Neganov-Luke effect can be used to lower the heat threshold of a detector and to increase the sensitivity for low-mass WIMPs. As a side topic of this thesis, a prototype unit was developed and successfully tested at the experimental site. Therefore, 10 cards were subsequently produced and are currently biasing EDELWEISS detectors with up to 140 V. First results with this hardware upgrade show a threshold and sensitivity improvement by a factor of 10.

This work shows for the first time the potential of discriminating near-surface events in EDELWEISS FID800 type Ge detectors via the spatial information obtained by a highly sampled ionization channel. Although in its prototype phase, we could show the strong potential of this ionization signal which is complementary to the surface rejection via a separate veto electrode signal.

Within this thesis, the electronics system necessary to read out the time resolved ionization channel within EDELWEISS-III was developed and finally installed. This new system also provides a global synchronization of all EDELWEISS readout channels, and it allows an FPGA based hardware trigger for an event based and dead time free data readout.

Finally, as a part of this thesis, a new adjustable detector biasing system for voltages up to ± 70 V has been developed, tested and fully implemented. This system will allow EDELWEISS to explore, via the Neganov-Luke effect, the yet unknown dark matter parameter space for low mass WIMPs down to mass values of the order of 1 GeV/c^2.

Zusammenfassung

Nur etwa 5% unseres Universums bestehen aus barionischer, sichtbarer Materie, wohingegen 26% aus Dunkler Materie aufgebaut sind und 69% die Dunkle Energie bilden. Die Zusammensetzung ist bekannt aus einer präzisen Vermessung der Kosmischen Mikrowellen Hintergrundstahlung mit den Instrumenten des Planck-Satelliten [1] und von vielen anderen Messungen. Die Entdeckung abgeflachter Rotationskurven bei nahezu allen Galaxien, die Geschwindigkeitsdispersion innerhalb der Galaxienhaufen und die Entdeckung dynamischer Galaxienhaufen nach Kollisionsprozessen liefern starke Argumente für eine Dunkle Materie in Form von neuen Teilchen. In der Teilchenphysik wird der experimentelle Nachweis dieser schwach wechselwirkenden massereichen Teilchen angestrebt. Die mit dem generischen Namen "WIMP"(weakly interacting massive particles) benannten Teilchen sind ein Kandidat für die Dunkle Materie im Universum, jedoch fehlt bislang ein experimenteller Nachweis. Die erwartete Masse im Bereich von GeV/c^2 bis zu TeV/c^2 bei einem erwarteten Wirkungsquerschnitt für WIMP-Kernrückstöße, der kleiner als 10^{-45} cm^2 sein könnte, machen einen direkten Nachweis sehr kompliziert. Solche Experimente suchen nach extrem seltenen Ereignissen innerhalb einer Vielzahl von Hintergrundereignissen. Dazu ist ein ausgezeichnetes Verständnis und eine Identifikationsfähigkeit von Hintergrundereignissen sowie ihre Vermeidung erforderlich.

Das EDELWEISS Experiment benutzt kryogene (Betriebstemperatur $T = 18$ mK) Detektoren aus hochreinem, monokristallinem Germanium für den direkten Nachweis der Dunkle Materie Teilchen. Dabei wird der Rückstoß eines Germanium-Kerns nach der Streuung eines WIMPs in Form eines Wärme- (Phononen-) und eines Ladungs- (Ionisations-) Signals gemessen und identifiziert. Die momentane dritte Phase des EDELWEISS Experiments nutzt bis zu 36 Detektoren mit einer Masse von je ~ 800 g. Jeder Detektor wird über 6 Kanäle ausgelesen. Zwei Wärmekanäle und vier Ionisationskanäle werden mit je 16 bit Auflösung und 100 kHz Abtastrate betrieben. Im Rahmen dieser Arbeit wurde ein neues modulares und skalierbares Datenaufnahmesystem (DAQ) entwickelt und am Experiment in Betrieb genommen. Besondere Neuerungen sind dabei eine zentrale Zeitreferenz für das gesamte EDELWEISS Experiment und externe Detektoren sowie die Möglichkeit, externe Detektoren, beispielsweise das Muonen-Veto-System, in die Datenaufnahme einzubeziehen. Das neue FPGA-basierte System ermöglicht außerdem einen Trigger, der zum Auslesen eines neuen zeitaufgelösten Ionisationskanal benötigt wird. Der Triggeralgorithmus muss einen stufenförmigen Puls im Ionisationskanal finden, der von einem Rechteck-Hintergrundsignal mit 500 Hz Wiederholfrequenz durch Übersprechen der Wärmekanäle umgeben ist. Dieses Hintergrundmuster muss vom Triggeralgorithmus unterdrückt werden, was durch einen kaskadierten Trapez-Filter in der FPGA Software geschieht.

Die physikalischen Ionisationspulse haben eine Anstiegszeit, die unterhalb der mit der EDELWEISS Abtastrate von 100 kHz gegebenen Auflösbarkeit liegt. Deshalb wurde der Prototyp einer Ausleseelektronik installiert, die mit einer Abtastrate von 40 MHz in der Lage ist, die Anstiegszeit der Signale zu vermessen. Eine Datenverarbeitungskette für diese zeitaufgelösten Pulse wird im Rahmen dieser Arbeit entwickelt und erklärt. Die damit aufgenommenen Signale sind mit rauschen überlagert und müssen gefiltert werden.

Dazu wurde ein mehrstufiger Filteralgorithmus implementiert, mit dem Ergebnis einer Rauschunterdrückung im Bereich des Pulses. Anschließend wird der Puls vermessen und seine Anstiegszeit und Form bestimmt. In einer darauf folgenden Analyse werden die aufgenommenen Daten statistisch ausgewertet. Es wird gezeigt, dass die zeitaufgelösten Ionisationssignale dazu geeignet sind, oberflächennahe Ereignisse von solchen im Inneren des Detektors zu unterscheiden. Eine Selektion anhand einer Anstiegszeit von über 425 ns unterdrückt 95% der Oberflächenereignisse, nur 5.75% der zentralen Ereignisse werden verworfen. Allerdings ist diese Separation aufgrund des hohen Rauschpegels auf Ereignisse oberhalb von 100 keV beschränkt.

Ein Vergleich der aufgenommenen Daten mit einer Simulation erfolgt im letzten Kapitel. Dazu startet ein Simulationscode Ereignisse in Form von Elektronen-Loch-Paaren an zufällig ausgewählten Koordinaten im Detektor. Das von den Elektroden angelegte elektrische Feld wird am Ort der Ladungsträger berechnet, wodurch diese zu den Elektroden driften. Das Ramo-Theorem wird ausgenutzt, um die beim Ladungsdrift induzierte Ladungen auf den Detektorelektroden zu berechnen. Anschließend werden die Ergebnisse der simulierten Pulse mit dem am Experiment aufgenommenen Rauschen überlagert und von der gleichen Datenverarbeitungskette analysiert. Die Ergebnisse werden mit den am Experiment aufgenommenen Daten verglichen und eine ausgezeichnete Übereinstimmung gezeigt. Damit ist nachgewiesen, dass die Anstiegszeit der Ladungssignale in EDELWEISS Detektoren korrekt von einer Simulation reproduziert wird. Zusätzlich wird ein Datensatz von simulierten Ereignissen mit einem reduzierte Rauschpegel erzeugt und analysiert. Diese Analyse zeigt das Potential der Anstiegszeitmethode für eine zukünftige Ausleseelektronik. Zukünftige Detektoren könnten mit einem vereinfachten Design aus zwei Elektroden, anstelle von vier, auskommen und die Anstiegszeit, anstelle von Vetoelektroden zum Unterdrücken von Oberflächenereignissen nutzen.

Während der Inbetriebnahme der zeitaufgelösten Ionisationskanäle fanden wir bei Arbeiten im analogen Teil der Ausleseelektronik eine Möglichkeit, mit wenigen Modifikationen die maximale Versorgungsspannung der Detektoren von 20 V auf 140 V zu vergrößern. Im elektrischen Feld driftende Ladungsträger erhalten zusätzliche Energie von diesem Feld. Der als Neganov Trofimov Luke Effekt bekannte Energiegewinn kann dazu benutzt werden, um den Ladungsträgern zusätzliche Energie zu geben und damit Signale, die bisher unterhalb der Empfindlichkeit von EDELWEISS lagen, sichtbar zu machen. Als Nebenthema dieser Arbeit wurde daraufhin ein Prototyp entwickelt und erfolgreich getestet. Weitere 10 Karten wurden gefertigt und versorgen derzeit EDELWEISS Detektoren mit bis zu 140 V Spannung. Erste Resultate mit dem Hardware-Upgrade ergeben eine Steigerung der Empfindlichkeit um einen Faktor 10.

Zusammenfassend zeigt diese Arbeit zum ersten Mal das Potential zur Diskriminierung oberflächennaher Ereignisse in Germaniumdetektoren des EDELWEISS FID800 Typs mittels räumlicher Informationen, die aus dem hochaufgelösten Ionisationssignal gewonnen werden. Bereits in der Prototypen-Phase können vergleichbare Erkennungsraten zur konventionellen Methode mit extra Veto Elektroden erzielt werden.

Im Rahmen dieser Arbeit wurde ein neues, für die zeitaufgelösten Signale benötigtes, Datenauslesesystem am EDELWEISS Experiment final getestet und erfolgreich in Betrieb genommen. Es bildet das Rückgrat der EDELWEISS-III Datenaufnahme. Ein globaler Zeitstempel wird benutzt, um alle in EDELWEISS involvierten Detektoren zu synchronisieren. Mit dem FPGA-basierten Hardware Trigger ist es möglich, das gesamte Experiment ereignisbasiert und totzeitfrei auszulesen.

Als weiterer Teil dieser Arbeit wurde ein einstellbares Spannungsversorgungssystem für die Detektoren entwickelt und erfolgreich in Betrieb genommen, mit deren Hilfe jede Elektrode im Bereich von ± 70 V eingestellt werden kann. Dieses System wird es EDELWEISS erlauben,

mittels des Neganov Trofimov Luke Effekt den noch unbekannten Parameterbereich für Dunkle Materie mit niedriger Teilchenmasse von $\mathcal{O}(1 \text{ GeV}/\text{c}^2)$ zu erforschen.

1. Dark matter in cosmology, particle and astroparticle physics

It is an ancient human desire to understand the mechanics of our Universe by observing the nightly sky. More and more complex models have been gradually developed and partially dropped again. The deepness of our view towards planets, stars, galaxies and finally clusters and superclusters of galaxies has increased with newer and ever better instruments. Today, we combine observations in almost the complete spectrum of electromagnetic waves, from radio astronomy to gamma-ray astronomy. Particles hitting the earth's atmosphere are studied directly above the atmosphere on the space station and satellite based experiments, or indirectly on the earth's surface through the induced particle showers. On the other hand, atmospheric or even galactic neutrinos are detected after crossing the center of the earth. Recently, gravitational wave astronomy has begun and we register the merging of black holes, the single event with the highest energy dissipation ever observed. We can expect a lot more to follow. As a puzzling surprise, many of the mentioned channels observe structures and dynamics that can not be explained by the present set of known particles.

Over all centuries, models were developed to explain observations and to predict the results of future measurements. One promising model that aims to describe the observational Universe is the standard model of cosmology, also ΛCDM or lambda (Λ) **C**old **D**ark **M**atter model. This model describes the present Universe with its constituents of baryonic matter, dark matter and dark energy and its behavior since the Big Bang. Λ is the so called cosmological constant, connected to dark energy which dominates the energy/mass content of the actual Universe.

Dark matter in form of a new particle is discussed in this chapter. Several particle candidates and their characteristics are presented, as well as methods for their detection. The detection can either be achieved directly by observing the scattering of dark matter with ordinary matter inside a detector, or indirectly, by the observation of particles from annihilation of astrophysical dark matter among cosmic ray particles that hit the earth, or by artificial production of dark matter in a particle collider.

1.1 Observational evidence for dark matter

Observations in the first half of the 20th century have shown a discrepancy between measured and expected velocities of galaxies confined in clusters. The total virial mass of a cluster had to be significantly larger than the luminous visible mass. Almost 30 years later,
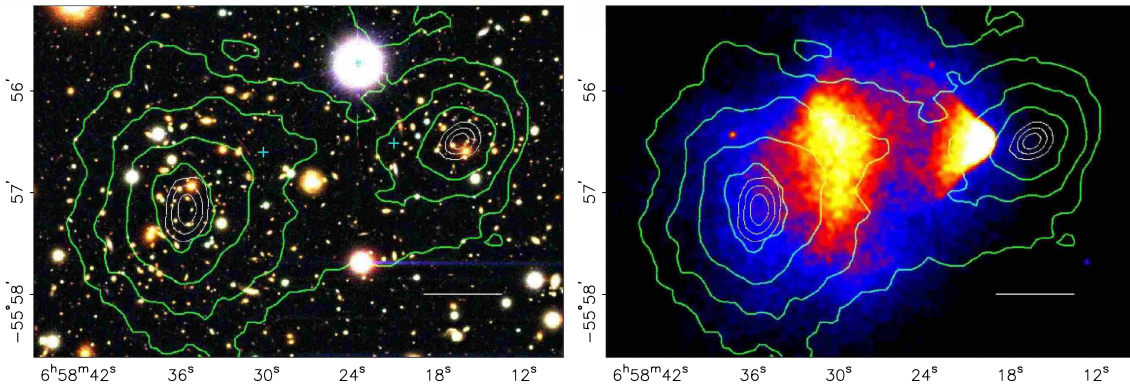
Figure 1.1: Left: Color image from the Magellan telescopes of the merging cluster 1E 0657-558 *Bullet Cluster*. The white bar indicates 200 kpc at the clusters distance. The green contour lines show the presence of mass, derived by weak lensing reconstruction. The two "+" show the center of mass of the intergalactic plasma. Right: Chandra X-ray image of the same region. Intergalactic plasma is concentrated in the white-red area and heated up from ram pressure. Details in text. Figures from [5]

a comparable effect was discovered in the rotational velocity of spiral galaxies. Stars in the outer region move with more than twice the rotational speed predicted by gravitation from the visible mass concentrated in the galactic center.

1.1.1 Observation of DM in galaxy clusters

In 1933 Fritz Zwicky measured the speed of 8 galaxies within the coma cluster by analysing their red shift using the Doppler technique [2, 3]. The measured velocity dispersion was ~ 1000 km/s. He assumed, that stars in the coma cluster have a similar mass to luminosity ratio as our sun and that 800 galaxies with an average mass of 10^9 $M_\odot$ are confined in a spherical volume of 10^6 light-years. The velocity dispersion along the line-of-sight was measured to be approximately 1000 km/s, whereas the expected value was 80 km/s. Zwicky expected the cluster to be in the state of equilibrium, thus applied the virial theorem (as known from thermodynamics)

$$\langle E_{\text{kin}} \rangle = -\frac{1}{2} \langle E_{\text{pot}} \rangle \tag{1.1}$$

to estimate the ratio of total mass to luminous mass to $M/L = 400$. This was the first time where the virial theorem was used to determine the mass of a galaxy cluster [4] and a huge amount of invisible mass was found.

With our modern scope of instruments for cosmological observations, discoveries as 1E 0675-558 (fig. 1.1), better known as the Bullet Cluster became possible. The left image in the figure was recorded by the Magellan telescopes at the Las Campanas observatory site in Chile. It shows two galaxy clusters within the Carina constellation at a distance of about 1 Gpc. One larger main cluster visible as the dense population of galaxies in the left half of the image, separated by a void (lesser populated area) from the smaller subcluster in the right half. The green contour lines indicate the localization of mass and are obtained with the weak lensing effect. The innermost three white contours show the center of mass with a 1σ (innermost) to 3σ confidence level. The right part of fig. 1.1 shows x-ray emitting gas in the same area recorded by the Chandra X-ray Observatory. The intensity of x-ray emission increases from blue over red to white and shows the position and the temperature of the plasma. The cluster is interpreted as a dynamic merger. The
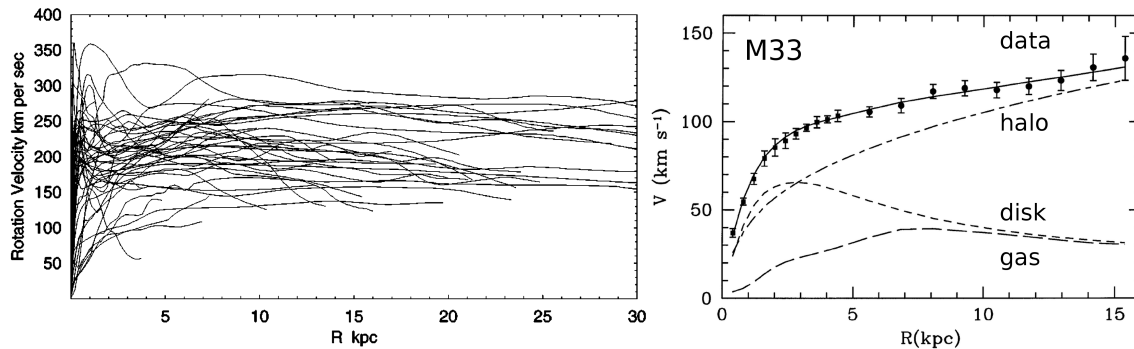
Figure 1.2: Rotational velocity versus distance from galactic center for a set of galaxies [9] (left) and for M33 [10] (right) itemized for gas, disk and halo contribution. The curves are flat, whereas a prediction by a mass constitution of gas and stars would rather follow a $1/\sqrt{r}$ dependence.

smaller subcluster moves towards the right side and has crossed through the main cluster. The density of galaxies inside the clusters is small and they can be treated as collisionless particles, whereas the intercluster plasma has a fluid-like behavior. It interacted and is slowed down and heated up by ram pressure. The resulting bow shock indicates a relative velocity of 4700 km/s, hence a time for the merging can be given as 100 Myr ago [5]. This was the first observation of a separation from visible and dark matter. The decoupling from dark matter and the plasma implies collisionless dark matter particles. An upper limit for the self-interaction cross section per unit mass of dark matter particles in the Bullet Cluster is derived as $\sigma/m < 1.25$ cm^2/g [6]. A more recent and similar observation is given with the cluster system MACS J0025.4-1222 from which a self-interaction cross section of $\sigma/m < 4$ cm^2/g is derived [7]. A much more complicated situation of separation from visible and dark matter was discovered in Abell 520, where a core of dark matter is surrounded by galaxies. The core itself is voided, unlike the previous cases. The limit for the self-interaction cross section in Abell 520 is $\sigma/m < 1$ cm^2/g [8]. More examples have been described (an overview is given in [4]) or are matter of current investigation.

1.1.2 Observation of DM in galaxies

Beside the evidences for dark matter on scales of galaxy clusters $\mathcal{O}(1-100$ Mpc) we have strong arguments for the existence of dark matter on galactic scales $\mathcal{O}(1-100$ kpc). In 1970, Vera Rubin and Kent Ford performed spectroscopical measurements on M31 Andromeda Nebula. They found a distribution of the star velocity versus distance to the galactic center, which is flat for the outer regions [11]. Many other galaxies have been observed and, as shown in fig. 1.2 left, have rather constant velocities in the outer regions. In the beginning, these observations were performed by spectroscopy of the HI absorption line. This line is caused by the energy absorption of an electron changing between the two hyperfine levels of the ground state in hydrogen. The corresponding wavelength is 21 cm and visible in radio telescopes. In fig. 1.2 right, a breakdown of the individual components is shown for M33. The contribution of interstellar gas and the stars in the galactic disk are not fitting the data points, whereas a dark matter halo can explain the data.

Based on N-body simulations, Navarro, Frenk and White derived a parametrization for the dark matter halo density of galaxies also known as the NFW profile [12]:

$$\rho(r) = \frac{\rho_{\text{crit}} \cdot \delta_{\text{c}}}{\frac{r}{r_{\text{s}}} \left(1 + \frac{r}{r_{\text{s}}}\right)^2} \tag{1.2}$$
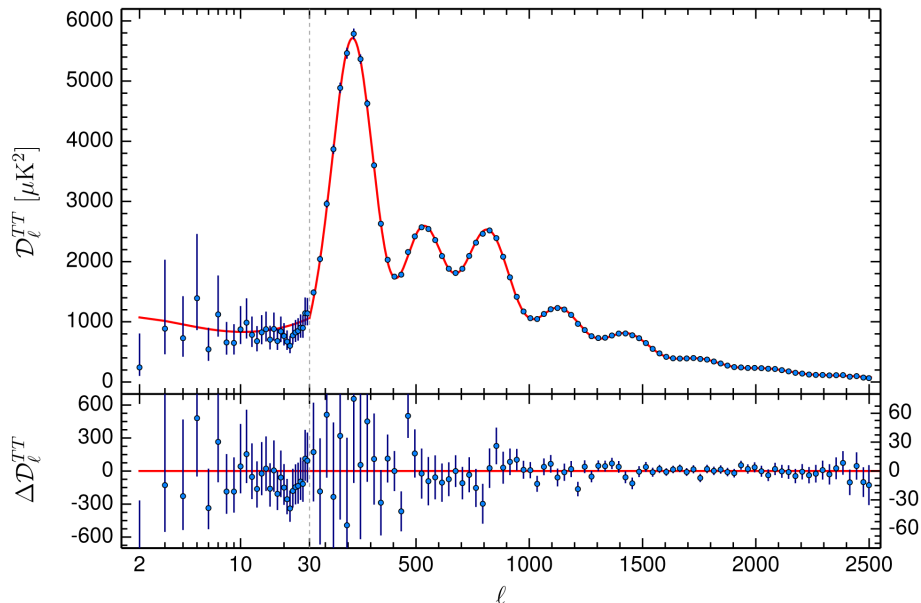
Figure 1.3: Top: The Planck 2015 temperature power spectrum measurement of the CMB, with a best-fit ΛCDM theoretical spectrum (red line). Error bars show $\pm 1\sigma$ uncertainties. Bottom: Residuals with respect to the ΛCDM model fit. Figure from [1].

where ρ_{crit} is the critical density for a flat Universe, $r_{\mathrm{s}} = r_{200}/c$ represents the radius at which the mass of the galaxy has an overdensity of $200 \cdot \rho_{crit}$ and c is a dimensionless parameter to be determined empirically. $\delta_{\mathrm{c}} = \frac{200}{3} \frac{c^3}{\ln(1+c) - c/(1+c)}$ is the parametrization for the characteristic overdensity of the halo. Another common profile for the parametrization of a galactic density is given by Einasto [13]:

$$\rho(r) \propto \exp(-A \cdot r^{\alpha}) \tag{1.3}$$

A comparison of the two models along several additional models is given in [14]. The Einasto and NFW model are compatible for most galactic profiles. However, differences occur for regions close to the galactic center or far outside at large r.

The density of our local dark matter halo determines the flux of dark matter particles through a detector, thus it is an important parameter for experimental searches. The NFW profile predicts a density at the distance of the Sun of $\rho_{\mathrm{DM}}(R_{\odot}) = 0.235 \pm 0.030 \,\mathrm{GeV}/c^2/\mathrm{cm}^3$ [15]. The observation of nearby stars also provides information about ρ_{DM} in the solar neighborhood. The resulting values of $0.2\,\mathrm{GeV}/c^2/\mathrm{cm}^3 - 0.56\,\mathrm{GeV}/c^2/\mathrm{cm}^3$ better fits the local region [16, 17]. The commonly used value is $\rho_{\mathrm{DM}} = 0.3\,\mathrm{GeV}/c^2/\mathrm{cm}^3$.

1.1.3 Cosmic microwave background radiation

A cosmic background radiation was predicted in 1948 by Alpher, Bethe and Gamow [18], and discovered by Penzias and Wilson as a temperature excess in a 20-foot horn antenna [19]. The background corresponds to a black body radiation with a temperature of 2.72548 ± 0.00057 K [20]. Angular fluctuations within the homogeneous temperature have been measured by balloon experiments, such as ARCHEOPS [21] and BOOMERANG [22], and by satellite based experiments. Especially the satellite based experiments were able to record a full sky map at different wavelengths. The sensitivity and angular resulution has been enormously improved from COBE[23] via WMAP[24] to Planck[1, 25]. The measured temperature fluctuations are in the order of µK and can be interpreted as a map of density and energy fluctuations of the early Universe, at an age of about 380.000 years when it

became transparent for photons. An expansion of the observed fluctuations in spherical harmonics is shown in fig. 1.3. The main peak of this power spectrum around a multipole moment of ~ 250 refers to the sound horizon, the largest possible standing wave at the time of recombination. The parameters of the ΛCDM model can be derived by fitting it to the observed power spectrum as [1]:

$$\Theta_{\mathrm{mc}} = (1.04093 \pm 0.00030) \cdot 10^{-2} \tag{1.4}$$
$$\Omega_{\mathrm{cdm}} h^2 = 0.1188 \pm 0.0010 \tag{1.5}$$
$$\Omega_{\mathrm{b}} h^2 = 0.02230 \pm 0.00014 \tag{1.6}$$
$$H_0 = (67.74 \pm 0.46) \ \mathrm{km/s/Mpc} \tag{1.7}$$
$$n_{\mathrm{s}} = 0.9667 \pm 0.0040 \tag{1.8}$$
$$\Omega_{\mathrm{m}} = 0.3089 \pm 0.0062 \tag{1.9}$$

with the dimensionless Hubble parameter $h = H_0/(100 \ \mathrm{kms}^{-1}\mathrm{Mpc}^{-1})$, the angular scale of the sound horizon Θ_{mc}, the baryon density Ω_{b}, the cold dark matter density Ω_{cdm}, the Hubble constant H_0, the scalar spectral index n_{s} and the matter density Ω_{m}. Furthermore, the age of the Universe is derived as 13.799 ± 0.021 Gyr. The ΛCDM model with the given parameters is the best fitting model for the measured data. By inserting the value for h in eq. 1.5 and 1.6, one can directly obtain the fractional abundance of cold dark matter and baryonic matter in our Universe as 25.9% and 4.8%, respectively.

1.2 Candidates for dark matter from particle physics

Constraints on the nature and characteristics of dark matter can be derived directly from the evidence and observations on galactic scales and cluster scales. The particle candidate must be

stable: Dark matter particles have to be stable on time scales of galactic ages and cluster ages of $\mathcal{O}(10^{17}$ s), otherwise these systems would not remain in a confined state. Furthermore, we observe clusters and galaxies of different ages but with consistent shapes, thus they do not crumble. Observations with the Fermi-LAT satellite experiment put lower limits on the lifetime of dark matter by searching for a signal of a decay into b$\bar{\mathrm{b}}$ as $\mathcal{O}(10^{26}$ s) [26, 27].

non-baryonic: From the shape of the multipole expanded CMB power spectrum and the therein fitted ΛCDM parameters, we derive the dominant part of matter in the Universe as non-baryonic dark matter. The ratio of non-baryonic to baryonic matter is ~ 5.3.

electrically neutral: Any electric charge would imply electromagnetic interactions typically leading to visible matter. Nevertheless, there are models of charged massive particles (CHAMPs) exist, but these particles would spare the region of the galactic disk as a result of the magnetic field and the Fermi mechanism. However, CHAMPs can explain the missing satellite problem, i.e. the lack of dwarf galaxies [28]. To be compatible with the CMB power spectrum, the CHAMP mass needs to be $m_{\mathrm{CHAMP}} > 10^{11}$ GeV [29]. However, since their predicted absence in the galactic disk, CHAMPs can hardly be detected in a direct search experiment.

weakly interacting: Dark matter particles have to be gravitationall interacting. A weak interaction is also allowed and expected in many extensions of the standard model. Limits for a self-interaction cross section are discussed in section 1.1.1

cold or warm: Since hot (relativistic) dark matter (e.g. neutrinos) is mostly excluded by an observation of structures on a galactic scale and by N-body simulations because of
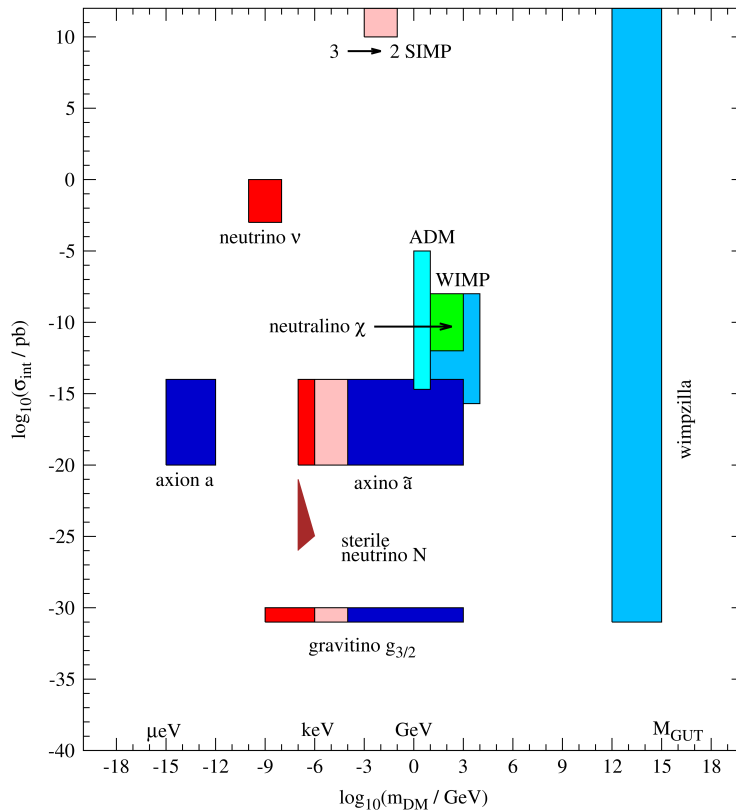
Figure 1.4: Overview of dark matter particle candidates with their expected interaction cross section and the particle mass shown in a double-logarithmic plane. The red, pink and blue colors represent HDM, WDM and CDM. Figure from [31].

a disagreement with structure forming processes [30]. But it can still be considered as a part of mixed dark matter scenarios.

The requirements listed above exclude all standard model particles as dark matter. An overview of candidates for particle dark matter beyond the standard model is given in fig. 1.4.

Wimpzillas are listed at the highest masses. A decay or annihilation of these particles into standard model particles would be a source of ultra high energetic cosmic rays, possibly exceeding the GZK cut off energy. This has not yet been observed [32].

Another non thermal dark matter candidate is the axion. These particles were postulated to solve the strong CP problem. The axion mass m_A is inversely proportional to the Peccei-Quinn symmetry-breaking scale f_A:

$$m_A = 6 \text{ eV} \cdot \left(\frac{10^6 \text{ GeV}}{f_A} \right) \tag{1.10}$$

Axions as dark matter candidates are mostly described in the hadronic KSVZ model (Kim-Shifman-Vainstein-Zakharov)[33] or the GUT model DFSZ (Dine-Fischler-Srednicki-Zhitnitskii) [34]. Exclusion limits for both models were derived by EDELWEISS-II and are described in section 2.2.5. Further non-thermal dark matter candidates are referred as axion like particles, ALPs.

Neutrinos are shown in fig. 1.4, but as discussed before, disfavored because of their relativistic character as hot dark matter which is not in agreement with the observed structure formation.
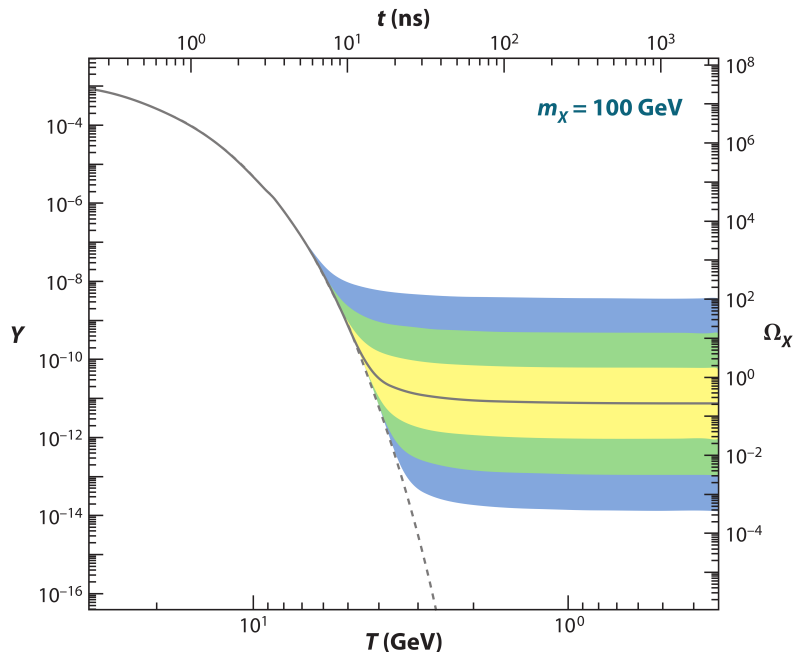
Figure 1.5: Comoving number density Y (left) and resulting relic density Ω_χ (right) for a 100 GeV WIMP as a function of the temperature T (bottom) and age of the Universe (top). Colored regions show the uncertainty of the cross section by a factor of 10, 100 and 1000. Figure from [41].

A hypothetical fourth neutrino flavor in form of a sterile neutrino can be considered as a dark matter particle. Such neutrinos are discussed as cold, warm and hot dark matter [35]. If sterile neutrinos mix with the known three flavors, a detection in a neutrino oscillation experiment would be possible. These experiments operate multiple neutrino detectors at different distances to a nuclear reactor which is a source of neutrinos. Limits for a sterile neutrino mixing are published among others by the Daya Bay collaboration with an excluded mass range of 10^{-3} eV$^2 < \Delta m_{41}^2 < 0.3$ eV^2 [36]. Sterile neutrinos with a higher mass of $\mathcal{O}(keV)$ are predicted to decay into the lighter standard neutrino by emitting a photon [37] which can be detected as an x-ray excess by the indirect dark matter searches. Such lines are currently discussed for the Andromeda and Perseus galaxies [38].

A non-particle dark matter candidate are the so called Massive Astrophysical Compact Halo Objects (MACHOs). These can be unconfined planetary objects and brown dwarfs, stars that emit almost no light and are thus not observed. Dedicated surveys searching for MACHOs constrain the maximum possible mass within these objects to a maximum of 20% of the dark matter mass [39, 40]. Furthermore, their baryonic nature contradicts the predomination of non-baryonic dark matter derived by the CMB.

1.2.1 WIMPs - Weakly Interacting Massive Particles

Weakly Interacting Massive Particles (WIMPs) are a generic set of dark matter particles beyond the standard model (SM). In supersymmetric models (SUSY), bosonic particles with an integer numbered spin can be converted in fermionic particles with a half-integer numbered spin. The model with the smallest number of additional new particles is known as the minimal supersymmetric standard model (MSSM), where to each SM-particle one SUSY partner with a higher mass is defined as a super-multiplet. SUSY models would predict a proton lifetime on timescales of 10^{-2} s. In order to keep the SUSY models in agreement with the experimentally observed lifetime of $> 10^{33}$ yr [42], the concept of

R-parity is introduced:

$$P_{\mathrm{R}} = (-1)^{3(B-L)+2s} \tag{1.11}$$

with the baryon number B, the lepton number L and the spin s. With the preservation of this symmetry, the lightest SUSY particle (LSP) with $P_{\mathrm{R}} = (-1)$ can not decay into SM-particles with $P_{\mathrm{R}} = (+1)$, thus it is stable and a convenient candidate for a WIMP. A candidate for the LSP is the neutralino. This is a linear combination of the four SUSY particles bino, wino and two higgsinos [43].

WIMPs were thermally produced in early stages of the Universe. They have been in an equilibrium state with SM-particles via production and annihilation. As the Universe expanded, the temperature decreased until a critical temperature was reached at which WIMPs decoupled from SM particles. This is referred as freeze-out. Before the freeze-out, the rate of WIMP annihilation is proportional to the product of their density and their annihilation cross section $\sigma_{\mathrm{A}}(\chi\overline{\chi})$ at a WIMP moving speed v. The production rate decreased exponentially during the freeze-out to a value below the Hubble expansion. Since then, the WIMP density is almost constant:

$$\Omega_\chi h^2 \simeq \mathrm{const.} \frac{T_0^3}{M_{Pl}^3 \langle \sigma_{\mathrm{A}} v \rangle} \simeq \frac{0.1 \ \mathrm{pb} \cdot c}{\langle \sigma_{\mathrm{A}} v \rangle} \tag{1.12}$$

with the current CMB temperature T_0, the Planck mass M_{Pl}, the speed of light c, and the velocity-averaged annihilation cross section $\langle \sigma_{\mathrm{A}}(\chi\overline{\chi})v \rangle$.

1.3 Direct detection of dark matter

A direct detection of dark matter particles in a detector depends on the local WIMP density, the WIMP velocity and the cross section for the spin-independent or spin-dependent WIMP-nucleon interaction. The local galactic halo is derived from a model, e.g. equation 1.2 or 1.3. Following the overview in [44], the local dark matter velocity distribution $f(v)$ is:

$$f(v)\mathrm{d}v = \frac{v\mathrm{d}v}{v_{\mathrm{e}}v_0\sqrt{\pi}} \left(\exp\left(-\frac{(v-v_{\mathrm{e}})^2}{v_0^2}\right) - \exp\left(-\frac{(v+v_{\mathrm{e}})^2}{v_0^2}\right) \right) \tag{1.13}$$

with the velocity of the Sun around the galactic center $v_0 = 220$ km/s and the mean earth orbital velocity $v_{\mathrm{e}} = 30.29$ km/s [45]. Thus, the WIMP flux through a detector with a WIMP mass $m_\chi = 100$ GeV is:

$$nv = \frac{\rho v}{m_\chi} \approx 10^5 \frac{1}{\mathrm{cm}^2\mathrm{s}} \tag{1.14}$$

The local WIMP flux has an annual modulation since the earth's orbital velocity changes direction with respect to the Sun orbital velocity resulting in a galactic WIMP wind of [46]:

$$v(t) = 220 \ \mathrm{km/s} \cdot (1.05 + 0.07 \cdot \cos(t - t_{\mathrm{m}})) \tag{1.15}$$

where t is in the unit of year and $t_{\mathrm{m}} = \mathrm{June}, 2\mathrm{nd}$ marks the day of maximum WIMP wind, when the earth's orbital velocity vector points in the same direction as the Sun's orbital velocity vector.

The recoil energy for an elastic scattering on a nucleus with the angle θ is

$$E_{\mathrm{rec}} = \frac{m_\chi^2 M}{m_\chi + M} \cdot v_{\mathrm{rel}}^2(1 - \cos\theta) \tag{1.16}$$

with a typical WIMP mass $m_\chi = 100$ GeV, the nucleus mass $M = 65.2$ GeV, the a relative WIMP-nucleus velocity $v_{\mathrm{rel}} = 300$ km/s, the maximum recoil energy is derived to be $E_{\mathrm{rec}} = 65$ keV.

The differential recoil spectrum is:

$$\frac{dR}{dE_{\mathrm{rec}}} = N_{\mathrm{T}} \frac{\rho_\chi}{m_\chi} \int_{v_{\mathrm{min}}}^{v_{\mathrm{esc}}} f\left(v(t)\right) \frac{d\sigma}{dE_{\mathrm{rec}}} \mathrm{d}^3 v \tag{1.17}$$

with the maximum escape velocity for the Milky Way $v_{\mathrm{esc}} = 533$ km/s [47] and the number of target nuclei per unit of mass N_{T}.

In SUSY models, WIMPs can couple to standard model particles via weak interaction processes either via a scalar coupling (spin independent, SI) or via an axial vector coupling (spin dependent, SD). In the spin-independent case the protons and neutrons of the target atoms in the detector are contributing equally to the cross section, whereas for a spin-dependent interaction, in general only isotopes with an odd number of nucleons contribute:

$$\frac{d\sigma}{dE_{\mathrm{rec}}} = \frac{M}{2\mu_t^2} \cdot \left(\sigma_0^{\mathrm{SI}} F_{\mathrm{SI}}^2(E) + \sigma_0^{\mathrm{SD}} F_{\mathrm{SD}}^2(E)\right) \tag{1.18}$$

where M is the target nucleus mass, μ_{t} the reduced mass for the target-WIMP system and F_i the spin-dependent and -independent form factors of the target nucleus. The spin-independent cross section can be described as

$$\sigma_0^{\mathrm{SI}} = \frac{4\mu^2}{\pi} \left(Z f_{\mathrm{p}} + (A - Z) f_{\mathrm{n}}\right)^2 \cdot F^2(q) \tag{1.19}$$

where μ is the reduced mass, Z the number of protons in the target atom and $f_{\mathrm{p/n}}$ the coupling strength of the WIMP to either neutron or proton. The form factor F depends on the momentum transfer q. In case of equal coupling strength of WIMP-proton and WIMP-neutron, the spin-independent cross section becomes proportional to the squared number of nucleons A in the target material.

For the spin-dependent interaction, the cross section results from a coupling of the dark matter particle to the total nuclear spin J of the target:

$$\sigma_0^{\mathrm{SD}} = \frac{32}{\pi} \mu^2 G_{\mathrm{F}}^2 \left(a_{\mathrm{p}}\langle S_{\mathrm{p}}\rangle + a_{\mathrm{n}}\langle S_{\mathrm{n}}\rangle\right)^2 \cdot \frac{J+1}{J} \cdot F_{\mathrm{S}}^2(q) \tag{1.20}$$

with the Fermi constant G_{F}, a form factor for the momentum transfer F_{S}^2. The coupling constants $a_{\mathrm{p,n}}$ define the WIMP-nucleon couplings for the proton and neutron spin, and $\langle S_{\mathrm{p,n}}\rangle$ the expectation values of their spin. Since a strong enhancement as $\sim A^2$ in the case of spin-independent cross section is not available for σ_0^{SD}, the achieved results for spin-dependent cross sections are typically three orders less sensitive.

An overview of different detecting channels for a WIMP-nucleus cross-section is given in fig. 1.6. The fundamental requirement for a detection is an energy transfer from the WIMP to the nucleus. The deposited energy is measured either as a phonon, a light or a charge signal. With a combined measurement of more than one of these channels, a discrimination between nuclear recoils and electron recoils is possible. The latter case is mandatory for the identification of background events. A huge number of dark matter search experiments was in operation during the last decade and is foreseen for the coming years. We will discuss here a selection that represents the different technologies.

1.3.1 Liquid noble gas based experiments

Liquid noble gas experiments use either a scintillation signal or a combination of a scintillation and a charge signal. Experiments with only scintillation signals and xenon as detector material are not able to discriminate between nuclear and electron recoils, thus have to be operated in an extremely clean environment without background. A strategy that is
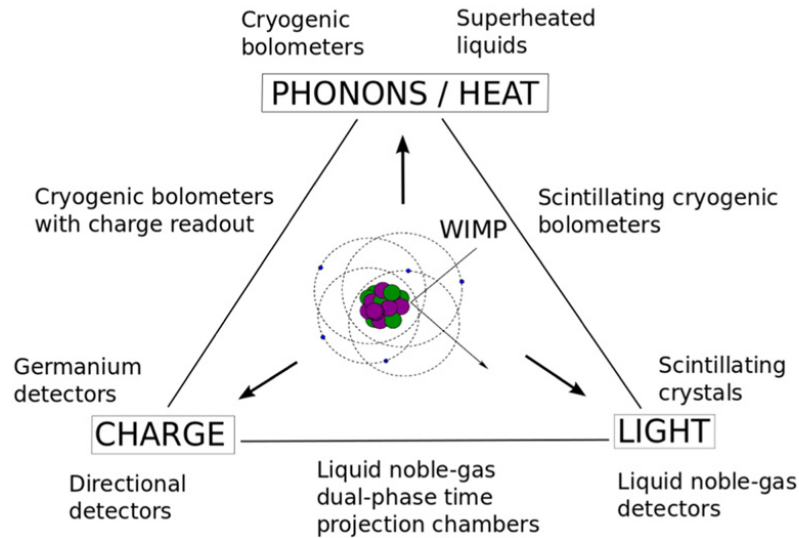
Figure 1.6: Overview of different channels for a direct detection of a dark matter particle. Figure from [48].

followed is to use a much higher total mass of detector material as in the actual sensitive volume, whereas the remaining liquefied gas is used as self shielding. These experiments have already reached the ton-scale size. The target material is either liquefied xenon or argon. The XMASS experiment [49] in the Kamioka laboratory (inside a mine) uses 835 kg ultra pure liquid xenon in the sensitive region of the detector. The scintillation is measured by PMTs (photomultiplier tubes), in total more than 700 channels sampled with up to 1 GHz. A comparable design but with liquid argon is followed by the DEAP-3600 experiment [50]. Since liquid argon is a brighter scintillator than xenon, argon based experiments can perform a pulse shape analysis as it is performed by DarkSide, in order to discriminate electron recoils and nuclear recoils with a rejection better than $1.5 \cdot 10^7$ [51].

Exemplary for noble liquid gas and two detection channels, namely a scintillation and a charge channel are the XENON100 [52] and XENON1T [53] experiments. A cylindrical detector chamber with the liquid and gaseous xenon is equipped with PMTs on the top and bottom faces. Additionally, electrodes are installed in two layers, creating an electric field along the z-axis of the detector volume. This makes the detector a Time-Projection-Chamber. A second and stronger electric field starts at the region of phase transition from liquid to gaseous xenon. An energy deposit is registered twice: First, by the scintillating xenon which emits ultraviolet photons of 175 nm wavelength. These photons are detected instantaneously by PMTs. This signal is also called S1 signal. Furthermore, the energy deposit creates electron-hole pairs. These are drifted by the electric field through the time projection chamber and once they reach the phase transition of liquid to gaseous xenon, they are accelerated and a second light emission event is artificially created. The second signal is also called S2 signal. The charge drifting time is resolved by the time differences between S1 and S2 and the z-axis value of the event deposit is resolved. Furthermore, the amplitude differences of several PMTs at one side is used to determine a resolution in the xy-plane. Thus, a fiducial volume can be defined within the ultra pure xenon, which is surrounded and shielded by more xenon. The fraction $S2/S1$ of the amplitudes of the registered events is used to discriminate between nuclear recoils and electron recoils. Technically very similar and following the same detection technology are the experiments LUX[54] and LZ[55]. The liquid xenon experiments are currently the most sensitive experiments for high WIMP masses, whereas for low WIMP masses the solid state detectors are superior.

1.3.2 Bubble chambers in direct DM search

Bubble chamber based dark matter searches are relatively new in the scope of direct search experiments. Different liquid materials like CF_3I or C_3F_8 are controlled by pressure variation in a super heated state. An energy deposit can create a bubble. By controlling the pressure and temperature of the liquid, it is possible to shift the necessary energy threshold that is needed for a bubble creation. Since the stopping power from nuclear recoils is higher than from electron recoils the pressure can be configured in a way that only nuclear recoils create bubbles.

In case of the PICO-60 experiment [56], a bubble chamber with 30 cm in diameter and a length of 1 m is read out by two 1088×1700 CMOS cameras, that are placed at a stereo angle of $60°$ and take photos with a frame rate of 50 Hz. LED strobe lights are used to illuminate the chamber synchronized to the camera shutter. Due to the stereoscopic alignment of both cameras is a three dimensional event localization realized. Additionally, a set of 13 piezoelectric acoustic transducers is used to record the sound emission of the bubble nucleation. In the data analysis are the sound and optic data used to define fiducial volumes. The camera signal is used as a trigger. The main part of the data analysis is performed on the acoustic information, whereas the camera signal is used to determine the event position.

Due to the large amount of fluorine in the target liquid and the fact that F nuclei have an unpaired proton, the bubble chamber experiments are sensitive for the spin-dependent WIMP-nucleon cross section.

The PICO collaboration is currently working towards demonstrating that a next generation bubble chamber with 250 l C_3F_8 detection volume can be operated with low backgrounds and high operational reliability.

1.3.3 Solid state detector experiments

The experiments based on solid state detectors can use phonon channels and, depending on the detector material, additionally a charge or a scintillation channel. SuperCDMS [57] and EDELWEISS combine phonon and ionization channels in germanium detectors, whereas CRESST [58] relies on phonon and scintillation channels with $CaWO_4$ detectors. From a technical point of view, CRESST has two heat channels, since the physical scintillation signal is dissipated as heat in a light absorber, which is read out via a thermometer. The light absorber is a silicon-on-sapphire waver which exploits the excellent phonon transport properties of sapphire [59]. The CRESST thermometers are Transition Edge Sensors (TES) that are read out via a Superconducting Quantum Interference Device (SQUID). Compared to the EDELWEISS NTD type thermometers with a high resistance of $\mathcal{O}(M\Omega)$, a SQUID readout has the advantage of a low impedance of $\mathcal{O}(10 \ \Omega)$. TES type thermometers enable time resolved phonon channels to obtain spatial event information.

SuperCDMS has ionization channels similar to those of EDELWEISS. However, they use a TES-SQUID combination as phonon channel and exploit the time resolved information [60].

1.4 Status of direct search experiments

An overview of the actual status of direct search experiments is shown in fig. 1.7. The spin-independent cross section is plotted versus the WIMP mass. For high WIMP masses the liquid xenon based experiments LUX followed by XENON100 are currently setting the best limits. For the low mass WIMP sector solid state experiments are better qualified. The predominance from solid state detector experiments for low-mass WIMPs results the
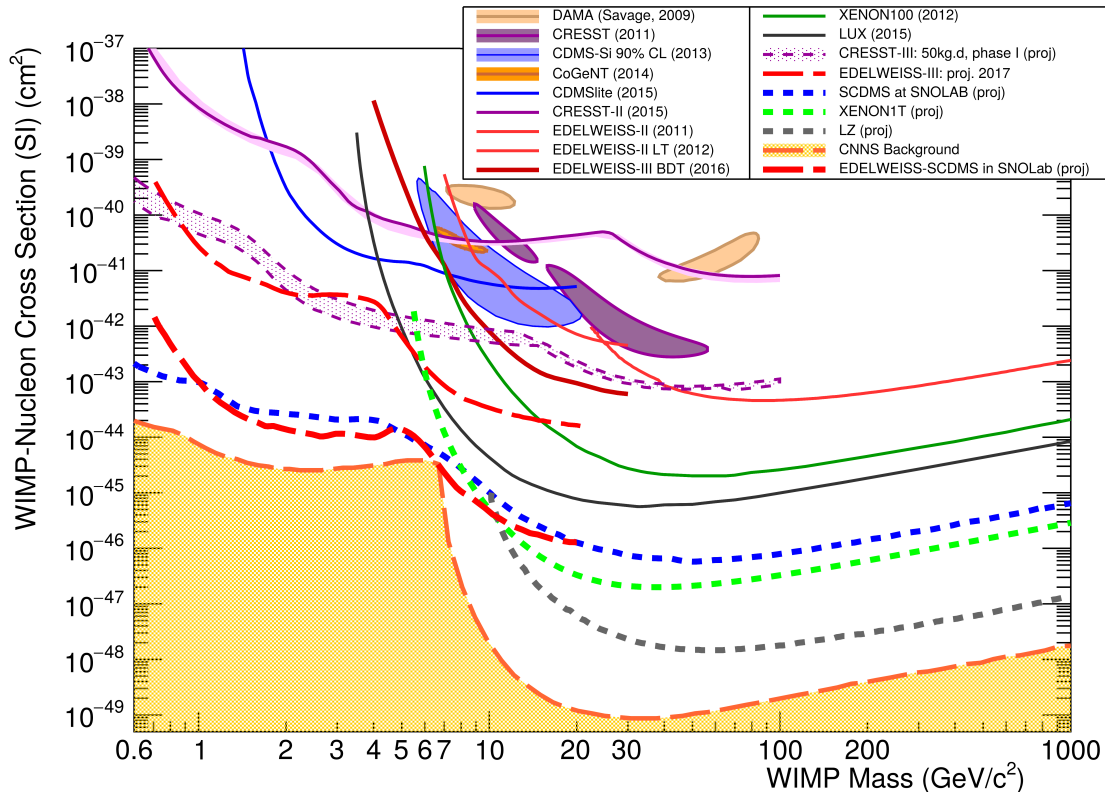
Figure 1.7: Overview of the parameter space of the spin-independent WIMP-nucleon cross section versus WIMP mass investigated by different experiments. Solid lines are 90% C.L. exclusion limits, dashed lines are projections for future experiments. The closed areas refer to signal regions of dark matter claims. The yellow area marks the neutrino-floor, where signals from coherent neutrino-nucleus scattering are expected as almost irreducible background.

smaller achievable registration threshold and from the smaller nucleus mass compared to xenon. This effect can be seen at the exclusion curve of CRESST-III (violet). $CaWO_4$ as a detector material has three different weighted nuclei, thus 3 different sections in the exclusion curve can be seen. The same effect explains the two completely separated signal regions of DAMA (closed beige contour) and CRESST (2011)(closed violet contour).

At one point the experiments will start to detect an almost irreducible background due to coherent neutrino scattering on the target nuclei. The sources of these neutrinos are solar neutrinos as a result of the ^7Be and ^8B production in the Sun, which will mimic a low-mass WIMP signal. For WIMP masses above 10 GeV these are atmospheric and DSNB neutrinos.

At the time of completing this thesis, no WIMP signal exists that is not excluded by at least one other experiment and no coherent neutrino scattering is observed.

1.5 Production of dark matter

Colliders, such as the Large Hadron Collider at CERN can produce a variety of particles inside a quark-gluon plasma that is created by parton collision with a center of mass energy up to $\sqrt{s} = 14$ TeV. If it is possible to create a SUSY particle, this could be likely the lightest one, thus a dark matter candidate. A dark matter particle would not be directly detected in the large detectors like ATLAS or CMS because of its weakly interacting
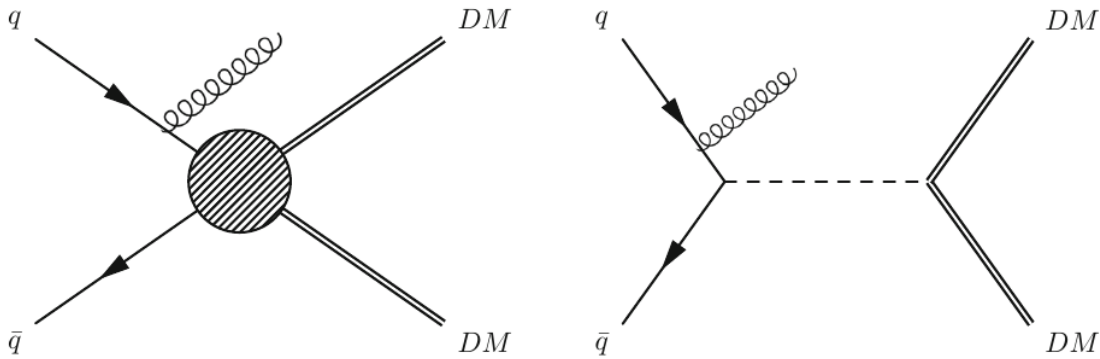
Figure 1.8: Feynman diagram for two possible dark matter production scenarios at a collider experiment. Left: Effective field theory with unresolved interaction vertex. Right: Description including a mediator particle exchange. The initial state radiation (spiral line) can be seen as a monojet event. Figures from [61].

nature. The signature of a dark matter particle would show up as an imbalance of the total momentum of all reconstructed particles in the transverse plane. The longitudinal energy is unknown in collider experiments, thus can not be used for analysis. The magnitude of the imbalance is the missing transverse energy. The missing energy signature is caused by the not visible dark matter candidate, whereas the detectable energy in form of a monojet is the signature from initial state radiation that is emitted before the dark matter candidate is created (see fig. 1.8). The jet can be purely hadronic or with contributions from bosons (γ, W, Z).

Collider production is, in comparison to direct search experiments, more sensitive to small dark matter particle masses and to spin-dependent interactions because the observed monojet is independent from the dark matter candidate's cross-section. Up to date, no SUSY particles were discovered at the LHC. A discovery would still keep the question open whether the produced invisible particle is the same type of matter that we suspect to see in cluster and galaxy dynamics, as well as in the CMB power spectrum.

1.6 Indirect detection of dark matter

Indirect detection of dark matter is performed by searching for a decay or annihilation signal within cosmic rays. The annihilation rate of dark matter exponentially decreases in the freeze-out scenario until the relic density is reached. The remaining annihilation rate is higher in regions where the dark matter density ρ_χ is higher.

Signals of dark matter annihilation are searched with earth-bound experiments by Imaging Atmospheric Cherenkov Telescopes, such as H.E.S.S.[62], MAGIC[63] or VERITAS[64] and the planned Cherenkov Telescope Array CTA[63]. The satellite based Fermi-LAT experiment has reported a possible signal from dark matter annihilation in photons at 130 GeV [65] which significance reduced after taking earth-limb photons into account [66].

An excess from 8 to 275 GeV in the positron-to-electron fraction $N_{e^+}/(N_{e^-} + N_{e^+})$ was reported by the PAMELA satellite experiment [67] and later confirmed by the AMS-02 experiment [68] on the International Space Station ISS. However, if this would be a dark matter annihilation signal one could expect a similar excess in the proton-to-antiproton channel, which is not measured.

The IceCube detector at the south pole station has searched for muon neutrinos from dark matter annihilation inside our Sun. All final state particles of a dark matter annihilation would be confined inside the Sun except neutrinos. A signal was not found, but exclusion

limits for spin-independent and spin-dependent WIMP-proton cross sections could be derived [69].

Another indirect detection method is given with the Greisen–Zatsepin–Kuzmin limit (GZK limit) which is an upper limit for particles propagating through the Universe. Particles with higher energy can couple to the photons of the CMB and thus dissipate their energy. The Universe is not transparent above this energy limit of $5 \cdot 10^{19}$ eV. Thus, if we could detect an event in a cosmic ray shower that has a higher primary particle energy, the primary particle must have been created close to us. Since sources or cosmic accelerators that could achieve this are not existing in our neighborhood, such a signal would likely come from a dark matter annihilation. However, such a GZK limit exceeding event was not detected by the Pierre Auger observatory [32].

2. EDELWEISS experiment and potential of time resolved ionization signals

The EDELWEISS experiment as other dark matter search experiments, has an expected rare event rate from dark matter signals to be distinguished from the much higher rate of background events. To achieve this goal, it is essential to avoid background events where possible and to identify remaining background events with the best efficiency. The complete experimental setup is designed by following these two principles. In 2009 it was demonstrated in [70] that a potential of time resolved ionization channels for background rejection is possible. Within this thesis, these channels have been installed for the first time at the experimental site of EDELWEISS and during 2015 more than 300.000 events have been recorded and analyzed, which is detailed in section 4.

After the EDELWEISS-II phase reached its limitations with the given background situation, the experiment was enhanced with a further reduced background and improved shielding (section 2.1.2). A completely new detector design (section 2.2.6) and a larger exposured mass is used in EDELWEISS-III. Furthemore, a new integrated DAQ system has been installed within the framework of this thesis (section 3), which brings an FPGA based trigger for the event based readout of the time resolved ionization channels.

To improve the sensitivity for the low-mass WIMP sector, the analog part of the detector biasing and readout electronics was upgraded to enable detector voltages of up to 140 V instead of 20 V (section 2.4). First results of this NTL amplified mode are presented.

2.1 Experimental setup

2.1.1 Laboratory

The EDELWEISS experiment is installed in the LSM (**L**aboratoire **S**outerrain de **M**odane, underground laboratory of Modane). The laboratory is in a side corridor, behind an emergency shelter, inside the Fréjus automobile tunnel in the Alps. The rock overburden of 1780 m reduces the cosmic muon flux by a factor $> 10^6$ to a remaining flux of 5 muon/m^2/day [71–73]. Since rock is different everywhere, the unit m w.e. (meter water equivalence) is preferred. The overburden of the LSM is 4800 m w.e. Access to the laboratory is possible with standard automobiles and trucks, which is an advantage for bringing larger parts to the experiment, compared to an elevator of a mine.
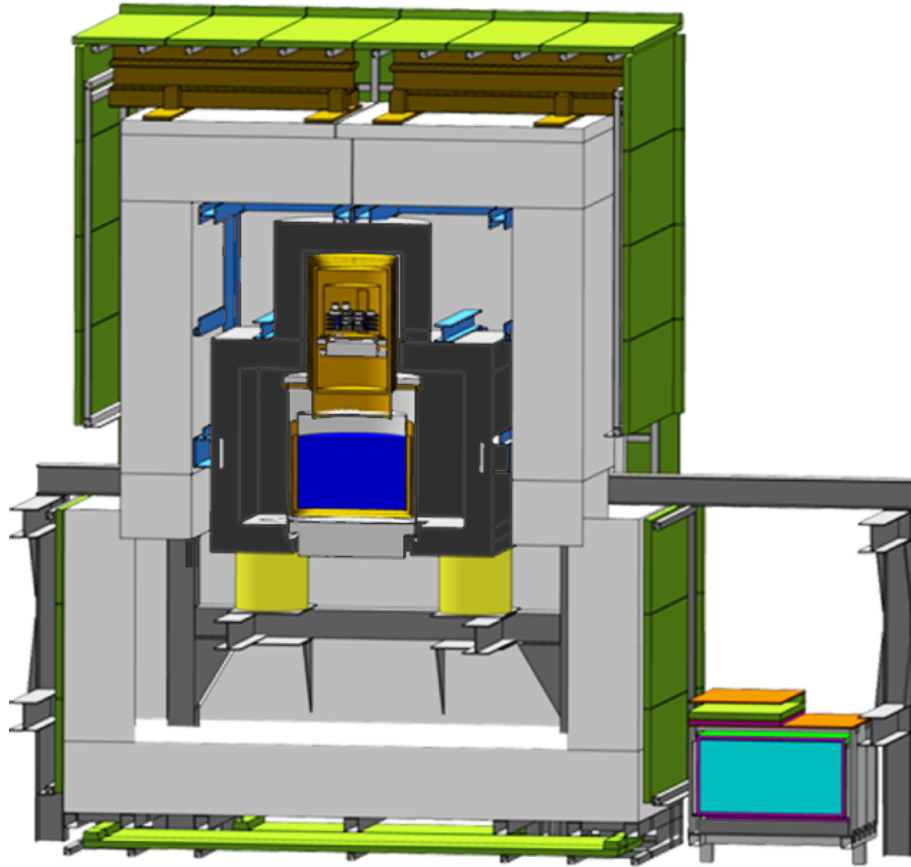
Figure 2.1: Cross-sectional view of the shields in EDELWEISS. Panels of the muon veto system (green), 50 cm of polyethylene (PE) (white), 20 cm lead (grey). The neutron counter (lower right corner) has been removed for EDELWEISS-III.

Inside the laboratory is a class 10000 clean room ($<$10000 particles with 0.5 µm per ft^3) installed. Additional, nitrogen N_2 flushed boxes are used for detectors stored outside the cryostat. The laboratory offers air conditioning and ventilation system that exchanges the complete laboratory volume of air every 1.5 h [74]. The later is important to reduce the radon background. The gaseous ^{222}Rn is created as a decay product of ^{238}U which is present in the rock. The radon level in the laboratory is $\sim$ 20 Bq/m^3 air and $\sim$ 10 Bq/m^3 inside the clean room. A radon trapping facility produces deradonized air which is used to flush the volume between the cryostat surface and the innermost part of the external shielding. The resulting radon activity is $<$ 20 mBq/m^3.

Furthermore, the LSM offers a fast, reliable and modern network infrastructure with sufficient bandwidth to remote control and monitor the experiment. Thus, human interventions at the experimental site are necessary only once per week for helium refills.

2.1.2 Shielding of the detectors

The outermost shielding is naturally the rock itself as described before. The artificial shielding around the detectors are arranged in two levels. The ground level below the clean room, housing the helium dewar and several supporting structures. The upper level inside the clean room houses the part of the cryostat with the detectors inside the experimental chamber and the readout electronics. The upper level of the shields is mounted on rails and can be opened into two halves. This is a crucial feature of the design, enabling a fast and easy access to the readout electronics and the cryostat. A LASER based distance
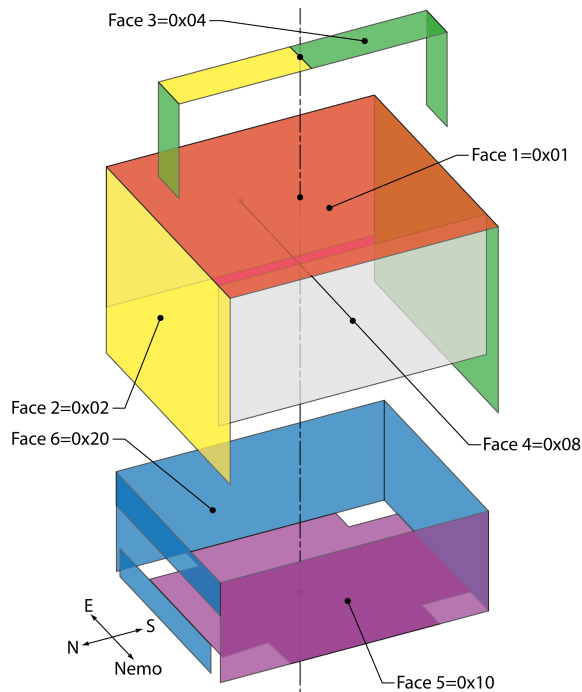
Figure 2.2: The muon veto system covering all faces of the experimental setup. Only minor spare regions are uncovered, such as cryogenic lines and steel supporting structure. The gap from the opening mechanism in the top side is additionally covered by extra modules. The modules are grouped and read out as "face bits". See text and section 3.1.3.

measuring system monitors the position of the two openable halves and openings are tagged inside the data.

The outermost part of the shields is an active muon veto system. In fig. 2.1 it is shown as the green panels. In reality, these modules are covered by a black plastic foil and are not green. 46 individual veto modules are used to cover the complete experimental setup corresponding to a surface of 100 m^2. Each muon veto module is made of an ashlar shaped plastic scintillator. On both end caps are four 2 inch photo multiplier tubes installed. These modules were adopted from the previous KARMEN experiment [75]. Each group of PMTs is individually biased with a HV of approx -1500 V that is adjustable. Adjustments can for instance compensate drifts due to aging effects. The geometric efficiency to detect a muon by requiring a detection by at least one module is $\sim 98\%$ [73, 76]. The remaining 2% are caused by small gaps in the veto geometry. However, muons passing through such gaps can still be detected by their electromagnetic and hadronic showers. Since most muons come from the top side, four additional modules cover the small gap (few mm wide) that comes from the opening mechanism. Furthermore, these additional modules are equipped with LEDs to artificially stimulate the scintillator and determine the long term stability of the setup.

The muon veto modules are organized in groups that correspond to one face of the setup. All six faces of the experiment are covered (see fig. 2.2). The status of each face is readout every 10 µs and further described in section 3.1.3. A rejections of muon induced events is performed within the offline analysis based on the time stamp of muon veto events. With the facebit readout integrated into the main DAQ system, it is possible to trigger EDELWEISS detectors on muon candidates.

Next to the muon veto comes a layer of polyethylene (PE). In fig. 2.1 and in reality white. With a thickness of at least 50 cm and a total mass of 35 tonnes, it moderates neutrons.
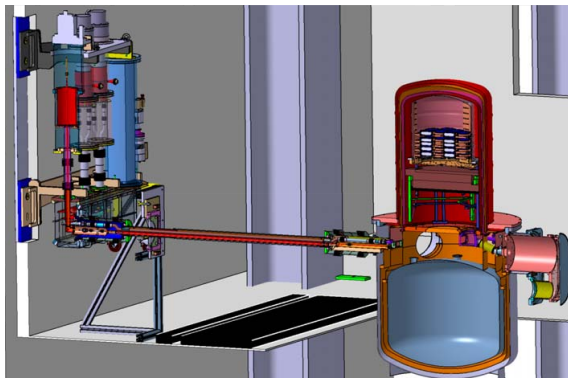
Figure 2.3: Cross-sectional view of the EDELWEISS cryostat connected by a cryoline to thermal machines mounted on the cavern wall to reduce vibrations and radioactive background inside the shields.

Neutrons are either produced by cosmic muons passing through the rock, or by spontaneous fission and (α,n) reactions from uranium and thorium inside the rock. Muon induced neutrons are produced by electromagnetic interactions of muons with nuclei in the rock and the materials of the experimental setup, especially lead. Muon induced neutrons have been investigated within the EDELWEISS-II phase [77, 78] (see section 2.2.5).

The activity by spontaneous fission of ^{238}U and ^{232}Th have been measured for the rock and the concrete of the laboratory. Uranium has an abundance of (0.84 ± 0.2) ppm in the cavern surrounding rock and (1.9 ± 0.2) ppm in the concrete. The values for thorium are (2.45 ± 0.2) ppm in the rock and (1.4 ± 0.2) ppm in the concrete [79].

Measurement with a ^{3}He proportional counter presented in [80] have found a factor 2 variance between the neutron flux on different spots inside the underground laboratory. Therefore the local 4π-flux inside the clean room, but outside the shields is measured as $\Phi = (3.57 \pm 0.05^{\mathrm{stat}} \pm 0.27^{\mathrm{syst}}) \cdot 10^{-6}$neutrons/cm^2/sec [80]. This neutron flux is reduced by the polyethylene. Geant4 based simulations reported in [74] have found that 50 cm of polyethylene attenuate the flux of fast neutrons by 5–6 orders of magnitude above 1 MeV.

The next shield is constructed of 40 tonnes lead and has a thickness of 20 cm. In fig. 2.1 this can be seen as dark grey elements around the cryostat. The lead shields against γ. Since lead naturally contains radioactive isotopes, mostly ^{210}Pb, ^{238}U and ^{232}Th, it constitutes to the background. Therefore, the innermost 2 cm are made of ancient lead, discovered in a sunken Roman ship. The abundance of ^{210}Pb with a half-life of $t_{1/2} = 22.3$ a is decreased and the remaining activity below 120 mBq/kg [74], whereas the conventional lead has an activity of (24 ± 1) Bq/kg [74]. The small spacing volume between the ancient lead and the cryostat is flushed with the deradonized air as described in section 2.1.1. The outside copper screen of the detector chamber on top of the cryostat is covered with an additional polyethylene shield. The analog readout electronics (bolometer boxes), that can be seen in the foreground of fig. 2.4 are covered topped with wide bars of polyethylene, since their PCBs have been found to be one of the prominent neutron sources. Further lead and polyethylene shields are installed inside the cryostat (section 2.1.3).

2.1.3 Cryostat

The cryostat used in EDELWEISS is an in-house designed (Institut Néel, Grenoble) ^{3}He/^{4}He dilution refrigerator with an effective volume of 50 liter for the detector setup. The cryostat is designed with the experimental volume on top of a helium dewar. In fig. 2.1 the dewar can be seen as the blue chamber in the center, the experimental volume with the thermal

detector chamber

internal PE shield at 1 K

internal lead shield at 1 K

FET boxes at 100 K

Bolometer boxes at 300 K
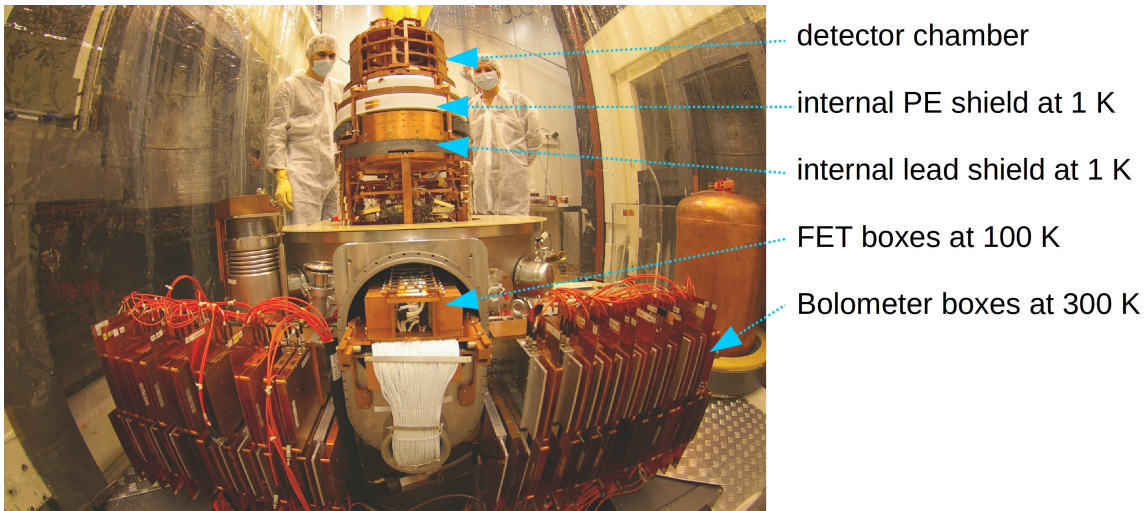
Figure 2.4: Picture of the opened cryostat with installed bolometer boxes and cold FET boxes. The internal lead and PE shield are visible below the detector chamber.

screens is above. Compressors and pumps are mounted to the cavern outside the shields and connected by a cryoline with mechanical decoupling elements. The part containing the experimental chamber is mounted on a pneumatic damper system to further reduce vibrations. This system can be controlled by a computer to change the level of the complete setup by a few mm, which can help in the case of disturbing vibrations.

A picture of the opened cryostat with mounted electronic components can be seen in fig. 2.4. The detector chamber is in the top of the cryostat and is covered by several copper screens like a matryoshka doll. The temperature decreases from the outermost screen at room temperature over 100 K, 50 K, 4.2 K towards 10 mK. In the standard operations the temperature at the detectors gaussian distributed and tuned to 18.000 mK with a variance of $\sigma_T = 2$ μK. With this temperature, a helium refill is once per week necessary, the consumption is ~ 10 l/day. The cooling power at the 100 K screen is 100 W, at the 50 K screen 20 W and 4.2 K it is 1.5 W.

To reduce the radioactive purity compared to EDELWEISS-II, new copper screens are introduced in EDELWEISS-III. They are constructed of extremely pure NOSV copper (AURUBIS AG [81]). This type of copper has been measured extensively at the Gran Sasso underground laboratory [82]. The expected γ and neutron induced background rates from radioactivity are 0.7-1.4 events in 40 detectors per year [74].

An additional shield of 14 cm roman lead is installed inside the cryostat at the 1 K stage (see fig. 2.4). Its main purpose is to shield the detectors from radioactive background of the bolometer box, the cold electronics (FET boxes at 100 K) and the connectors and cables at 1 K. For EDELWEISS-III the detector volume was slightly decreased to get space for an additional PE shield. This shield is mounted between the 1 K lead shield and the detectors, and has a temperature of 1 K. The polyethylene moderates neutrons that are reflected by the lead, thus further reduces neutron background. The remaining volume of the experimental chamber houses 12 towers. Each tower has 4 slots where a detector can be installed. They are thermally connected to the 10 mK screen, which serves as a thermal bath.
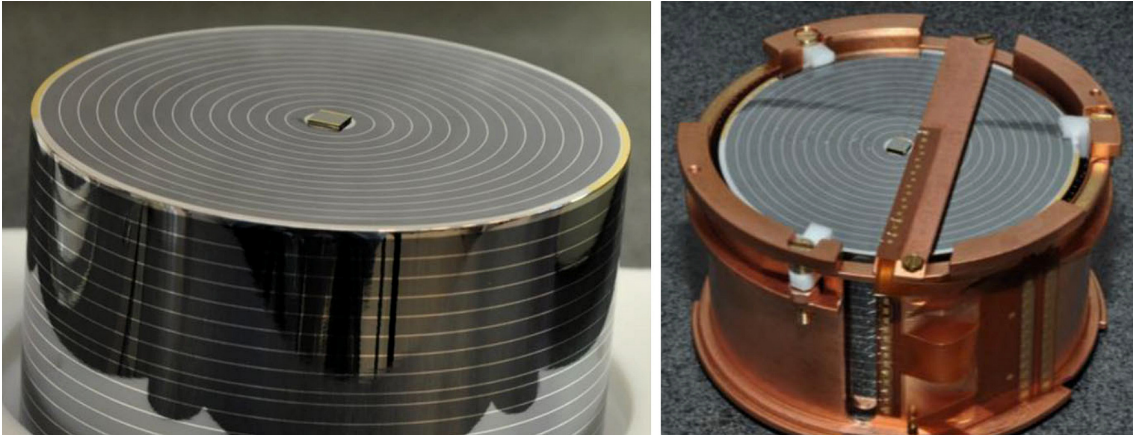
Figure 2.5: FID800 type detector as used in EDELWEISS-III with NTD glued to the central electrode. A second NTD is on the bottom side. The bright stripes are evaporated Al electrodes for charge collection. Right photo shows a wired detector fixed with Teflon clamps in a copper holder, ready for installation in the cryostat.

2.2 Germanium detectors in EDELWEISS

EDELWEISS relies on the simultaneous measurement of temperature (phonon) and charge signals in high purity monocrystalline Germanium detectors. The cylindric shaped detectors have a size of 70 mm in diameter and 40 mm in height. The detector mass is in the range of 820 g to 890 g [83]. The remaining density of impurities in the Ge absorber is $< 10^{10}/\text{cm}^3$. Each detector is equipped with two independent thermometers for measuring the phonon signal with 2 channels. Four groups of electrodes that can be biased independently between -10 V and $+10$ V generate an electric field for charge collection and measurement of the ionization energy. The detection and readout methods are explained, as well as the upgrade of the electrode biasing to ± 70 V for the NTL amplified mode.

2.2.1 Heat measurement with NTDs

The thermometers are NTDs, **N**eutron **T**ransmutation **D**oped Germanium resistors. They are produced by exposing Ge wavers to the neutron flux of a nuclear reactor by the following neutron capture induced processes[84]:

$$^{70}\text{Ge} + {}^1\text{n} \rightarrow {}^{71}\text{Ge} \xrightarrow{+\text{e}^-} {}^{71}\text{Ga}$$

$$^{74}\text{Ge} + {}^1\text{n} \rightarrow {}^{75}\text{Ge} \rightarrow {}^{75}\text{As} + \beta^-$$

$$^{76}\text{Ge} + {}^1\text{n} \rightarrow {}^{77}\text{Ge} \rightarrow {}^{77}\text{As} + \beta^- \rightarrow {}^{77}\text{Se} + \beta^-$$
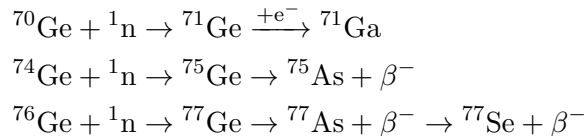
The process has to be controlled and results need to be checked because ^{71}Ga is a $\text{p}^+ - \text{type}$ doping, whereas ^{75}As is $\text{n}^- - \text{type}$ and ^{77}Se an $\text{n}^{2-} - \text{type}$ doping[85]. The doped wavers are cut in ashlar-formed pieces with a size of either $3 \times 5 \times 1$ mm^3 or $4 \times 4 \times 0.45$ mm^3. Afterwards Au electrodes are bonded to electrode pads. EDELWEISS uses two different geometries for these pads [86]. In one version two stripe shaped electrodes are placed on two opposing edges on the top face of the NTD. With the second used geometry, the electrodes are enlarged, wrapping around the edges and cover two complete side faces of the NTD, additionally to the small stripes on the top. The resistance of the NTDs is in the order of a few MΩ. An equipped EDELWEISS detector has a typical heat capacity of $C \approx 2\text{nJ/K}$. For an event with a deposited energy of E_{rec} in the absorber, the temperature rise of the detector, that has to be measured, is

$$\Delta T = \frac{E_{\text{rec}}}{C(T)}. \tag{2.1}$$
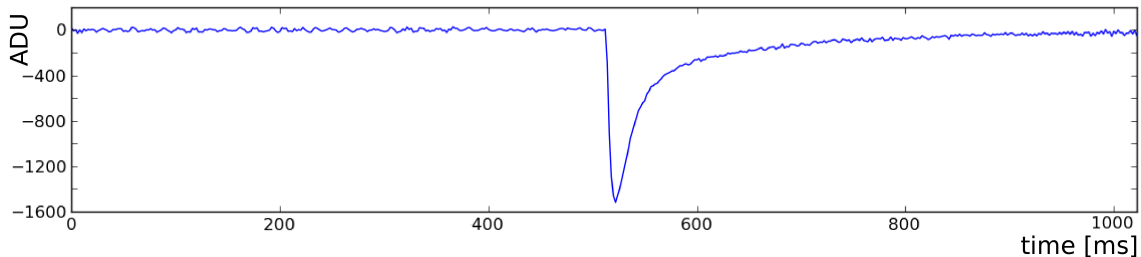
Figure 2.6: Heat pulse after demodulation and baseline subtraction. Figure from [90].

The heat capacity $C(T)$ is composed of the individual components whih are the Ge-absorber, the two NTDs and a hypothetical parasitic heat capacity. Further materials, such as the Al electrodes, the bonded wires and the glue for the NTDs are expected to be at least three orders of magnitude smaller than the considdered components and can be neglected. A detailed analysis of the thermal model of an EDELWEISS detector as a 6 body system is published in [87]. $C(T)$ follows the Debye law for low temperatures

$$C(T) = \frac{12\pi^4 N k_{\mathrm{B}}}{5} \cdot \frac{T^3}{\Theta_{\mathrm{D}}^3} \tag{2.2}$$

with the number of Atoms in the crystal N, Boltzmann's constant k_{B} and the material dependent Debye temperature for Ge [88]

$$\Theta_{\mathrm{D}}(\mathrm{Ge}) = \frac{\hbar\omega_{\mathrm{D}}}{k_{\mathrm{B}}} = 374 \pm 2 \text{ K}. \tag{2.3}$$

In EDELWEISS, the temperature is measured via the temperature dependent resistance of the NTD [89]

$$R(T) = R_0 \cdot \exp\sqrt{\frac{T_0}{T}} \tag{2.4}$$

with the NTD specific constants $R_0 = \mathcal{O}(0.1\ \Omega)$ and $T_0 = \mathcal{O}(1\ \mathrm{K})$. The NTD is biased with a modulated current and the temperature fluctuation is measured as a voltage variation as described in section 2.2.7. Typical EDELWEISS parameters are a total heat capacity of $C \approx 2$ nJ/K giving a temperature increase of $\Delta T \approx 0.1$ µK/keV. Pulses in the heat channel have a typical rise time of 10 ms, followed by two exponential decay phases. A fast decay with a time constant of 10 ms and a slow decay of 100 ms. An unprocessed raw data pulse is shown in fig. 2.16 and the more telling plot of a processed pulse is shown in fig. 2.6. The measured temperature increase is always a superposition of the initial recoil energy E_{rec} and E_{Luke}, the work carried out by the electric field on the drifting charges, the Neganov-Luke effect. In the classical operational mode, the additional energy is hold small by using low detector voltages of 8 V. Within EDELWEISS-III measurements are performed that use higher detector voltages of up to ~ 100 V to amplify the heat signal (see section 2.4).

The NTD requires a bias voltage which is discussed together with the readout channel in chapter 2.2.7. The EDELWEISS control software SAMBA (section 3.2.1) performs a continuous demodulation of the heat signals which is technically necessary to get a shape as shown in fig.2.6. SAMBA further uses the demodulated heat stream for event building by applying a trigger algorithm.

2.2.2 Ionization measurement in Ge detectors

Simultaneously to the heat signal EDELWEISS measures the ionization energy E_{ion} of each event. An energy deposit in the crystal lattice can create electron-hole pairs. The
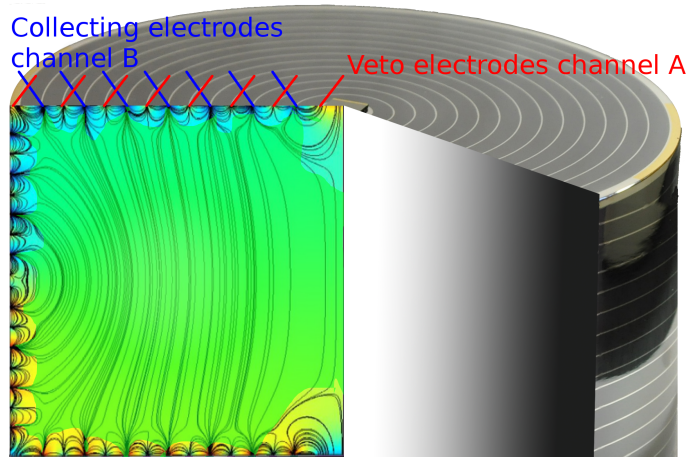
Figure 2.7: Visualization of the electric field of an FID detector. The electrodes on the upper half are typically set to +4 V on channel B and −1.5 V on channel A.

necessary energy to create one electron-hole pair by γ radiation in Germanium is [91]

$$\epsilon^\gamma = 2.96 \pm 0.02 \text{ eV} \tag{2.5}$$

or ~ 340 pairs/1 keV. The achievable sensitivity is limited by fluctuations in the number of created electron-hole pairs caused by an energy splitting in phonons and pair production and an inaccuracy of ϵ^γ [92]. It is given as

$$\Delta E = \sqrt{E_{\text{rec}} \epsilon^\gamma F} \tag{2.6}$$

with the material dependent Fano factor F. A theoretical calculation of the Fano factor for Ge is $F = 0.13$ [93]. With these numbers, $\Delta E \approx 20 eV$ is derived for $E_{\text{rec}} = 1$ keV. The technical realization of the ionization measurement is described in section 2.2.8.

To detect the ionization inside the crystal, an electrical field of ~ 2 V/cm is applied. In EDELWEISS-III are four groups of electrodes with individual voltages used to create an electric field parallel to the surface at the surface regions and parallel to the z-axis in the center or fiducial region (see figures 2.7, 2.10, 2.12). Charges created inside the fiducial field mainly drift to the electrode groups B and D, whereas charges created close to a surface ($1 - 2$ mm) are registered by additionally one of the electrodes in group A or C. The different electrode channels allow a discrimination in surface events and bulk events. A detailed description of the detectors is given in sections 2.2.5 and 2.2.6.

2.2.3 Combined heat and ionization measurement

The combined measurement of ionization and heat energy allows to discriminate events in nuclear recoils and electron recoils on an event-by-event basis. Therefore, the quenching factor or ionization yield

$$Q = \frac{E_{\text{ion}}}{E_{\text{rec}}} \tag{2.7}$$

is introduced as the fraction of ionization energy and recoil energy. The recoil energy is not directly measurable, since the total measured heat energy E_{tot} has to be corrected for the Neganov-Luke effect

$$E_{\text{tot}} = E_{\text{rec}} + E_{\text{Luke}} \tag{2.8}$$

which describes the work induced by the electric field on the drifting charges in form of additional heat

$$\begin{aligned} E_{\text{Luke}} &= N \cdot e \cdot U_{\text{BD}} \\ &= \frac{E_{\text{rec}} \cdot U_{\text{BD}}}{\epsilon_e^\gamma} \end{aligned} \tag{2.9}$$
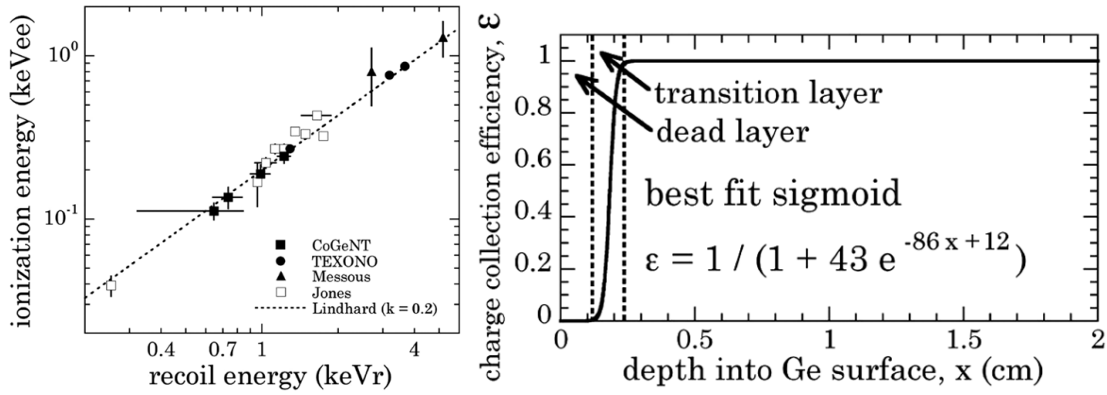
Figure 2.8: Left: Measurements [94–97] and Lindhard model [98] ($k = 0.2$) showing the ionization energy as a function of recoil energy. Right: Dead layer problem reducing the charge collection efficiency in the surface region of a CoGeNT point contact Ge detector. Figures from [97].

where the unit charge e is integrated into $\epsilon_e^\gamma \cdot e = \epsilon^\gamma$. The energy contribution from the Neganov-Luke effect is proportional to the applied bias voltage U_{BD} and the number of drifting charges, which itself can be written as $N = \frac{E_{rec}}{\epsilon^\gamma}$. Thus, the Luke effect can be used to amplify the signal in the heat measurement which is used for lowering the threshold and improving the sensitivity (see section 2.4).

Equation 2.8 and 2.9 can be combined as

$$E_{tot}^\gamma = \left(1 + \frac{U_{BD}}{\epsilon_e^\gamma}\right) E_{rec} \tag{2.10}$$

and for nuclear recoils with charge quenching

$$E_{tot}^n = \left(1 + \frac{Q \cdot U_{BD}}{\epsilon_e^\gamma}\right) E_{rec}. \tag{2.11}$$

The detectors are calibrated with a ^{133}Ba γ source and the quenching factor is normalized to be 1 for electron recoils

$$E_{heat}^\gamma = E_{rec} \tag{2.12}$$
$$E_{ion}^\gamma = E_{rec} \tag{2.13}$$

$$E_{heat}^n = \left(\frac{1 + \dfrac{Q \cdot U_{BD}}{\epsilon_e^\gamma}}{1 + \dfrac{U_{BD}}{\epsilon_e^\gamma}}\right) E_{rec}. \tag{2.14}$$

With this we can calculate the recoil energy as a function of the measured heat- and ionization energy and the known voltage of the collecting electrodes of typically $U_{BD} = 8$ V as

$$E_{rec} = \left(1 + \frac{U_{BD}}{\epsilon_e^\gamma}\right) E_{heat} - \frac{U_{BD}}{\epsilon_e^\gamma} E_{ion} \tag{2.15}$$

with $\epsilon_e^\gamma = 3$ V the mean electron-hole pair creation potential of Ge [99].

This quenching factor for nuclear recoils is described by the Lindhard model. The left part of fig. 2.8 shows multiple measurement and the theoretical prediction from the Lindhard model for Germanium. Events induced by γ interaction have a quenching value close to

1 (normalized), whereas a nuclear recoil band is defined at ~ 0.3. Neutrons and WIMPs interact with the Ge nucleus and appear in this band. However, γ events with an incomplete charge collection can appear in the nuclear recoil band as well. Therefore, it is essential to achieve a charge collecting efficiency of 1 which is difficult at the surface region. In EDELWEISS, events which are close to the surface are detected with the FID electrode design on the veto electrode and can be deselected in the analysis.

The right plot of fig. 2.8 shows the charge collection efficiency as a function of the event depth for a point contact Ge detector used in the CoGeNT experiment [97]. Regions below 2.5 mm suffer from an incomplete charge collection. An effect named *dead layer problem* [97, 100, 101] appears at the surface region of Ge detectors. Events that are very close to an electrode can suffer a loss of charge carriers. The measured ionization energy is smaller than it should be. Events where this effect occurred can be misinterpreted as nuclear recoils. Several methods to avoid this effect are discussed in [100]. In EDELWEISS the Aluminum electrodes are evaporated not directly on the Germanium crystal. An amorphous layer of hydrogenated Ge is deposited under the Al electrodes, whereas the spacing between the electrodes is not passivated [102].

Another difficulty with the detector operation are so called *leakage currents*. The electrodes are charged to the designated voltage and afterwards, the relay switch (S1 in fig. 2.17) is opened, making the electrode floating at its voltage. If there is a leakage current in the order of $\mathcal{O}(\text{pA})$ a Joule heating of a few MeV/s make the detector operation impossible. Due to carrier trapping, ambient space charges form at the location of the leak. Removing such distortions require a detector regeneration, which costs 1 h of data taking. A smaller leakage current is less critical but still increases the baseline noise level on all channels of the affected detector. Furthermore, the potential of the floating electrode will not remain stable for about 1 h of runtime between two maintenances in which the relay S1 is used to recharge the electrode. The leakage current problem is addressed in [102] and a solution is presented. Dry-edging of the detector (after installing the electrodes) with XeF_2 reproducibly solves the problem. Therefore, the detector is put into an expansion chamber where the XeF_2-preasure is adjustable. Further free parameters are the exposure time and the number of cycles of the process. The chemical reaction is

$$\text{Ge} + 2\text{XeF}_2 \rightarrow \text{GeF}_4 \uparrow + 2\text{Xe} \uparrow \tag{2.16}$$

with removable gaseous products. The edged detector has a rougher surface as before, which is visible by eye (see figures in [102]). Edged detectors still show leakage currents, but at much higher voltages. Within this thesis, leakage currents have been measured for the NTL amplified mode(see section 2.4).

2.2.4 Charge migration and ionization signals described by the Shockley-Ramo theorem

Simulation of charge migration inside the Ge absorber is an important stage for understanding the EDELWEISS typically pulse shape, especially for the time resolved ionization channel. Historically, Shockley and Ramo described an algorithm to calculate the induced current of moving electrons in vacuum tubes [103, 104]. Beginning from a radiation energy deposit in the absorber crystal, free charges q are created in form of a local cloud. Driven by the external applied electric field the charges drift towards the electrodes. During the drifting process the charges Q are created by influence in the electrodes and read out by the described electronic system (section 2.2.8). Q can be derived by computing

$$Q = \oint_S \epsilon \boldsymbol{E} \cdot \mathrm{d}\boldsymbol{S} \tag{2.17}$$
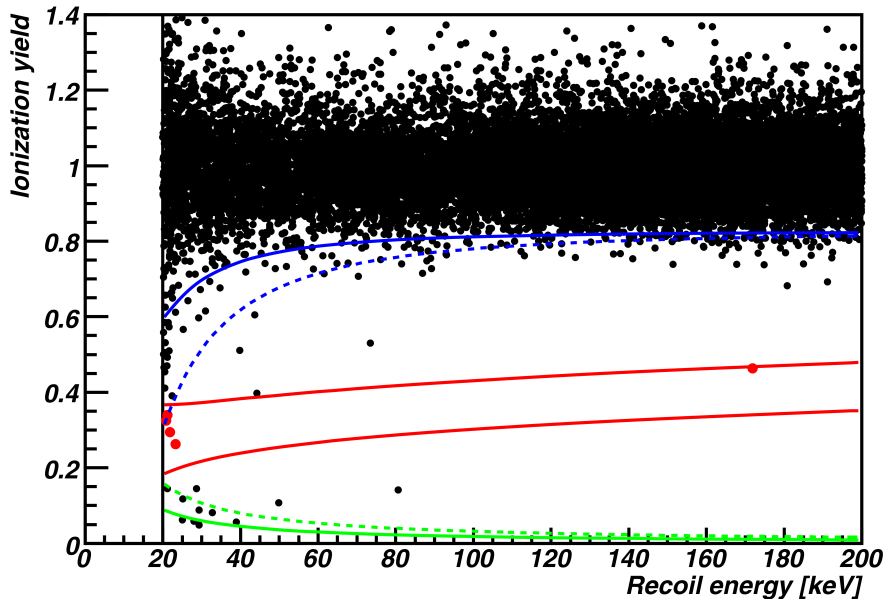
Figure 2.9: Q-Plot with 427 kg·d final results of EDELWEISS-II. Red marked band corresponds to 90% around Lindhard model prediction for nuclear recoils. 5 events are inside that region (red dots). The 99.99% one-sided rejection limits for electron recoils (worst limits - dashed blue line, avarage - continuous). The ionization threshold is drawn in green (worst - dashed, average - continuouse). Figure from [106].

with the instantaneous electric field $\boldsymbol{E}$ from the drifting charge q and the dielectric constant of the absorber material ϵ. This computation is time-consuming and expensive since the integral has to be evaluated for each charge q at each time step of the drifting process. The Shockley-Ramo theorem simplifies the complexity of the problem to

$$Q = -q\varphi_0(\boldsymbol{x}) \tag{2.18}$$
$$i = q\boldsymbol{v}\boldsymbol{E}_0(\boldsymbol{x}) \tag{2.19}$$

with the current i induced in the collecting electrode by q at the position $\boldsymbol{x}$ and the instantaneous velocity $\boldsymbol{v}$. Furthermore, the weighing potential and weighing field φ_0 and $\boldsymbol{E}_0$ are calculated under the assumption of removed space charges, target electrode raised to unit potential, and all other electrodes grounded. The weighing potential and field need to be calculated only once for the detector geometry, because they are independent of the actual drifting charges q. This is essential for an effective computer simulation based on time steps. A detailed review of the Shockley-Ramo theorem and a proof for its compatibility to be applied on semiconductor detectors is given in [105].

2.2.5 EDELWEISS-II detectors, limitations and final results

The EDELWEISS-II phase was completed in 2012 after 6 years. The major part of data taking was achieved during a 14 month run in 2009-2010. 10 ID type detectors as shown in fig. 2.10 center, were used. A total exposure of 427 kg·d was obtained, which corresponds to an effective exposure of 384 kg·d. The final Q-plot is shown in fig. 2.9. The red lines are parametrized by a 90% band around the function $Q(E_{rec}) = 0.16 \cdot E_{rec}^{0.18}$. The parameters 0.16 and 0.18 are derived by a neutron calibration with ^{252}Cf and are compatible with the Lindhard model prediction [99]. Within this nuclear recoil band appear 5 candidates for a WIMP interaction. The background expectation was 3 events. The 5 observed events are interpreted as a fluctuation of the background estimation and not as a WIMP signal.
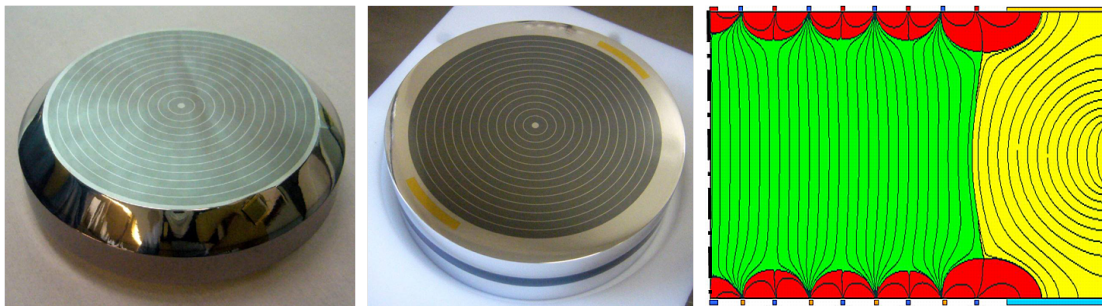
Figure 2.10: Interdigitized detectors as used in EDELWEISS-II with 6 ionization channels. Left: 360 g detector with beveled edges. Center: 400 g detector with edge wrapping guard electrodes. Right: Cross-sectional view with simulation of the electric field for the 400 g ID detector.

A value of the elastic spin-independent cross-section of $4.4 \cdot 10^{-8}$pb is excluded at a 90% confidence level for a WIMP mass of 85 GeV/c² [106].

In a combined analysis of the CDMS and EDELWEISS-II experiments data, an exposure equivalent of 614 kg·d was available. With a best sensitivity for a WIMP mass of 90 GeV/c², a cross-section of $3.3 \cdot 10^{-8}$ pb is excluded at 90% confidence level [107].

The background in form of muon induced neutrons inside the LSM was investigated during the EDELWEISS-II phase [77, 78]. A muon passing through the rock interacts by ionization, e^+/e^--pair production, bremsstahlung or deep inelastic scattering. Thus, starting a electromatgnetic and hadronic cascade that can include or via consecutive interactions create neutrons. Since neutrons are the most dangerous background for the EDELWEISS dark matter search it is important to analyze the abundance of these neutrons in the experiment location by measurement and simulation. This was performed by a muon veto module combined with a device filled with 1 m³ of Gd-loaded scintillator that detects and counts neutrons. The position of the neutron counter can be seen in the lower right corner of fig. 2.1. Muon-neutron coincidences can be detected in an offline analysis. The count rate of these coincidences was found to be ∼ 0.32/day and a yield for muon induced neutrons of $\langle Y \rangle = (2.71^{+0.98}_{-0.10}) \cdot 10^{-3}$ cm² g⁻¹ which was in good agreement with the MC simulation[77, 78].

The sensitivity of EDELWEISS for electron recoils at low energies enables us to search for axions and axion-like particles, ALPs. In [108] the analysis of a 448 kg·d dataset is presented, where axion-induced electron recoils down to 2.5 keV are accepted. A 95% exclusion limit for the axion-photon coupling $g_{A\gamma} < 2.13 \cdot 10^{-9}$ GeV⁻¹ and for the axion-electron coupling $g_{Ae} < 2.56 \cdot 10^{-11}$ is set. For DFSZ axions a mass range of 0.91 eV $< m_A <$ 80 keV and for KSVZ axions a mass range of 5.73 eV $< m_A <$ 40 keV is excluded.

A weakness of the ID detectors used in EDELWEISS-II was the electric field design for the outer region. In fig. 2.10 a cut through half of an ID detector is shown. The green field is where events drift charges to the collecting electrodes and a fiducial event is read out. The red regions drift charges to the veto electrodes and the events are rejected as surface events. The electric field in the yellow marked region is made by 2 additional ionization channels, the so called *guard electrodes*. It turned out that the design with the guard field can be problematic for charge reconstruction in certain rare but not negligible events. Double scattering γ events for instance, that deposit energy in in the fiducial volume and by a second interaction in the guard volume can lead to an incomplete charge collection. Thus the measured ionization energy E_{ion} for an event is smaller than it should be. In the Q-Plot this effect will move an event from the electron recoil band around 1 to an arbitrary smaller

Figure 2.11: EDELWEISS-II ID detector: calibration with ^{133}Ba source. 6 events out of $3.47 \cdot 10^5$ appear inside the nuclear recoil band (red lines). [109]

value that can be inside the nuclear recoil band. The calibration with γ events from the ^{133}Ba source showed 6 events inside the nuclear recoil band in a dataset of $3.47 \cdot 10^5$ events (see fig. 2.11) [109].

2.2.6 EDELWEISS-III detectors

The prototype of a new generation of Ge detectors was first tested in EDELWEISS-II and is now used as the standard detector in EDELWEISS-III. The crystals have a diameter of 7 cm and a hight of 4 cm. The mass is 820-890 g and the full surface is covered with interdigitized electrodes, giving it the name FID (**f**ully **i**nterdigitized electrode **d**etector). A cross-sectional view with a simulation of the internal electric field is presented in fig. 2.12 and fig. 2.7. Pictures can be seen in fig. 2.5. The fiducial volume marked as the green area in fig. 2.12 corresponds to a germanium mass of ~ 625 g. Thus, more then $70\% - 75\%$ of the invested Ge is used for WIMP search. The fiducial mass of an EDELWEISS-II 400 g ID detector was ~ 160 g or 40%. Furthermore the number of readout channels per detector could be decreased to 6 channels (2 heat + 4 ionization). The electrodes are made of Aluminum and evaporated onto the detector with the help of a shadow mask. Beside some special R&D detectors the standard width of the electrodes on top and bottom is 150 μm and the pitch between the center of two neighboring electrodes is 2.2 mm. The electrode in the center is massive and has a radius of 3 mm. The NTD is glued on top of the center electrode. The edges of the cylinder are wrapped by wider electrodes with a width of 1.2 mm on top (bottom) and 0.8 mm around the edge. On the detectors side are wider electrodes with a width of 200 μm and a pitch of 2.3 mm. At the geometrical equator of the detector are two neighboring electrodes with a reduced spacing of 1.4 mm (see fig. 2.12).

The electrodes are contacted by bonded gold wires. Biasing and readout is organized within four groups (channels) as shown in fig. 2.12. Every second electrode on the top and on the upper half of the side is concentrated in channel A which is a so called *veto* channel. These group of electrodes includes the center electrode with the NTD on top and the electrode wrapping around the edge of the cylinder. All remaining electrodes on this half of the detector are concentrated in channel B and are called *collecting electrodes* or *collectrodes*. The same principle is continued on the bottom half of the detector. There, channel C has the veto electrodes and channel D the collecting electrodes. In the normal

Figure 2.12: Cross-sectional illustration of an FID800 type detector with the biased electrode configuration and the different electric fields.

operational mode, also named FID mode, the collecting electrodes are set to $U_B = +4$ V and $U_D = -4$ V. Whereas the veto electrodes are on a potential of $U_A = -1.5$ V and $U_C = +1.5$ V. This voltage configuration results in parallel field lines in the fiducial volume. In the area close to surfaces are the field lines orientated semicircle like and pointing to the next veto and collecting electrode. Electron-hole pairs created in the bulk volume drift to the collecting electrodes B and D on both sides of the detector, whereas events closer to the surface are registered by a veto channel, A or C. Furthermore, charge carrier clouds can be generated in the transient region of surface field and fiducial field. These events are visible on three channels. The analysis uses cuts on the four ionization channels per event and can discriminate each event into a fiducial or non-fiducial event. All data taking for the time resolved ionization channel within this thesis was taken in the FID mode (see section 4). Another operational mode is the planar mode in which the electrodes of each side are at the same voltage $A = B$ and $C = D$. This configuation is mainly used for the NTL amplified mode with higher detector voltages (see section 2.4). The fact that each detector is now equipped with a second NTD thermometer brings a redundancy in case of an NTD failure, and it enables a better analysis of the event energy.

The quality of surface rejection with the FID design is shown in to be better than $4 \cdot 10^{-5}$ at $90\%CL$ above 15 keV recoil energy [110]. The results of the surface rejection analysis are shown in fig. 2.13. A ^{210}Pb source was used to produce more than 10^5 surface events. The decays are described by the chain

$$^{210}\text{Pb} \xrightarrow{\beta^-(4+16 \text{ keV})} {}^{210}\text{Bi} \xrightarrow{\beta^-(389 \text{ keV})} {}^{210}\text{Po} \xrightarrow{\alpha(5.3 \text{ MeV})} {}^{206}\text{Pb}(100 \text{ keV}) \qquad (2.20)$$

with the average β^- energies. The individual populations can directly be seen in the first plot with the given energies. The group around 100 keV recoil energy with a very low

Figure 2.13: First plot: Ionization yield as a function of recoil energy observed in two 800 g FID detectors exposed to 10^5 ^{210}Pb decays. Second: same data after after selection of fiducial events. The remaining events at 1 are mostly γ background. The 10 keV group comes from cosmogenic activation ^{68}Ge and ^{65}Zn. 90% of nuclear recoils are expected within the red dot-dashed band. The full and dashed blue lines indicate the 90% and 99.99% regions for γ events, the green dashed line shows the 2 keV ionization threshold. Figure from [110].

ionization yield of < 0.2 comes from the back scattering ^{206}Pb nuclei after the α decay. The α particles are in the presented range of recoil energies not visible, but the dynamic range of the ionization and heat channels is large enough to measure them. That is one of the reasons for using 16 bit ADCs (**A**nalog-to-**D**igital **C**onverter) (see section 2.2.10). The second plot of fig. 2.13 shows the same data set after applying the so called *fiducial cut*. All events for which one of the veto electrodes (channel A or C) shows a signal above a defined threshold are rejected. These thresholds are defined dynamically for each event and depend on the full width half maximum (FWHM) value of the recorded baseline in this hour. Furthermore, the electrode-to-electrode cross-talk is taken into account and corrected. A second criteria is a symmetric weighing of the signals recorded by the fiducial electrodes (channel B or D). In a WIMP search analysis are additional rejection criteria, such as coincidences with other detectors or the muon vetoadded.

One event in fig. 2.13 passed this cuts and appears within the nuclear recoil band marked by the red dashed lines, at a recoil energy of 15 keV. A second event at $\sim 150 \; keV$ appeared close to the nuclear recoil band but is still outside. For these events, with high recoil energies, is a particular interest of using a time resolved ionization channel as presented in this thesis.
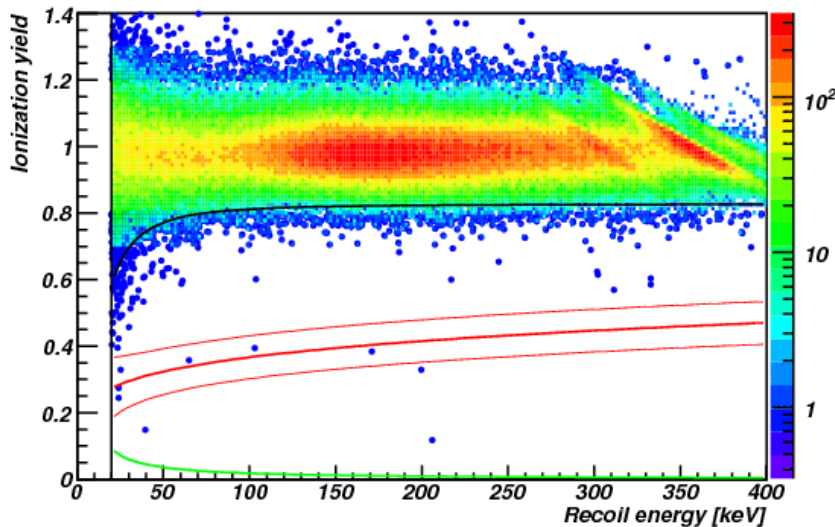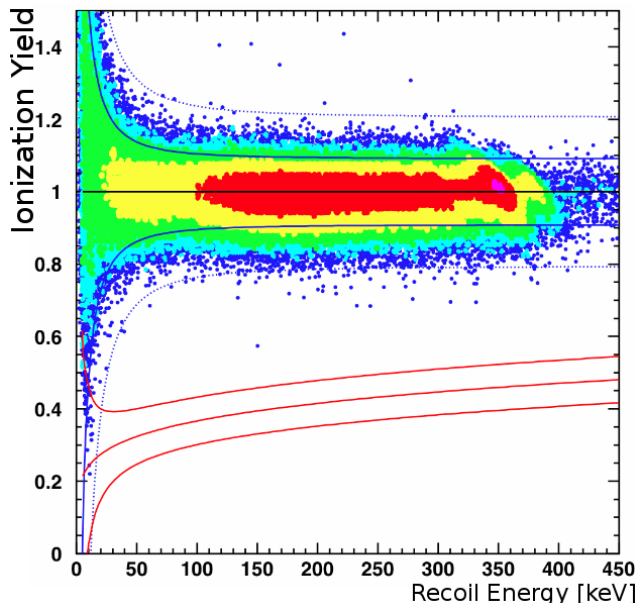
Figure 2.14: EDELWEISS-III FID detector: calibration with a ^{133}Ba source. No events out of $4.11 \cdot 10^5$ appear inside the nuclear recoil band (red lines), (see improvement over fig. 2.11). Figure from [109].

A ^{133}Ba γ calibration was performed with the new FID detector [109]. In a dataset of $4.11 \cdot 10^5$ events is no event found inside the nuclear recoil band. This sets an upper limit for the gamma rejection of of $R_{\mathrm{FID}}^{\gamma} < 6 \cdot 10^{-6}$. These measurement shows that the FID detectors are better than the ID detectors used in EDELWEISS-II.

2.2.7 Heat channel biasing and readout

Each detector in EDELWEISS-III is equipped with two NTD thermometers that are read out as two independent heat channels. The heat channels represent the calorimetricly measured total event energy. They are the trigger channels of the EDELWEISS data acquisition. Typical heat pulses have a rise time of 10 ms. Afterwards a thermal link to the cryostat causes a cooling of the detector which is best described by two exponential functions (see eq. 3.4) with a decay time of 10 ms and 100 ms [87].

The NTD is best operated in a temperature regime of 18 mK to 20 mK where it has temperature dependent resistance of $0.5 - 2$ MΩ. Measuring weak signals on a high impedance require a special readout design. In EDELWEISS the NTD is biased with a square modulated current (500 Hz) of a few nA. The advantage of this kind of measurement is the separation of the modulated signal and the unmodulated noise. Especially the $1/f$ noise of the JFET is avoided for low frequencies by shifting the measurement and readout of the signal to higher frequencies. The biasing of the NTDs is done by the bolometer box with DACs (**D**igital-to-**A**nalog **C**onverter) and additional analog electronic components. The simplified circuit diagram is shown in fig. 2.15. A square wave signal of 500 Hz with a variable amplitude is created by DAC 9, located on the analog board of the bolometer box (section 2.2.10). It is integrated (and inverted) by an operational amplifier utilized as an *inverting analog integrator* with a 22 nF capacitor in the feedback branch. The resulting inverted triangular signals amplitude depends on the amplitude of the initial square signal, controlled by DAC 9. The triangular signal is split in two branches of which one is inverted by a second operational amplifier (gain: $v_{\mathrm{u}} = -1$). Both signals are forwarded into the FET box at the 100 K screen. The triangular signals appear in fig. 2.15 as Excit+ and Excit-. Each signal is differentiated by an AC coupling capacitor back to a blurred square-like
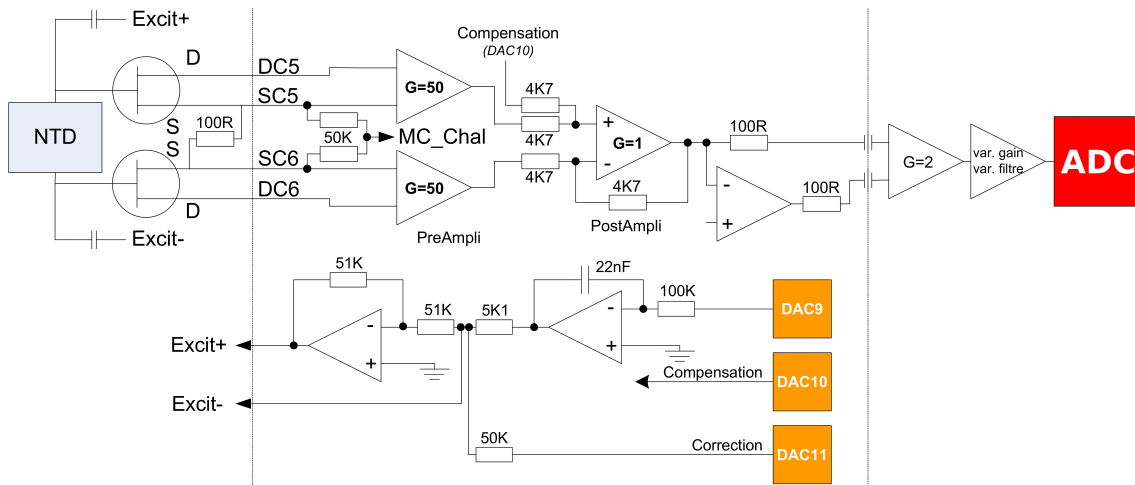
Figure 2.15: Simplified biasing (lower half) and readout (upper half) of an EDELWEISS heat channel [111]. The left vertical line indicates the transition from cold electronics (FET box at 100 K) to warm electronic (bolometer box at room temperature). The right vertical line shows the transition from the analog board to the digital board inside the bolometer box.

shape (see fig. 2.16). The inverted and non inverted signals are respectively connected to the NTD. This modulated readout method [112] has been developed for the cosmic microwave background experiments Archeops balloon [21] and the HFI experiment (**H**igh **F**requency **I**nstrument) on the Planck satellite [113].

The simplified and reduced analog readout path for one NTD is shown in fig. 2.15. Two n-type JFETs on a single substrate (bi-JFET, IFN860[114]) are used as a source follower in a first amplification stage (gain = 1) inside the FET box at 100 K temperature. This is necessary to guide the signals out of the cryostat into the bolometer box. There, the positive and negative part of the signal is respectively amplified with a gain of 50. A square shaped signal with a reference amplitude can be subtracted before the second amplification stage. This is necessary to keep the signal within the dynamic range of the ADC. The signal is split and one part is inverted because the differential signaling technique has a higher resistance against ambient cross-talk and noise interferences inside the bolometer box. The analog event is guided as a differential signal onto the digital board. The digital board is equipped for each channel with a differential amplifier that has a gain of two and a combined configurable amplification and anti aliasing filter. ADCs sample the amplified and filtered signal at 100 kHz with a resolution of 16 bit. The readout channels have a fixed voltage gain of ~ 200 and a variable gain before the ADCs with a factor 0-15. A digitized example pulse can be seen in fig. 2.16. A demodulation of these pulses is performed in the readout software SAMBA. During normal data taking runs is the demodulation performed before the pulses are stored on the hard disk. Therefore, a pulse as shown in fig. 2.16 is not visible for the data analysis.

2.2.8 Ionization channel biasing and readout

The FID detectors in EDELWEISS-III have four ionization channels. Technically, such a channel is made of one branch that provides a voltage to the assigned set of electrodes and a readout branch that measures charges collected by the electrodes. The functional principle of an ionization channel is shown in fig. 2.17. First, a voltage has to be applied to the electrode. Therefore, the relay controlled switch inside the 100 K electronics stage is closed and the voltage source *Pol1* is directly connected with the electrode at the detector. After
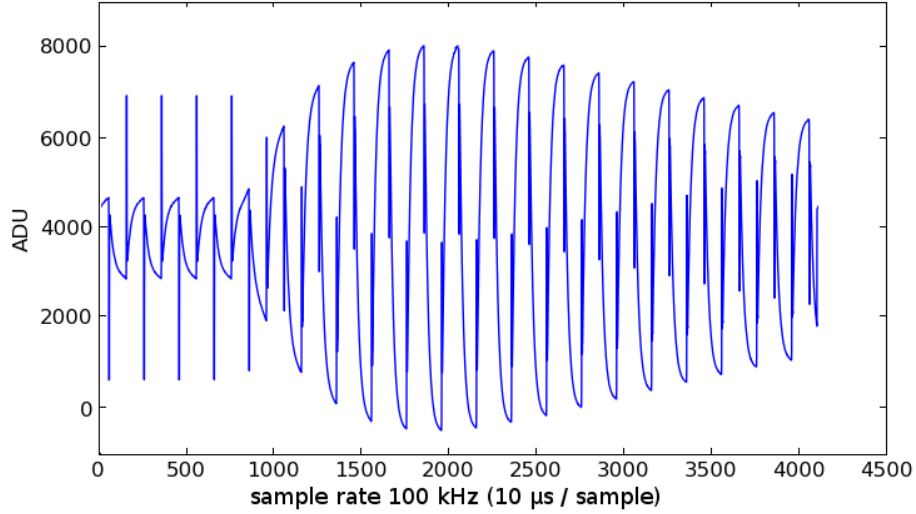
Figure 2.16: Unprocessed ADC record of a heat pulse. The pulse can be seen as an amplitude modulation of the distorted square like NTD biasing, beginning at $t \approx 750 (10\mu s)$. A processed heat pulse can be seen in fig. 2.6.
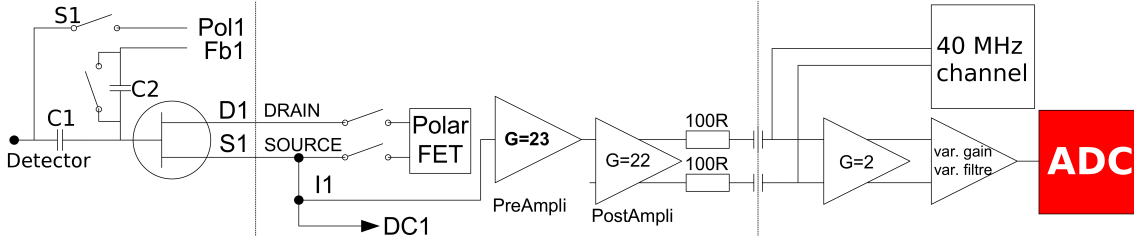
Figure 2.17: Biasing and readout of one ionization channel [111]. The left vertical line indicates the transition from cold electronics (FET box) to warm electronics (bolometer box). The right vertical line shows the transition from analog to digital board inside the bolometer box.

about one minute, the relay is opened and the detector remains floating at the assigned voltage for the next hour.

If charge carriers are collected on the electrode, the voltage changes. This fluctuation passes the AC coupling capacitor C1 and is integrated on C2. The JFET (IF1320[115]) is installed as a voltage follower with a gain of 1. It protects the sensitive electrode voltage from the remaining readout electronics as an impedance converter. On the analog board of the bolometer box a first amplification stage with a gain of 23 is followed by a second stage with a gain of 22. The signal is converted into a differential voltage signal as a protection against common mode interferences. On the digital board of the bolometer box are both polarities split into two branches, one to the 40 MHz readout card, if present, and one to the standard 100 kHz sampling. Since the splitting reduces the signal amplitude by a factor 2, an additional amplifier is installed for compensation. Before the signal is digitized, a variable gain and variable frequency filter is applied. In the standard EDELWEISS operation the cutoff frequency of this anti aliasing filter is set to 40 kHz and the amplification to 1. The ADC samples at 100 kHz and 16 bit resolution. It could be operated at 200 kHz, but the FPGA software of the bolometer box and the optical fiber transmission cannot handle such high data rates. The total readout gain per keV can be estimated as:

$$\frac{\Delta U}{1 \text{ keV}} = \frac{Q}{C} \frac{1}{\text{keV}} = \frac{338 \frac{\text{electrons}}{\text{keV}}}{C_{\text{det}} + C_{\text{cables}} + C_{\text{FET}}} = \frac{338 \cdot \text{e}}{300 \text{ pF}} = 180.5 \frac{\text{nV}}{\text{keV}} \qquad (2.21)$$

The ionization readout needs an active control since each event in the detector adds charge at the gate of the FET. The baseline voltage is changed by each event. This looks like a Heaviside function from the ADC point of view. After several events the ADC reaches saturation. To avoid this, DAC controls the potential at Fb1 (fig. 2.17). The bolometer box-FPGA calculates the necessary amplitude, based on the current ADC value and every 64 s changes the potential of Fb1. The change of the Fb1 voltage passes the capacitor C2 and thus corrects the gate potential of the JFET. These *reset pulses* are performed simultaneously for all ionization channels on all detectors. These artificial events are during later recognized by their time stamp and excluded in the offline analysis (see section 4.2.2 and eq. 4.4).

2.2.9 Cold electronics and cold cables

EDELWEISS has a first electronic amplification stage installed inside the 100 K zone of the cryostat. It powers up the signals before they are forwarded to the digitization in the bolometer boxes. All components (except the NTD) that are drawn left of the left vertical line in fig. 2.15 and fig. 2.17 are installed in the so called FET-box. Each detector is connected with one FET-box, which houses 2 heat channels and 4 ionization channels. For a heat channel, one bi-FET (bi-JFET, IFN860[114]) and a 100 Ω resistor are installed. The FETs have the function of an impedance converter and the resistor suppresses reflections on the differential output line. Two 5 pF capacitors differentiate the input signal for the NTD as described in section 2.2.7. Each ionization channel has two relay controlled switches. In the FET box, relays with two switches per coil are installed. Thus, 4 relays are needed for one detector. The relays are connected two by two in series. Therefore, all polarization switches of one detector are operated simultaneously, and all feedback switches are operated simultaneously, but independent from the polarization switches. In the picture in fig. 2.4 the FET-boxes are visible in the center above the white cables.

PCBs (printed circuit boards) are usually a source of radioactive background. Therefore, the EDELWEISS design aims to avoid unnecessary components inside the FET boxes. However, the relays have to be inside the cryostat vacuum because the leakage current of an opened switch in a normal environment is unacceptable for EDELWEISS requirements. The FETs have a too high noise level at room temperature and need to be in the cryostat as well. Furthermore, the FETs have to amplify the signal power in form of an impedance converter. However, 100 K is not their optimal temperature. Tests at KIT were performed in [116] and showed a temperature of 110-120 K for the FETs to be optimal. Applications and further R&D at the experimental site are foreseen.

Another crucial part of the EDELWEISS design is the detector cabling. The used cables have to be as radiopure as possible since they end very close (some mm) to the detectors. The only shielding element between the cables and the crystal is the cylindric shaped detector housing made of NOSV copper. The connection pad for the cables can be seen on fig. 2.5 as a vertical structure at a 5 o'clock position. Another challenge for the cable is cross-talk between adjacent channels. Cross-talk increases with the length of the cables and depends on the geometric distance between two conductors and the presence of a conductor shielding as in a coaxial cable. Further noise, in form of electromagnetic interferences, couples into the readout channels through the cables. Usual technical approaches such as differential signaling are no option, since the cables end passively on the detector and it is not possible to install a line driver that close to the detectors because of radiopurity requirements. The cables have to pass through all temperature zones of the cryostat. Since their electrical conductor and shielding also transfers heat from the warmer parts to the colder, cables are thermalized at every temperature level by pressing them in enclosing copper blocks. In EDELWEISS the radioactive background due to cables is reduced by a careful material selection and the aim of using as few as possible mass. However,

Figure 2.18: Two opened detector readout and biasing units, *bolometer boxes*. An older
bolometer box version 1 in the left photo and the newer bolometer box version
2-3 including the upgrade for higher detector voltages in the right photo. Both
boxes connect at the outer surface of the cryostat with the 3 connectors on
the right side to the cold electronics. The digitized data is sent on the optical
fibers to the DAQ crate. Further details in text.

minimization of the cable mass comes together with smaller cables and higher capacitances.
The higher capacitance $C_{cable} = 40$ pF/m reduces the ionization signal gain as can be seen
in eq. 2.21. Furtheremore, cables can catch up microphonic vibrations and guide them to
the detectors. The thermal conductance, microphonics and partially the cross-talk can be
avoided by an optimized geometrical design of the routing. The length of the cables for the
detectors to the FET boxes is about 2-3 m.

Different type of cables are used in EDELWEISS-III for the signal transmission between the
detectors and connectors at the 1 K stage. For the signal transmission close to the detectors
in the mK and 1 K zone, in-house designed *Kapton cables* are used [117]. These are made
of a multilayer sandwich structure including three separated layers of 18 μm thick copper as
a conductor. The other layers are polymide (Kapton) and adhesives. These copper-Kapton
cables are connected to similar cables with more layeres and stainless steel as conductive
material. The stainless steel-Kapton cables forward the signals to connectors at the 1 K
stage and from there coaxial cables with a PTFE (Teflon) cleading. Technical problems
with delamination [118] of the stainless steel Kapton cables caused the experiment to reuse
coaxial cables in the 18 mK to 1 K zone as in EDELWEISS-II. These cables are made by
Axon and use a constantan wire as conductor in a coaxial setup. The Axon cables have the
disadvantage of a higher mass and with this a higher radioactive background contribution
inside the detector chamber. Furthermore, their PTFE coating contains fluorine, which is
a source for (α, n) reactions, thus a neutron background.

2.2.10 Analog-Digital conversion and detector biasing

The bolometer boxes shown in fig. 2.18 constitute the *warm* part of the detector readout
and biasing electronics. They are mounted at room temperature in two rows on a connector
panel, which is directly attached to the cryostat (see fig. 2.4, bottom left and bottom right).
They are fitted with three connectors, visible in the right part of the photos in fig. 2.18,
to the connection panel, where they are held in place by a screw. The boxes are inside
the shielding at ground level. A water cooling system reduces their temperature during
operation to $30° - 50°$C.

Several different versions of bolometer boxes evolved during the progress of EDELWEISS. They have a modular setting in common, made of the components:

- Analog board: PCB with filters, amplifiers, DACs

- Digital board: ADCs, anti-aliasing filters, FPGA, optical fiber connectors, socket for time resolved channels (section 3.3)

- DC-DC board: power supply system for all components

Each detector is connected via one FET box to a pair of bolometer boxes. These pairs are either composed of an old version 1 box (fig. 2.18 left) together with one of the newer versions or of two new boxes (fig. 2.18 right). In EDELWEISS-III, the bolometer box version 1 is used only for read out of some heat channels and to control relays. Their difference to the newer versions is a 14 bit sampling instead of 16 bit and a completely different FPGA firmware without the ability to provide a status, which is one of the main arguments to replace these boxes. The next stage of development was the bolometer box version 2 which had 16 bit ADCs and 6 identical channels. These boxes had no special analog implementation of the heat channel, which showed during the R&D phase to be a disadvantage. All boxes of this type have been upgraded to bolometer box version 2-3 by exchanging the analog board.

The bolometer box version 2-3 is shown in the right photo in fig. 2.18. It has a copper housing and the three internal compartments are separated by copper walls. Copper has the advantages of a low radioactive level which is here distinguished, because the boxes are located inside the outer polyethylene and lead shields. Furthermore, copper is an excelent thermal conductor. The completely closed box forms a faraday cage around the electronic systems. The upper right part is the DC-DC board. Ground and $+18$ V_{DC} is provided through a 6 pin connector on which only these two pins are used. The DC-DC converters [119] chop the input voltage with a frequency of 1.1 MHz to efficiently transform it into lower voltages. Several converters are used to generate all needed voltages inside the bolometer box such as 2.9 V and 3.7 V for the FPGA and other digital components, and ± 15 V for the output stage of the detector biasing. The noise created by the converters is uncritical for the 100 kHz sample rate of the conventional EDELWEISS readout. But for the time resolved ionization channels (section 3.3), it turned out to be a real problem with a peak-to-peak amplitude of ~ 300 keV equivalence (see fig. 4.7). Even though several options to reduce the noise have been implemented, such as operating the DC-DC converters in a mode where the phase of the oscillation is 180° shifted for each output voltage, the remaining noise is problematic. Since the converters chop the voltage to a square shape with 1.1 MHz, several harmonics are included as the FFT in fig. 4.6 shows.

The analog board of the bolometer box version 2-3 and version 3 is almost identical. It houses 1 heat channel and 4 ionization channels. In the EDELWEISS-III design each ionization channel has to be controlled by 2 DACs: One for the polar voltage which biases the detector electrode in the range of ± 10 V with a 16 bit fine resolution. The second DAC controls the baseline of the FET in the cold electronics. This is necessary because the voltage follower is not equipped with a feed back resistor, thus it drifts towards saturation. A reset pulse is injected once per minute from this DAC. The gate potential is corrected to keep the baseline around 0. The heat channel is controlled by 3 DACs, two for the biasing and one for the readout. One DAC (DAC 9 in fig. 2.15) creates the modulated bias voltage named *excitation*. DAC 11 creates a correction to adjust capacitive distortions of the excitation signal and DAC 10 creates a compensation signal that is added in the heat readout channel before the last amplification and digitization. With different improvements and modifications on the experimental setup, it may happen that the detector cabling changes and the analog board of the bolometer box has to be adopted. To keep the

input/output pin configuration of the analog board fully flexible, all tracks are intersected with double-breasted connector. A small and passive PCB is plugged as a mezzanine card in this connector and connects the analog board pins with the detector side pins. In the case of cabling modifications on the detector side, only this PCB has to be renewed and not the complex and expensive analog board. The possibility to place any electronics as a bridge in this connector is used for the NTL-effect detector upgrade (see section 2.4.1).

All EDELWEISS bolometer boxes have only one heat channel, whereas every bolometer has two NTDs. Therefore, it is necessary to use two bolometer boxes for reading out one detector. One box controls and reads the four ionization channels and one of the heat channels. A second box the other heat channel. This box has unused DACs from the ionization channels. These are then used to provide bias to control the relays inside the FET-box assigned to this detector. Furthermore, a detector heater or an LED can be operated by the unused DACs. Specific PCBs are plugged on the double-breasted connector of the analog board that enable a reuse of the DACs for different purposes, such as the heater, LED or relay switch.

The digital board of the bolometer box houses the anti aliasing filters, the ADCs, an FPGA and the optical fiber transmitter and receiver. A Manchester coded signal is sent to the bolometer box via the clock fiber. In this code, each transmitted bit is translated into two bits named *period*. If a logic 0 is transmitted, the first bit of the period is 0 and the second bit is 1, and vice versa for a logic 1. The advantage is that for a long series of constant logic value the coded signal alternates. A long series of 256 times 0 transmitted by the much simpler NRZ coding (**N**on **R**eturn to **Z**ero) for instance requires the receivers clock to be very stable to identify the exact number of 256 zeros, and not 255 for instance. With the Manchester code this problem is solved, the receiver always receives the clock within the signal. One disadvantage is that out of N transmitted bits only N/2 carry logic information. In the case of EDELWEISS the frequency of the transmission is 12 MHz (baudrate = 12 MBd), whereas logic signals are transmitted at 6 MHz (bitrate = 6 Mbit/s). The clock fiber constantly transmits the logic value 0. This is interrupted every 1 ms by the transmission of the 1 kHz strobe which is a logic 1-0. This kHz strobe can be followed by a 32 bit long command to the bolometer box's FPGA. Furthermore, after each 1 s phase the 1 Hz strobe, or 1 pps strobe is transmitted as a logic 1-1 signal. It is followed by the 48 bit long time stamp. Based on this time stamp each bolometer box calculates a modulus. All bolometer boxes release the FET reset pulse at the same moment, normally after 64 s. This is important because these resets cause a temporary high noise level in the experiment and have to be excluded from later analysis. To exclude as few as possible data, all detectors have the reset pulse synchronously. The interval can be changed by the operator to each value of 2^{n-1} s with $n \in \mathbb{N}_0 \mid n < 16$. A setting of $n = 0$ completely deactivates the reset pulse. The maximal interval is $n = 15$ with a reset pulse every 4.5 hours.

An Because of the lack of an EPROM (**E**rasable **P**rogrammable **R**ead-**O**nly **M**emory) the FPGA needs to be reconfigured with its software after each power cut and the code has to be transmitted via fiber. A microcontroller in the bolometer box receives the code and configures the FPGA. This procedure is controlled from the acquisition computer by an operator. The FPGA reads the 6 ADCs from which only 1 to 5 are used. A serial bit stream of all 6 ADC values is organized and transmitted through the second optical fiber, the data fiber to the DAQ crate (described in section 3.1). Sending data is implemented with a traditional NRZ code. The advantage here is that the bit rate is as high as the baud rate, in this case 12 Mbit/s. This code can be used because the DAQ crate is the source of the clock, therefore, there is no need to transmit the clock together with the data. Every 10 μs one set of sample points is transmitted, followed by 24 unused bits that can be used from the time resolved channel card (see section 3.3.1). The full configuration of all FPGA registers, containing all DAC and filter values, is sent as a 912 bit long status packet once

per second. Therefore the least significant bit of the 6th channel (unused ADC channel) is overwritten and after 9.12 ms the status is transmitted. Based on these status information, the software SAMBA (section 3.2.1) or ORCA (section 3.2.2) displays the values for the operator interface.

Furthermore, the digital board houses anti aliasing filters that are controlled by the FPGA. These are configurable low pass filters with integrated amplifier. Each channel has such a device before the data is digitized by the ADCs. Typically the cutoff frequency of the filter is set to 40 kHz. It can be configured in steps of 10 kHz from 0 kHz to 150 kHz. With a setting of 40 kHz and a sampling rate of 100 kHz on the ADCs, the aliasing effect is suppressed. Furthermore, the filters have an integrated gain, it is normally configured to 1, but can be set to values from 0 to 15.

In the present run EDELWEISS uses bolometer boxes of the version 1, 2-3 and 3. The version 1 is only used for heat channels and constantly replaced by newer version 3 boxes. The differences between version 2-3 and 3 are marginal: For instance the number of connection pins that pass through the wall between analog and digital board is reduced which turned out to be a disadvantage for the NTL amplified mode upgrade (section 2.4.1). The bolometer box version 3 has more available space for a larger sized time resolved channel card with 4 instead of 2 channels. However, such a card has never been produced. Further versions and modifications of bolometer boxes are used at the cryostat to readout the LUMINEU [120] detectors that are installed in the EDELWEISS cryostat.

2.2.11 Procedures within a typical EDELWEISS run

Periods in which the experiment is operated under a stable cryogenic conditions are named *run*. Each run in EDELWEISS-III has an assigned number of the form 3XX which is incremented once the cryostat is opened and the experimental configuration is changed. Predefined tasks and measurements are executed within a run, for instance, R&D testing of new electrode configurations, new electronic systems, calibrations, or data taking for WIMP search. The cool down takes about 12 d which is mainly caused by the low heat conductivity of the polyethylene at the 1 K stage which cools down during 6 d. Measurements are typically done once the detectors reached a temperature of $18 \text{ mK} - 23 \text{ mK}$. Once per week the cryostat needs a helium refill. The consumption of liquid helium is in the order of 10 l/day [83].

The number of trapped charges accumulates during the detector operation and constitutes to the space charges, thus influencing the electric field geometry and charge collection efficiency. Therefore, data taking is stopped for 1 h once per day and a detector regeneration is executed.During regeneration the polarization DACs of all ionization channels (Pol1 in fig. 2.17) are set to 0 V and the relays (switch S1) are closed. This results in a discharging of the detector and cabling capacitances. Two ^{60}Co sources, each with an activity of ~ 200 kBq, are moved by stepper motors out of a lead shelter and irradiate the experimental setup with 1.17 and 1.33 MeV γ rays. The energy of the radiation effectively removes charges from a potential well in which they got trapped. During the regeneration the time period for the FET's baseline correction by the bolometer box reset pulse is set to 1 s. For the actual regeneration, this is not necessary, but it prevents the readout FET and ADC of the ionization channels from saturating. Thus, the restart procedure of the next data taking is shortened. After at least 1 h of detector regeneration the sources are moved back to their shelter and the run is continued with a maintenance phase.

A detector maintenance phase is automatically executed after a defined time, typically about 1-2 hours. Since the detectors are floating during measurement (S1 is opened) the charges may decrease due to leakage effects. Furthermore, with each new event the charge on C2 increases and the potential of Fb1 is changed with each bolometer box reset pulse to

keep the baseline of the channel centered. This can not be performed endlessly because the DAC behind Fb1 reaches a limit. Before such an effect has any impact on the data integrity, the maintenance phase is started. Both relay controlled switches are closed, which removes charges from C2 and C1 (fig. 2.17)) and the electrode potential of the detector is reset to the potential of Pol1. After about one minute the relays are opened again and the time constant for the reset pulse remains at 1 s for a short time until the baseline is centered. Afterwards the reset pulse interval is set back to 64 s and data taking continues.

2.3 EDELWEISS-III analysis and recent results

EDELWEISS-III has 36 Ge detectors of the FID800 type, each with a mass of $820 - 890$ g. Due to a technical problem with the cabling between mK and 1 K zones inside the cryostat, only 24 detectors can be operated simultaneously. The initial goal of EDELWEISS-III was to probe the parameter space for WIMP-nucleon spin-independent cross-section down to 10^{-45} cm^2 with an effective exposure of 12000 kg $\cdot$ days. One other goal is to improve sensitivity to low-mass WIMPs by implying the NTL amplified mode, which is a detector operational mode with significantly increased voltages of up to 140 V (detailed in section 2.4). Several improvements are introduced with EDELWEISS-III to achieve these goals. The most important are the new detectors of the FID800 type that are described in section 2.2. Compared to EDELWEISS-II these detectors bring a higher total mass, an improved internal field geometry with a better charge collection for the outer parts and a much higher percentage of usable fiducial volume. Furthermore, the number of ionization channels is decreased from six to four, which simplifies data taking and analysis. The number of heat channels per detector is increased from one to two, which adds redundancy in the case of a problematic NTD and a better heat signal reconstruction if both NTDs are working.

The other major differences compared to EDELWEISS-II is the reduction of radioactive background. Therefore, the internal screens of the cryostat were exchanged by newer screens of high purity NOSV copper as described in the cryostat section 2.1.3. A new additional shield of polyethylene in the 1 K zone is described there as well and shown on the picture in fig. 2.4.

2.3.1 Neutron background in EDELWEISS-III

Since EDELWEISS-III detectors have an excellent rejection of surface events (see fig. 2.13) and identification of γ events (see fig. 2.14). The remaining background are neutrons with the potential to produces nuclear recoils. Neutron and WIMP induced signals are similar and can be rejected only by a coincident detection in multiple detectors or by the muon veto system. Sources for neutrons are the decay chains of ^{238}U and ^{232}Th inside the ambient materials. Further sources are (α, n) reactions and cosmic muons. All materials used for the experimental setup inside the shields have been measured for their radiopurity which, however, often resulted in upper limits only. Energy spectra for all materials were computed with the software SOURCES4A [121] and normalized on the measured levels of radioactive contaminations. These spectra are used in GEANT4 based simulations [122, 123], where neutrons are propagated through the EDELWEISS setup to estimate the event rate at the detectors [74].

Fission of the mainly present decay chains of ^{238}U and ^{232}Th is evaluated by measurements of the materials. A detailed overview is given in [124]. The most prominent sources related to electronic components discussed in this work, the PCBs of the FET boxes and those of the bolometer boxes are extracted and presented in table 2.1. The cryostat internal cold shields (lead and PE) and the extra polyethylene on top of the bolometer boxes have the special purpose to reduce neutrons from the warm electronics, the cold FET boxes and the connectors at 1 K.

| Element | Mass [kg] | ^{238}U series | | ^{232}Th series |
		^{210}Pb	^{238}U	
PCB: FET Boxes	0.55	$(1.4 \pm 0.3) \cdot 10^4$	$(7.5 \pm 0.2) \cdot 10^3$	$(10.1 \pm 0.1) \cdot 10^3$
PCB: Boloboxes	10.4		<1660	<1215
Al Boloboxes	27.8	88 ± 36	4 ± 3	<2

Table 2.1: Selected entries related to readout electronics. Activities in mBq/kg. Excerpt from [124].

With 24 installed detectors, an effective exposure of 5431 kg · days and an energy threshold of 10 keV for the main hit detector and 3 keV for any other detector in coincidence, the expected number of neutron events is 4.8, while the expected number of single detector hits is 1.4 [124]. Single detector neutron events can not be distinguished from a WIMP event, therefore this is the most critical background for EDELWEISS. For an analysis with a higher threshold of 20 keV for the primary hit and 10 keV for a hit in any other detector in coincidence, the expected number of neutron events gets smaller: 3.2 with detector coincidences and 1.1 for single hits [124].

A different source of neutron production is the interaction of atmospheric muons in the vicinity of the experimental setup. The cosmic muon flux is reduced by a factor of 10^6 in the underground laboratory. A remaining flux of 5 muons/m^2/day is measured. In order to detect remaining muon candidates, EDELWEISS experimental setup is covered with the muon veto system. Through passing muons are detected and a dedicated analysis branch is used to search for coincidences with the EDELWEISS detector array. For EDELWEISS-III, the muon veto system was improved by adding 4 panels on top of the gap, where the two halves of the shields are opened. The added modules are equipped with LEDs to control aging effects and long term stability (see section 2.1.2). The rate of bolometer events in EDELWEISS-III in coincidence with the muon veto system where at least 2 muon veto modules (M ≥ 2) had a signal above the muon veto threshold was found to be [76]:

$$\Gamma^\mu_{M \geq 2} = 1.02 \text{ events/day}$$

The rate of WIMP like events, where only one bolometer had a signal in coincidence with at least one muon veto module (M ≥ 1) is given by an upper limit (90% C.L.) since no event was found [76]:

$$\Gamma^{\text{WIMP}-\text{like}}_{M \geq 1} < 0.017 \text{ events/day}$$

The efficiency of the muon veto system is derived by identifying a sample of muon-induced bolometer events on the basis of the bolometer multiplicuty and the total energy desposit. All observed candidates from this selection have been identified by the veto system in the present EDELWEISS-III analysis, giving a lower limit for the efficiency of the muon veto of $\epsilon_{\mu\text{veto}} > 93\%$ with 90% C.L. [76].

The new DAQ system (detailed in section 3.1) of EDELWEISS-III allows to integrate the muon veto system into the readout of the bolometers via the face bit information (see fig. 2.2 and sections 2.1.2, 3.1.3). The clock of the new DAQ system generates a 100.000 kHz reference time stamp which synchronizes all EDELWEISS detectors and the muon veto. The ADCs of all channels digitize the analog data with this frequency reference. In EDELWEISS-II, it has been 99.205 kHz. However, this has almost no quantitative impact, beside that some filter parameters in analysis functions were adopted. The real improvement is that the time stamp is stable and not reset after a power cut, but always continues relative to a fixed t_0. Since all detectors and the muon veto system are synchronized by

this time stamp, coincidence detection in EDELWEISS-III becomes very reliable, whereas it had to be manually tuned in previous phases of the experiment.

2.3.2 Pulse Processing in EDELWEISS-III

The signal processing in EDELWEISS-III can be divided into two stages. The online stage applied on the continuous data stream by the acquisition software SAMBA, with the focus on trigger and event building, and the offline pulse processing which is performed by a software framework called ANA on the triggered data. Both stages can be further subdivided into a heat channel processing branch and an ionization channel processing branch.

SAMBA triggers on the heat channels (detailed in section 3.2.1). The main reason for this is that by a comparable noise level typically more energy of an event is transfered into the heat channel. This can be seen from the nuclear recoils that have an ionization quenching of ~ 0.3. The trigger algorithm is schematically shown in fig. 3.8. First, the stream of modulated 100 kHz heat data is demodulated by computing mean values of the plateaus. Samples close to the transitions of the modulation are skipped. This is simple because the modulation frequency and phase are strictly related to the time stamp, hence very well known and stable. The resulting 500 Hz stream of demodulated heat channels is filtered by a high-pass Butterworth filter (FIR) and then convolved with the template (equation 3.4), that is filtered as well. In case the convolved signal exceeds a predefined threshold (trigger threshold), the event to be recorded is built around this time stamp, containing a 2 s window of demodulated heat data (1024 demodulated sample points). From the ionization streams are 2 sort of channels recorded: The 100 kHz raw data with 4096 samples around the trigger time stamp which corresponds to 40 ms length, and a down sampled 1 kHz ionization channel. In the latter case, each 100 kHz ionization channel is averaged on 100 sample points, which corresponds to one plateau of the heat modulation. 2048 samples are included per event record, which corresponds to 2 s.

The offline pulse processing is performed at the Tier-1 computing center in Lyon. The main purpose is to process the individual events and extract a set of variables for the EDELWEISS analysis. These variables are stored in so-called flat files. The pulse traces are not included in these files to keep them small and handy for the statistical analysis. The processing chain is named ANA, followed by a letter that refers to the version. The flat files used for the time resolved channel analysis presented in section 4 correspond to version b. The triggered events are reanalyzed in ANA. First, the base line the heat channel is fitted with a linear function and subtracted, which removes a constant offset and a slope, if present. Afterwards the template (equation 3.4) is fitted and from the parameters, the amplitude E_{heat} and a preliminary event time stamp t_{heat} are derived. If $E_{heat} < 5\sigma(\text{baseline})$ the event time stamp t_{event} is defined by the value obtained from the heat template fit, $t_{event} = t_{heat}$, which has a precision of milliseconds. If $E_{heat} > 5\sigma(\text{baseline})$ one can expect to identify the event as well inside the ionization channels. In the latter case, the 1 kHz ionization channel is filtered for instance by a moving average filter that removes the crosstalk pattern due to the heat channel modulation. In the 1 kHz channel, the period of the pattern is only 2 samples long. The acquisition software SAMBA performs the down-sampling of the 100 kHz channels in a way, that half of the crosstalk period is compressed into one sample point. Thus, one point of the 1 kHz channel represents the positive plateau and the next the negative plateau. This effect can be seen as a broadening of the pulse trace (in the time scale of 2 s) in fig. 2.19(a). In the next step, the pattern, the baseline a slope are removed, fig. 2.19(b). Then, the pulse and a Heaviside function are filtered by a high-pass Butterworth filter. Afterwards the filtered Heaviside template and the filtered data are cross-correlated. The point of maximum correlation provides the ionization time stamp $t_{1\,kHz}^{ion}$. It has a slightly better precision than t_{heat} from the heat channel fitting, but this
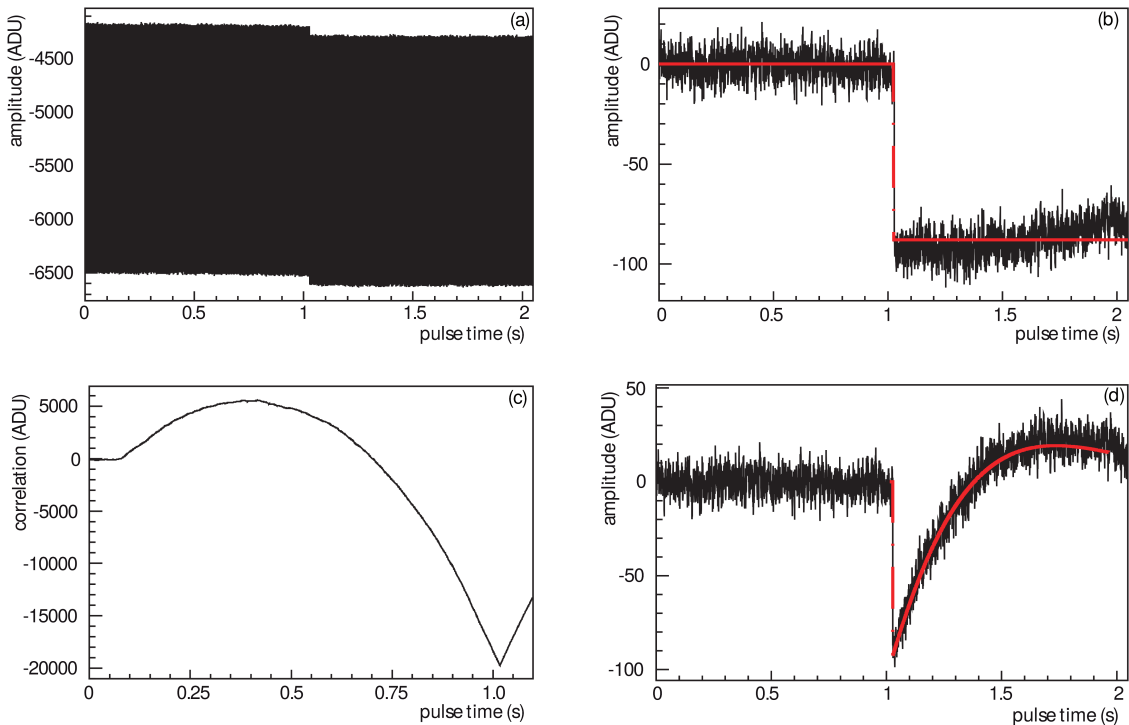
Figure 2.19: Stages of the ionization pulse processing: The raw pulse trace of the down-sampled 1 kHz ionization channel (a) and after pattern removal, common noise rejection and single frequency noise rejection (b). The data and a template (Heaviside function) are filtered by a high-pass Butterworth filter and then cross-correlated (c). The point of maximal correlation provides the ionization time stamp $t^{\mathrm{ion}}_{1\,\mathrm{kHz}}$ and the ionization amplitude (d). Figures from [125].

stage of analysis is not possible for all events, since some events do not have a strong enough signal on the ionization channels. If it is possible, the event time stamp is reassigned to the value obtained by the 1 kHz ionization channel. In the next stage the $t^{\mathrm{ion}}_{1\,\mathrm{kHz}}$ is used as a start parameter to find the event in the 100 kHz ionization channel.

Sometimes, a further pulse analysis within the 100 kHz record is not possible because the initial event building by the DAQ software in some cases misplaces the readout window, especially in the case of very high amplitude events that saturate the heat channel. If the event is inside the 100 kHz channel's readout window, it can be further analyzed. The template is again a Heaviside function this time filtered by a 40 kHz low-pass filter. This is equivalent to the anti-aliasing filter inside the bolometer boxes that is applied on the analog data before digitization. Since the rise times of ionization pulses are in the region of 10-3000 ns, the shape of the digitized data would always be a Heaviside function. The anti-aliasing filter limits the bandwidth of the signal to 40 kHz, which changes the shape the ionization pulse, giving it a rise time of $\sim 10-20$ μs. The digitized data can thus be cross-correlated with the filter response of the Heaviside function and a time stamp with a < 10 μs precision is obtained.

In conclusion, the event time stamp is first obtained by analyzing the heat channel pulse and, if the energy is large enough, it is improved with the 1 kHz ionization record and further improved with the 100 kHz signal. The heat energy is measured by fitting a template to the demodulated and filtered heat trace, and the ionization energy is measured in the 1 kHz ionization record where long integration times improve amplitude reconstruction compared to the 100 kHz record.

2.3.3 Statistical analysis and energy calibration

The basis for statistical analysis is the data set created by the pulse processing described as described in the previous section. The data set contains all obtained variables but not the pulse traces. The amplitudes are not calibrated in energy. The energy calibration is performed by using a ^{133}Ba source and creating an energy calibration histogram for each channel. The decay via electron capture of ^{133}Ba into ^{133}Cs produces γ lines with energies and relative intensities of: (data from [126])

E_γ [keV]	Int [%]
356.013	62.05
80.998	32.9
302.851	18.34
383.849	8.94
276.399	7.16
79.6142	2.65

Not all of these lines can be resolved to calibrate on them. Calibration is typically performed at 303 keV, 356 keV and 384 keV lines. The strongest line is at 356 keV and has been used to calibrate the time resolved channel in this thesis (section 4.3.1).
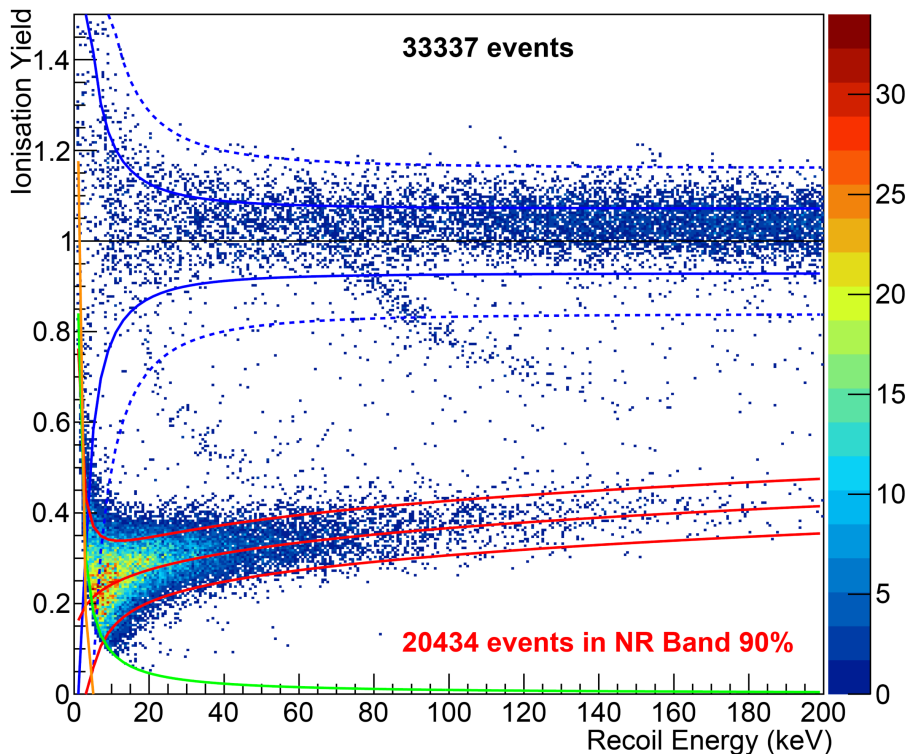
Figure 2.20: Ionization yield versus recoil energy for a calibration with an AmBe source. Neutrons are visible inside the nuclear recoil band indicated by red full lines at 90% C.L., whereas the main γ population is inside the electron recoil band, indicated by dashed blue lines for 99.98% C.L. and blue full lines 90% C.L. Figure from [76, 83].

A neutron calibration is performed to validate the parametrization of energy quenching. Here, a low activity Americium Beryllium source of 21 ± 4 Bq is placed close to the detectors, 8 cm above the top of the cryostat but inside the lead shielding. The results of such a calibration are shown in fig. 2.20. The neutrons are emitted with up to 11 MeV energy and

scatter on the Ge nuclei, producing nuclear recoils which appear inside the nuclear recoil band around an ionization yield of 0.3 in fig. 2.20. The AmBe source also emits a 4.4 MeV γ radiation, which results in the populated electron recoil band, around an ionization yield of 1. The inelastic scattering of a neutron on a nucleus of the isotope ^{73}Ge can activate its excited states. One state decays into the ground state within $T_{1/2} = 2.92$ μs by emitting a γ of 13.3 keV. Another excited state decays with $T_{1/2} = 1.7$ ns and a γ of 68.75 keV. Due to a rather slow response of the ionization and especially the heat channels, the γ is measured in coincidence with the neutron and creates the events between the two bands. The parametrization of the nuclear recoil band as

$$Q_{NR} = \alpha \cdot E_{rec}^{\beta}$$

with $\alpha = 0.16$ and $\beta = 0.18$ is verified in the AmBe neutron calibration.

Once raw pulses are processed and amplitudes are calibrated in energy, one can apply statistical methods to search for a potential dark matter signal. The first analysis branch of EDELWEISS-III uses a Boosted Decision Tree (BDT) algorithm. Simulated signal and background events are used to train the BDT. The output of this algorithm for each event is a single variable, containing a value between -1 (background like event) and +1 (signal like event). An individual BDT is trained for each detector. A detailed description of the BDT analysis is given in [127]. An EDELWEISS detector has 6 channels (2 heat, 4 ionization), in the BDT analysis this is teated as a 6 dimensional parameter space. In a first phase, the BDT algorithm is trained with classified (signal or background) events. In a second phase new unclassified data is passed through the algorithm. Based on the parameters learned in the training phase, the BDT classifies now this new events by assigning each event the described characterization variable. Boosting of these algorithm means, that at the end of the training phase some misclassified events are selected and weighted. The training is repeated with the reweighted events, resulting in a new decision tree. After several loops of these steps the average of all individual decision trees is computed as the final boosted decision tree.

For the recently published analysis dedicated to low mass WIMPs [128], a subset of the 8 best performing detectors with lowest thresholds and baseline FWHM is selected. 10 BDTs are trained for every detector, each BDT targeting a tabulated WIMP mass in the range of $4 - 30$ GeV/c^2. The resulted excluded region is shown in fig. 2.21. A cross-section for spin-independent WIMP-nucleon scattering of $\sigma = 4.3 \cdot 10^{-40}$ cm^2 for a WIMP-mass of $M_\chi = 5$ GeV/c^2 is excluded at 90% C.L. For a mass of $M_\chi = 20$ GeV/c^2 the excluded cross-section is $\sigma = 9.4 \cdot 10^{-44}$ cm^2.

The main limitation within the presented analysis for low mass WIMPs at $M_\chi < 10$ GeV/c^2 comes from *heat-only events*. These sort of events is characterized by a normal heat pulse and a missing corresponding charge signal on all electrodes. The exact source of these events needs to be understood and solved. The most probable sources are mechanically created energy deposits that warm up the crystal without charge creation. In the ongoing run, different mechanical supports that hold the detector inside the copper casing, are being tested.

A second branch of statistical analysis performed within the EDELWEISS-III phase utilizes a multidimensional maximum likelihood method [137, 138]. The BDT analysis computes limits without a subtraction of backgrounds, whereas the maximum likelihood analysis models all known relevant backgrounds for each detector individually. A likelihood fit with the known backgrounds and an additional potential signal effectively subtracts the background. Stricter cuts and a lower acceptance of events lead to a reduced exposure. But this is compensated by the benefits of the subtracted background and an increased signal efficiency. The BDT method has a drastically reduced efficiency for low WIMP masses,
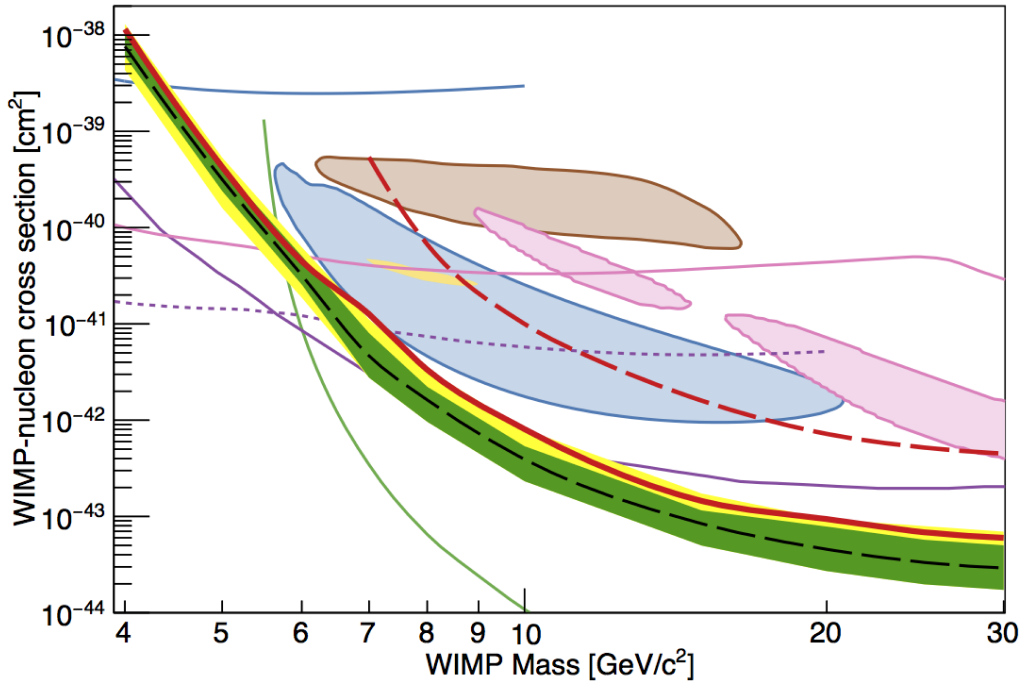
Figure 2.21: Exclusion limits published in [128]. Red full line: EDELWEISS-III low-mass
WIMP search 90% CL limit on the spin-independent WIMP-nucleon cross-
section, green (yellow) band showing 1σ (2σ) sensitivity region in the absence
of a signal. The yellow, blue, pink and brown contours are respectively from
CoGeNT [129], CDMS-Si [130], CRESST-II [131] and DAMA [132]. We also
represent other limits by EDELWEISS-II [133] (dashed red), LUX [134] (green),
DAMIC [135] (blue line), CRESST [58] (pink line), CDMSLite [136] (dashed
violet line) and SuperCDMS [57] (violet line).

for which the discrimination of signal and background is difficult. For these events, the
maximum likelihood method reaches better sensitivity compared to the BDT analysis. The
results of the maximum likelihood method are about to be published [137].

2.3.4 Upcoming methods for a further reduction of the threshold

Beside the success with boosted decision tree and maximum likelihood analysis, EDEL-
WEISS follows additional strategies for a hardware based improvement of the detection
threshold and baseline noise level. One method in order to achieve these goals is the
application of higher voltages on the detector electrodes. This exploiting of the Neganov-
Trofimov-Luke effect is detailed in section 2.4. Another promising approach to improve
the signals quality is the replacement of the JFETs in the FET box at 100 K by so called
HEMTs (**H**igh-**E**lectron **M**obility **T**ransistor) placed at the 4 K stage. HEMTs have the
advantage of a lower power consumption per channel of 1.4 mW and a lower input noise
voltage of 0.35 nV/$\sqrt{\text{Hz}}$ at 1 kHz [139]. Measurements with a HEMT on the SuperCDMS
readout showed an impressive 106 eV (35 electrons) resolution and an open loop voltage
gain of several hundrets. The achieved leakage currents are $< 4 \cdot 10^{-15}$ A [140]. Further
improvements by reducing the intrinsic noise of the HEMTs are possible. Using HEMTs at
4 K reduces the length of the detector-amplifier cabling. Stray capacities of the readout
path and channel-to-channel cross-talk are hence be decreased, which further helps to
improve the overall signal quality.
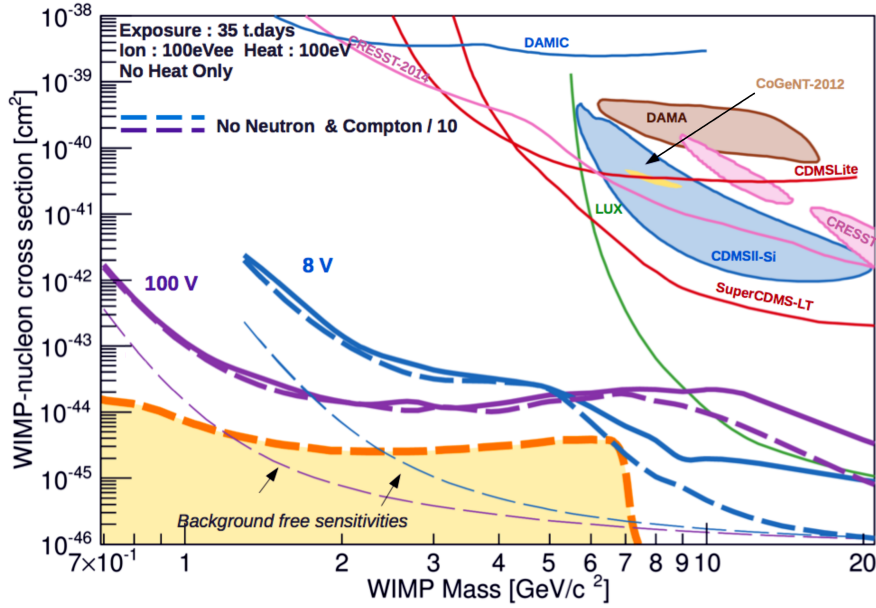
Figure 2.22: Projections for EDELWEISS with $35000 \, \text{kg} \cdot \text{days}$ exposure, considering possible improvements by NTL amplified mode with 100 V detector bias for the low-mass sector. For WIMP masses $M_\chi > 5.5 \, \text{GeV/c}^2$ the conventional biasing with 8 V is preferred. Figure from [141, 142], (Citations to other curves are given in caption of fig. 2.21).

2.4 NTL-effect amplification with EDELWEISS detectors

Charges that are drifted by an electrical field through a detector produce additional energy in form of heat [92, 143]. This Neganov Trofimov Luke effekt (NTL-effect) is normally corrected when analyzing events (see section 2.2.3 and eq. 2.15). The normal detector biasing with 8 V has been selected amongst others to keep the influence of the NTL-effect small. If, however, one increases the detector voltages significantly, the additionally produced heat is proportional to the created amount of free charges drifting in the crystal. Events below the normal threshold become visible. The initially deposited heat energy becomes negligible and dominated by the ionization signal which is now measured in the heat channel. Therefore, the discrimination between nuclear recoil and electron recoil, thus the particle identification is lost. With this strategy the experiment's sensitivity is especially enhanced for the search of low-mass WIMPs, which deposit smaller recoil energies.

Such a measurement has been performed by the SuperCDMS collaboration in CDMSlite (**l**ow **i**onization **t**hreshold **e**xperiment) and resulted in an energy threshold of 170 eV_{ee} [144]. This was later improved by reducing the threshold and redefining the fiducial volume cut, to 56 eV_{ee} [136]. The applied potential was -70 V on one detector side and 0 V on the other.

EDELWEISS projections in fig. 2.22 show what potential is expected for low-mass WIMP search with a voltage increase from 8 V to 100 V total detector voltage (± 50 V on electrodes) in the case of EDELWEISS. The presented curves also include further improvements such as HEMTs (**H**igh **E**lectron **M**obility **T**ransistors) replacing the FETs and reduction of background, especially a solution of *Heat Only* events, which have no measured charge signal, has to be achieved. But these improvements mainly optimize the standard WIMP mass sensitivity, whereas the new NTL amplified mode directly reduces the sensitivity for low mass WIMPs. As it can be seen by the crossing of the exclusion projection curves, the standard mass WIMP search is not benefiting from higher detector voltages. Therefore,
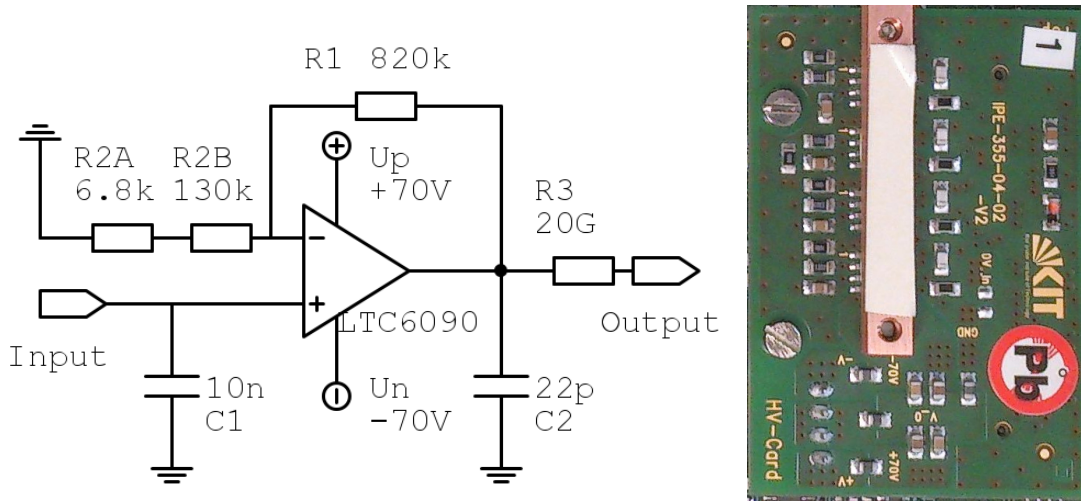
Figure 2.23: Reduced circuit diagram of one output channel, based on a non-inverting amplifier with a gain of 7 (left). Photo of the final PCB (3.8 cm × 5 cm). The copper connects the four amplifiers with the lid of the bolometer box for heat dissipation (right). See section 2.4.1 for details.

EDELWEISS decided to operate a part of the detector array with higher voltages and the other part with standard voltages.

2.4.1 Hardware upgrade for higher detector voltages

The standard detector readout and biasing electronics of EDELWEISS, the bolometer box, provides a software configurable output voltage in the range of -10 to $+10$ V on each ionization channel. The voltage sources are DACs, further described in section 2.2.10. For the NTL amplified mode readout higher detector bias voltages are needed. Therefore, an upgrade for the bolometer box was developed within the work of this thesis. It features a range of -70 to $+70$ V on each channel. The interface board that normally connects the experiment side cables with the read out electronics is replaced with new upgrade PCB. The functionality of the conventional PCB is reproduced for the analog data coming from the detector, whereas the detector biasing tracks are intersected. In each of these four intersections an operational amplifier is placed as shown in fig. 2.23. It is operated as a "non-inverting amplifier". In this configuration the input voltage (DQ2), which has to be amplified, is the standard output voltage of the bolometer box, which is connected to the non-inverting input (marked with a "+") of the amplifier. A voltage divider (R1A) connects the output of the amplifier with its inverting input (marked with a "-") and with ground (R2A1, R2A2). The resulting amplification is

$$v_{\mathrm{u}} = 1 + \frac{R_1}{R_2} = 6.99 \tag{2.22}$$

with the feedback resistors $R_1 = 820$ kΩ and $R_2 = 136.8$ kΩ. The operational amplifier (LTC6090)[145] was selected because of the highest possible rail-to-rail output voltage of all commercially available amplifiers at that time. Rail-to-rail means that the output voltage can be varied over the full supply range of ±70 V. Furthermore, it can be set to 0 V. The amplifier's output is connected to the detector via a resistor $R_3 = 20$ GΩ, which limits the maximum current to the detector to 3.5 nA. In the first two constructed prototypes a smaller output resistor of $R_3 = 1$ GΩ with a residual current of 70 nA has been used. These cards were later replaced by the newer version with 20 GΩ. The detector current is critical because it heats up the bolometer and induces waiting time until the temperature has decreased again. The output power of the operational amplifier is $\mathcal{O}(\mathrm{nW})$ and can

be neglected. The idle running load of the amplifier is 385 mW which adds up 1.54 W for four channels. To avoid overheating, a thermal conducting pad and a piece of copper create a thermal link to the lid of the bolometer box. This can be seen in fig. 2.23. Each card is equipped with four of the described amplifiers, one for each ionization channel of a detector.

To operate the amplifiers several additional components are necessary. As shown in the circuit diagram in fig. 2.23 capacitors are used to avoid oscillations. Furthermore, the operational amplifier need the symmetrical supply voltage of ± 70 V. Since such a high voltage is not available inside the bolometer box it has to be generated outside. Therefore, a standard laboratory power supply (EA PS-2843) [146] that can provide up to 84 V and 3 A on two channels is used. The two channels are connected in series. The output is filtered in an additional box, that houses 3 stages of low pass filters. With a shielded coaxial cable the supply voltage is forwarded to an adapter box which is located inside the clean room and the lead shielding. The adapter box splits the supply voltage to 10 sockets, providing up to 10 bolometer boxes with the higher voltage. Since it was not acceptable to drill additional holes inside the bolometer box, an existing but unused hole which normally accepts the screw of a connector is used to enter the box. Inside are standard copper cables with a 1000 V tight isolation used to deliver the supply voltage to the amplifier card. The complete upgrade of a bolometer box can be rolled back within a few minutes, if needed.

Modifications on the bolometer box FPGA software are not needed, but in the SAMBA software (see section 3.2.1) a new class of bolometer box is defined. The only difference compared to the standard version is, that the displayed voltages are multiplied by a factor of 6.99, which is exactly the voltage amplification v_u of the hardware upgrade. This helps the operators to configure a detector for the Luke amplified mode.

On the analog readout part of the detectors no modification is necessary. Since the detectors in EDELWEISS-III are connected via capacitors (see fig. 2.17, section 2.2.8) the constant voltage is not forwarded to the FET and to the bolometer box. The maximal current during charging and discharging of the detector is limited by a 20 $G\Omega$ resistor. Therefore, there is no risk of causing damage to the readout electronics.

Two prototype cards of the upgrade have been tested at the experiment within the framework for this thesis. In this campaign, all EDELWEISS detectors that showed no leakage current at ± 10 V were tested with the higher voltages. The goal of these measurements was to see, how many detectors are suitable for NTL amplified measurement and up to which voltage. Therefore, the heat channel was monitored while increasing the voltages for different electrode configurations. The heat channel reacts to every change in the voltages mainly because trapped or free charges in the crystal are drifting, but at a critical value, which is different for each channel, the heat channel immediately saturates and the detector heats up. Furthermore, the *boloplate*, on which the detectors are mounted and which acts as the thermal bath, is heated up as well. The temperature of the boloplate was continuously checked during these tests and used as an indicator for leakage currents. It takes several seconds to a few minutes until the detector recovers to the normal temperature of 22 mK (during these tests). The reason for this voltage dependent heating effect is interpreted as a leakage current from the charged electrode to either another electrode or via the thermal link or the NTD to the boloplate and ground potential.

The measurements were first executed in *planar mode* with equal biasing of the electrodes on one detector side ($A = B = -C = -D$). In this operational mode the highest electric field occurs at the equator of the detector where the electrodes A and C are neighboring with a spacing of 1.4 mm. Once the maximal voltage in planar mode was known, the *FID mode* was measured. There, the biasing is $A = -C, B = -D$ and $|A| < |B|$. The measurment was performed by first trying to further increase the collecting electrode

voltages B and D without changing the veto electrode voltages A and C. If this is not possible, B and D is kept constant, whereas A and C is decreased until the leakage effect occurs. In the planar mode the maximal voltage difference between the electrodes on each side AB and CD is from interest.

Since the detector has an electric capacitance, each manipulation of the voltage causes a current that heats up the bolometer as long as the current is present. The time can be estimated with $\tau = R \cdot C_{\text{tot}}$, where C_{tot} is the total capacitance that has to be charged. It constitutes of the detectors capacitance of $C_{\text{bolo}} \approx 100 - 150$ pF (varies for each detector) and additional 300 pF from the cabling and connections to $C_{\text{tot}} \approx 400$ pF. With the current limiting output resistor $R_3 = 1$ GΩ the time constant is $\tau = 0.4$ s. The charging current decreases by $> 99\%$ after a time $5\tau = 2$ s. Note, this estimation counts for the prototype card. The final version for run 310 and later has an output resistor of $R_3 = 20 \pm 4$ GΩ enlarging a the estimated waiting time to $5\tau = 40$ s until the detector is fully charged.

A detector has a capacitance of $C_{\text{bolo}} \approx 100$ pF thus, the stored electrical energy at the maximum voltage of 140 V can be calculated as

$$E_{\text{cap}} = \frac{C_{\text{bolo}}U^2}{2} = 1.96 \text{ μJ} = 12.23 \text{ TeV} \qquad (2.23)$$

from which a small part during the charging process is dissipated as heat. In case of an electrode to electrode leakage current a fraction of this energy is continuously dissipated as heat. Physics measurement during the presence of a leakage current is impossible. A comprehension of the results of the performed measurements is listed in table 2.2.

Table 2.2: Overview of the results from measured maximal voltages in the NTL amplified mode

Detector	Planar Mode: $A = B$, $C = D$	FID Mode: A, B, C, D
FID803	-55, +55	-55, -60, 55, 60
FID804	-70, +70	-55, -70, +55, +70
FID824	-17, +17	10, 17, -10, -17
FID828	Problem with channel A, discontinued	
FID829	-26, +26	26, 36, -26, -36
FID 834	-22, +26	-22, -30, +22, +30
	+22, -26	+20, +25, -26, -31
FID836	-18, +18	0, 18, 0, -18
FID837	-13, +13	-13, -20, 13, 20
FID839	-15, +15	-15, -25, 15, 25
FID841	-19, +19	-19, -30, 19, 30
FID844	-13, +13	-13, -20, 13, 20
FID211	-35, +35	-35, -50, 35, 50

An obvious difference in the stability against leakage current can be seen for FID803 and FID804 (in table 2.2). Both detectors have been produced at a different company and underwent a different post processing treatment compared to other detectors. FID803 and FID804 are polished at CSNSM (Centre de Sciences Nucléaires et de Sciences de la Matière, Paris Orsay, [147]) whereas the others are polished by BSI (Baltic Scientific Instruments, [148]). Both detectors can accept more than twice the voltage compared to the others. The CSNSM polished detectors showed no leakage effects at ± 10 V, whereas the other detectors had to be reworked with the XeF$_2$ edging to handle the standard voltages. All tested detectors, except FID834, showed a symmetric behavior. The applied voltage can be inverted (slowly) and the same absolute limit is reached. FID834 showed an asymmetric

behavior. Electrode A never accepts more than ± 22 V. A leakage current at the equator from electrode A to C cannot be the reason. A leakage current from the center electrode A into the NTD, which is glued on top of this electrode could explain the observed effect. A relative high difference in the FID mode with $\Delta U_{\mathrm{AB}} = 18$ V was achieved on FID836. Furthermore, the smaller detector FID211 with $m = 200$ g and larger electrode spacing was tested as well. This detector is especially designed and installed for measurements in the NTL amplified mode.

As an outcome of these measurements it was decided to keep the two prototype cards connected to FID803 and FID829 until the end of run 309 which corresponds to two weeks of intensive testing with higher voltages. During this period, strategies were determined how to best integrate the NTL amplified mode into the conventional EDELWEISS run procedures. As mentioned above, increasing of the electrode voltage induces heat to the detector and via the heat sink to the bolo plate and to all other detectors. For 8 V this is no issue and the relay controlled switch can be directly closed and the voltage is set instantaneously by the polar DAC. For the higher voltage, a simple closing of the switch is not an option since the high current that charges or discharges the detectors capacity produces to much heat inside the detector. This heat spreads to the boloplate and other detectors. The induced dead time is 10-30 minutes, which would be 50% with a hourly maintenance pattern. Therefore, scripts where developed that ramp up the voltage slowly. Furthermore, the detector is no longer discharged for the hourly maintenance (section 2.2.11). This reduces the number of charge-discharge cycles to the number of detector regenerations (section 2.2.11), normally once per day. It was observed that applying the full bias inverted for some seconds, followed by 0 V, and then ramp up the detector to the dedicated voltage, reduces the leakage current, thus minimizing the heat and dead time until measurements can be started. The complete operation procedures are difficult because each detector shows an individual behavior and thus, needs individual parameters, scripts and procedures. Sometimes a leakage current occurs at a voltage configuration where it was not present before. It also happened that a present leakage current disappeared again, without decreasing the voltages.

Based on the described measurements and tests, it was decided to construct 10 HV-upgrades with minor modifications, such as additional capacitors in the power supply of the operational amplifiers to prevent each amplifier from oscillating. Furthermore the design of the final PCB is slightly larger to enable space for a screw mounted heat sink. All 10 HV-upgrades are operated in run 310 started in March 2016. The goal is to extensively test the NTL amplified mode, further improve the procedures and measurements with new detector types that are optimized for higher voltages. The HV-upgrade cards have been produced in-house at KIT institute IPE.

2.4.2 Results with higher detector voltage

One of the goals of the ongoing run 310 is the application of higher voltages for the NTL amplified mode on 10 detectors simultaneously and over an extended period of time. First preliminary results are shown in fig. 2.24. For FID803 a SAMBA threshold of ~ 250 eV at 50 V and ~ 150 eV at 100 V has been achieved. The SAMBA threshold is the trigger energy threshold which is automatically adopted to trigger at a constant target rate, typically 50 mHz during WIMP search runs. With FID829 are even lower values reached: ~ 150 eV at 25 V and ~ 50 eV at 45 V. The given voltages referring to the fiducial electrodes, thus 100 V refers to an electrode voltage of ± 50 V. These two detectors have a better sensitivity with higher voltages. The FWHM values of the heat channels are ~ 100 eV$_{\mathrm{ee}}$ at 50 V and ~ 50 eV$_{\mathrm{ee}}$ at 100 V for FID803 and ~ 150 eV$_{\mathrm{ee}}$ at 25 V and ~ 100 eV$_{\mathrm{ee}}$ at 45 V for FID829. The values presented within the EDELWEISS-III low-mass analysis [128] are in the range of $620 - 1150$ eV for the SAMBA threshold and $300 - 590$ eV$_{\mathrm{ee}}$ for the heat
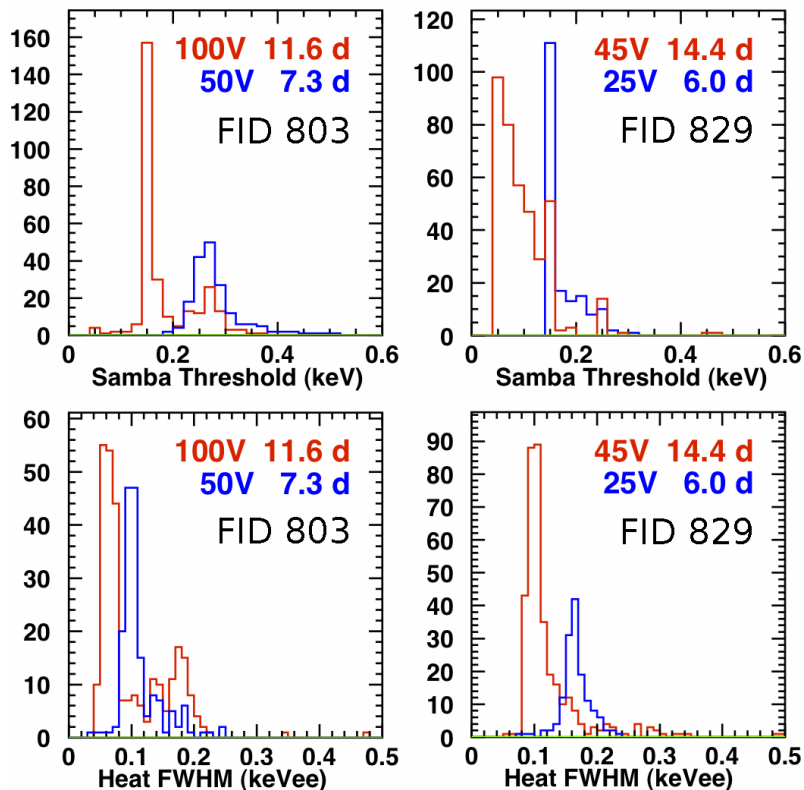
Figure 2.24: Intermediate results for two detectors operated at higher voltages in run 310: The online trigger threshold (SAMBA threshold, upper row) and the heat channel FWHM (bottom row) of the detectors 803 (left) and 829 (right) are shown for a high voltage close to the maximal non leaking value and a smaller voltage.

channel FWHM. Compared to these values the NTL amplified mode shows an improvement by a factor of 5-10.

Furthermore, the ongoing run 310 recycled some EDELWEISS-I detectors of the GGA and GSA type [149] that have been used inside the EDELWEISS-II cryostat before the ID detectors were developed [150]. These detectors are with a mass of $\sim$ 320 g much lighter and smaller than the FID800 detectors. The detectors are shaped as the one shown in fig. 2.10 left, with beveled edges. The GGA detectors have 4 electrodes, two planar ones at the top and bottom face referred as collecting electrodes and two veto electrodes, planar on the beveled edges. The electrodes are made of aluminum and evaporated on a passivated layer of germanium, whereas the GSA detector has a passivated layer of silicon beneath the electrodes. The reason to use these old detectors is mainly to learn more about the NTL amplified mode with a larger plurality of different electrode and detector geometries and the influence of an amorphous germanium layer versus an amorphous silicon layer beneath the electrodes.

Another new type of detector that is currently operated with the NTL amplified mode are the P900 named detectors. This type is based on 800 g cylindrical Ge crystals as used for the FID800 type detectors, but with two ionization channels only. One planar aluminum electrode per face (top, bottom) evaporated on a passivated germanium layer, wrapping around the edge and covering $\sim$ 30% of the mantle. The idea of reducing the number of electrodes follows the observation that with higher voltages the interdigitized electrodes can not be used in the way they have been designed for. Furthermore, the low energy events which are amplified in heat to a measurable signal do not create enough charges to
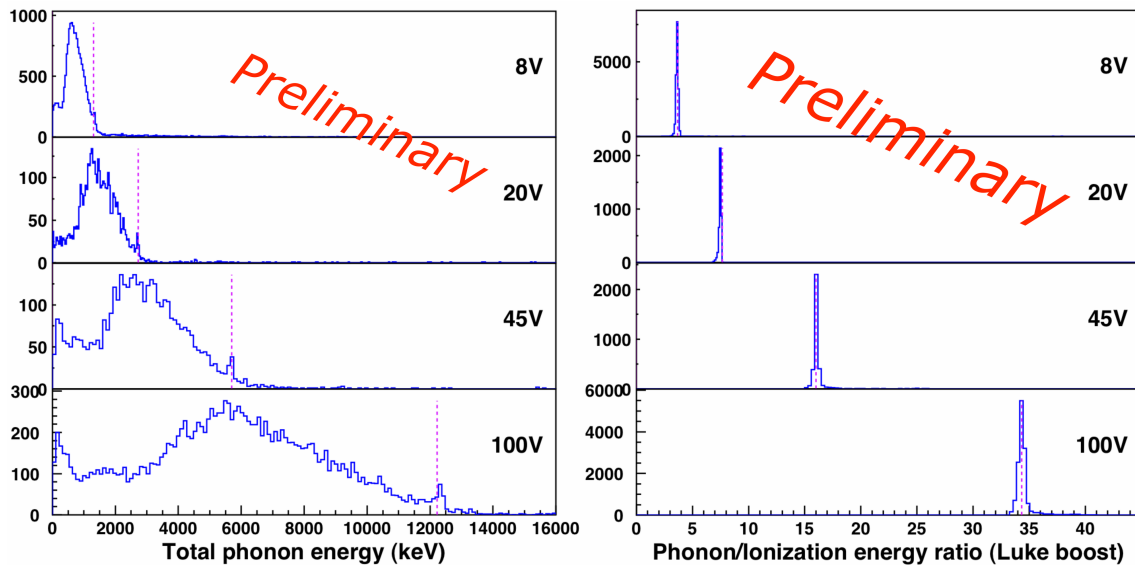
Figure 2.25: Scaling of the energy resolution by application of the NTL amplified mode for different voltages on an FID800 type detector. (^{133}Ba spectrum) Left: Energy calibrated to 8 V, 356 keV peak shifted to the predicted positions for higher voltages according to eq. 2.9. Right: the ratio of measured heat to ionization for different voltages. Figure from [151].

measure a signal on the ionization channels. Therefore, a veto-ionization channel is not usable.

With these first measurements of detector biases up to 140 V inside the EDELWEISS cryostat, an important milestone towards the sensitivity for lower WIMP masses has been achieved. It is shown that all relevant components of the detector biasing and readout are fully compatible with the increased voltages. The scaling of the energy with the Luke effect (equations 2.8 and 2.9) is shown in fig. 2.25. For higher voltages, the heat spectrum is amplified and the 356 keV peak of the ^{133}Ba source is shifted by the additional thermal energy from the NTL-effect to higher readout energies. The same shifting appears for the energy threshold of the readout trigger. Therefore, the higher detector voltage directly improves the energy sensitivity. However, the number of created charges by an energy deposit (eq 2.5) is not affected. Thus, the ionization signals are not improved and for the new accessible region of low energy recoils, the ionization channels have signals within the noise level. The right plot of fig. 2.25 shows the ratio of the measured heat energy to the ionization measurement. In the Q-plots (for instance figures 2.9, 2.11, 2.14) is the peak position for γ events normalized to 1. Events with almost no measurable ionization signal broaden this peak. A future improvement here can be achieved with the HEMT technology replacing the actual JFET amplifier stage and improving the noise level on ionization channels (see section 2.3.4).

2.5 Potential of background suppression with time resolved pulses

Pulses on ionization channels have rise times of typically < 500 ns for events in the surface region and $500 - 2000$ ns for events within the bulk volume. The standard EDELWEISS ionization readout with a sampling rate of 100 kHz, can not resolve these rise times. In order to study if one can distinguish surface and bulk events by the rise time of their ionization pulses, dedicated measurements on ID detectors as used in EDELWEISS-II have
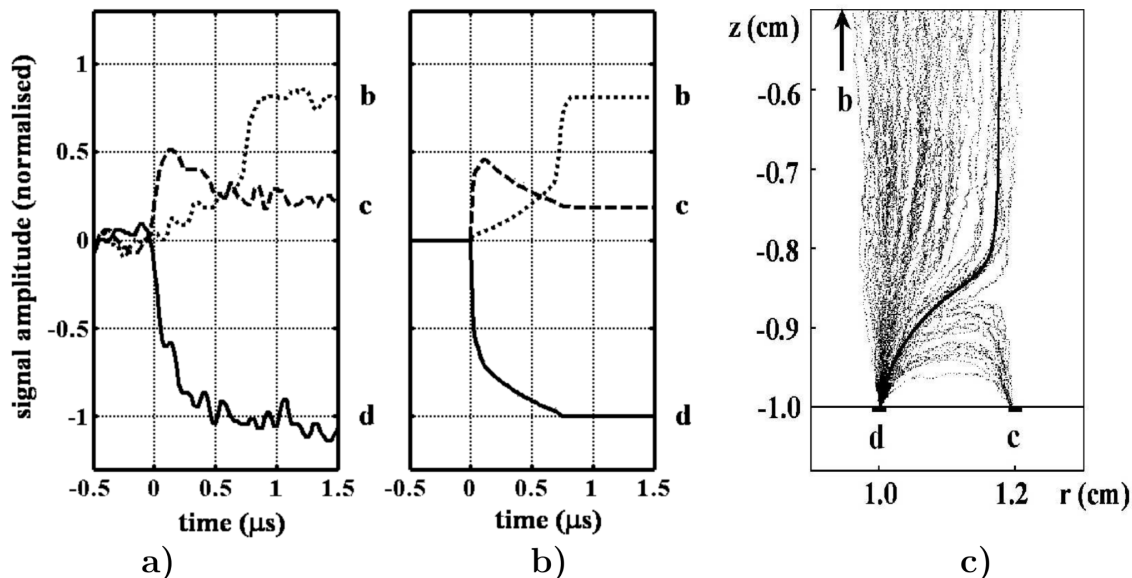
Figure 2.26: a) Example for time resolved sampling of an event in the D channel electrode induced by a ^{109}Cd source. b) Simulated event hitting the D electrode. c) Trajectories of charge carriers of the simulated event in a cut through the detector. Figures from [70].

been performed in [70]. A collimated ^{109}Cd source (62 keV and 84 keV β and 88 keV γ) has been mounted on one of the channel D electrodes. The setup produces a large number of energy deposits in the electrode and the close environment. An example pulse of these measurements is presented in fig. 2.26a. The amplitude is normalized with respect to the D electrode. The time axis is scaled in µs with $t = 0$ at the beginning of charge collection. In fig. 2.26b a simulated pulse is shown for a β impact centered on the electrode stripe. Fig. 2.26c shows the trajectories of the propagating charges for the simulated event. The experimental event as well as the simulated pulse show a side dependent pulse shape. The pulses registered by the electrodes located at the side of the energy deposit (here c veto and d collecting) show a distinctive increase with a rise time significantly below 500 ns whereas the b electrode on the other side of the detector reaches 90% amplitude $\approx$ 500 ns later. The ionization signals rise time yields a different approach for surface event rejection and its potential is investigated within this thesis.

As can be seen in fig. 2.26, the rise time of ionization signals can provide additional information about the origin of an energy deposit, possibly its z-coordinate within the detector volume. Compared to EDELWEISS-II ID detectors, also used for fig. 2.26, the FID800 type detectors are larger and have a new electrode geometry, resulting in a different shape of the electric field. Within the framework of this thesis, measurements of time resolved ionization pulses are performed on such a new detector for the first time. Data taking and analysis with the time resolved ionization channels installed on the FID837 detector inside the EDELWEISS cryostat during was performed during run 309. The event processing is discussed in section 4.2 and the analysis in section 4.3. A comparison with simulated events as in fig. 2.26 is presented in section 4.4

3. The EDELWEISS-III data acquisition system

The EDELWEISS data acquisition system (DAQ) has to bias and control the detectors as well as to ensure recording, processing and storing the available data. This is done by a modular system made of an analog stage close to the detectors and several FPGA based digital stages. The last element of the chain are run control computers which act as the user interface and write triggered data to hard disks. The modular design of individual parallel working branches make the system scalable and robust against hardware failures. With EDELWEISS-III it is possible to operate up to 40 bolometers, each with 6 analog channels: 2 heat- and 4 ionization. Every channel is sampled with a resolution of 16 bit and a sampling frequency of 100 kHz. The total physics data rate adds up to:

$$40 \text{ detectors} \cdot 6 \ \frac{\text{ch}}{\text{detector}} \cdot 16 \ \frac{\text{bit}}{\text{ch}} \cdot 100 \text{ kHz} = 384 \text{ Mbit/s} \tag{3.1}$$

This is the rate of relevant physics data from the detectors. The technical data rate is higher because of unused channels and protocol overhead. Technically a detector produces 24 Mbit/s which accumulates up to 960 Mbit/s for the full EDELWEISS-III experiment. The DAQ system has to process the technical data rate and where possible reduce it by discarding unused channels to get it closer to the physics data rate.

3.1 A new DAQ system for EDELWEISS-III and beyond

Prior to the EDELWEISS-III phase the experiment used a DAQ system of parallel working readout units named "OPERA cards". They had their name from the OPERA experiment wherefrom they were adopted. Each of these cards was equipped with a 100 MHz RISC processor, FPGA, 4 MB flash memory and 16 MB ram memory, optical- and Ethernet interfaces. The FPGA and optical interfaces were used to communicate with one single bolometer box. In EDELWEISS-II, up to 4 bolometer boxes were needed to read out one detector. Another optical connector pair was used to receive and forward a time stamp signal from a central clock generator named "Super Cluzel". The receiving and forwarding of time stamps made it necessary to correct each time stamp in each OPERA card by an individual delay. All the optically transmitted and received data flows were connected via an FPGA with the processor. Each OPERA box runs a Linux system with an EDELWEISS specific software named cew (**c**ontrôle par **e**thernet pour edel**w**eiss). This software acted as a server and streamed the detector data on an Ethernet network to the DAQ computers. In
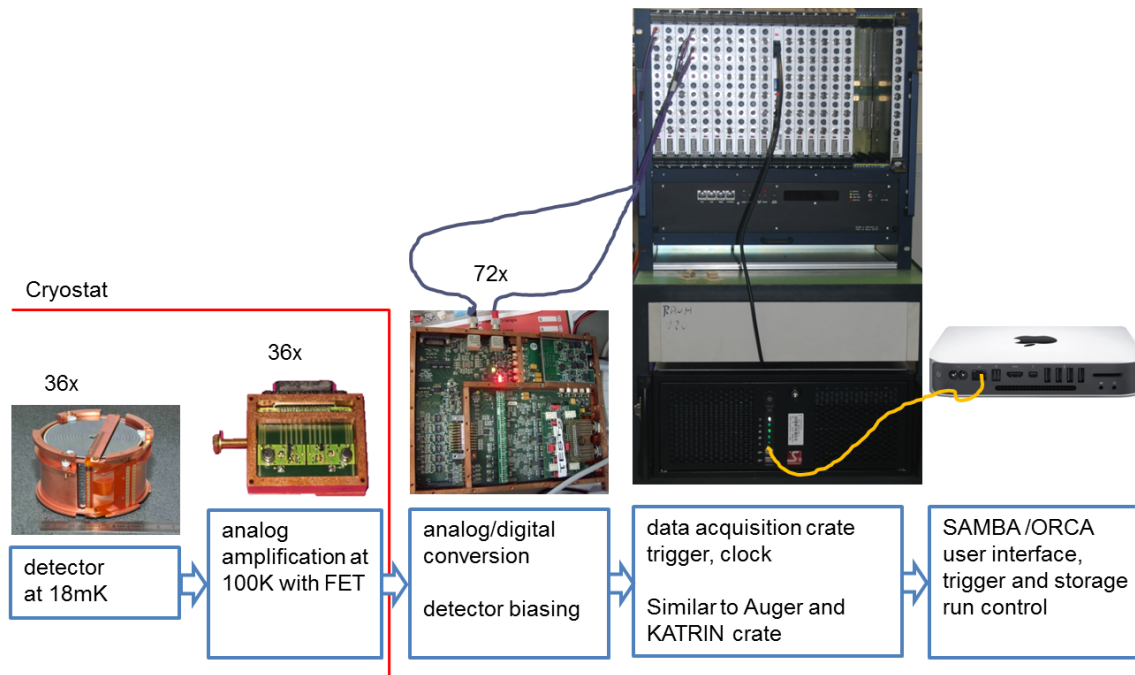
Figure 3.1: Full EDELWEISS-III data path. 36 detectors are read out via an analog amplification inside the 100 K zone by 72 digitizer boxes. Each box sends 12 Mbit/s on fiber optics to the DAQ crate. This connects via a server PC and a network to the user interface PCs.

total up to 60 OPERA cards were used for 10 detectors, some as backup only. A weakness of the system were unused channels that could not be deactivated which resulted in either zeros or ADC noise that had to be transmitted through the network towards the readout computers just to be deleted there. With the EDELWEISS-III configuration, this would have lead to only half of all channels carrying relevant physics data. In EDELWEISS-II, the time stamp was a 48 bit integer, incremented by one every 10.08 μs or with 99.205 kHz, which defined the sampling rate for the whole experiment. After electronic resets, caused by a power cut for instance, the time stamp began by 0 again. This had to be corrected in the data analysis by comparing time stamps with the additionally recorded UNIX time for events. This and other frequent problems led to the decision to develop a new DAQ system for EDELWEISS-III.

The new system should be integrated without any modifications on the bolometer boxes side and just minor changes on the readout software SAMBA. It had to be a transparent system for operators and runs stable over a long period of time. The demands to the new DAQ were:

- integrated system (1 box)

- scalable for 40+ bolometers in EDELWEISS-III and beyond

- data reduction by removing unused channels from the data stream

- time stamps generated by one central clock

- integration of external detectors such as the muon veto system or LUMINEU detectors [120]

- FPGA based trigger for the readout of 40 MHz time resolved ionization channels

- optional data reduction by an event based readout
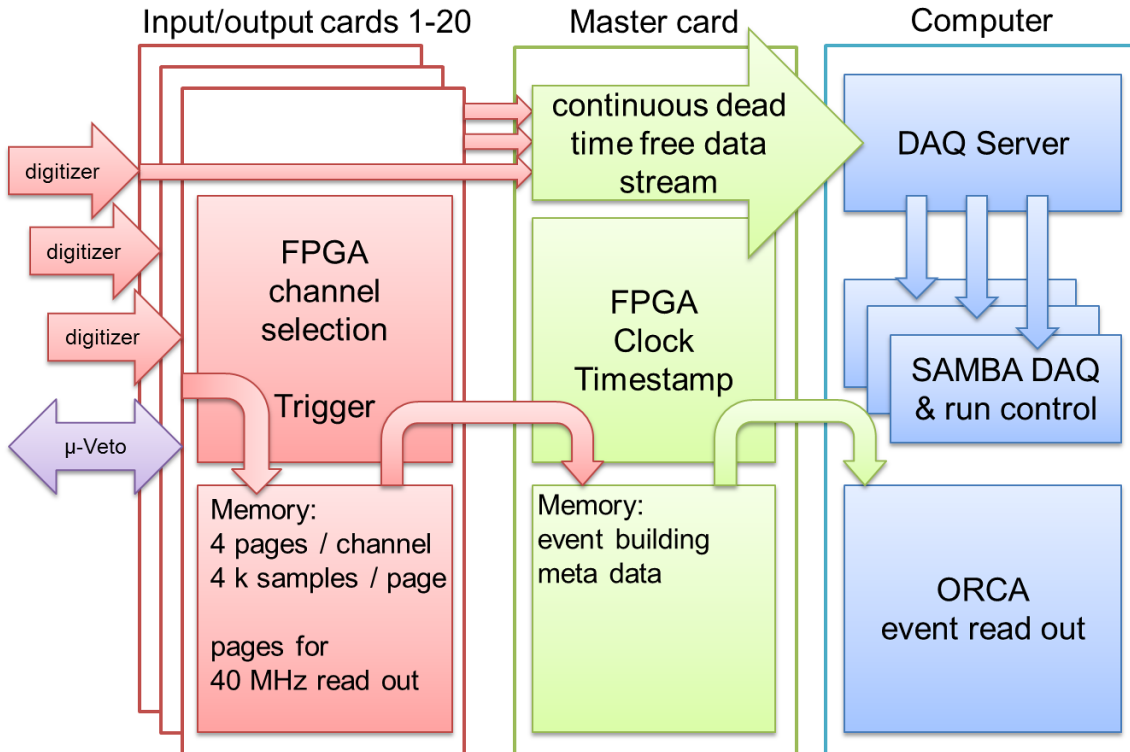
Figure 3.2: Schematic and simplified view of the data flow in the integrated DAQ system. The system combines an event based readout branch (ORCA, sec. 3.2.2) with an independent trigger logic and the traditional dead time free data stream to the EDELWEISS computers (SAMBA, sec. 3.2.1).

A good candidate for such a DAQ system existed at the KIT. It is already used in other experiments [152]: The Piere Auger observatory [153] uses an older version of this DAQ for the fluorescence telescopes [154] and three crates of the actual version for the High Elevation Auger Telescopes (HEAT) [155] which are an enhancement to lower the energy threshold of the fluorescence sensitivity of a primary particle energy of 10^{18} eV down to 10^{17} eV. In the KATRIN neutrino mass experiment [156] the focal plane detector [157], the focal plane detector's muon veto system and the monitor spectrometer [158] are read out by these data acquisition systems. Furthermore, USCT a medical technology project, is using a version of this DAQ for an early state detection of breast cancer with ultrasound [159]. This DAQ system was modified for the EDELWEISS needs, e.g. to read out a digitized data stream of the bolometer boxes through optical fibers.

In the EDELWEISS-III phase the system is used as the central part for the new detector readout, time distribution and muon veto system integration. Figure 3.1 shows the crate in its position of the readout chain. It consists of a 19 inch crate, housing a power supply and a backplane through which 20 custom purpose input/output cards (io-cards) communicate with one central master card. The internal work flow is diagrammed in fig. 3.2. During a test and development phase it was shown that an embedded Linux computer on the master card is too weak for EDELWEISS. Therefore an external computer is used, which makes the crate not a stand-alone box, but a unit of two boxes that both fit inside a 19 inch rack and are interconnected by a cable.

3.1.1 Input/output cards

The io-cards are custom designed for the application in EDELWEISS. Historically they are also named "first level trigger card" or FLT. A schematic drawing of their internal data

Figure 3.3: Logical blocks and data flow of an EDELWEISS input/output card. For details see text.

flow is given in fig. 3.3. The io-cards receive the digitized data stream from the detectors, concentrate it, remove unused channels and forward the stream towards the master card. In parallel a trigger for the event based readout is implemented. Thus, these cards can either just forward the data stream of selected channels or build events by applying a trigger algorithm, or -most important for this thesis- the io-cards do both simultaneously. Up to 20 of these cards can be installed in one crate. Each card can connect to 6 bolometer boxes from which up to 3 can be of the type bolometer box version 1. In this case an additional adapter card at the backside of the backplane is used because the bolometer box version 1 needs a third optical fiber for receiving commands.

As shown in fig. 3.3, the optical communication links are connected to a logic block named Data Link Transceiver. It manages protocol handling, for instance the Manchester code for sending time stamps and commands to the bolometer boxes, as well as reading the data stream from these boxes. The incoming data stream is split into two branches: One for the event based readout goes into the trigger unit, whereas the second branch is directly forwarded as a reduced stream to the Pixel Bus. In this case the reduced stream is the incoming technical data stream but without channels that are not connected to the detectors. From this stage on, the data stream corresponds to the bit rate given by eq. 3.1. A controller unit on each io-card uses a phase locked loop (PLL) to generate a 120 MHz internal clock signal from a physical 20 MHz reference that is received via the GTL Bus (Gunning Transceiver Logic Bus [160]) from the master card. The GTL-Bus is an unidirectional communication which is implemented on the backplane. It is used for time critical signals between the master card and each io-card, such as the clock signals. A special layout of the backplane with identical track length for equal signal run times to all io-cards makes them work fully synchronized. 120 MHz is the base frequency for all logic blocks of the card. It influences the FPGA's power consumption as well as the time needed to do a specific calculation. For the data link transceiver, which receives a 12 MHz data stream from the bolometer boxes, the 120 MHz enables a factor 10 oversampling of the incoming data stream via fiber optics. Every incoming bit is 10 times probed to ensure if it

is a logical 0 or 1 which makes transmission errors unlikely even if the optical quality of the signal has suffered for instance due to a partially damaged fiber.

The FPGA on the io-card runs a trigger unit (detailed in section 3.3.3) that constantly writes the detector data to ring buffers while in parallel analyzing the data stream for possible events. A ring buffer is a memory mode in which a writing pointer circles along an array of memory addresses with a fixed length. After one completed circle the old data is overwritten by new data. The length of this array defines the depth of the memory, and with the given data rate, the time range of passed data that can be read out. Once the trigger logic detects a pulse inside the data stream it waits for a predefined post trigger time and then switches the write pointer to the next memory page. This conserves the actual page with the pulse stored inside. Now the controller can read the stored page and send the data via the so-called PE-Bus to the master card where the data is reorganized and put together to an event. Afterwards the memory page is marked as free for being reused. This is a dead time free readout design as long as the trigger rate remains below the critical rate with which the memory pages can be read out. The performance of the PE-Bus to transmit the events is 80 MB/s. This bus is, however, not parallel for each io-card, but all cards have to share it. From eq. 3.1 results an upper limit for the amount of data to be transferred as 48 MB/s for a continuous stream. Following this, the PE-Bus bandwidth is large enough to stream all EDELWEISS data. It could even handle the extreme case of a continuous trigger on noise level. Even though this can be handled, the event mode is secured by a user defined maximum trigger rate. In this thesis, a maximum of 5 Hz per ionization channel was defined. The physical memory has to be large and fast enough for the expected data rate. The EDELWEISS version of io-cards is designed to fulfill this by using QDR memory. QDR stands for **q**uad **d**ata **r**ate which means that the memory is written with the rising and falling edge of the operational clock frequency of 120 MHz. The writing speed is given by

$$120 \text{ MHz} \cdot 2 \cdot 36 \text{ bit} \cdot \frac{1 \text{ Byte}}{9 \text{ bit}} = 960 \ \frac{\text{MByte}}{\text{s}} \tag{3.2}$$

with the factor 2 coming from the QDR technology and 9 bit per byte because technically there is a parity bit added. Reading is done the same way but by a 90° phase delayed clock. The memory is therefore much faster than the expected data rate by eq. 3.1. The implemented memory on each io-card has a size of 9 MB from which 8 MB can be used for physics data. It is split into 8 pages per channel. For each io-card a maximum of 72 channels is foreseen: Each io-card has 6 input fibers, each carrying up to 6 ionization channels, 4 time resolved ionization channels and 2 heat channels. With an event length of 4096 samples per channe, this adds up to a designed maximum memory size for on io-card:

$$\frac{4096 \text{ samples}}{\text{channel} \cdot \text{page}} \cdot \frac{16 \text{ bit}}{\text{sample}} \cdot 72 \text{ channels} \cdot 8 \text{ pages} = 4.72 \text{ MByte}. \tag{3.3}$$

8 Pages are implemented to prepare the system for a series of consecutive events, which is further discussed in the sections 3.2.3 and 3.3.3. The remaining memory is free for future improvements. The complete design is obviously overdesigned for EDELWEISS-III. However, it was not clear how many channels per detector should be readout in the event mode. For safety reasons, such an overdesign was thus accepted. Note that for this thesis only 6 channels were continuously activated in event mode while in parallel the full experiment data is streamed to the acquisition computers by this DAQ.

The register block is a memory which an operator fills with configuration and initialization parameters. Registers can be compared to variables in source code. The FPGA of the io-card reads a dedicated address that corresponds to a certain functionality. For instance the so-called stream mask is stored in the register block and tells the FPGA which channels

Figure 3.4: Logical blocks and data flow of the EDELWEISS master card. See text for details.

of the bolometer boxes carry relevant physics data and which channels are unused and filled with nothing but ADC noise. Based on this mask, the pure noise channels are not forwarded in the readout chain, saving many resources on the network and readout computer side. This was one of the fundamental demands to the new DAQ system. All trigger related constants like the shaping length or the post trigger time are represented by memory addresses in the register block as well. The FPGA does not only read registers for its configuration, but also writes in certain registers. For instance, the FPGA can post status information such as the actual trigger rate, event counter, noise level and error codes. The stored variables can be read by software automatically, or by a user. The acquisition software ORCA and SAMBA, described in detail in section 3.2.2 and 3.2.1 read these registers for instance when the operator opens the related control window on one of the acquisition computers. The stored information is then displayed by the software in a human readable format.

3.1.2 Master card, clock and time reference

One FPGA based master card in the central slot of the DAQ crate manages all 20 io-cards (ch. 3.1.1). Historically, and in other experiments, this card is also known as "second level trigger" or SLT card. It communicates through a PCIe (PCI Express) interface with a DAQ server. Three independent bus systems on the backplane make up the communication between the master card and all io-cards. These buses are implemented as so called low voltage differential signaling lines or LVDS. With this technology the sender sends a bipolar signal on two neighboring tracks. On the receiver side the tracks are connected by a 100 Ω resistor, twice the size of the track impedance to avoid reflections. A differential amplifier is used as a receiver. If an external electromagnetic source radiates a crosstalk signal on the track, it would appear as a symmetrical crosstalk (common-mode interference) on both inputs of the differential amplifier. The signal, but not the common-mode interferences, is amplified. This increases the signal to noise ratio (SNR).

The master card is the interface between FPGA based electronics and computer based readout software. All detector data that arrives from the io-cards via the pixel bus is stored in one of 6 FIFO memories. FIFO stands for "first in first out" and is a memory mode used as a buffer between two communication partners that are not strictly synchronized or if a

continuous stream has to be forwarded into packets and vice versa. Here, a continuously transmitted data stream has to be divided up in network packets. The server PC can read the FIFOs through a PCIe interface and serve the data on a Gigabit Ethernet network to the acquisition computers.

The event based readout branch sends triggered events via the PE bus interface to the master card. The event manager receives and stores the events in a dedicated event FIFO which the server can read as well. Coincidence between multiple detectors are identified by their time stamp and put together into one event. Each event packet gets a special event header that contains meta data about the event, such as the trigger time stamp, energy, channel, trigger rate and noise level.

A very important and fundamental task of the master card for the EDELWEISS experiment is its function as the central clock and time reference. A 20 MHz quartz oscillator feeds a phase locked loop that generates a 240 MHz frequency. Based on this, several dividers generate signals of 120 MHz, 12 MHz, 100 kHz, 1 kHz and 1 Hz. Most important for EDELWEISS are the latter three frequencies because they constitute the 10 µs time stamp, the 1 ms strobe, which initializes a command broadcast, and the 1 s strobe, followed by broadcasting the time stamp. A time stamp is a 48 bit long unsigned integer that is incremented by 1 each 10 µs. It was initialized with the value 0 on the 11.11.2014 at 11:11:11 Unix time which makes this date the beginning of the "EDELWEISS epoch". In case of a power cut or a restart of the crate the time stamp restarts with 0, however, data taking is not possible at this moment. Once the DAQ server has restarted (about 2 minutes later) the time stamp is reset by software to the reference date again and data readout can be started. The necessary offset is calculated from the PC system time, which itself is using the LSM network gateway as reference. Unlike other experiments that have to synchronize events from different locations or at different laboratories, EDELWEISS has no demand in a world-wide precise time stamp. But internally the time stamp has to be explicit and unique. It is used to detect bolometer-bolometer coincidences and coincidences with the muon veto system. Furthermore the time stamp is forwarded to the LUMINEU DAQ system which allows to detect coincidences between the muon veto system and LUMINEU detectors as well. Except from the initialization through the DAQ server, the time stamp is a free running quartz oscillator based clock, which of course drifts during time. This drift is influenced by effects like the environmental temperature inside the crate, humidity, variations of the power supply and aging effects. The computer clock is not better, but it is regularly synchronized via the NTP protocol with a network reference, which is again synchronized with one of the global NTP servers. However, the PC time can be used to estimate the drift of the EDELWEISS time stamp. This has been done within this work and a drift of $+6.4 \cdot 10^{-11} \frac{s}{s}$ or approximately 3 s per day was found. Since the crate is running normally $\mathcal{O}(100 \text{ days})$ without being restarted, several minutes offset can accumulate. During a restart, the crate clock is turned back compared to the global time with which it is reinitialized. This could lead in a worst case scenario to multiple events with the same time stamp. However, restarting the DAQ and afterwards the data taking, needs several human actions. It is very unlikely that this worst case scenario can happen. Additional safety is provided by the PC time which is stored in each event header, either from ORCA or from SAMBA, enabling a time stamp recalibration during the offline data analysis. To conclude, each EDELWEISS-III time stamp is a 48 bit unsigned integer that tells the number of 10 µs that have passed since 11.11.2014, 11:11:11 UTC.

The bolometer boxes have to be configured by commands that are normally sent from the SAMBA software. These commands have to be forwarded from the crate to their destination. A bolometer box accepts commands by an identifier that acts like an address. Unfortunately these identifiers are not unique and can not be fixed. Therefore each command is encapsulated with a second command that is addressed to the io-cards and
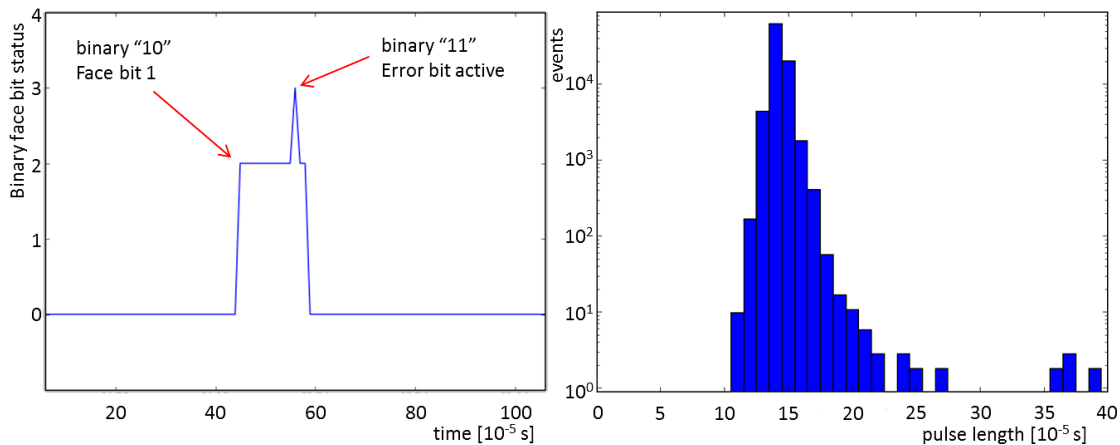
Figure 3.5: Readout of the veto system through the new DAQ. Each face of the veto system (section 2.1.2) is reported as a bit status once per 10 μs. In case a veto trigger occured the bit remains active until it is reset. The io-card interprets it as a conventional channel and shows the status as a function of time (left plot). The spectrum of status pulse lengths for $8.9 \cdot 10^4$ muon veto events (right plot) shows a minimum pulse width of 110 μs, giving the minimum dead time after a triggered event.

tells which optical transmitter should send the bolometer box command. The master card broadcasts all this encapsulated commands via the GTL-bus to each io-card. With this workaround it is ensured that a command is always delivered to the right destination and nowhere else. The EDELWEISS protocol allows to transmit these commands only after the 1 kHz strobe. Therefore the controller of the master card has a small memory array working as a command FIFO.

The master card is equipped with an EPROM memory on which the firmware (FPGA software) is stored. After a power cut or a system restart, the FPGA has to reload this firmware. Once this is done, the master card broadcasts the special io-card firmware to these FPGAs. It takes about 2 s until the crate has booted. The FPGA firmware had to be corrected or updated with new features a couple of times for this thesis. Upgrades are done with the help of a "JTAG programming interface" which is connected to the master card on the front panel. We can upgrade the firmware from a programming software that is installed on the ORCA computer. By doing this the old firmware in the ERPOM is overwritten by the newer version and after a reboot the FPGAs execute the new version. The DAQ crate power supply has a micro controller which can be accessed via the http protocol with a browser. Actual sensor information like internal voltages, fan speed and different temperatures can thus be checked. Most important is the ability to switch the DAQ crate off and on remotely via this page.

3.1.3 Integration of the muon veto system in the DAQ

A special operation mode of the io-cards is the muon veto system mode. In EDELWEISS one of the cards is operated in this mode. Only the first pair of fiber input and output is used and connected with the DAQ system of the veto. There, every 10 μs the central card (Time Base Board)[161] receives the 48 bit time stamp. The veto system reads the time stamp and uses it internally for its own independent data acquisition. Additionally it attaches six status bits also called face bits [76, 77]. Each of these bits represents one of the six faces of the veto system (see section 2.1.2). It is set to 1 if one of the corresponding modules has registered an event. The time stamp is sent back to the io-card followed by

the face bits. The FPGA receives this and processes it like 4 bolometer channels: Three are dedicated to the 48 bit time stamp, since it is split in 16 bit values, and in a fourth channel the face bits and one error bit is written: the error status in the least significant bit, followed by the faces 1 to 6. The FPGA checks if the received time stamp has the same value as the one that was previously sent. If both stamps mismatch, the error bit is set to 1. The io-card running in veto mode is streamed into a dedicated FIFO on the master card that can be read by all acquisition computers simultaneously. Therefore it is possible to trigger any EDELWEISS detector on muon signals. In fig. 3.5 an example pulse is shown of a muon veto event with face bit 1 set. This is the case if only the top side of the veto detected a signal. The length for which a face bit remains set after a muon hit adds up to the systematic dead time. From the histogram one can see a minumum dead time of 110 μs. Furthermore, the pulse in fig. 3.5 shows that the error bit was activated for 10 μs which indicates that one single time stamp was not sent back from the muon veto system correctly.

During this thesis the error bit was used in test measurements to check the quality of the transmission between both DAQ systems. On the test stand at KIT the error bit set to 1 appeared 3 times during a 140 h long test run, giving the error rate of $5.95 \cdot 10^{-11}$ transmission^{-1}. For this test, a function generator was connected to the face bit input. It simulated pulses of 150 μs length at a frequency of ~ 1 Hz to have a comparable condition as in Modane. Furthermore, it was observed that external electromagnetic interferences (EMI) can trigger hundreds of such errors. The EMI was produced by switching a hot air gun (1600W) frequently on and off. Since different power supply circuits and an additional decoupling transformer on the 230 V supply were used, it is unlikely that the interference coupled through the power line. A measurement with the full system at the EDELWEISS experiment showed an error rate of $1.28 \cdot 10^{-9}$ transmission^{-1} which is higher as the measured rate at the KIT test stand. These error rates are not problematic, since individual transmitted time stamps are affected. Further tests were performed to see if a similar transmission error occurs in the bolometer readout path, which is not the case. Since the important part of the transmission is to send the time stamp to the muon veto system and not back, this effect was not further investigate it.

3.1.4 DAQ server and data transfer

In the first R&D applications of the new DAQ system, the DAQ server PC was not existing as a stand alone machine. Instead, the master card had a small top mounted adapter card, named "processor mezzanine card" on which an embedded CPU was running with a Linux system. This card was limited by a too slow 100 Mbit Ethernet connection which according to eq. 3.1 is not sufficient for EDELWEISS-III. Furthermore, the processor was slow compared to standard consumer products and the memory was limited. A processor mezzanine card with 1 Gbit Ethernet was not available at that time, therefore we replaced the mezzanine card by an adapter for an external PCIe interface. The PCIe cable can be up to two meters long and is connected to a stand alone PC. It is thus possible to select powerful hardware and keep the option for a later upgrade of the DAQ system with a GPU (graphics board for standard PC). The DAQ server is placed inside the same 19 inch rack as the DAQ crate. The operational system is a SUSE Linux with deactivated graphical user interface. The remote access to this machine is done via the ssh protocol. A server software named *ipe4reader* manages the data flow and communication with all EDELWEISS acquisition computers. The DAQ server has a hardware clock which is synchronized automatically with the LSM networks Internet gateway. When *ipe4reader* is started, it sets the absolute value of the 48 bit time stamp in the master card to the actual real time value as described in ch. 3.1.2.

The main task of the DAQ server during EDELWEISS operations is to act as an interface

between the FPGA based hardware level of the DAQ and the acquisition computers. Two software servers are executed in parallel. One of them, *ipe4reader*, serves the continuous data stream of the full experiment including the muon veto system to 2-6 acquisition computers. This is done by reading the FIFOs $\#1-6$ (fig. 3.4), concentrating the data of each FIFO in individual packets and sending the packets via udp protocol to the acquisition computers. Since unused channels have been removed from the stream when passing the io-cards and one FIFO accommodates data from 12 detectors, the data rate is 115.2 MBit/s/FIFO, according to eq. 3.1.

Reading the FIFOs is done by a method named "polling". Each FIFO can set a flag "FIFO half full". The value of this flag can be either 0 or 1. If the value is 0, the task sleeps and polls again after a second. If the value of the flag is 1, the FIFO is read. The data is transfered to the DAQ servers memory. This memory has a size of 8 GB and is thus much larger than necessary. Writing the data from the PCIe interface to memory is done by DMA (*D*irect *M*emory *A*ccess), a mode in which a dedicated controller manages the data flow and reduces work load for the CPU. The data stream contains the status bits of the bolometer boxes (see section 2.2.10). Each bolometer box sends 10^5 status bits per second from which the first 912 are used. These status bits are collected for all bolometer boxes that are assigned to this FIFO and sent with a separate network packet to the associated SAMBA instance. It is done once per second, enabling SAMBA to display once per second new information of the bolometer box status, for instance the electronics temperature. After each second the 48 bit time stamp is injected from the master card inside the data stream of the FIFO. This is detected by *ipe4reader*. For each assigned bolometer box the collected status packets are extended with the time stamp and sent as 280 Byte long packets to SAMBA. For one FIFO with 12 detectors and 24 bolometer boxes this adds up to 6.72 kB/s being negligible in comparison with the network capacity of ~ 125 MB/s. However, sending the detector data on the network is not negligible. SAMBA expects the data to be sent with UDP protocol. This is done by putting the data inside a UDP-packet with a UDP header, which is then put inside an IP packet with an IP header, which is put inside an Ethernet frame. The Ethernet frame is finally transmitted on the network. The maximal efficient payload of an Ethernet frame is 1500 Byte. Larger payloads per package are split and the number of packes increases, thus, more headers and protocol overhead has to be transfered. The optimal size of data per packet is given by subtracting the fixed size of each header from the 1500 Byte payload. 20 Byte IP header and 8 Byte UDP header gives 1472 Bytes for data. Actually we use 1440 Byte data which corresponds to 100 μs data of 12 detectors. Additionally we add an EDELWEISS header that constitutes a 16 bit packet counter and the 16 least significant bits of the time stamp to which the first sample point of this packet belongs to. With this design we are $\sim 2\%$ below the optimal network usage.

The conventional EDELWEISS data recording and experiment control is performed with the software SAMBA (section 3.2). For experimental tasks, such as the readout of the time resolved ionization channels, a second software named ORCA is used. Since ORCA has to communicate with the DAQ as well, a second server task is executed on the DAQ server as a back end for ORCA. This interface is used for the event mode readout, thus, the data rates are much smaller. In the present setup, one event is constituted of 2 time resolved channels, 4 standard ionization channels and 2 heat channels. Each channel is read out as a 4096 sample points long trace. With a high trigger rate of 1 Hz (typical EDELWEISS trigger rate is 20 mHz) the event mode data rate adds up to 65 kB/s for one detector. Compared to the network capacity this is 6 orders of magnitude below and can be disregarded. This is the main motivation of a hardware trigger concept, a tremendous reduction in data flow.

3.1.5 GPU based trigger for EDELWEISS detectors

The DAQ server hardware has been selected with the option to later upgrade it with a GPU. Historically, GPUs were special processing platforms, designed to compute the graphical output of a computer. Actual standard hardware has a screen resolution of 1920 pixel horizontal and 1080 pixel vertical, which corresponds to a matrix with $\sim 2 \cdot 10^6$ elements. Today, GPUs are available for computing clusters. This modern hardware is also known as GPGPU (**G**eneral **P**urpose computation on **G**raphics **P**rocessing **U**nit). The design is optimized to apply different algorithms on even larger matrices or on large vectors in a fast and efficient way, whereas the CPU would need a longer time and more energy for the same computation. GPUs follow the SIMD (**S**ingle **I**nstruction, **M**ultiple **D**ata) design, meaning that one simple instruction can be evaluated for many data points in parallel. The EDELWEISS event building can benefit in two ways from SIMD: First by a parallel processing of all channels and second by further parallelization of the algorithms (especially FFT) that are applied to each channel.

A GPU implementation for EDELWEISS can be achieved in the following way: The io-cards' FPGAs remove unused channels from the data stream. The master card concentrates the stream of all io-cards and forwards it through the PCIe interface to the DAQ server. The technical data rate will be close to the physics data rate of 384 Mbit/s (eq. 3.1). The server has to forward the data stream to the GPU which is done via PCIe as well. In the PCIe standard of version 3.0, a bandwidth of 985 MB/s is foreseen on each line and a GPU uses 16 parallel lines. For EDELWEISS, only 48 MB/s is needed, which is a factor 320 below the limitation. Once the data is transferred to the GPU memory, the same demodulation, trigger and event building algorithms can be applied as on the acquisition computers. The advantage of the GPU is here the parallel computing of each channel by using the SIMD principle. For instance the EDELWEISS heat trigger algorithm (further described in section 3.2.1) on the GPU would work with individual heat template pulses that are stored and kept as Fourier transformed pulses in the GPU memory. Incoming data arrives in packeges that for instance correspond to 1 s of the stream. Each channel is represented by a vector type object. The demodulation can be accelerated because each demodulated sample point is calculated by a fixed length subset of the input vector for which the GPU uses several parallel working processing units, whereas a CPU would need to calculated all sample points serially. Once demodulated the signal has to be convoluted with the template pulse. The most efficient way for this calculation is the fast convolution, which utilizes the FFT as well. A discrete convolution has a computational complexity of $\mathcal{O}(N \cdot K)$ with N sample points in the input vector and K sample points in the template. In the Fourier space the convolution can be executed as a multiplication. Therefore, the best way to filter the heat channels is to transform them into the frequency space by Fast Fourier Transformation, which has a complexity of $\mathcal{O}(N \log N)$ for $N > K$. The GPU manufacturer NVIDIA provides the software toolkit CUDA [162] and the cuFFT package [163], for an efficient implementation of FFT based algorithms on GPUs. Tests with an EDELWEISS-like setup and simulated data have been successfully performed at KIT [164], but not yet on the experiment site at Modane. These tests have shown that EDELWEISS typical data flows can be directed with standard hardware to a GPU where digital signal processing is performed. EDELWEISS specific signal processing, such as the heat channel demodulation and trigger algorithms were not performed in these tests.

If one compares the potential of a GPU event building with the FPGA event building presented in this thesis, and the CPU event building, which is the standard in EDELWEISS, the GPU has the great advantage of having less software restrictions compared to the FPGA (for instance divisions, and flexibility to change algorithms) and much more memory (factor 1000) available. Compared to the CPU based trigger, the parallelism is the main advantage. Within the EDELWEISS-III phase, 3 parallel working computers with CPU based triggers

are needed for the event building process, and trigger algorithms are only applied to heat channels. The same performance could be achieved by 1 GPU including trigger algorithms on both heat and ionization channels. Additionally, the requirements to the network are obviously less stringent if the event building is done before the data is sent on the network. The GPU is perfect as a trigger for data reduction. The eligibility for triggering the readout of the time resolved ionization channel has to be considered differently. Here, it is mandatory to detect the pulse within 4 ms (further discussed in section 3.3.3) but the GPU computes most efficiently large input vectors containing $\mathcal{O}(< 10^5)$ sample points which corresponds to 1 s of streamed data. Therefore, the trigger from a GPU would be delayed too long (factor 250) to be used as a readout trigger for the time resolved channel. This could be addressed either by using a larger sized memory (inside the bolometer box) for buffering the 40 MHz data with $\mathcal{O}(4\text{ GB})$ capacity or by working with smaller data packets on the GPU, or a combination of both. Increasing the memory to that size is impossible with the restrictions given by the bolometer box (available space, power consumption). However, decreasing the packet size on the GPU reduces the potential speed up compared to a CPU. Thus, a GPU based trigger seems to be an option to replace the conventional EDELWEISS DAQ computers but the expected delay between a physical event and the trigger decision due to the data transfer in (larger) packets to the GPU make it problematic for an application as a trigger to read out the time resolved ionization channels.

3.1.6 Acquisition computers

The EDELWEISS acquisition computers are the interface through which operators on shift control all parameters of the run mode and data taking. The conventional data recording is performed with 2-3 Mac Mini PCs, each can read out one FIFO which corresponds to up to 12 detectors. An in-house designed software named SAMBA (section 3.2.1) with a graphical user interface is used to control run parameters, start and stop runs and change the run mode (Barium, WIMP search). The acquisition computers are connected with a 1 Gbit/s Ethernet interface to the EDELWEISS acquisition network and with a second interface to the internet. The detector data is recorded with these DAQ computers, stored and transfered to the Tier-1 computing center at the University of Lyon. A special case is given by the 6th FIFO, which connects only to the muon veto system. It is copied to all acquisition computers, offering to trigger all detectors on a potential muon event.

Additionally a fourth Mac Mini is installed to receive the events triggered by the FPGA together with the 40 MHz time resolved ionization channel. It was used to record all 40 MHz channel data for this thesis, more than 750 GB. The Mac Mini with ORCA is additionally used to maintain and upgrade the FPGA related firmware through a hardware programming interface as described in ch. 3.1.2.

3.2 EDELWEISS acquisition and run control software

The main EDELWEISS software for data taking and run control is "SAMBA", an in-house designed software which is constantly enhanced with new features [165]. SAMBA runs on the Mac Mini DAQ computers which are located inside the EDELWEISS control room at LSM, described in section. 3.1.6. In the EDELWEISS-III phase each SAMBA instance controls up to 12 detectors which adds up to a data stream of 115.2 Mbit/s plus protocol overhead. Additionally another Mac Mini with the alternative DAQ software "ORCA" is installed inside the DAQ rack. This computer gives a second option to control all detector related parameters and provides a full control interface for the DAQ crate. But the main task for which ORCA is used is the event based readout of the 40 MHz time resolved ionization channels.

Figure 3.6: Data taking interface of SAMBA during a run. See text for details.

3.2.1 SAMBA readout and event building

SAMBA (**S**ysteme d'**A**cquisition **M**ulti-**B**olometres sur **A**pple, acquisition software for multiple bolometers on Apple computers) is used by the operators in shift to control the run and the data recording. This is done by a graphical user interface which is either controlled directly in the control room on site or remotely through a VNC session. The main window during run operation is shown in fig. 3.6. It allows the user to perform fundamental tasks, such as start and stop data taking or begin and end a detector regeneration phase. For all typically used run modes and regeneration procedures are different configurations of the detector readout electronics foreseen. The electronic components are configured by several hundreds of individual commands. These commands are bundled in scripts. Based on the operator's selection for the run mode, SAMBA dynamically selects the right commands and sends them to the hardware. Once the run is started and the data stream is active, the central part of this window shows the last triggered event and the filter output. Additional information like the recent and the global trigger rate are calculated and presented. The right part of the window shows computer related information. In case of a too high trigger rate the CPU or memory usage can reach saturation. If this happens the system would lose data. The operator can see this and if necessary change run settings, for instance the trigger thresholds. Other important features of SAMBA are the options to present data instantaneously. An oscilloscope-like mode and FFT based spectra can be used for the fine tuning of channels.
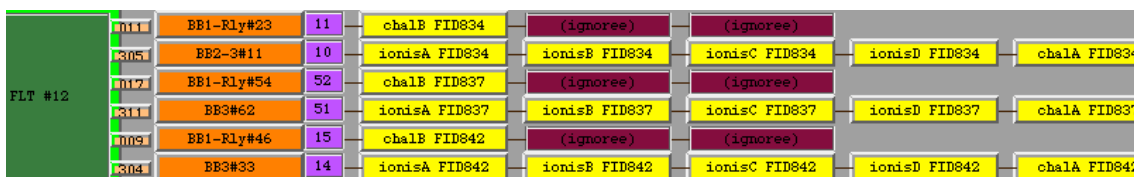
Figure 3.7: Excerpt of the SAMBA experiment configuration window, showing detector/channel names (yellow), digitizer box type with number (orange), on which station the box is connected to the experiment (violet) and to which FLT card (green).

Another layer of parameters represents experiment specific configurations that go beyond the normal operation. SAMBA can display several more windows in which for instance channel specific trigger settings or detector specific hardware settings like the anti aliasing filters or electrode voltages can be configured. The philosophy behind the presentation of this information is that the operator can configure a detector without thinking of the electronic components between SAMBA and the detector. To achieve this, SAMBA needs a complete map of the experiment and the information, how all components that can be addressed are interconnected. This is done with ASCII files that can be graphically

visualized to help with the configuration. An excerpt of such a visualization is shown in fig. 3.7. For one of the topics of this thesis, two prototypes of modified bolometer boxes in order to provide higher detector voltages at the experiment (see ch. 2.4.1) had to tested on all 24 installed detectors. Therefore, we had to change the experimental setup a couple of times and often used the presented SAMBA function for mapping the experiment.
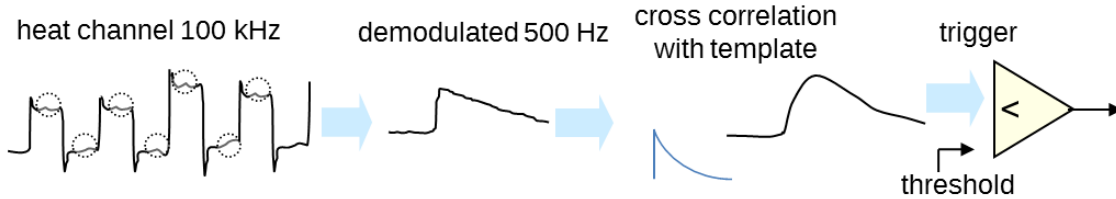

Figure 3.8: Principle of heat channel demodulation and trigger with sketched data.

During a normal run SAMBA receives a continuous dead time free data stream of each detector. The software performs the complete event building procedure for which it applies a trigger algorithm on the heat channels and stores the recorded data on the computer's hard disk. The whole event building is based on a pulse detection in the heat channel. The principle of the SAMBA heat trigger algorithm is shown in fig. 3.8. First, the continuous heat channel stream is demodulated. An example of raw data before demodulation can be seen in fig. 2.16. The rectangular modulation has a frequency of 500 Hz. Each plateau is made of 100 sample points. To avoid chaotic effects from the phase transitions of the modulation, only 20-50 sample points are typically used to calculate the plateau's mean value. The difference of the mean of a positive plateau and the mean of the following negative plateau is one demodulated sample point. This results in a 500 Hz sample frequency for the demodulated channel. Such a demodulated pulse is shown in fig. 2.6. The demodulated channel is filtered by a FIR (**F**inite **I**mpulse **R**esponse) Butterworth high-pass filter. In the next step the demodulated channel is continuously cross-correlated with a template pulse, filtered by the same Butterworth high-pass filter. Each heat channel has its own template. The templates are characterized by a rise time and two exponential declines. The template equation is:

$$f(x) = p[1] \cdot \left(1 - e^{\frac{x-p[0]}{p[2]}}\right) \cdot \left(e^{-\frac{x-p[0]}{p[3]}} + p[5] \cdot e^{-\frac{x-p[0]}{p[4]}}\right) \tag{3.4}$$

The five parameters $p[i]$ are channel specific. The relative position of the pulse is defined by $p[0]$. An amplitude is given by $p[1]$. Since all templates are fitted with a 356 keV pulse, $p[1]$ is a channel specific gain. The different pulse shapes are modeled by the rise time parameter $p[2]$, the fast decline parameter $p[3]$ and the slow decline parameter $p[4]$. With $p[5]$ the transition from fast to slow decline is controlled, it is equivalent to an amplitude. To define the parameters, EDELWEISS uses measurements with a ^{133}Ba calibration source. An operator has to select exemplary 356 keV pulses by eye. The pulses are chosen to be as good as possible with a stable baseline around and no pile-up pulse overlapping in the decay time. SAMBA stores the fitted parameters in configuration files and uses them to generate the channel specific heat template.

The convolution filter output is compared with a constant value, the so called trigger threshold. If this threshold is exceeded the event building process is started. The value of the trigger threshold can be automatically changed during the run to maintain a stable trigger rate, or it can be set to a fixed value. The event is assembled from demodulated heat data with a predefined number of data points before and after the event time stamp. It is possible to change the event length. In EDELWEISS-III it is always set to 1024

demodulated sample points for a heat channel which corresponds to a record time of 2 s. The time stamp at which the convolution of real data and template reaches its maximum is used to calculate the event time stamp, which is done by subtracting the rise time used in the template. Based on this event time stamp, other channels are added to the event record. It is possible to read out just the triggered channel or all channels of one detector, several detectors or the complete experiment. Usually the detector on which the event was detected are read out and all channels of the neighboring detectors are recorded as well. During this event building process EDELWEISS faces the special requirement of merging the "slow" demodulated heat channel of 500 Hz with the 200 times faster ionization channels of 100 kHz. This is done by selecting a time window of ± 2048 sample points around the estimated event time stamp. Furthermore, SAMBA generates for each real ionization channel a virtual so called slow ionization channel. This is done by down sampling the 100 kHz channel to a 1 kHz sampling frequency by averaging over 100 sample points. Each channel record has a length of 2048 down sampled points, which corresponds to a recorded length of 2 s. These long records are used in the analysis to get a long integration time for the amplitude measurement. The channel records are written to the hard disk together with an event header that contains data such as time stamp, information which channel triggered, PC-time of the event and a serial number.

The SAMBA event files are regularly transferred via internet using the sftp protocol to the Tier-1 computing center at Lyon where an offline processing is performed. This includes the pulse localization in the 100 kHz ionization channels and trimming these channels to 4096 sample points length with the pulse in the center. The event time stamp is redefined based on the ionization signal which is more precise due to its higher bandwidth. The anti aliasing filter of the bolometer box, which is a configurable low pass filter, typically set to 40 kHz, reshapes the pulse rise time from typically $< 1\ \mu s$ to values of $10 - 20\ \mu s$. Software convolution with the step response function of the filter results in a precision better than $10\ \mu s$. Section 2.3 presents the offline analysis.

3.2.2 ORCA readout software

For the event based readout of the time resolved ionization channels and for low level hardware access, EDELWEISS uses a second readout software named ORCA (**O**bject-oriented **R**eal-time **C**ontrol and **A**cquisition)[166]. ORCA is programmed in Objective-C, uses Apples Cocoa Freamework for the graphical user interface and runs under MAC OS X. It was designed for the SNO and SNO+[167] experiments. ORCA provides common tools for all DAQ related tasks, such as data recording, storing and hardware monitoring. Furthermore, ORCA brings a scripting language to program more complex tasks for the run control. Within this thesis such a script was developed to automatically initialize the trigger threshold for the time resolved channel readout. ORCA uses libraries to connect to external devices such as oscilloscopes, waveform generators or motors, connected by common interfaces like Ethernet, USB or RS232.

For the EDELWEISS application, ORCA graphically presents all register settings of the master card (section 3.1.2), every io-card (section 3.1.1) and the bolometer boxes (section 2.2.10). Configuration of the hardware can be done by ORCA scripts or by manually executed commands. ORCA can read either the continuous data stream or the event FIFOs on the master card. The read out data is stored in ORCA files. This format combines an XML header and the binary data. The header provide information for further processing. It tells the converter how many channels have been activated, which is necessary to reorganize the recorded events channel wise. An additional program *orcaroot* can be executed in a Linux shell and transforms the ORCA data files into the ROOT [168] format. For this thesis, all data recorded with the time resolved channel have been converted by orcaroot into ROOT files (see section 4.2.1).

ORCA can display the current detector state like an oscilloscope. Either 10.000 sample points of selected channels are plotted once per second from the continuous upstream, or, with activated trigger and event readout, the last observed event is shown. This channel monitoring is very useful when changing detector relevant settings, for instance the voltages. It enables a fast feedback for the operator without waiting for an offline data processing. The ORCA plotting interface can be scaled by a calibration factor to change the generic ADU scale into mV or keV. Furthermore, it is possible to display the spectrum of a channel. This is calculated with the FFT and a selection of different window functions.

Within this thesis it was necessary to activate the event based readout after each detector maintenance and to stop it again before the next maintenance begins. Since the detectors and the maintenances are controlled by SAMBA, an ORCA-SAMBA interface was developed. With this interface SAMBA can stop the ORCA recording and restart it after the maintenance phase is completed.

3.2.3 Pile-up handling in the FPGA triggered readout branch

Most experiments with an event based readout need a mechanism to deal with pile-ups. EDELWEISS as a rare event experiment has an event rate of $\mathcal{O}(10 - 100 \text{ mHz})$ per channel, when the calibration sources are deactivated. The trigger rate of the FPGA based readout is around 0.3 Hz, since the threshold is set close to the noise level. Thus, most recorded events contain no pulse. The readout window of the ionization channel has a width of 4096 sample points or 40 ms. Thus, pile-ups are expected in 1.2% of all events. However, three different situations with consecutive events have to be considered for the event building mechanism:

1. within the post trigger time of 20 ms $\rightarrow$ pile-up

2. between 20 ms and 40 ms after the first pulse

3. between 40 ms and 64 ms after the first pulse

In the first case, the trigger registers the second event but no memory page change or extra readout is initialized. The consecutive pulse is visible in the previously triggered event. The readout of the first event also makes the second pulse available for the analysis.

In the second case, the first event is completely recorded and after a post trigger time of 20 ms, the write pointer is switched to the next memory page. The second event appears after the write pointer changed the page, but before a full cycle of 40 ms is written in the new page. This produces an artifact when the event record of the consecutive pulse is read, since old and arbitrary data from the memory appear in the baseline of the pulse. These events are skipped in the analysis of this thesis, further discussed in section 4.2.2. One could think of a mechanism that delays a consecutive trigger to at least 40 ms. Then, the described effect would not appear, but the pulse is not longer centered inside the event record.

In the third case, with a delay of more than 40 ms, the consecutive pulse can be accepted as an individual event. However, there can be an artifact appear inside the readout of the time resolved ionization channel. These channels are transmitted individually and only after a trigger command. This command is sent 4 ms after the physical pulse appeared. Then, receiving the time resolved channel record takes additional 40 ms. Therefor, the complete time span in which the system is busy with event building adds up to 64 ms.

3.3 Time resolved ionization channel

Dedicated simulations and measurements [70, 169] have shown that a rise time analysis can help to discriminate surface and fiducial events. The results are shown in fig. 3.9 for a
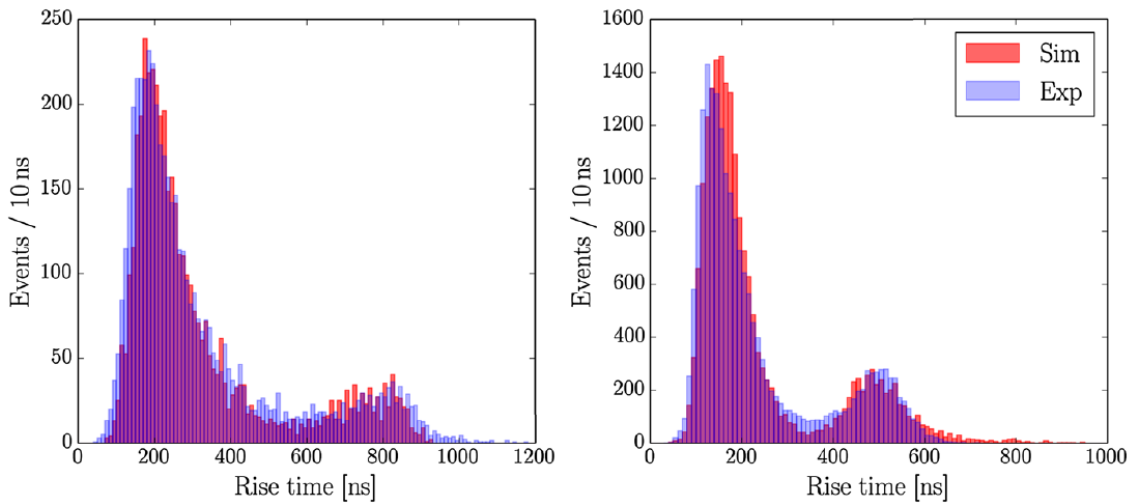
Figure 3.9: Simulation and experimental rise time analysis with a comparable but smaller ($m = 200$ g) FID detector in a sea level laboratory for different electric fields. Left $E = 2$ V/cm, right $E = 50$ V/cm. Figure from [169].

measurement with an FID-type Germanium detector of $m = 200$ g exposed to a ^{241}Am source. The source was shielded by 1 mm lead to achieve a $\gamma - $ rate of 1 Bq and remove α particles. The fiducial electric field is with $E = 2$ V/cm comparable to EDELWEISS but the veto electrodes A and C have been grounded. The right part of the fig. 3.9 shows the measurement with higher electric field of $E = 50$ V/cm which is comparable to the EDELWEISS NTL amplified mode discussed in ch. 2.4. Furthermore, the used readout electronics has a -3 dB cutoff frequency at 4 MHz, whereas the EDELWEISS electronics features a 10 MHz cutoff frequency.

In order to study the potential of a rise time analysis with FID800 type detectors in the EDELWEISS cryostat, the prototype of a 40 MHz time resolved channel readout was installed. This is a mezzanine card shown in fig. 3.10, that is plugged inside a bolometer box. It receives two analog channels from the detector which are the same as the standard 100 kHz channels B and D. A splitting into a 100 kHz and a 40 MHz branch is done between the analog amplification and the anti aliasing filters inside the bolometer box. The data rate of this prototype card is 1.28 GBit/s and exceeds the free bandwidth of 3.2Mbit/s from the fiber optics communication between bolometer box and DAQ crate. Therefore, an event based readout for this type of channel is mandatory.

3.3.1 Hardware upgrade for time resolved ionization channels

For the 40 MHz time resolved ionization channel a mezzanine card (fig. 3.10) has to be placed inside a bolometer box version 2. This additional card is equipped with two independent channels, one FPGA and a memory. From the bolometer box two of the four ionization channels are split and forwarded through a connector to the mezzanine card. In the drawing and the photo, this is in the very left part. From ther, the analog signals, as differential voltage signals, are processed by a differential amplifier with an integrated 10 MHz low pass Chebychef filter [170]. This filter damps with -3 dB at 10 MHz and -25 dB at 20 MHz, the so called Nyquist frequency which is half the sampling frequency. Each channel's filter output is connected with an AC-coupling capacitor to an ADC sampling at 40 MHz and 16 bit resolution. The ADC values are read by an FPGA and written into an 8 MB large memory. The FPGA design was done with the option to use it on a projected card with 4 channels, therefore only 2 MB of memory is used for each channel. This is further divided into 2 memory pages to enable a dead time free readout for up to two
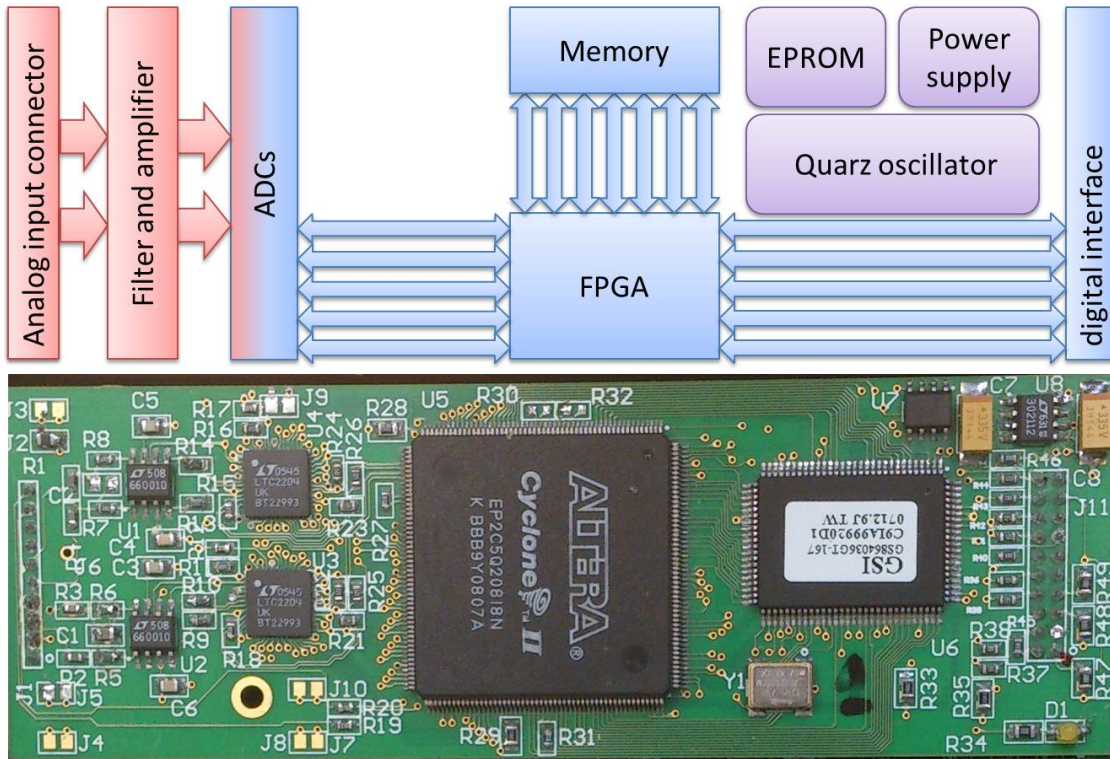
Figure 3.10: Principle and photo of the 40 MHz time resolved ionization channel mezzanine card. The data flow is from left to right, made by a stage of analog filter and amplifier, digitizer, FPGA, memory and a digital interface connector to comunicate with the bolometer box.

consecutive pulses. Each page is designed with a length of 256 kSamples or 512 kB which corresponds to 6.4 ms in time. For technical reasons a trigger command from the DAQ FPGA to the time resolved channel card is always delayed by 3 to 5 ms (see ch. 3.3.3). The remaining 50% of the memory is unused and free for other implementations. In case of an external trigger command, the FPGA receives the time stamp at which the physical pulse is expected to be. From this information a memory address can be derived and 4096 sample points are sent though the digital interface towards the bolometer box FPGA from where the stream is just forwarded to the fiber optics driver. Sending has to be organized without disturbing the continuous data stream from the standard EDELWEISS ionization channels. A bolometer box sends 120 bits per 10 µs out of which only 81 bits are used (5 channels with 16 bit and one status bit). 32 of the remaining 39 bits are then used to send the 40 MHz sampled event without disturbing the EDELWEISS data stream. In total 8192 sample points have to be transfered for one event, 4096 per channel. With a transmission speed of 32 bit/10µs this results in a total transfer time of 41 ms per event. A constant trigger rate of 24 Hz is the theoretical design limit without losing data. However, the event building process on the io-card in which the time resolved channels have to be merged with the 100 kHz channels has cycle time of 64 ms (see section 3.2.3). Therefore, the maximum achievable constant trigger rate is 15.6 Hz. Even with the Barium calibration source activated this rate is not exceeded. However, physical events have no constant rate, therefore, the rate of pile-ups increases with the actual trigger rate.

3.3.2 Modifications on the electronics to incorporate the 40 MHz channel

EDELWEISS has two prototype mezzanine cards for the 40 MHz channel readout. The identical cards where designed at Saclay, but without FPGA software. This software was

designed and developed at KIT, tested here and afterwards at the experimental site. It was decided to reroute the full bolometer box FPGA output stream through the mezzanine card instead of directly send it to the DAQ. On the mezzanine card the FPGA modifies the data stream by injecting the time resolved event data into the unused bits of the bolometer box stream. The modified stream is sent back to the bolometer box FPGA and from there rerouted to the optical transmitter. This could be implemented with almost no changes to the EDELWEISS hardware. The standard acquisition is not affected by the presence of the 40 MHz card. The modified bolometer box has about 2.5 W higher power consumption compared to others, resulting in a higher temperature, but below critical values. The 40 MHz mezzanine card is oversized to fit inside the bolometer box. The FPGA sticks out by 2 mm too high for closing the copper lid. To solve this issue, a new lid was designed in order to close the bolometer box completely without weakening the electromagnetic shielding.

3.3.3 Trigger and event building

Two completely different trigger algorithms are used in the EDELWEISS experiment. One is optimized for heat channels and heat pulse shapes. The other algorithm has it focused on ionization channels. The heat trigger algorithm is identical to the one described in ch. 3.2. EDELWEISS has a good working heat trigger system given by SAMBA. Since the dominant part of the total event energy divides into the heat channel, whereas the fraction in the ionization channels is smaller, the EDELWEISS readout uses a heat trigger. It was considered to replace the software trigger in SAMBA by a hardware trigger on the FPGA level. But this is complicated because each channel uses an individual and optimized template pulse. Furthermore, it is technically possible to stream all channels continuously to the acquisition computers. Since the new DAQ system was not planned to replace SAMBA as the main trigger system, the development of a heat trigger was abandoned and focus was put on the ionization trigger. The latter is essential for the 40 MHz time resolved channels, that can not be streamed continuously due to the high data rate.
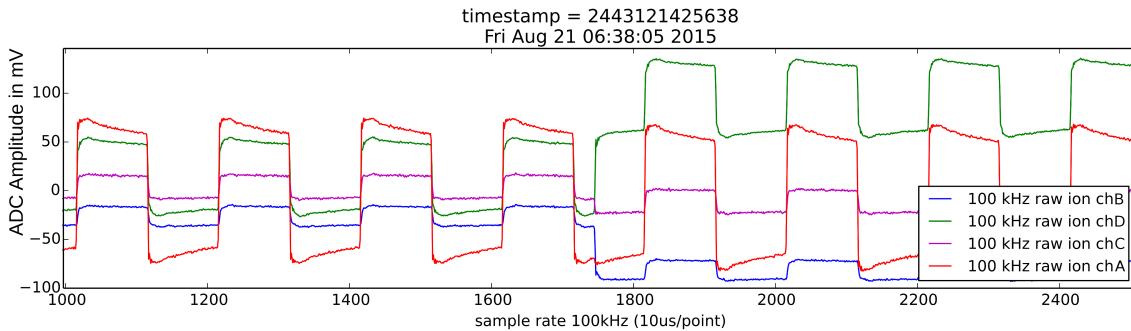

Figure 3.11: Raw ionization data with a ~ 400 keV pulse as seen on the 100 kHz readout ADCs. The time axis is centered to the pulse region at $t \approx 1748 \cdot 10$ μs. The trigger correctly detected the pulse and ignores the surrounding heat crosstalk pattern.

The crate-internal FPGA based trigger is designed to enable an event based readout and to provide a *fast* and *precise* time stamp to initialize the readout process of the 40 MHz ionization channels. In this sense *fast* means the ability to send a trigger command to the bolometer box within a maximal time delay of 4 ms between command and physical pulse. If the pulse is detected later and the command sent later, the data of interest in the ring buffer memory is already overwritten and lost. *Precise* means to identify the time stamp of the pulse with a precision better than ± 20 μs. Otherwise, the 40 MHz sampled pulse is not inside the 4096 samples wide readout window, or too far shifted from the center

of this window, which would make it unusable for later analysis. Such a trigger can only be implemented on the ionization channel because the time constants of the heat channel (10 ms rise time, 500 Hz demodulated sample rate) are too high.
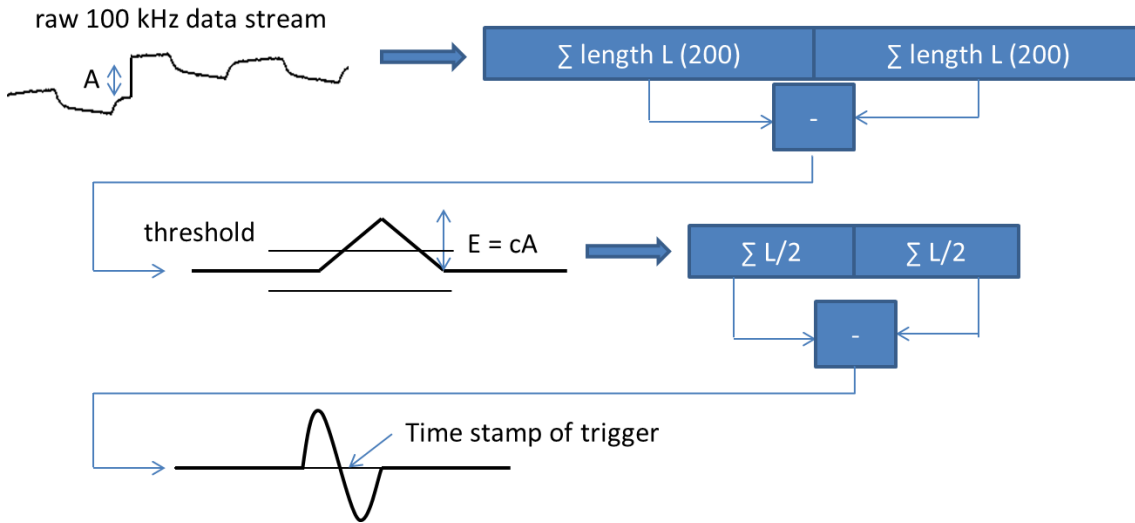

Figure 3.12: Principle of the ionization trigger as a cascaded trapezoidal filter.

The ionization trigger is designed with the main focus on the 40 MHz ionization channel readout. Unfortunately the heat channel modulation frequency shows up as a crosstalk effect on all ionization channels (see fig. 3.11). An edge of the rectangular modulation is not distinguishable from a physical pulse in the ionization channel. To prevent the trigger algorithm from triggering on the crosstalk heat pattern, a so called cascaded trapezoidal filter as visualized in fig. 3.12 is used. Each continuous incoming data point is pushed through two memory arrays that are following the FIFO principle. Both have a length of 200 data points, which corresponds exactly to the period of the heat modulation. It is also possible to change the length. An optional gap of variable length can be configured between both FIFOs. In this case a sample point leaving the first FIFO will not appear immediately in the second, but delayed by the length of the gap. However, in the case of diffuse edges or a jitter effect on the crosstalk pattern the gap can improve the performance. The crosstalk pattern in the case of EDELWEISS is uniform and has no jitter. The FPGA constantly calculates the sum of all 200 data points in one FIFO. This is done by adding the incoming ADC value and subtracting the outgoing value with 100 kHz. The sum of the complete FIFO is calculated with only two operations. The difference of both sums is used in the next stage of the filter.

Fig. 3.12 shows the filter's response to a Heaviside function combined with the crosstalk and a gap of the length 0. The step response output of the first filter stage is a triangular pulse. With a gap longer than 0 it would be a trapezoidal pulse, giving the filter its name. The amplitude of the triangle is proportional to the amplitude of the initial pulse. The proportional constant is the shaping length of the filter, which is 200 in EDELWEISS. The crosstalk pattern is completely removed by the first filter stage. This is possible because the crosstalk is a self made artificial signal from the bolometer box which has a very precise and constant phase and frequency. Because both sums are calculated continuously for each new data point, the output signal has the same sample rate as the input, 100 kHz. A second stage of the filter with half the length of each FIFO will further transform the triangular signal to a composition of two parabolas. The FPGA detects the zero crossing which corresponds to the time stamp of the initial pulse + 300 stamps that come from the filter's shaping length.

The trigger condition is a boolean AND operation of a zero crossing in the second stage with a threshold exceeding of the first stage. This threshold exceeding condition can be configured for positive pulses above a positive threshold (as in fig. 3.12), negative pulses below a negative threshold, or both cases simultaneously. In EDELWEISS only one polarity per channel is of interest, i.e. negative pulses for the collection of electrons and positive pulses for the collection of holes.

After a valid trigger the event building process starts. First of all the information about a valid trigger is sent to the master card. Simultaneously a timer is started to wait for a configured post trigger time. With a fixed event length of 4096 sample points per channel and consideration of the filter's shaping time, the post trigger time has to be $2048 - 300 = 1748$ time stamps to get the pulse in the center of the event record. After this post trigger time the master card sends a *page change* command to all input cards. Every channel's write pointer is now writing new data in the next memory page, while the previous memory page contains the event. If the 40 MHz ionization channel is activated, it receives the trigger command with the first 1 kHz strobe after the event trigger. At the latest delayed by 1 ms, the fast channel pulses are sent to the io-card and recorded together with the 100 kHz channels. The transfer of the fast channel event from the bolometer box to the DAQ crate takes 40 ms. Once all data is bundled it is sent to the master card. An event header that contains so called meta information of the event, such as estimated amplitude, time stamp, identifier of the channel on which the trigger appeared and an event serial number. The further readout is performed through the ORCA back end server which is running on the external PC (section 3.1.4), from there the event is sent via network to the Mac Mini running ORCA. The event is stored on the hard disk in an ORCA run file that can be converted into a ROOT file. The subsequent processing is described in section 4.2.

It is necessary to configure the threshold values for the trigger algorithm, depending on the actual noise situation. Within this thesis, an ORCA script was developed to regulate the threshold for each time resolved channel. EDELWEISS data taking is always started and stopped by SAMBA. When the run is started by the operator, SAMBA automatically sends a command to ORCA to initialize the event readout as well. ORCA activates the trigger units inside the hardware with the latest threshold in use. Since the baseline noise situation may have changed, the script is executed and tries to lower the threshold until the trigger rate exceeds 10 Hz. This indicates that the noise level is reached. The script will then increase the threshold until the trigger rate drops below 5 Hz. Once this is the case, an additional value is added to the threshold to achieve a stable condition for the next hour of run. The same procedure is applied on the second channel immediately after the first channel is configured. It takes about 20 seconds to finish the script and continue with data taking. After about one hour of data taking SAMBA initializes a maintenance phase to reset the electrode voltages and discharge the capacitors of the analog readout part. Before this phase is started, a stop command is sent to ORCA and the event readout is stopped. The file with all recorded events inside is closed and written to the hard disk. This leads to individual files that contain typically one hour of data taking and a new and different configured trigger threshold for each hour. The trigger threshold configured in this way is not optimal for highest sensitivity and recording of events with very low energy. Instead, it provides a stable run condition for the 40 MHz channel readout which was important for the first proof-of-principle study and therefore had higher priority for this work.

4. Data processing and analysis of the time resolved ionization signal

One of the goals of the EDELWEISS run 309 (June - December 2015) is to evaluate the potential of a rise time analysis in the ionization channels to discriminate surface and fiducial events. Since a continuous stream of the 40 MHz channels is impossible with the existing hardware, an event based readout is essential. Therefore, an FPGA based trigger was introduced described in section 3.3.3. The efficiency of this new trigger algorithm is compared to the conventional EDELWEISS readout SAMBA and the main analysis framework ANA (ch. 2.3.2) in section 4.1. Within this thesis it is for the first time that a highly sampled ionization channel is recorded and analyzed. So far, the experiment never used sampling frequencies higher than 100 kHz. As a consequence the readout electronics was not optimized for low noise in the targeted bandwidth of 1 to 10 MHz. Therefore, a raw data processing chain with several filter stages was necessary and is introduced in section 4.2. The 40 MHz channels have to be calibrated. This is done with the 356 keV photo peak of a ^{133}Ba calibration source and described in section 4.3.1 together with a comparison of the time resolved channel calibration with the conventional EDELWEISS calibration. Further statistical analysis, focusing on the rise time and delay between electrons and holes, is then performed with the calibrated data. To cross-check the results, a dataset of simulated pulse traces with real noise added is processed and compared with the run 309 data. Furthermore, in section 4.4, a dataset of simulated data with *optimized* noise, i.e. real noise reduced by a factor 10, is compared to estimate the benefits of an improved 40 MHz hardware.

4.1 Trigger efficiency on ionization signals

The efficiency of a trigger system is the ratio of detected events to physically existing events. For different reasons a trigger can miss physical events. Most obvious reasons are event amplitudes smaller than the sensitivity of the trigger algorithm. One expects the trigger mechanism less efficient for smaller pulse amplitudes. Another impact is caused by pile-ups and the way they are handled. The overall trigger efficiency can be measured in a dedicated test setup with a well known source, such as a pulse generator that mimics the detector signals together with noise. In the case of EDELWEISS, this is difficult because too many unpredictable parameters slowly vary during a run and the detectors are very heterogeneous in their properties. Nevertheless, it is possible with the new DAQ to compare two readout branches of the same detector. The trigger efficiency of the FPGA based event

mode can be compared to the conventional EDELWEISS event building by SAMBA in the acquisition computers and the following post-processing from ANA analysis.

To evaluate the FPGA based trigger algorithm, which is used for the time resolved channel, it is directly compared with the available events in ANA. The ANA events are the reference. A direct comparison has to be interpreted carefully because ANA events are triggered by SAMBA software on the heat channels, while the FPGA based trigger is applied on ionization channels. Events that have no ionization energy (heat only events) will be visible in the ANA branch, but not in the FPGA triggered files. Therefore the following logic for evaluating the trigger efficiency is used:

1. loop over all reference events in ANA

2. check if ionization energy of ANA event is above 2 keV

3. search for a coincidence in files with events triggered by the crate FPGA

4. identify the coincidence by time stamp with a window of acceptance

5. plot an amplitude-dependent ratio of identified coincidences over all selected ANA events
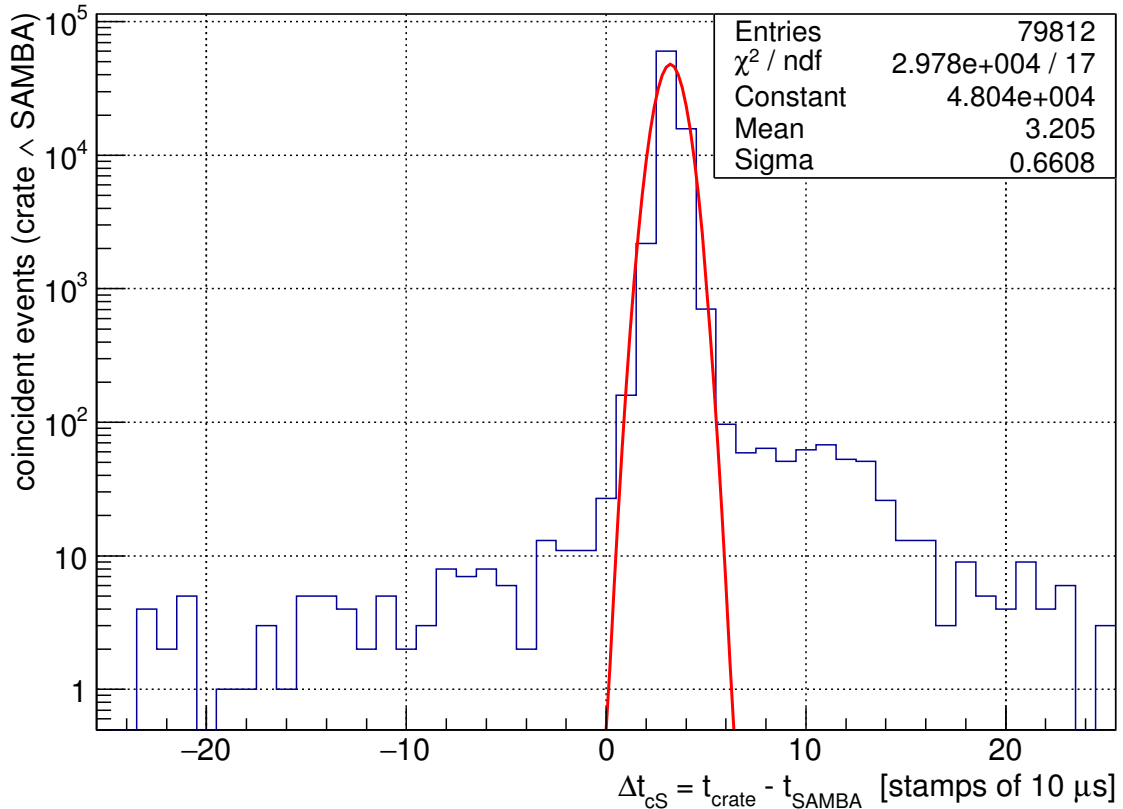
Figure 4.1: Time difference for event time stamps of both systems. The FPGA based event readout registers events delayed on average by 3.2 stamps. Crate time stamps are integers detected as in fig. 3.12, SAMBA time stamps are recomputed during the offline analysis ANA as float numbers with resolution better than 10 µs (ch. 3.2.1).

A coincidence of both systems is detected by a matching event time stamp within a margin of ±2000 stamps. With a recorded length of 4096 samples per event and centered pulses, this large evaluation window guarantees that the coincident pulse is visible in both systems. Fig. 4.1 shows the difference of time stamps from the FPGA based event readout system
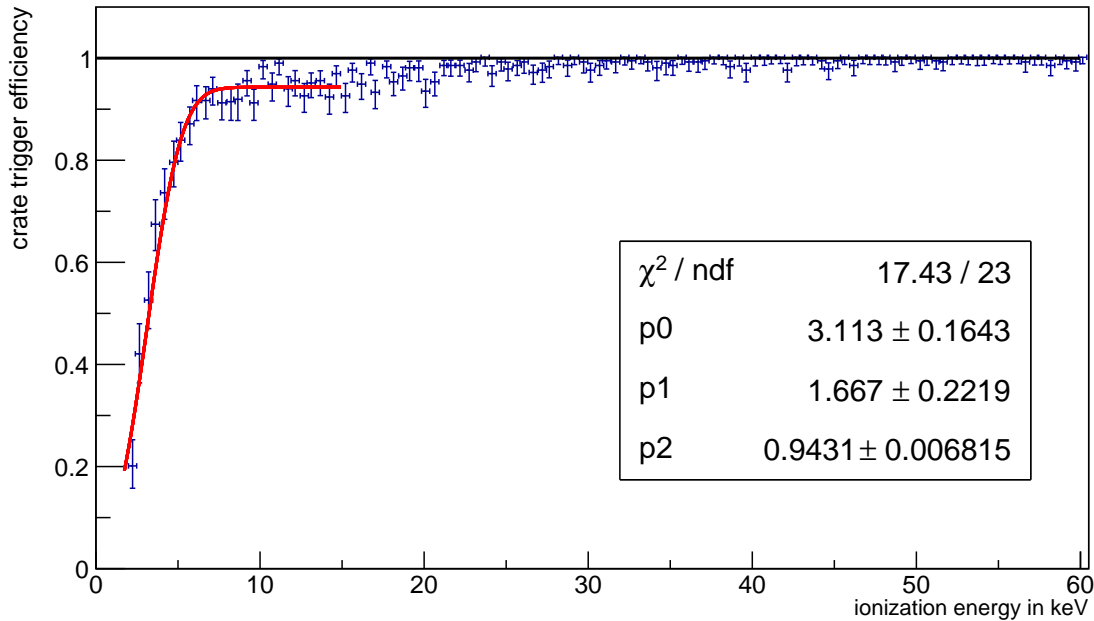
Figure 4.2: Efficiency of the FPGA based ionization trigger with respect to the main EDELWEISS analysis as a function of ionization energy extracted with ANA. See eq. 4.1 for fit parameters.

t_{crate} and the EDELWEISS standard readout t_{SAMBA}. The major part of coincidences appears within a very small time window of ± 30 µs around $\Delta t_{\mathrm{cS}} = t_{\mathrm{crate}} - t_{\mathrm{SAMBA}} = +30$ µs. This delay does not play a role for the following analysis. The event based readout seems to be systematically delayed by 3 time steps or 30 µs. A systematic effect ot the event trigger algorithm could be the reason for this observation. The trigger algorithm (see fig. 3.12) has a shaping length of 300 time steps until a pulse can be seen as a zero crossing in the second stage. These systematic effect is corrected in the presented analysis. However, to detect the zero crossing the FPGA waits for the sign change, which happens with the next sample point, thus adding one more step, which is not corrected. The two remaining time steps are unknown. A comparable but more detailed coincidence analysis was performed in [76] and found for the same period of data taking a systematic delay of $\Delta t_{\mu S} = t_{\mu - \mathrm{veto}} - t_{\mathrm{SAMBA}} = -64 \pm 12$ µs between the EDELWEISS detectors and the muon veto system, which receives the same global time stamp from the DAQ crate. Thus, on a time line, a coincidence of all three systems would appear first in the muon veto system, then ~ 64 µs delayed in the ANA analysis and additionally delayed by ~ 30 µs in the event based readout. It is not clear which of the systems causes the offsets, most likely each system brings its individual offset. However, the systematic delays have no impact on the following analysis and are therefore not further investigated.

4.1.1 Energy dependent trigger efficiency of the FPGA based system

To measure the trigger efficiency according to the 5 step-procedure mentioned above, several additional selections had to be applied. Normally the FPGA based readout system receives a start command once SAMBA has prepared the detector in the run configuration and a stop command before the detector enters the next regeneration phase. However, this did not work properly during the first weeks of run 309 resulting in phases where the detector was in regeneration mode but the FPGA trigger was active. The worst case scenario would be that the crate trigger receives the start command before the end of the regeneration is reached. After the start command, the threshold for the trigger algorithm is derived as

described in ch. 3.3.3, and, as it is set during the detector maintenance phase, it would be higher because of the higher noise level due to the closed relays and the frequent FET reset pulses which are repeated with a frequency of 1 Hz during the maintenance phase. Each reset pulse causes several triggers, giving a high trigger rate, which the starting script tries to correct by increasing the threshold. This higher threshold makes the system less sensitive to low energy events. The described failure has no negative impact for the later presented (section 4.2) 40 MHz time resolved channel data taking and analysis, since analysis of these pulses is not reliable below ~ 100 keV and not possible below ~ 50 keV ionization energy (see section 4.3). However, for the discussion of the trigger efficiency, the effect has a negative impact: the obtained threshold is shifted to higher energies. As seen in fig. 4.2, the crate trigger efficiency above 50 keV is better than 95% and can be rather well described with the error function of the form

$$f_{\text{threshold}} = p_2 \cdot 0.5 \cdot \left(1 + \text{erf}\left(\frac{x - p_0}{\sqrt{2} \cdot p_1}\right)\right) \qquad (4.1)$$

with the 50% value $p_0 = 3.1$ keV, the detectable minimum $p_1 = 1.7$ keV and the maximum plateau $p_2 = 94.3\%$. Since the reinitialization of the threshold after each maintenance leads to a superposition of several efficiency curves, one per hour, a more correct analysis of the trigger efficiency would be based on an analysis for each 1 h data set individually. However, with an event rate below 1 Hz, the statistics of such a limited period is not sufficient to successfully apply any fit. Therefore, fig. 4.2 contains all available Barium data of run 309. Phases in which the FPGA readout was not activated at all are detected and excluded from the analysis. Additionally the first three minutes and the last minute each data taking period are excluded because in the first phase, the FPGA based trigger is initializing the threshold, and in the end of each hour it could be stopped earlier or later than the reference system. This is not a problem for the 40 MHz analysis, but it can cause effects that should not appear in the efficiency analysis. To avoid impact from the heat only events, all events with an ionization energy < 2 keV in ANA are ignored. With this cut it is clear that a trigger efficiency below 2 keV cannot be derived. which is compatible with the fit results in fig. 4.2, where $p_1 = 1.7 \pm 0.2$ keV correctly represents the threshold.

4.1.2 Reverse efficiency analysis of the SAMBA - ANA analysis branch

With the 40 MHz time resolved readout and analysis chain there is, for the first time in EDELWEISS, a completely independent readout system with a different technology and approach than SAMBA. This enables to reverse the efficiency analysis considering the FPGA based readout being the reference. Fig. 4.3 shows the result for all run 309 Barium data. The source for this plot are the processed events of the 40 MHz channels. Their abundance is not equal to the triggered events, since only about 5% of all triggered events pass the processing chain. Beginning at the end of this processing chain, the events are cross-checked for a corresponding coincidence in the ANA data. The ratio of both energy dependent histograms is given as the efficiency plot in fig. 4.3 for Barium runs and WIMP search data. The efficiency of ANA is compared to events analyzed in the 40 MHz channel and not to the FPGA based trigger directly. The ionization energy on the x-axis (FIC event energy) is based on the 40 MHz channel analysis which suffers of a 50 keV baseline noise level. Hence the efficiency curve below 50 keV is not reliable: It can not be excluded that the FPGA triggers on noise fluctuations, generating a huge number of events for which the processing chain fits amplitudes within the noise level. The result would be a large number of pure noise events with arbitrary amplitudes of up to 50 keV. These events are not inside the ANA dataset if we expect the SAMBA trigger to work reliable even below 5 keV. This makes the SAMBA - ANA analysis appear inefficient but this is not the correct interpretation. The situation for events above ~ 50 keV is different. In this energy range
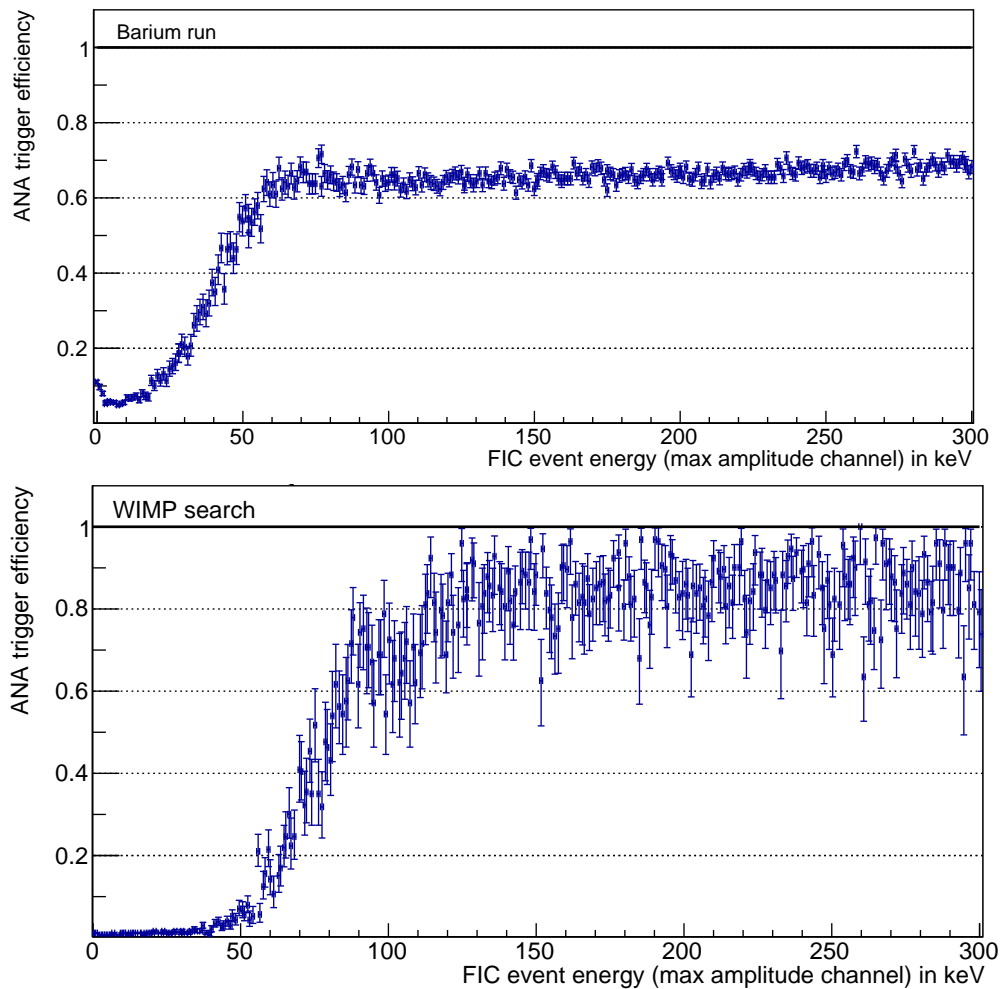
Figure 4.3: Reversed efficiency analysis for Barium (top plot) and WIMP search data (bottom). SAMBA-ANA is compared to the 40 MHz channel as the reference. The low ANA efficiency of $< 75\%$ for high energies is a dead time driven effect. The energy scale taken from the 40 MHz channel (**F**ast **I**onization **C**hannel, FIC) with a noise level of ~ 50 keV, making the region below 100 keV unreliable. Details in section 4.1.2.

the FPGA based trigger algorithm as well as the 40 MHz channel have proven to work reliable. The efficiency of the SAMBA - ANA readout and analysis in this energy scale is below 75% in a Barium run. The main reason for the surprisingly lower efficiency of the common EDELWEISS acquisition system is additional dead time. If SAMBA triggers an event it is based on the heat channel as described in ch. 3.2.1. With a heat channel readout window length of 1024 sample points or roughly 2048 ms and a centered pulse, the next window for the next off-centered pulse is available only 1 s later. During this period the trigger is in a muted state and not detecting pulses. The physical pulse rate during a Barium run in EDELWEISS is depending on the relative position of the bolometer and the Barium source. For FID837 in run 309 it is about 0.2 Hz. With these numbers, the fraction of missed pulses by the SAMBA trigger, caused by systematic dead time, can be estimated to

$$1024 \text{ ms} \cdot 200 \text{ mHz} = 20.48\% \tag{4.2}$$

of all physical pulses, or a readout efficiency of 79.5%. The same dead time induced effect accounts in principle for the FPGA based trigger, too. But different values enter here: The trigger algorithm is applied on the ionization channel, which has a sample rate of

100 kHz. The readout window has a length of 4096 sample points or 40.96 ms. Unlike the SAMBA trigger, the FPGA based trigger does not remain inactive for the full window length. As described in section 3.2.3, after 20.48 ms a new event readout will be initialized. The physical event rate is the same, the fraction of systematically missed events is only:

$$20.48 \text{ ms} \cdot 200 \text{ mHz} = 0.41\% \tag{4.3}$$

Obviously, the dead time effect for the event based readout is negligible. Furthermore, by definition, it cannot be seen in fig. 4.3 because the FPGA triggered events are the reference. Instead, it would show up in fig. 4.2 but is too small compared to the uncertainties.

The lower plot in fig. 4.3 shows the same analysis for the WIMP search runs during the run 309 campaign. The difference in the SAMBA trigger configuration between WIMP search and Barium run is the threshold management. During WIMP search, the trigger is configured with a dynamic threshold to a relative constant trigger rate of ~ 20 mHz. Eq. 4.2 has to be recalculated with the lower rate which gives an expected efficiency of 98%. This can be seen in the plot by a higher efficiency around 90%. The larger error bars result from the lower statistics during WIMP search runs.

The efficiency in fig. 4.3 is approximately 10% lower than expected. Several effects are difficult to estimate. Additional dead time from the acquisition computer that operates SAMBA could be one reason. It may also happen that SAMBA stops writing an event to hard disk due to high CPU load. Furthermore, the discrepancy can be explained by a large uncertainty of the trigger rate which is not constant during different Barium runs that have been integrated in fig. 4.3. The operator can select a high threshold for instance to select 356 keV Barium pulses to optimize the parameters for the convolution template. In general, changes on the trigger threshold of SAMBA are not noticed by the FPGA based readout. For a quantitative analysis of the efficiency of both systems a dedicated run is needed, in which trigger related parameters are fixed. For the analysis in this thesis, it is necessary to proof the efficiency of the FPGA based trigger compared to the standard analysis trigger, which is done in fig. 4.2 with a result of $\sim 100\%$ efficiency above 50 keV. Thus, we can expect that the 40 MHz event based readout detects all events in its region of interest which is above 100 keV ionization energy.

4.2 Processing chain of time resolved ionization signals

The described trigger has been tested and fine tuned since the EDELWEISS run 305. In run 309 it was continuously operating and the 40 MHz channels were read out from 25th of June 2015 until 7th of Dec 2015 generating in total 412 GB of data. The data files are recorded on the Mac Mini which runs ORCA. From there they have to be transferred to KIT for further processing and analysis. This is split into several stages: In a preparation phase the ORCA files are converted to the ROOT format. Systematic artifacts from corrupted files are removed which may occurs if the run is stopped shortly after starting, before the first trigger is recorded. Then follows the processing chain in which further artifacts, such as triggers on bolometer box reset pulses, are removed and finally a pulse processing phase in which the parameters of each event are computed and stored as meta data in a file. This meta data files are the basis for the analysis described in section 4.3.

4.2.1 Preparation of the recorded data

The ORCA software running on a Mac Mini is used for the event mode readout. Once the experiment is configured for data taking, SAMBA sends a network command which informs ORCA about the readiness. Thereupon, ORCA activates the FPGA based trigger, the event readout and it creates a new file in which detected events with the 40 MHz sampled data are stored. These files are organized according to the structure

```
YYYY/MM/Data/YYYY-MM-DD_R309_RunNNNN
```

where YYYY stands for the year. In the case of run 309 always 2015. MM stands for the month, DD for the day and NNNN is a per file incremented number. Typically the size of such a file is between 50 MB and 200 MB, depending on the trigger rate, the number of activated channels in the event readout and the runtime during which the file is filled with data. This time is controlled by SAMBA. If a maintenance phase is started, SAMBA sends a stop command to ORCA. Normally, EDELWEISS has an automatic maintenance after 3600 s measuring time, but this can be changed by the operator. After the maintenance, the data recording is continued in a new file and NNNN is incremented by one.

The recorded files are moved to the local computing cluster at KIT-IKP by using rsync via a secured ssh connection. A c++ program named *orcaroot* is used to convert the ORCA files into the ROOT format. They contain a ROOT typical TTree with the branches (variables) from the trigger algorithm output and the pulse records of each event and channel. The tree is organized like a table where the columns correspond to the branches. Each row in the table contains one channel and a block of rows form one event. In the current EDELWEISS version of the DAQ the relevant branches are:

- *runNumber*: same as in NNNN in the file name

- *wfLength*: waveform length - the number of sample points per channel and event

- *timeStamp*: 48 bit time stamp for the real time at which the trigger decision was taken

- *crate*: only one DAQ crate is used by EDELWEISS, this value is always =0

- *card*: address of the io-card on which the event was recorded

- *fiber*: from which fiber cable the event was recorded (detector)

- *channel*: to which channel the pulse trace belongs, each io-card processes up to 36 channels at 100 kHz plus 24 channels at 40 MHz

- *energy_ad*: corresponds to the trigger energy E in fig. 3.12

- *waveform*: array containing the sample points of this event

Since this analysis has only one target detector in focus, the FID837, which has never been changed in position or cabling configuration during run 309, the tree branches *crate*, *card* and *fiber* always contain the same values. The processing code is flexible in a way that *wfLength* can have any value, but it is always 4096 in the present data set. Having the waveform length as a power of two is important for an efficient run time especially for functions using the fast Fourier transformation. *Energy_ad* is the amplitude of the pulse after the first stage of the cascaded trapezoidal filter, which is E in fig. 3.12. For this analysis, this value was checked but not further used. Instead, either the main EDELWEISS analysis ANA event energy is taken, or the energy from the 40 MHz channels directly. The variable *channel* indicates whether the pulse trace belongs to the B or D electrode of the detector. The branch *waveform* contains the raw data as read from the analog digital converter. It is stored as an array of the length *wfLength*. With two 40 MHz channels per event this adds up to $2 \cdot 4096 \cdot 16$ bit $= 16.385$ kB and constitutes the major volume of the 412 GB data. Performing statistical analyses on this raw data yields a too large computing time. Therefore the processing chain is applied to reduce the data to a necessary amount that is needed to describe the event, such as time stamp, amplitudes, baseline noise level and, most important for this thesis, the rise time. The results are stored in files that are much smaller than the input data. In fact, the output files add up to only 350 MB. The same principle is performed in the conventional EDELWEISS analysis ANA. There the

output files are called flat files. For each processed event, the processing chain developed within this thesis searches for a coincidence in the ANA flat files. If a coincidence is found, a copy of the relevant ANA variables is stored in the output files as well, to have everything needed for the analysis merged into one file.

4.2.2 Processing the recorded data

The processing chain is written in the Phython programming language and is extensively using the NumPy package [171] for fast and efficient computing on large array structures. Furthermore, the SciPy library [172] is used for filtering and applying FFT based functions. Plotting of pulse traces is achieved with Matplotlib [173], a Python package for data visualization. The *orcaroot* converted files are opened and the time stamp of the first and last event in the file is compared. The file is skipped and not used for analysis, if the runtime of this recorded file is shorter than 300 s. Sometimes the operator who starts the run realizes an error or a bad configuration and stops the run again. Automatically started runs and proper data runs should last longer than 5 minutes.

Next, the event in the middle of the file is selected and its time stamp is searched in all ANA flat files within a margin of (± 200 s). The name of the ANA file in which a similar time stamp is discovered gives the information about the type of the run which is a priori unknown to the event readout branch. This type can either be Barium, Thorium, WIMP search or test. If the time stamp look-up fails, a next time stamp, exactly centered between the last tested stamp and the end of the file is tried. If after 5 tested time stamps still no run type is detected, the value "unknown" is assigned to the events of this file. This can happen in the case that SAMBA was not reading data from FID837 while ORCA did. The detected run type is assigned as a string type variable to each event in the output file. This function has to be executed once for each input file, because the type can be changed between two runs, but never during a run or inside one input file.

Then, the pulse processing chain starts at the first event of the opened file, processes it until the event is completely processed or an escape condition rises. In both cases the processing chain continues with the next event, until the end of the file is reached. The procedures described in the following are applied for each event in the file: Before any analysis of the actual pulse trace is started the event is checked for systematic artifacts that have to be excluded from the analysis. This is done with time stamp related variables: EDELWEISS ionization channels periodically need reset pulses to hold the baseline centered in the ADC range. Every reset pulse leads to multiple valid triggers and events that are unphysical and have to be removed. They are detected computing the modulo of the event time stamp t_{event} and the known delay between two reset pulses $t_{\mathrm{delay}} = 6.4 \cdot 10^6 \cdot 10$ μs, which is 64 s in run 309. For each event time stamp t_{event},

$$t_{\mathrm{exclude}} = t_{\mathrm{event}} \mod t_{\mathrm{delay}} \tag{4.4}$$

is computed and if $t_{\mathrm{exclude}} = (10 \pm 5) \cdot 10^5$ μs the event is rejected as an artificial reset pulse. The excluded time interval has a length of 1 s and appears every 64 seconds, adding 1.56% of systematic dead time to the experiment. The EDELWEISS analysis package ANA uses a slightly different exclusion window, which has been taken into account for the comparison between both analysis results in ch. 4.1.2. After skipping the reset pulses from the input data, the same principle has to be applied for events that are close to the bipolar transition of the heat modulation. This has only an effect on the 40 MHz channel analysis because the heat modulation crosstalk can be completely removed in the 100 kHz channels. In an event sampled at 40 MHz the physical pulse can not be distinguished from the modulation transition. Furthermore, the noise level in the fast channel is much higher close to the transition. Rejection of the affected events is achieved with eq. 4.4 as well, but
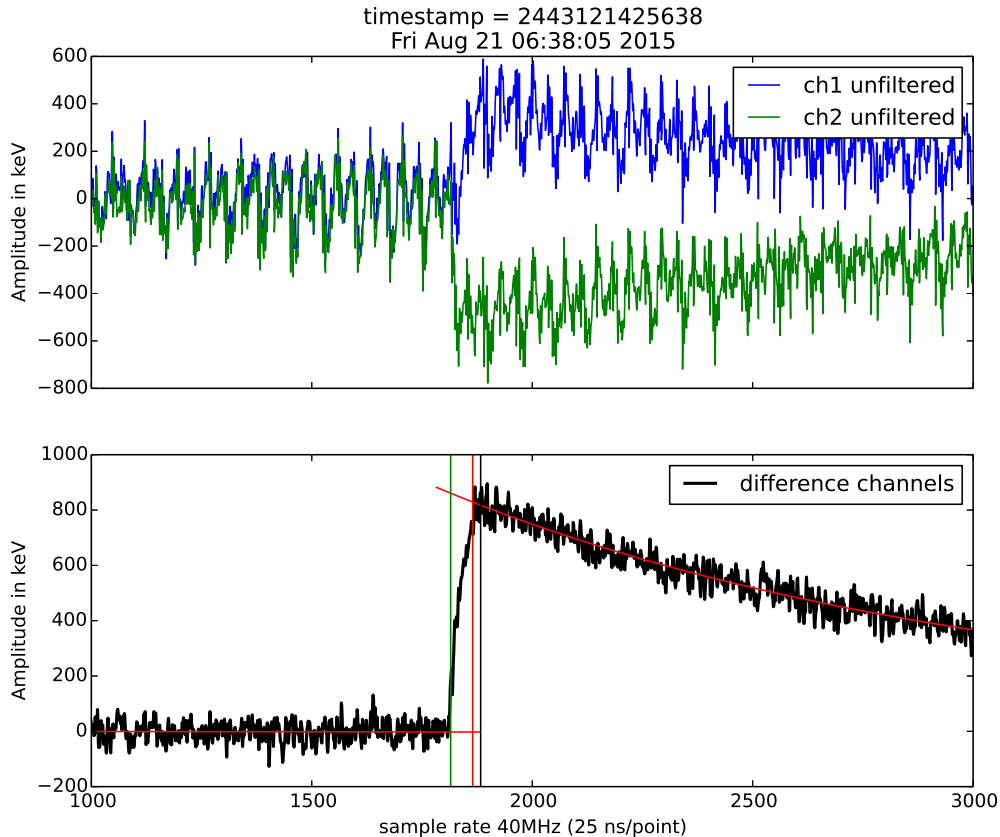
Figure 4.4: The two raw unfiltered 40 MHz channels of an event in the top plot. Their difference in the lower plot shows an improved signal to noise ratio. This virtual channel is used to find the end of pulse position in the event record (black marker line) at which the amplitude between the two fitted curves is measured. The rise time is taken from 10% to 90% amplitude and marked as t_{10} in green and t_{90} in red. (zoomed version in fig. 4.5).

with $t_{\mathrm{delay}} = 100 \cdot 10$ µs and excluding the interval $t_{\mathrm{exclude}} = [3, 13] \cdot 10$ µs. It adds 11% of systematic dead time for the 40 MHz channels. To avoid this, one could think of deactivating the modulated heat readout for future runs, or reducing the modulation frequency. However, such a modification would require changes on all levels of the experiment. The capacitors for the NTD biasing in the cold electronic have to be removed, the bolometer box FPGA design has to be modified, the SAMBA software readout and the offline pulse processing would need to be adopted.

It became apparent that for some consecutive pulses or high trigger rates the 40 MHz channel readout is disturbed and several data points are replaced with a constant value. These events have to be identified and skipped. The detection is performed by searching for the ADC value "-6554", which is a normal and valid ADC value, but the event is skipped if it appears in more than 5 successive sample points in the pulse record. Searching for a series of a number is very inefficient because the algorithm has to scan through the complete array. It turned out that this sort of error appears only if the previously triggered event is closer than 350 ms or the following event is closer than 130 ms which corresponds to a temporary trigger rate of 2 Hz or higher. To save computing time only in these two cases the pulse record is scanned for the error.

Having removed reset pulses and systematic artifacts, the next stage is to process the pulse

traces. Both 40 MHz records are copied into two NumPy arrays. The data format is 16 bit unsigned integer. A flat baseline with the permanent value 0 would show up with an offset of 32767 in this data type. It is more natural to have the pulse trace around 0 and allow negative values. A type cast to signed integers of 16 bit and in a next step to 64 bit float is executed. The two 40 MHz channel pulse records have a cyclic shift that originates from the FPGA implementation. That means that the first sample point is not stored in the first address of the array. In a future firmware revision this could be corrected, but for the moment it has to be corrected in this processing chain. The first sample point is manipulated by the FPGA to have the value -32768 and it can be on any of the first 120 addresses in the array. It is identified and the array is rolled back. Afterwards the first sample which is now in the first position is overwritten with the value of the second sample point. This is done because a single sample point at the maximum possible amplitude would look like a $\delta-$pulse for the filter functions. It would excite oscillations of the filters. Alternatively one could remove this sample point which would trim the array to a length of $4096 - 1$ entries. This would be very inefficient for the computing time of all FFT based functions.

Next, the two arrays with the pulse traces are multiplied with a constant calibration factor from a preliminary calibration. That changes the unit of the event amplitude from ADC counts to keV. This is a first calibration stage. It is possible to re-calibrate the output in a second stage during the statistical analysis if necessary.

Before the two individual channels are further processed a third, virtual 40 MHz channel is created and analyzed. This is done by constructing a new array that contains the difference of the two recorded channels (see fig. 4.4). The motivation of this is that the dominating part of the noise couples in from the power supply and therefore appears symmetrical and in phase on both channels, whereas the pulse amplitudes the two channels are always bipolar. In the virtual channel the noise is suppressed and the pulse amplitude is increased by the subtraction. Since the above described noise of both channels is correlated we call the third channel "decorrelated channel" or pseudo decorrelated channel because it is not a decorrelation in a mathematical meaning. A 15 MHz 4th order low pass Butterworth filter is applied to this virtual channel to reduce high frequency noise. The filter is implemented as a forward-backward algorithm which has the advantage of zero phase shift. The SciPy package brings a function *filtfilt* that provides this. The index of the maximum amplitude marks the end of the pulse and is named t_{end}. For the next analysis steps it is important that the pulse position is reasonably centered, giving a sufficient long baseline and enough after pulse trace for analysis. If $t_{\text{end}} < 1200$ or $t_{\text{end}} > 3800$ the event is skipped. The window of acceptance has a width of 2600 sample points at 40 MHz or 65 µs. This corresponds to 6 sample points in the 100 kHz channel. The trigger precision has to be as good as ± 30 µs or better to readout an analyzable event. Events with the pulse position outside of this acceptance window are skipped. The region from the beginning of the recorded event trace to $t_{\text{end}} - 400$ sample points is defined as the baseline. -400 sample points corresponds to 10 µs which has been selected to ensure that the baseline does not contain the beginning of the pulse. The safety buffer is large enough, given that typical pulse rise times are < 3 µs. The standard deviation of the baseline in the pseudo decorrelated channel is used to estimate the significance of the detected pulse. In case the amplitude at t_{end} is smaller than twice the standard noise deviation, the event is skipped. If the baseline standard deviation exceeds 50 keV, the event is skipped as well. The last condition removes bolometer box reset pulses that are outside the 64 s scheme. A 1st order polynomial function

$$f_{\text{lin}}(t) = mt + q \tag{4.5}$$

is fitted to the baseline of the pseudo decorrelated channel. The fit procedure is utilizing the SciPy optimize curve fit package that relies on non-linear least squares minimization
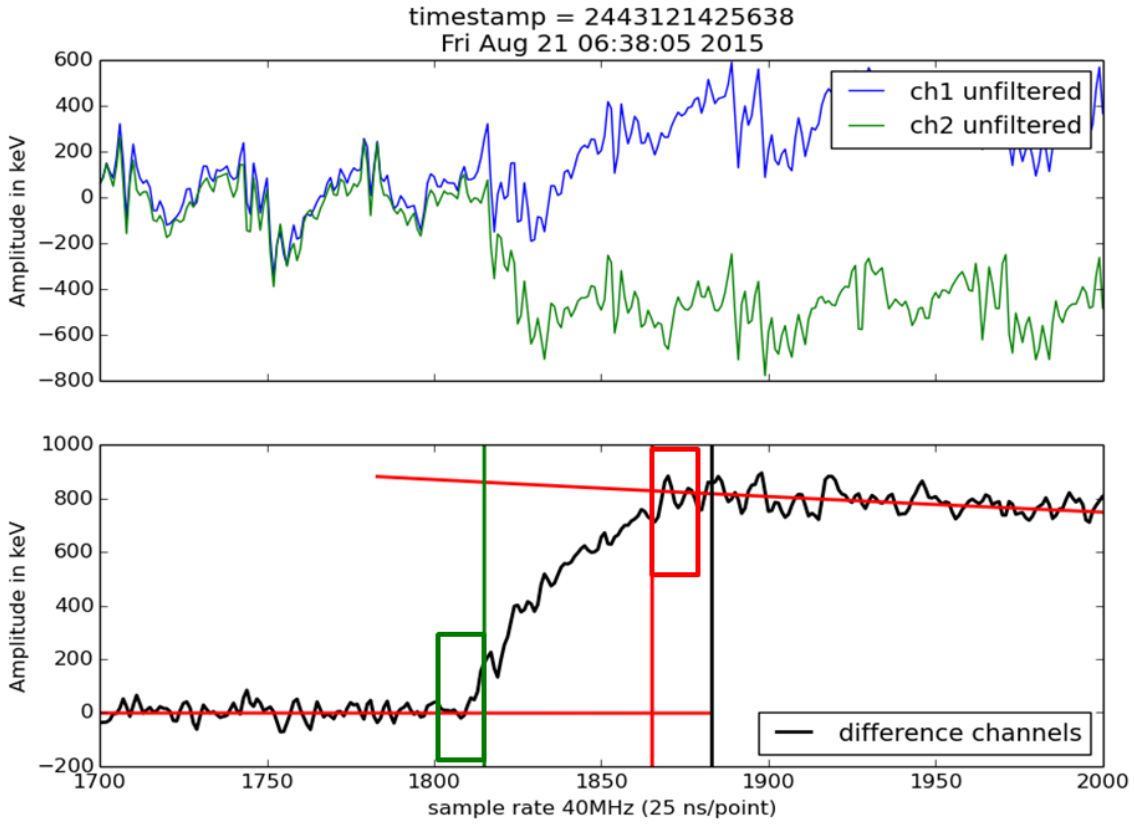
Figure 4.5: top: raw pulses zoomed to the pulse regoin. Same event as in fig. 4.4 bottom: Difference of both 40 MHz channels. showing the moving window filters to detect t_{90} and t_{10} as described in the text.

with the trusted region reflective algorithm [174],[175]. The same curve fit algorithm is used to fit an exponential function of the form

$$f_{\exp}(t) = a \cdot e^{b \cdot t} + c \qquad (4.6)$$

to the decay after the pulse, starting at the estimated end of pulse and ending at the last sample point of the event. The pulse amplitude in the decorrelated channel A_{dec} is computed by inserting the estimated end of pulse value as t_{est} in eq. 4.6 and as $t_{\text{est}} - 100$ in eq. 4.5:

$$A_{\text{dec}} = f_{\exp}(t_{\text{est}}) - f_{\text{lin}}(t_{\text{est}} - 100) \qquad (4.7)$$

In the next step the estimated end of pulse is used to measure the rise time and find t_{90} and t_{10}, the time indices at which the pulse trace reaches 10% and 90% of the amplitude. The event rise time is then given by $t_{\text{rise}} = t_{90} - t_{10}$. For detecting t_{90} a moving window filter with variable length n is moved along the sample points of the pseudo decorrelated channel and the mean value of the window is computed in the form

$$P(t) = \frac{1}{n} \sum_{i=0}^{n-1} P(t + i) \qquad (4.8)$$

with the filter output $P(t)$ as a function of the time. The window is oriented to the right side. A while loop moves the window along the data points from left to right by incrementing t until the index is reached at which

$$P(t_{90}) > f_{\exp}(t) - 0.1 \cdot A_{\text{dec}}, \qquad (4.9)$$

i.e. the filter output exceeds the exponential fit minus 10% of the amplitude (see also fig. 4.5). Now, the start of the pulse, t_{10}, is searched. Therefore the window in eq. 4.8 is changed to a left orientation with $P(t - i)$ and a while loop moves the window to the left side or backwards in time by decrementing t until the inequation

$$P(t_{10}) < f_{\text{lin}}(t) + 0.1 \cdot A_{\text{dec}} \tag{4.10}$$

becomes true. For the final analysis a window width of $n = 5$ sample points was chosen. Tests on a selection of a few tens events with several values showed $n = 5$ to work best. Furthermore we investigated a moving median filter instead of the moving average filter but could not see any advantages.
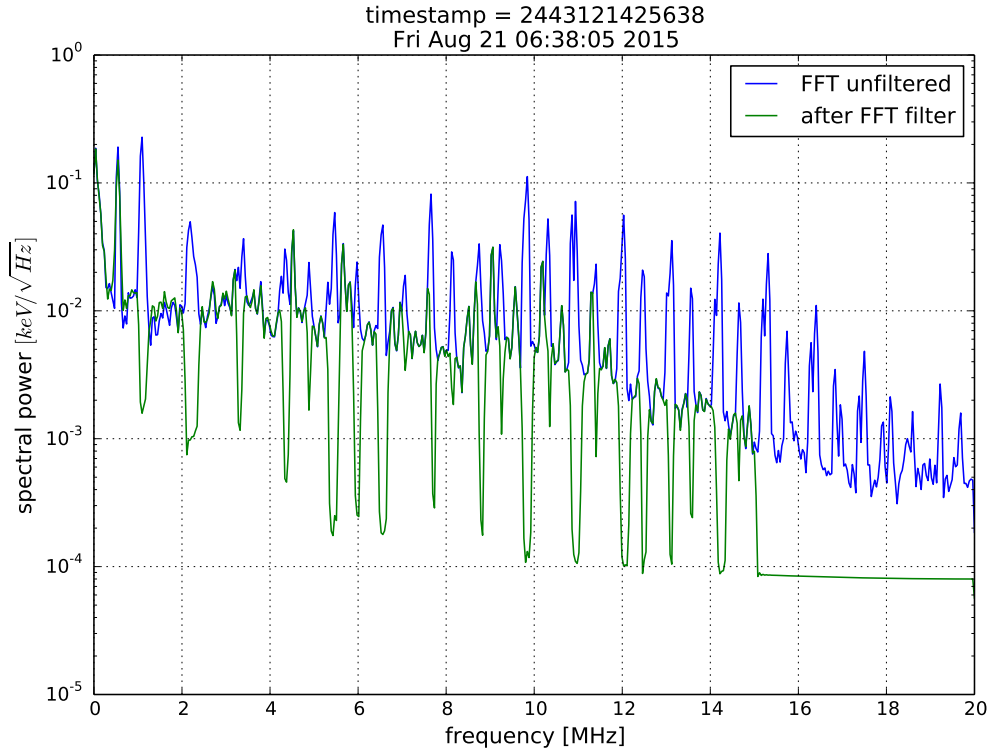
Figure 4.6: FFT spectrum calculated with the Welch method. The unfiltered raw data signal in blue and in green the signal after application of the multiple band-stop FFT filter. Surpression of the harmonic noise frequencies is clearly visible. Source pulses are shown in fig. 4.7 as ch1 unfiltered and ch1 FFT filtered.

Since the pseudo decorrelated channel contains channel 1 and channel 2 the computed rise time refers to the rise of the complete charge collecting process for electrons and holes. In the next steps of the processing chain the signals on the two individual channels are independently analyzed. Therefore the channels are first filtered.

A Fourier spectrum of the noise can be seen in fig. 4.6. A dominant 1.1 MHz frequency and all its harmonics up to 20 MHz make up the major part of the noise. It can be reduced by stopping the frequencies in the frequency domain. This is done by applying the FFT, replacing the amplitudes of the disturbing frequencies with 0 and applying an inverse FFT afterwards. An alternative that was tested is a series of band-stop filters each with a different stop frequency. But the number of disturbing frequencies is too high and 25 successively applied band-stop filters added too much computing time. Fig. 4.7 shows the two channels before (top plot) and after (middle plot) application of the FFT band-stop filter. The peak to peak baseline noise is almost reduced by a factor 2 from
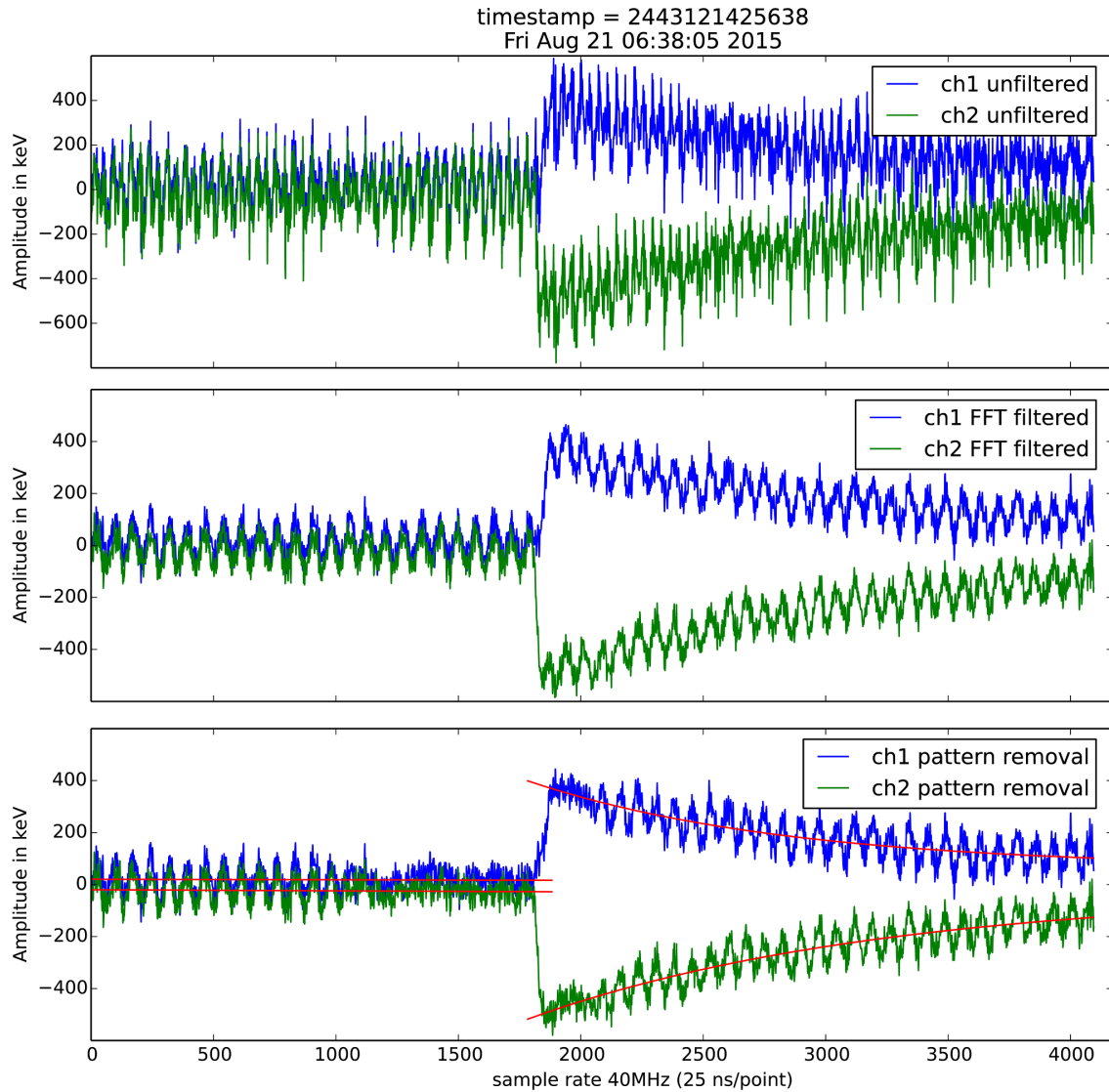
Figure 4.7: Three filter stages of the same event. Raw data is shown in top plot. Middle plot shows the multiple band-stop FFT filter output. The baseline pattern is subtracted in the pulse region and fits are applied in bottom plot.

~ 600 keV to ~ 350 keV without changing the pulse rise time. In the next step, a template of channel 1 is created by copying the first 1024 samples of the event record to a new array. This is low-pass filtered with a second order Butterworth filter to remove HF components. The filtered template is correlated with the complete channel record. The position of the maximum correlation in a region of interest around the pulse shows where the template and the noise are in phase. The noise is then subtracted in the pulse region, which can be seen in the bottom plot of fig. 4.7. The same is done for the second channel, with its own template. Computing time is saved by skipping the auto correlation and using the already known position of the first channel. This is possible because the noise originates from the same source and is correlated and in phase on both channels. A disadvantage of this method would be an event in which the noise significantly changes. The noise changes and looks different but on longer time scales only, and depending on the operational mode of the digitizer electronics. This is, however, not the case inside a single event. For the rise time analysis of the two channels it is important to reduce the noise at special frequencies between 100 kHz and 20 MHz: The spectrum above 3 MHz is dominantly affected by the FFT band stop filter, and the lower frequency part from < 100 kHz to 3 MHz by

template subtraction. Both ranges have some overlap. The order of application of the two methods must not be changed, because the raw data event with its HF-noise would make it likely for the auto correlation to return the wrong maximum at which the phase of the LF-noise is not matched. Subtracting the template out of phase would result in the antipode. Therefore, the RMS of the pulse region is determined and compared with its value after the template subtraction.

Once the last filter stage is successfully applied, the same functions as for the virtual channel are fitted to the baseline (eq. 4.5) and to the afterpulse decline (eq. 4.15). An example with fitted functions is shown in the bottom plot of fig. 4.7. The channel specific amplitudes are measured and the rise time parameters t_{10} and t_{90} are determined for each channel by the same algorithms with the same moving window functions as described before for the virtual third channel. To save some computing time the already known parameters t_{10} and t_{90} from the third channel are used as initial starting values, reducing the numbers of iterations for the fit procedures.

The event processing is now complete. All variables are computed. Based on the time stamp, the conventional EDELWEISS event record as given by the ANA analysis is searched for a coincident event. If one is found, the relevant variables from ANA are merged. The last procedure of the processing chain is to write all computed variables of this event in a file.

This is done only in the case that no condition for escaping the event was hit. In case no coincidence is found, the ANA related variables are all filled with 0. SAMBA and ANA event building is different and incomplete event records can occur. In this cases normally the heat energy is present, because it is processed first and the ionization channel related parameters can be (partially) missing.

The processing chain is executed on the IKP computing cluster TESLA. The input files are bunched to "jobs". Each job contains 10-20 input files that are successively processed, whereas the jobs are executed in parallel. This is possible because the jobs do not depend on each others' parameters. It takes about 30 hours to process all run 309 data. Each job creates one output file and when finished it prints statistical information about the number of processed pulses and the number of different escapes to a protocol file. An example for such a statistical output is given below:

```
1  total number of processed events:     17100
2  remaining events after escapes from...
3  ...BB reset pulses:                   16146
4  ...heat pattern sync:                 14229
5  ...pileups:                           10798
6  ...reverse pileups:                    9121
7  ...artifacts:                          9120
8  ...pulse after window:                 8302
9  ...pulse before window:                4632
10 ...pulse significance:                 1406
11 ...template subtraction:               1406
12 ...error during fit:                   1013
```

Listing 4.1: Remaining number of events after each escape scenario of the processing chain. Such an output is printed for each processed input file.

From 17100 events in the input file 1013 events remain after all possible escape conditions. This corresponds to a timing reconstruction efficiency of 5.9% only. The "reversed efficiency analysis" in ch. 4.1.2 shows that the majority of discarded events is not affecting real physics data. Most rejections are due to trigger on noise that can hit any of the above listed conditions. The asymmetric rejection number between pulse before window and pulse after window results from the asymmetric position of the acceptance window respectively

to the event length. 1800 samples are required for the baseline and 300 for the decay. One can expect skipping up to 6 times more events because the pulse is detected before the acceptance window. Pulse before window and pulse significance are the relative most common event skipping reasons. The first can be improved by reducing the necessary baseline length of 1800 samples to maybe 600. Therefore the template needs to be generated from the after pulse trace which has the exponential decay. The decay can be fitted in the template and then subtracted to provide a flat template. Afterwards it can be shifted to the region of interest and be applied there. Compared to the implemented algorithm with the template generated in the baseline, this needs one additional exponential fit, though adds computing time. It is not implemented for this analysis. The escapes because of missing pulse significance indicate that the noise level in the pseudo decorrelated channel baseline has exceeded a configured threshold. Or the pulse amplitude is not at least two times higher than the baseline rms value. Another small aspect that appears to be an advantage for later analysis is that the output files are naturally sorted by the time stamp. This is strictly followed inside each individual output file and it spans over several output files that differ by their filename. For example the file output.145 contains smaller time stamps than output.146.

4.3 Analysis of time resolved channel pulses

The obtained data in the output files of the previously described processing chain are now analyzed with the goal of a rise time based event discrimination and the ability to determine the z-axis coordinate of an energy deposit. This is performed with scripts written in Python and ROOT through the interfaces provided by rootpy. This combines the intuitive way of Python programming with the powerful analysis tools of ROOT. Results are graphically presented in form of ROOT plots. Since the cumulative size of all processed files is below 1 GB it is possible to read all available data into the memory. The data is written into a single structured numpy array on which cuts can be applied. The results filled either in ROOT histograms or displayed as scatter plots.

4.3.1 Amplitude analysis and energy calibration

The two 40 MHz channels share the cold electronics (cabling, FETs) with the conventional EDELWEISS ionization channels. Splitting into 100 kHz and 40 MHz sampling branch is done after the first analog amplification inside the bolometer box. After the splitting both branches pass the signals through a filter-amplifier combined integrated circuit and in the 40 MHz case through an additional AC-coupling to the ADCs. Since these components differ in their gains, an individual calibration for the 40 MHz channels has to be applied. This is achieved by selecting data from Barium runs and fitting the Gaussian function for each channel to the 356 keV photo peak of the Barium energy spectrum. The final amplitude spectrum of all available 40 MHz recorded Barium run data from run 309 is shown in fig. 4.8. The x-axis is titled "precalibrated amplitude in keV" because it has been calibrated with an early dataset after 60 days of run time. The photo peak is detected by fitting a Gaussian to both channels, resulting in -356.8 keV with a width of $\sigma = 19.8$ keV on channel D (holes) and (357.7 keV with $\sigma = 24.4$ keV for channel B (electrons). Hole collecting electrodes have a better energy resolution than electron collecting electrodes which can be seen in the larger value for σ. This is reproduced in charge carrier simulations and dedicated experiments [176]. Beginning from a point like γ impact, holes drift in a cylindrically shaped cloud with lower anisotropy, whereas electrons expand in a cone-shaped cloud with higher anisotropy and diverging path length. A Barium calibration with the conventional EDELWEISS readout is discussed in [125] where a $\sigma = 6.913$ keV is presented for the hole collecting electrode. The difference between the 40 MHz channels σ and the
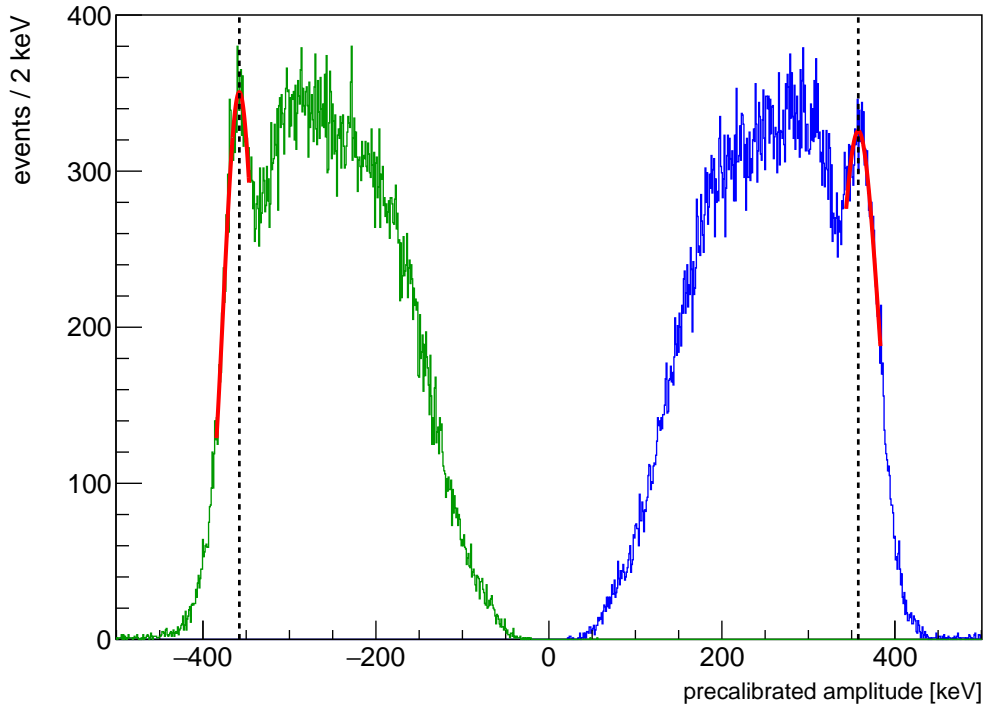
Figure 4.8: Calibration of 40 MHz channels (B blue, D green) using the 356 keV photo
         peak (dashed lines) of the ^{133}Ba spectrum. Only events that hit the fiducial
         criteria as given in eq. 4.16 are accepted in this histogram.

standard analysis shows the superior energy resolution of the 100 kHz channel as well as
the downsampled 1 kHz channel in which the highest energy resolution is reached.

The gain of the 40 MHz readout channels from detector to analog digital converter (ADC)
can be derived from the presented calibration as

$$
\begin{aligned}
\text{channel } B: \quad & 1 \text{ ADU} \widehat{=} 4.238 \text{ keV}, \\
\text{channel } D: \quad & 1 \text{ ADU} \widehat{=} 4.504 \text{ keV}.
\end{aligned}
\tag{4.11}
$$

Another feature that can be seen in fig. 4.8 is the absence of events below amplitudes
of 150 keV. This comes from the escapes in the processing chain. Especially the cut on
the pulse significance compared to the baseline rms strongly reduces the efficiency for
reconstructing small pulses (see listing 4.1). Although the FPGA based trigger is sensitive
at energies < 10 keV, the 40 MHz channel processing has its threshold at ∼ 50 keV, which
corresponds to its baseline noise level.

A direct comparison of the 40 MHz calibration results and the EDELWEISS standard
analysis ANA is shown in fig. 4.9. The two plots show, for different energy ranges, the
energy fitted in the time resolved channel on the y-axis and the ANA energy on the x-axis.
Whether an event is colored black, red or blue is decided by the ANA cuts for fiducial, side
A or side B events. The data set based on which fig. 4.9 is plotted is the full run 309 data
collected in WIMP search mode. Since this calibration was performed with the 356 keV
peak one can expect a systematic offset for much higher energies. For events at an energy
of 1400 keV in ANA, the 40 MHz analysis shows energies between 1400 and 1500 keV. It
would be perfect if the fiducial events in fig. 4.9a would be spread around the red marker
line, but they have a trend to higher energies which comes from the extrapolation. The
observation that surface events (side A or B) appear with a different slope arises from the
situation that the 40 MHz readout is connected to electrodes B and D only and charges
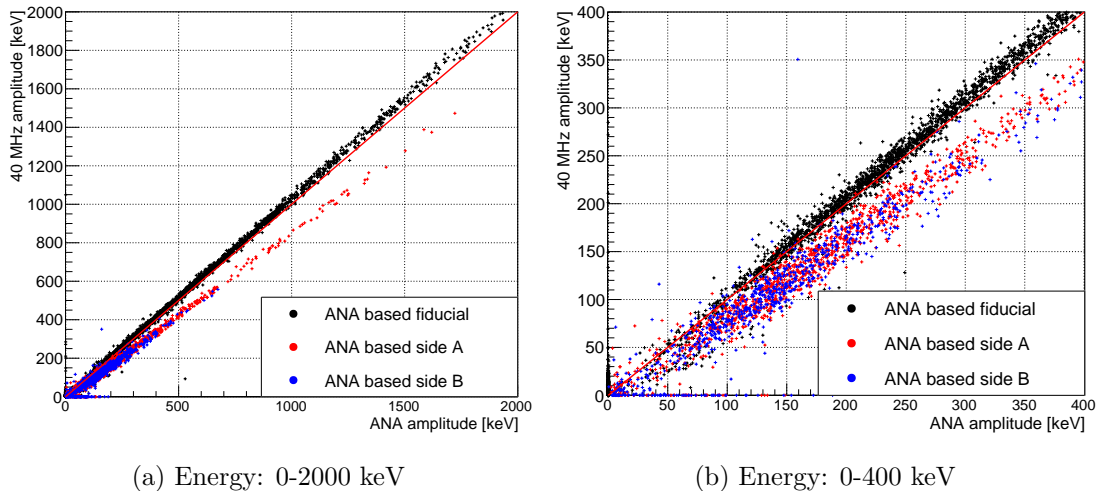
(a) Energy: 0-2000 keV (b) Energy: 0-400 keV

Figure 4.9: Comparison of the 40 MHz calibration of this thesis with the standard EDEL-WEISS ANA calibration. The small mismatch (deviation from red line) of fiducial (black) and surface (red, blue) events arises from the missing channels A, C in the 40 MHz readout. See text for details.

collected on the veto electrodes A and C are unknown. A surface event on side A deposits charge on the electrodes A and B. The amplitude on the fiducial electrode B is reduced by $\sim 25\%$ through crosstalk from the neighboring veto electrode A. The same happens on the detector side B with fiducial electrode D and veto electrode C. Fiducial events on electrodes B and D have crosstalk as well. In ANA, all 4 electrodes are available and the crosstalk from each possible electrode combination is corrected. 12 coefficients are necessary because each electrode influences all others with an individual coupling constant. All couplings are $< 5\%$ except the AB and CD as described above. Another feature one can see in fig. 4.9a is that side A events appear with higher energies, up to 1500 keV. The plotted data are recorded during WIMP search run without any calibration sources. Therefore, the asymmetric event distribution on side A and B can not be explained as a result of Barium or Thorium sources. A pollution with decaying Bismuth and Polonium on the detector or the surrounding copper could explain why the observed events are only on side A.

$$^{210}\text{Bi} \xrightarrow{\beta(1162 \text{ keV})} {}^{210}\text{Po} \xrightarrow{\alpha(5304 \text{ keV})} {}^{206}\text{Pb} \tag{4.12}$$
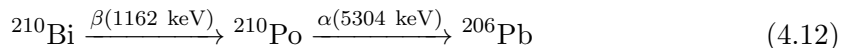
The number of events is not large enough for analysing an energy spectrum, but the $\beta-$decay of ^{210}Bi with a half life of $t_{1/2} = 5.012$ d [177] and an end point energy of 1162.2 keV is compatible with the observation. At the time this analysis has been performed, the official EDELWEISS analysis that is used as a reference providing the calibration the x-axis in fig. 4.9a, was in a preliminary state. Therefore, it can not be excluded that the applied cut (see listing 4.2), will change and explain the observed asymmetric rate and energy spectra of surface events.

4.3.2 Rise time analysis

The rise time analysis is based on the event rise time, defined as $t_{\text{rise}} = t_{90} - t_{10}$ in the pseudo decorrelated channel (ch. 4.2.2) which combines the pulse shape of the electron collecting electrode B and the hole collecting electrode D. Additionally, the rise times for channel B and D analyzed independently are available, too. The results are computed from the processing chain and based on all data from EDELWEISS run 309. Selecting subsets of data based on the run mode, for instance Barium, is possible.
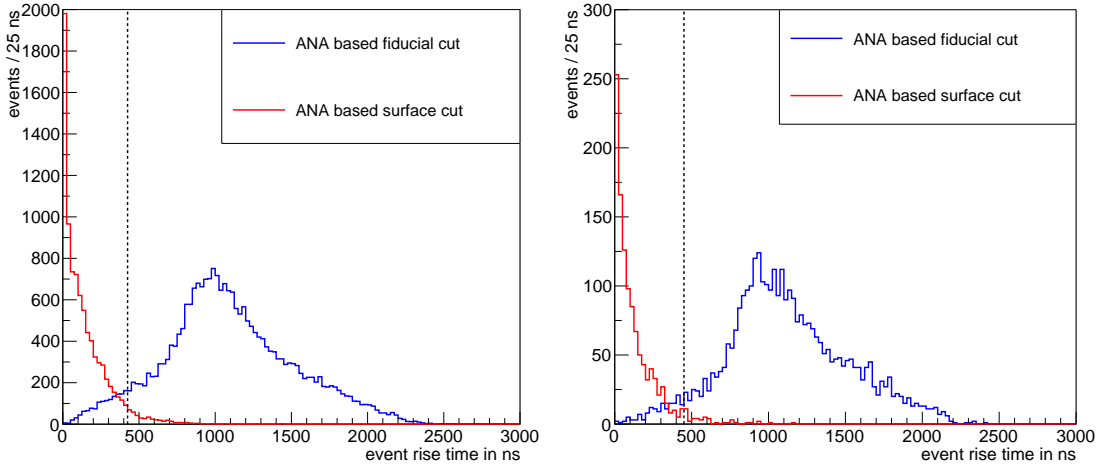
Figure 4.10: Left: Rise time (of pseudo decorrelated channel) spectrum of Barium data. A cut at 425 ns (dashed line) can reject 95% of surface events and 5.75% of fiducial events. Right: WIMP search data with cut at 450 ns discards 4.37% of fiducial events while rejecting 95% of surface events. Color coding is applied on ANA variables based cuts. All accepted events have energies of $E_{40\ \text{MHz}} > 100$ keV.

In fig. 4.10 a spectrum of the event rise times of run 309 is shown for Barium calibration (left) and WIMP search runs (right). Only events with ionization energies above 100 keV are accepted. The rise times are analyzed in the pseudo decorrelated channel (event rise time), which has a superior signal to noise ratio compared to the individual channels. The color coding is based on cuts of ANA variables and is therefore independent of any 40 MHz channel related analysis. The applied cuts are a χ^2-cut followed by a cut to select either fiducial or side A and side B events. Fiducial events are counted in the blue histogram, whereas side A and side B are both counted in the red histogram. The reduced code used to perform these cuts is shown in listing 4.2 and the declaration of variables is given in table 4.2. The obtained results for a surface event rejection by the event rise time for $E_{40\ \text{MHz}} > 100$ keV are presented in table 4.1

Table 4.1: Results of fig. 4.10

Run type	95% rise time cut [ns]	loss of fiducial events
Barium	425	5.75%
WIMP search	450	4.37%

The 40 MHz time resolved ionization channel contains important information about the event rise time. For Barium runs, a cut at 425 ns event rise time and $E_{40\ \text{MHz}} > 100$ keV rejects 95% of surface events and 5.75% of fiducial events. In WIMP search runs, a cut at 450 ns rejects 4.37% of fiducial data and 95% of surface events. Thus, a rise time based event discrimination in EDELWEISS-III FID800 type detectors is possible.

All variables for discriminating fiducial and surface events are taken from the ANA analysis (version ANA-b). The first 4 rows in table 4.2 describe variables from the time resolved channel and are written in a *camelCaseStyle*. The remaining variables (capital letters) are extracted from the ANA analysis. In line 1 of listing 4.2 a first preselection is applied to accept events with an amplitude in the pseudo decorrelated channel of > 100 keV. This energy cut is necessary because the rise times can not be resolved for pulses with smaller energies. Furthermore, only events of Barium calibration runs are accepted in this example.

Listing 4.2: Cuts to discriminate fiducial and surface events. ANA based variables are in capitals.

```
1  if pdcAmp>100 and runType == "ba":
2    if CHIA−RCIA<0.25 and CHIB−RCIB<0.24 and CHIC−RCIC<0.34 and CHID−RCID<0.23:
3        if (abs(EIA−(0.001)*EFID)<((FWIA/2.35*2.576)+(0.017)*EFID)) and (abs(
   EIC−(0.01)*EFID)<((FWIC/2.35*2.576)+(0.02)*EFID)) and (abs(EDIF−(−0.003)*
   EFID)<((FWDI/2.35*2.576)+(0.019)*EFID))):
4            hist1.Fill((endOfPulse_pdc − beginOfPulse_pdc)*25)
5        elif (EIA>5 * (FWIA/2.35)) and (EIB>5*(FWIB/2.35)) and (EIC<5*(FWIC
   /2.35)) and (EID<5*(FWID/2.35))):
6            hist2.Fill((endOfPulse_pdc − beginOfPulse_pdc)*25)
7        elif (EIA<5 * (FWIA/2.35)) and (EIB<5*(FWIB/2.35)) and (EIC>5*(FWIC
   /2.35)) and (EID>5*(FWID/2.35))):
8            hist2.Fill((endOfPulse_pdc − beginOfPulse_pdc)*25)
```

Table 4.2: Declaration of variables used for the cuts.

Variable	Unit	comment
pdcAmp	keV	amplitude in 40 MHz channel (pseudo decorrelated ch)
runType	string	Type of the run, "ba" for Barium
endOfPulse_pdc	25 ns	position at which 90% amplitude is reached
beginOfPulse_pdc	25 ns	position at which 10% amplitude is reached
CHIx	ADU^2	$\log_{10} \chi^2$ of 1 kHz ch. A,B,C,D fit in time domain
RCIx	ADU^2	average of $\log_{10} \chi^2$ of 1 kHz ch. A,B,C,D in this hour
EIx	keV	1 kHz ionization A,B,C,D energy
EFID	keV	Fiducial ionization energy: (EIB + EID)/2
FWIx	keV	FWHM of 1 kHz A,B,C,D in this hour
FWDI	keV	FWHM of (EIB-EID)/2 in this hour

A quality cut is applied in line 2. The quality of pulse template fitting in ANA is measured by the χ^2 value for each event. A width of 5σ is accepted and other events are skipped. Afterwards, it is probed if the event is fiducial (line 3), or surface (line 5 and 7). The rise time histograms (figures 4.10, 4.11) and the scatter plots (fig. 4.9) are filled according to these cuts.

The energy dependence of surface event rejection and energy scales is presented in fig. 4.11. For the smallest energies, a rise time cut would classify nearly all fiducial events as surface events. This is not dangerous in a sense of misidentified surface events, but it reduces the detector efficiency by 73% compared to the conventional analysis. For larger energies a rise time based event discrimination is more reliable. The reason for this is the method that is used to determine the rise time. As seen in fig. 4.5 the baseline noise level is at almost 75 keV in the filtered channel. The algorithm used to find the t_{10} and t_{90} markers for the rise time determination yields small rise times for small amplitudes. However, this is acceptable for a rise time analysis with the goal of surface event rejection, since events are rather rejected than misidentified as fiducial events. On the other hand, almost no events remain as fiducial, thus, the efficiency decreases which can be seen in the results of fig. 4.11 summarized in table 4.3

The results of the energy dependent surface event discrimination are based on the rise times obtained in the individual channels, whereas the results in fig. 4.10 and table 4.1 are based on the pseudo decorrelated channel. The latter has an improved SNR and yields much better results. However, the energy dependent analysis shows an improving surface event rejection quality with increasing pulse amplitudes.
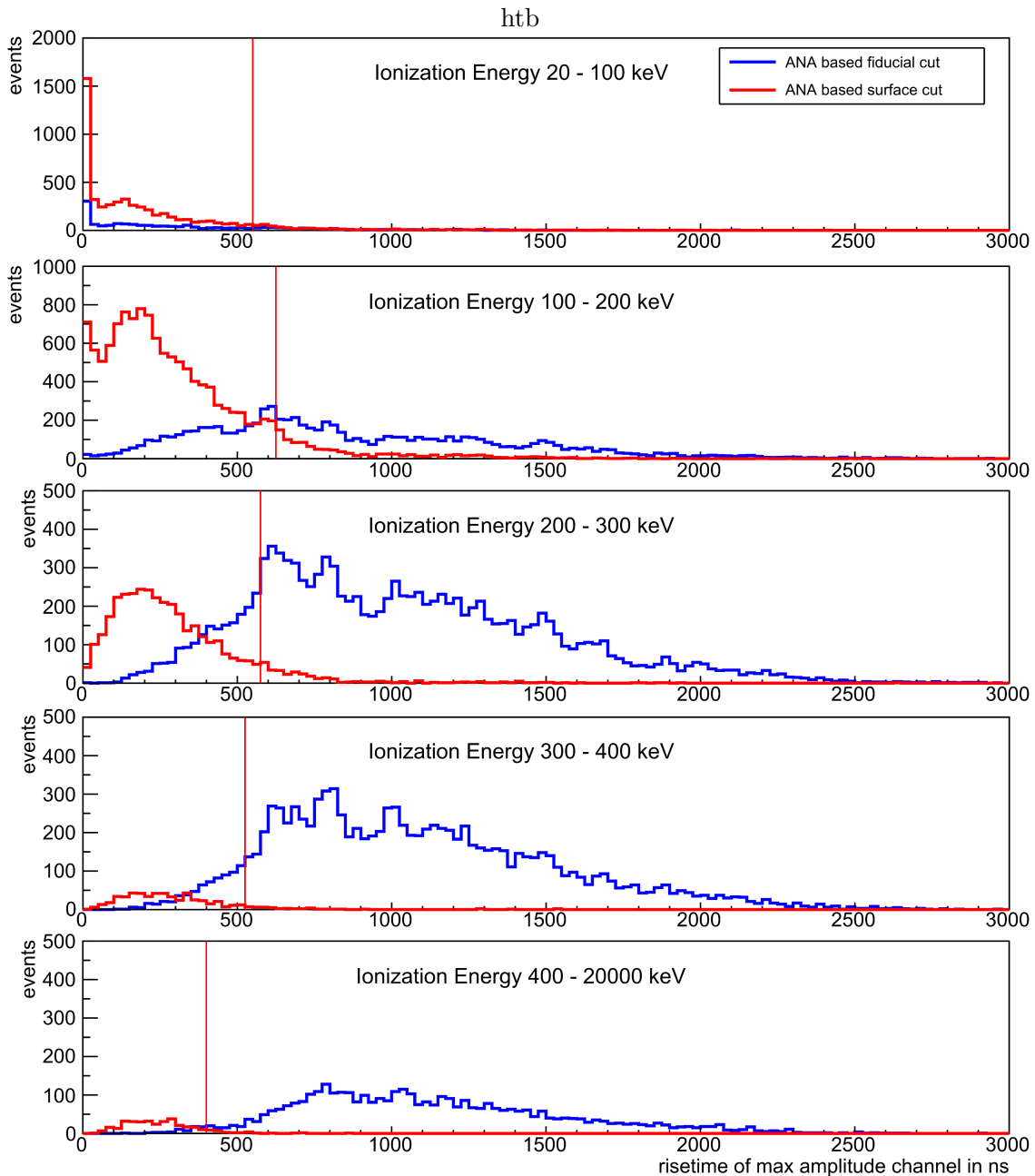
Figure 4.11: Spectrum of rise times (maximum amplitude channel) for different energy scales (data set contains Barium, Thorium and WIMP search data). The selection of surface/fiducial is based on the ANA variables of the 100 kHz channels. The red marker indicates 90% of all surface events. Results summarized in table 4.3.

Table 4.3: Energy dependend surface event rejection potential. Results of fig. 4.11.

Energy range [keV]	90% rise time cut [ns]	fiducial efficiency loss [%]
20-100	550	73
100-200	625	36
200-300	575	15
300-400	525	7
>400	400	1.6

To conclude one can say that a cut on the rise time is less reliable in comparison to the efficiency of the conventional EDELWEISS method relying on veto electrodes. Especially the impossibility of identifying fiducial events at ionization energies $< 100 \; keV$ is ruling out the idea of replacing the veto electrode method by a rise time method. However, a combination of a rise time cut on time resolved channels with the conventional amplitude cuts on veto electrodes is a promising approach to investigate a certain class of events: High energetic events inside the nuclear recoil band, such as the few out laying events at high energies in figures 2.9 or 2.11 and 2.13 (see section 4.5). We showed the power of the time resolved channel to reject 95% of surface events by a fiducial efficiency loss of 4.37% above 100 keV. The latter improves for higher energies. Furthermore, we can expect a future hardware with a different designed power supply to improve the time resolved channel results for lower amplitudes and better event discrimination.

4.4 Comparison with charge migration simulations

Simulations of charge migration processes in the FID800 type detector are an important tool for understanding the measured rise time distribution. The known impact coordinates of simulated energy deposits allow a spatial verification of the rise time based surface event rejection. Furthermore, simulated distributions can be designed to have a certain signal to noise ratio. Based on this, an outlook for, and the potential of, a future electronic readout system with a noise level reduced realistically by a factor 10 is presented.

Besides the comparison of measured and simulated results, the simulated events also allow for a benchmark test of the processing chain (section 4.2). These tests helped to identify deficiencies and to optimize the analysis. Except for time stamp related tasks and readout artifact detection, simulated event traces are processed by the same algorithms applied in the same order as for the experimental events. The results of this analysis are presented in this chapter and show that the data recorded in the experiment and the simulated events are in an excellent agreement and that electronic noise is the leading limiting factor for the time resolved ionization channels.

4.4.1 Simulated events

The event simulation is performed within the framework of another PhD thesis [178] using a MATLAB and C code with a Monte Carlo algorithm similar to the simulations published in [169]. For this application, the migration of charges in a modeled FID800 type detector is simulated. The electric field of the electrodes is chosen to be as in the EDELWEISS standard mode, the FID mode, with voltages according to the same conditions as for the data taking at the experiment: $A = -1.5$ V, $B = +4$ V, $C = +1.5$ V and $D = -4$ V. The resulting electric field is computed by a finite element method.

A MC event consists of initial electron-hole pairs that are created in a spherical volume around the start point. The number of electron-hole pairs and the size of the start volume depends on the simulated energy deposit and the absorption length for γ or X-rays
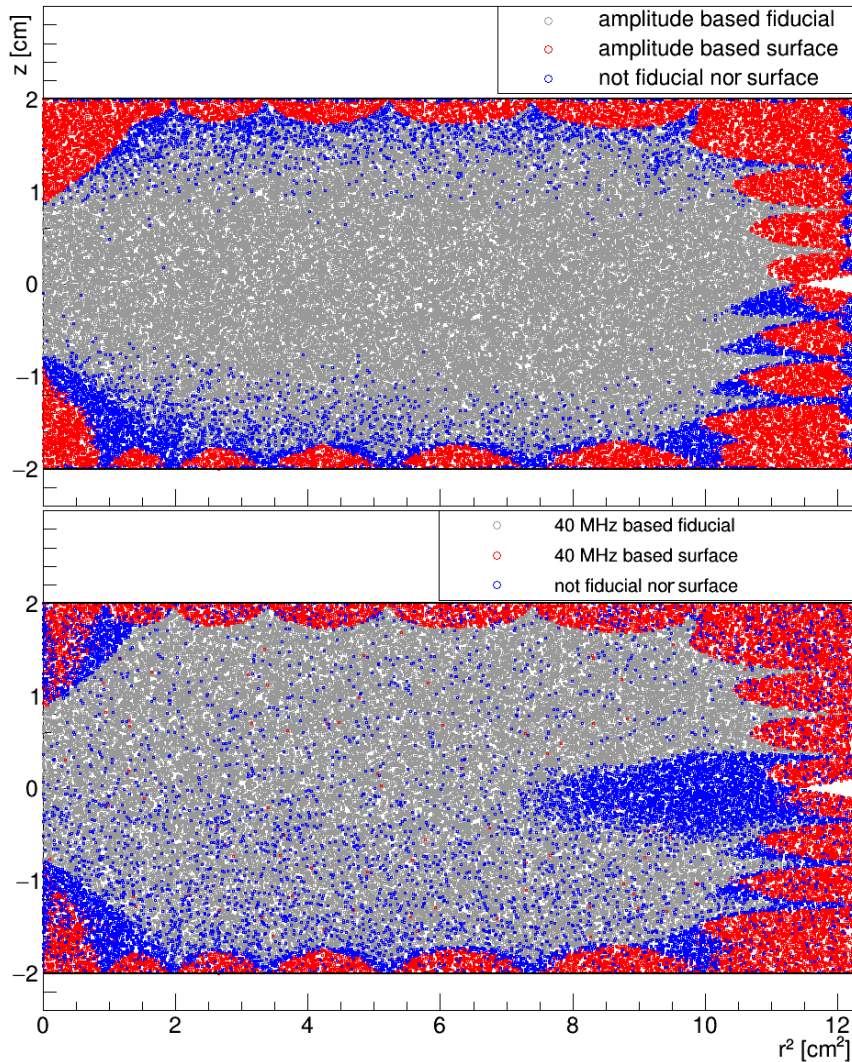
Figure 4.12: Starting positions of events with simulated charge migration. Discrimination in the top plot is based on initially simulated amplitudes of the electrodes *A,B,C,D*. In the bottom plot (after adding noise and applying the processing chain), the discrimination relies only on amplitudes (symmetry of electron and hole signals as in eq. 4.13) of the channels *B*, *D* and on the rise time.

in germanium. In this simulation, the energy deposit is selected to be 60 keV for all events. Thus, a start volume of 1 mm^3 is given. The charge migration is modeled by the phenomenological model of Nathan [179] which describes anisotropy of the conductivity of n-type germanium at higher electric fields of $\mathcal{O}(\mathrm{kV/cm})$ as detailed in [180]. The code used for the charge migration simulation is the same as in [180] with small adoptions to better fit the given situation of the time resolved ionization channel readout hardware. The time steps in which the electrons and holes are propagated by the simulation are enlarged from the published 1 ns to 25 ns to match the time resolved channel ADCs that sample with the same sampling width. The simulation uses the electric field dependent velocity laws for electrons and holes as described in [181]. The readout signal on the electrodes is computed with the Shockley-Ramo theorem [103, 104], based on the charge position, charge velocity, the weighing potential and field (eq. 2.18, 2.19).

The simulation process of one event is stopped once no new charges are induced on any of the four electrode channels. Charge trapping is included, which means that the overall charge collecting efficiency not necessarily sums up to 100%. Note that trapped charges do

not contribute to the space charge situation for the next simulated event. Simulation thus does not take into account the degeneration due to trapped charges accumulating with time. Each simulated event returns the information about the starting point and ~ 5 to ~ 100 time steps in which the initial charges migrate. For each time step, the simulation provides the signal amplitude on the individual electrodes. The amplitude values always start at 0, there is no noise or preceding baseline. In the final state of a fiducial event, the amplitude of the collecting electrodes (B and D) is close to ± 1 and the amplitude on both veto electrodes (A and C) is below ± 0.1. Small deviations for 1 or 0 arise from trapped charges and incomplete charge collection. The starting coordinates of each simulated event are generated by a spatially uniform random distribution.

Fig. 4.12 shows a cut through half of the detector, with the detector's z-axis on the y-axis and the radius squared on the x-axis. Since the simulation was performed with a flat distribution per volume element, r^2 is plotted to keep a homogeneous distribution along the x-axis. Each colored point represents the start coordinates of one simulated event. Discrimination in the first plot is based on the simulated final amplitudes of all four channels in the final state, in analogy to the fiducial cut applied in the ANA analysis. In the processing of simulated events discussed below in detail, these simulated amplitudes are used together with the coordinates of the energy deposit.

Fig. 4.12 top shows the starting points of simulated events in z and $r^2 = x^2 + y^2$ coordinates. The starting points are colored in three different groups. The fiducial events (gray), in red and blue the non fiducial events that can be subdivided into surface events (red) and other events (blue). Events are discriminated by their amplitudes on all four electrodes at the end of the simulation process. The fiducial and surface cut is defined as

$$\begin{aligned} \text{fiducial:} \quad & (A < 0.1) \wedge (C < 0.1) \wedge (-0.24 < B^2 - D^2 < 0.1) \\ \text{surface:} \quad & ((A > 0.9) \vee (C > 0.9)) \wedge ((B < 0.1) \vee (D < 0.1)) \end{aligned} \tag{4.13}$$

where B and D represent the amplitudes on the collecting electrodes and A and C the amplitudes on the veto electrodes. The terms are linked with the boolean operators **AND** $\wedge$ and **OR** $\vee$. The asymmetric numbers in the last term of the fiducial cut arises from the different drifting behavior of electrons and holes. These cuts follow closely the corresponding cuts applied to real data within the standard ANA analysis.

In fig. 4.12, a total of 82189 events from the simulated dataset of 100.000 are shown. The 82% efficiency arises due to the fact that some events do not pass the processing chain since the simulated amplitudes vary from 0-600 keV, thus, several events are invisible for the processing chain inside the noise level. From the passed events, 57675 are selected as fiducial events according to the cut described in eq. 4.13. Since the events are uniformly distributed it is possible to derive the fiducial volume from the percentage of fiducial events. The effective fiducial volume with the selected cut parameters corresponds to 70% of the detector's volume, which is compatible with the (detector specific) EDELWEISS values of 70%-80% [83]. Within a distance of 1 mm to the detector surface, 8028 events are counted out of which 114 passed eq. 4.13 as fiducial events, which corresponds to 0.2% misidentified fiducial events. A rate of characterized fiducial events within a 1 mm surface layer can be interpreted as a benchmark for the following comparison with a discrimination of events by rise time. The acceptance rate in the surface volume with the conventional method is

$$R_{\text{surface}}^{\text{veto}} = \frac{114}{8028} = 1.4\% \tag{4.14}$$

These 1.4% of events are located beneath the collecting electrodes B and D. Events at the volume around the equator are missing, which can be seen as the small triangle shaped region in fig. 4.12. The reason for this effect is that the processing chain relies on channel B
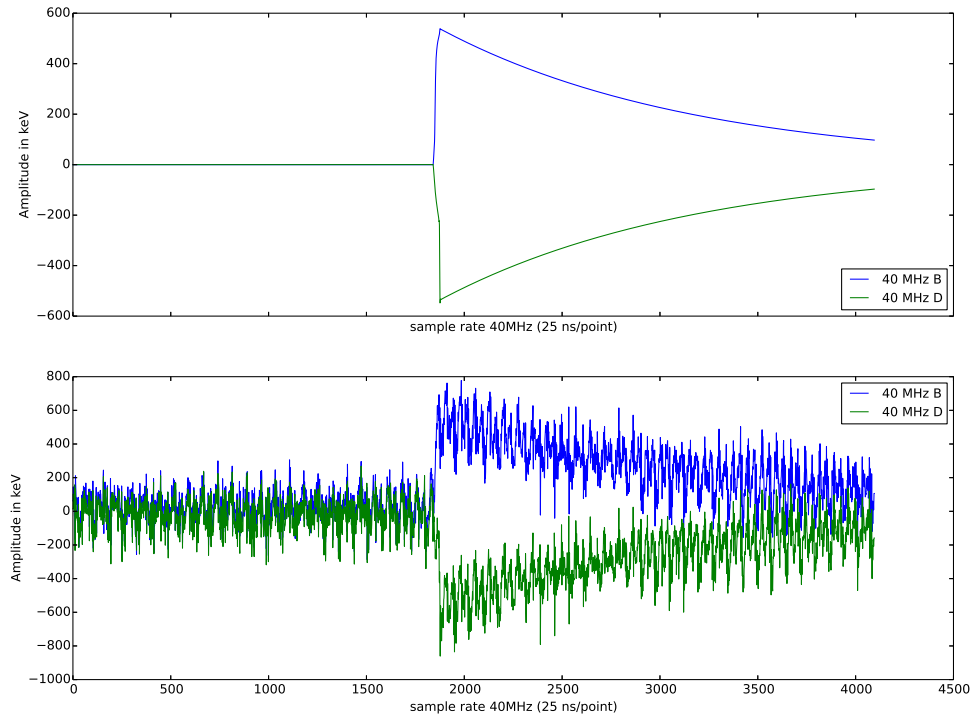
Figure 4.13: A simulated fiducial event with its signal traces on channels B and D before and after adding real data noise.

and D only. The small region can have events with charge deposits exclusively on electrodes A and C, thus, they are escaped by the processing chain. It does not affect the resulting statistics, since events in that region are predominantly seen on the veto electrodes and therefore rejected anyway. A misinterpretation as fiducial event is excluded.

4.4.2 Simulated events processed by the time resolved channel data processing chain

The raw data format of simulated events significantly differs from real data events. To render simulated events compatible with the processing chain described in ch. 4.2 it is necessary to pad them to a length of 4096 sample points. This is done with a padding of 1800 zeros in the pulse trace before the event. A random number between -200 and +300 is added to the 1800, which makes the pulse position arbitrary and more challenging for the pulse finding algorithm. The electrode amplitudes which are at this stage in the interval $[-1, 1]$ are now scaled by multiplying each simulated sample point with a random number from the interval $[0, 600]$. The lower value was selected in order to generate pulses within the noise level, whereas the upper limit is selected above the barium energy to study effects that may be, due to low statistics, not visible in the experimental data. Afterwards, the event is padded on the right side with an exponential function of the form

$$y = A \cdot e^{bx} + c \tag{4.15}$$

with the last simulated point taken as the amplitude A. The parameter $b = 7.709 \cdot 10^{-4}$ is the decay constant coming from AC-coupling and was measured in the experimental data of run 309. The constant c is set to 0 because an offset is not necessary. In real data, c would be important in the case of consecutive events. The total length of the event is fixed

to 4096 and realized by a variable padding length of eq. 4.15. The event is then filtered by a 10 MHz 2nd order low pass Butterworth filter that smoothes the edges from padding. The event at this stage can be seen in fig 4.13 top before adding noise.

For a better understanding of the effects from noise in the real data, a selection of noise events from run 309 without any pulse is used. It is important that neither on the B electrode, nor on the D electrode an amplitude higher than noise level is visible. These events are recorded via a trigger on noise or via software induced trigger commands. About 10.000 events that fulfill these requirement were found in the run 309 data. Out of these, a database is generated that contains 50 zero amplitude events with their complete trace. One entry of this database is now randomly chosen to modify one of the simulated events. The resulting phase space of simulated events has a theoretical size of $1.5 \cdot 10^{12}$ different events, derived from 10^5 simulated events combined with 500 possible pulse starting positions, 600 different amplitudes and 50 different real noise pulses. Because of limited memory and CPU time only 10^5 arbitrary combinations of the phase space are used for this analysis, each simulated event once.

The processing chain described in ch. 4.2 was slightly modified for the simulated events. All algorithms for removing time related artifacts in the real data, such as bolometer box reset pulses or pile-ups, could be skipped. Additionally it is not necessary to search for coincidental events in the standard EDELWEISS analysis which reduces the number of output variables and the output file size. All 10^5 events were processed in 4 h on a single CPU core. In comparison, the same number of real data events takes about 40 h on a single core. This demonstrates that about 90% of CPU time in data processing is used for the identification and removal of artifacts in the raw data and for searching and finding the corresponding EDELWEISS event by time stamp. Here, only the pulse processing functions are executed, such as the pseudo decorrelated channel and noise pattern removal.

4.4.3 Suppression of near-surface events using the rise time information

The output of the processing chain with simulated events is stored in ASCII formatted files that are read by scripts written in Python and ROOT for a statistical analysis. The main difference compared to the analysis of real data is the availability of the coordinates of the starting point at which the energy deposit occurred inside the detector. Furthermore, all time related effects such as pile-up induced readout artifacts or crosstalk from the heat modulation are missing.

The simulated events now modified with real noise as described in ch. 4.4.2 and analyzed by the 40 MHz data processing chain are shown in the lower plot of fig. 4.12. The cuts for color coding are now performed by using the 40 MHz channel specific variables: the amplitudes of channel B and D and the rise times. The applied cuts are

$$
\begin{aligned}
\text{fiducial:} \quad & ((0.8\ D < B < 1.2\ D) \lor (0.8\ B < D < 1.2\ B)) \land t_{(B+D)} > 450 \text{ ns} \\
\text{side B:} \quad & (D < 50 \text{ keV}) \land (B > 2 \cdot D) \land t_B \leq 450 \text{ ns} \\
\text{side D:} \quad & (B < 50 \text{ keV}) \land (D > 2 \cdot B) \land t_D \leq 450 \text{ ns}
\end{aligned}
\tag{4.16}
$$

with the analyzed rise times of the pseudo decorrelated channel t_{B+D} (10%-90%) and the side specific pulse rise times t_B (10%-90%) and t_D (10%-90%). The total number of 82189 entries in the scatter plot is unchanged. With 54810 events detected as fiducial events, the effective volume decreased to 66.7% compared to 70.2% on the standard variables without a rise time cut. The number of events within a 1 mm thick volume beneath the surface that passed as fiducial is 131, compared to 114 with the conventional variables. This corresponds to a fraction of accepted events in the 1 mm surface volume of

$$
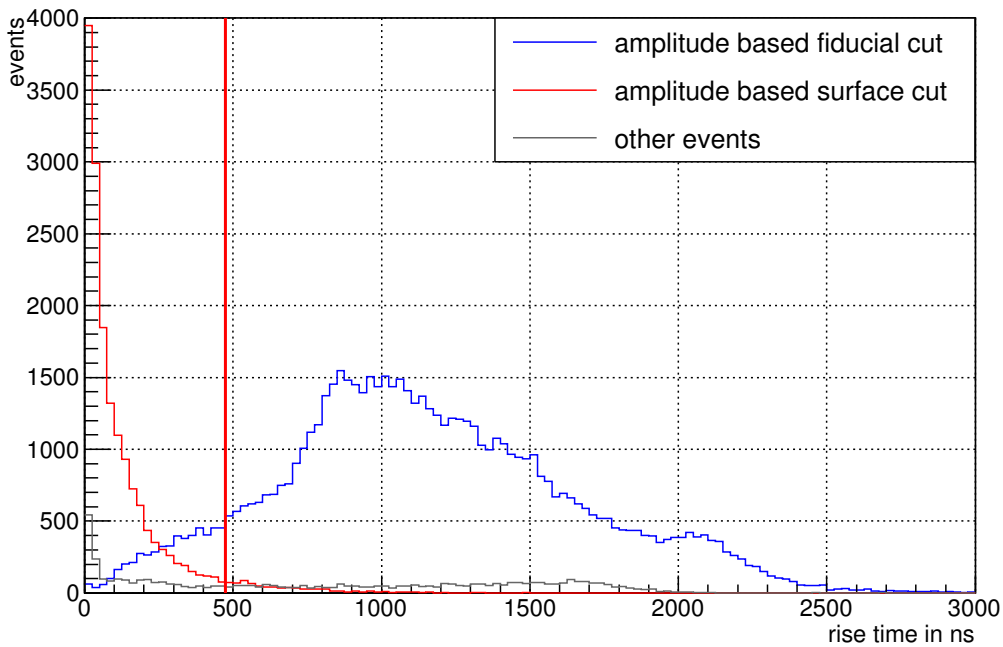R_{\text{surface}}^{\text{risetime}} = \frac{131}{8028} = 1.6\%.
\tag{4.17}
$$

Figure 4.14: Rise time spectrum of simulated events grouped by the final state amplitude on the four electrodes. The red line marks 95% of surface events with a risetime below 475 ns. A cut based on rise time would exclude 7.9% of fiducial events.

A rise time spectrum for the simulated time resolved channel events is shown in fig. 4.14. The rise time is taken from the virtual third channel in which the difference of both individual channels is computed. Therefore, it refers to the complete drifting process of electrons and holes. The color coding is based on the amplitudes of all four electrodes as defined in eq. 4.13. A cut exclusively on the rise time at 475 ns would cover 95% of surface events and discard 7.9% of fiducial events. This is in excellent agreement with the analyzed rise times of experimental data shown in fig. 4.10.

In [70] and fig. 2.26 the pulse shape of a *shared event* is shown. Shared events have a signal on 3 electrodes, on one detector side the collecting and veto electrodes, on the other side only the collecting electrode. Thus, these events can not directly be identified as a shared event with only two 40 MHz channels. Figure 2.26 shows that the pulse shape on the two collecting electrodes B and D differ in the time stamp of t_{90}, where 90% of the channel specific signal amplitude is reached. Since channels A, C are not available on the time resolved readout hardware, we analyze the potential of using the different signal shape to analyze the z coordinate of the initial energy deposit. A time difference $\Delta t_{90} = t_{90}(\text{ch}_B) - t_{90}(\text{ch}_D)$ is computed on an event-by-event basis and compared with the z coordinate of the simulated energy deposit. The results are shown in fig. 4.15 for the simulated data with real noise and with the same noise spectrum, but reduced in amplitude by a factor 10.

Negative values on the x-axis represent events where electrons reach 90% of the amplitude earlier, whereas positive values result from the hole collecting electrode reaching 90% amplitude at first. One can see that there is no symmetry with respect to the center of the crystal. Electrons are collected by channel B and holes by channel D. The maximum for equal rise times of electron and hole collection is at $\Delta t_{90} = 0$. Its z value is at $z = -2.5$ mm, shifted towards the side where holes are collected. At $z = 0$, the signal amplitude for hole collection reaches 90% amplitude ~ 300 ns later than the electron collecting channel. The
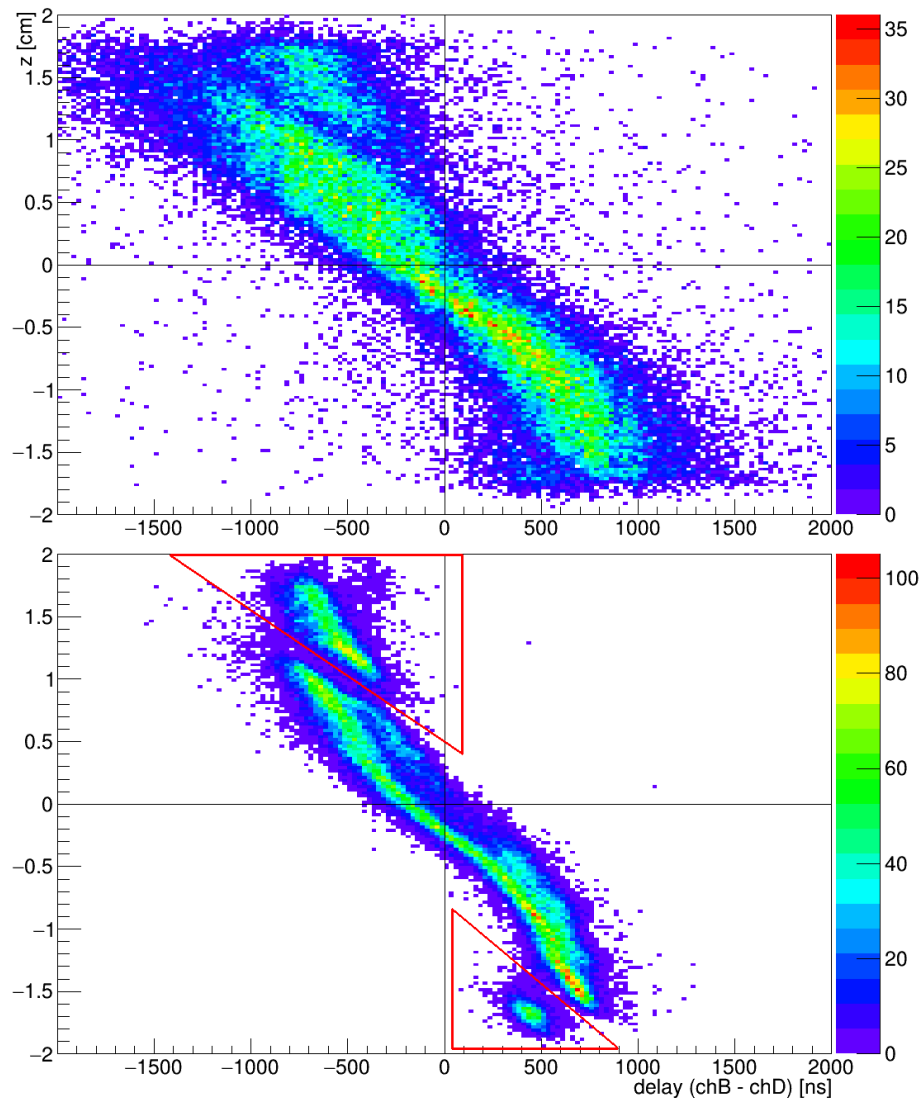
Figure 4.15: Two dimensional histogram showing z dependence of pulse shape $\Delta t = t_{90}(\text{ch}_B) - t_{90}(\text{ch}_D)$ for simulated fiducial events with real noise (top) and a noise amplitude reduced by a factor 10 (bottom). Marked areas are described in text and used for fig. 4.17.

drift velocity for electrons in ultra pure germanium detectors at mK temperatures in an electric field of 2 V/cm is $v_{e^-} = 3 \cdot 10^6$ cm/s [181]. The velocity for holes at the same parameters is $v_{h^+} = 2 \cdot 10^6$ cm/s [181].

For equal rise times $\Delta t_{90} = 0$ we can solve the linear system of equations

$$S_e = t_e \cdot v_e \qquad S_h = t_h v_h \qquad t_e = t_h \qquad S_e + S_h = 4 \text{ cm} \qquad (4.18)$$

in order to obtain the drifting distances for electrons and holes $S_{e,h}$. For electrons we find $S_e = 2.4$ cm which corresponds to an energy deposit at $z = -4$ mm The value $z = -2.5$ mm obtained from fig. 4.15 is smaller but still within the broad distribution. Based on the equation system 4.18 the drift distance for $\Delta t_{90} = 0$ depends on the ratio of v_h and v_e. Accordning to [181], this ratio is not precisely known. The error bars allow values of $v_e = (3 \pm 0.4) \cdot 10^6$ cm/s and $v_h = (2 \pm 0.2) \cdot 10^6$ cm/s. Furthermore, the drift velocities are measured in much smaller detectors with a mass of ~ 200 g. Here, they are consistently reproduced for the simulated events in the FID800 type detector.

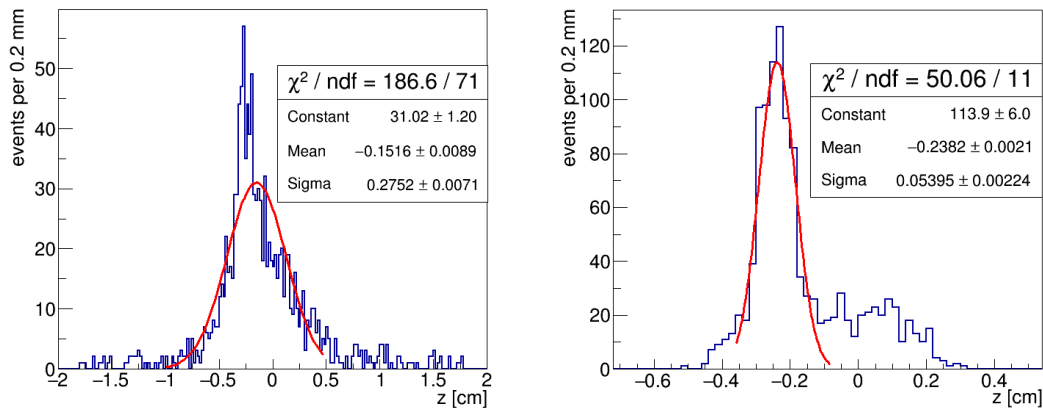### 4.4.4 Spatial resolution derived with time resolved pulses

Figure 4.16: Spatial resolution of time resolved channel with real noise (left) and fictive noise (right). Details in text.

The potential to obtain a spatial resolution in the z coordinate by comparing the rise time information was shown in fig. 4.15. A selection of fiducial events by eq. 4.16 and the requirement of $|\Delta t| = t_{90}(\text{ch}_B) - t_{90}(\text{ch}_D) \leq 25$ ns corresponds to a projection of the $\Delta t = 0$ line in fig. 4.15. The resulting 1d histogram is shown in fig. 4.16 for the simulated data with real noise (left) and fictive noise (right). The Gaussian fit yields a spatial resolution for the z-axis of

$$\Delta z = 0.28 \text{ cm} \tag{4.19}$$

for the simulated data with real noise. The potential of an improved 40 MHz readout hardware is estimated by the histogram showing the simulated data with fictive noise fig. 4.16(right). A resolution of

$$\Delta z = 0.05 \text{ cm} \tag{4.20}$$

is obtained. However, the red marked separated regions in fig. 4.15 constrain the possibility for spatial sensitivity for $|\Delta t| \gtrsim 400$ ns. Although this analysis is preliminary and a position-resolved cut would need more investigation, it demonstrates the potential of sub-mm spatial resolution along the z-axis of a cylindrical detector.

A separated region around $\Delta t \approx -500$ ns and $z > 1.1$ cm is visible in both data sets with real and fictive noise. A dedicated analysis has shown that the events belonging to the separated region do not differ in their spatial distribution along the radius from the events in the the main population (see bottom plot in fig. 4.17). This excludes explanations for instance by field anomalies for large r or at the edge of the cylindric detector. However, the events in the separated region differ in their rise time in the combined channel as shown in the top plot of fig 4.17. They have rise times larger than the events of the main population. Their contribution to the spectrum shown in fig. 4.14 is visible as a small feature at $t > 2000$ ns. The same holds for the second separated population around $\Delta t \approx +400$ ns and $z < -1.5$ cm.

A comparison of the spatial distributions with the experimental data can not be performed directly because of the unknown z variable in the experimental events. Therefore, an integration of $\Delta t_{90\%}$ for both MC and experimental populations is computed and shown in fig. 4.18. To enable comparability, the three histograms are normalized to an integral of 1. The experimental data and the simulated data with experimental noise are in a excellent agreement. The histogram of simulated pulses with optimistic noise conditions shows two maxima at $\Delta t_{90} = \pm 550$ ns, whereas around $\Delta t_{90} \approx 0$ all histograms are compatible. The simulated data with fictive noise have an obvious double-peak structure. Events
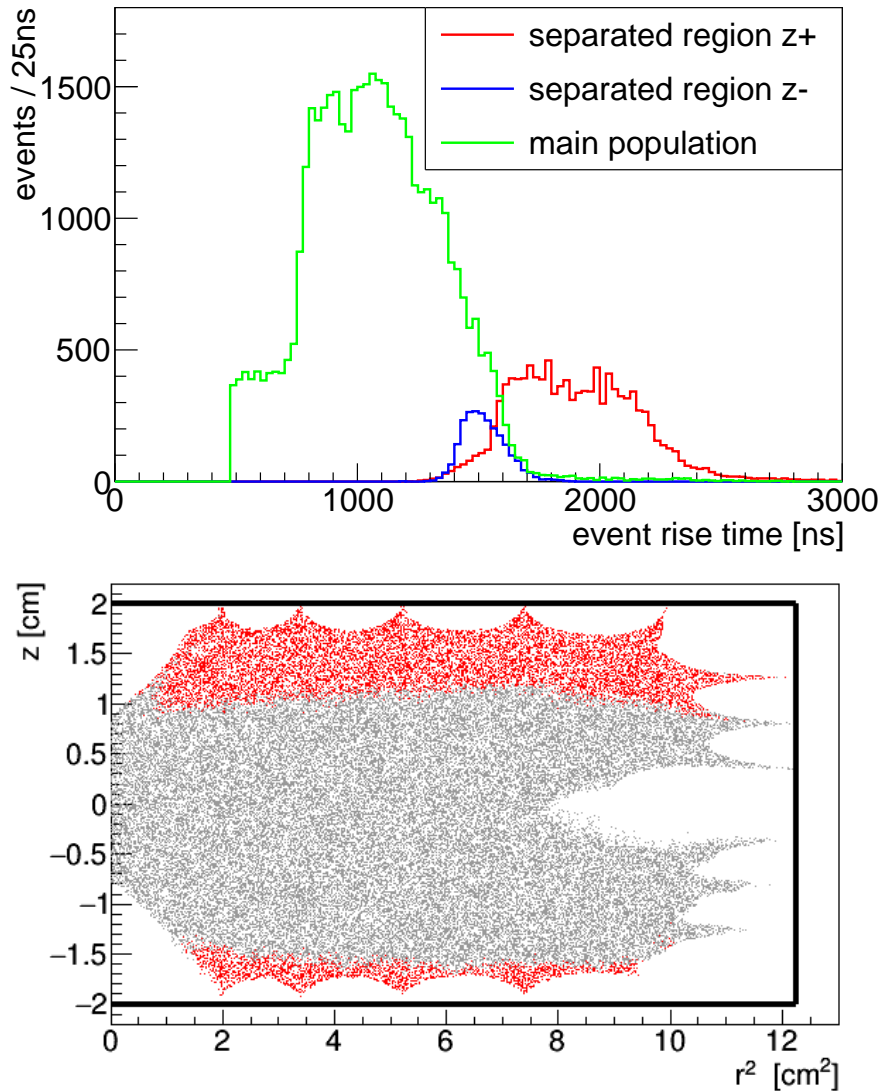
Figure 4.17: Investigation of the two separated groups marked in fig. 4.15. Both groups contribute to the upper end of the rise time spectrum and are uniformly distributed (red markers) along r^2 in the cross sectional view. Holes drift towards negative z.

with $|\Delta t_{90}| > 1000$ ns exist almost only in experimental data and simulated events with experimental noise. Thus, the widening of the distribution is caused by noise. Here, the two separated groups of fig. 4.15 constitute the two maxima.

In conclusion, the cuts based on the conventional variables (here without noise) have a better efficiency and a better rejection of events close to the surface. The comparison as it was presented has to be interpreted carefully, because the time resolved channel variables were modified with real experimental noise, whereas the reference group of simulated variables is noise free. Furthermore, because of the high noise level in the 40 MHz channel, events with energies below 100 keV cannot be analyzed at all, whereas with the conventional EDELWEISS ionization channels with 100 kHz digitization and software down sampling by software to 1 kHz, present baseline resolutions between 490 and 750 eV (FWHM), could be achieved which is about 100 times better. However, for events with larger ionization amplitudes of at least 100 keV the time resolved channel is an alternative for surface event rejection. The usability improves with higher amplitudes. It was shown that sub-millimeter resolution for the spatial z coordinate of events is achievable with a noise level reduced by
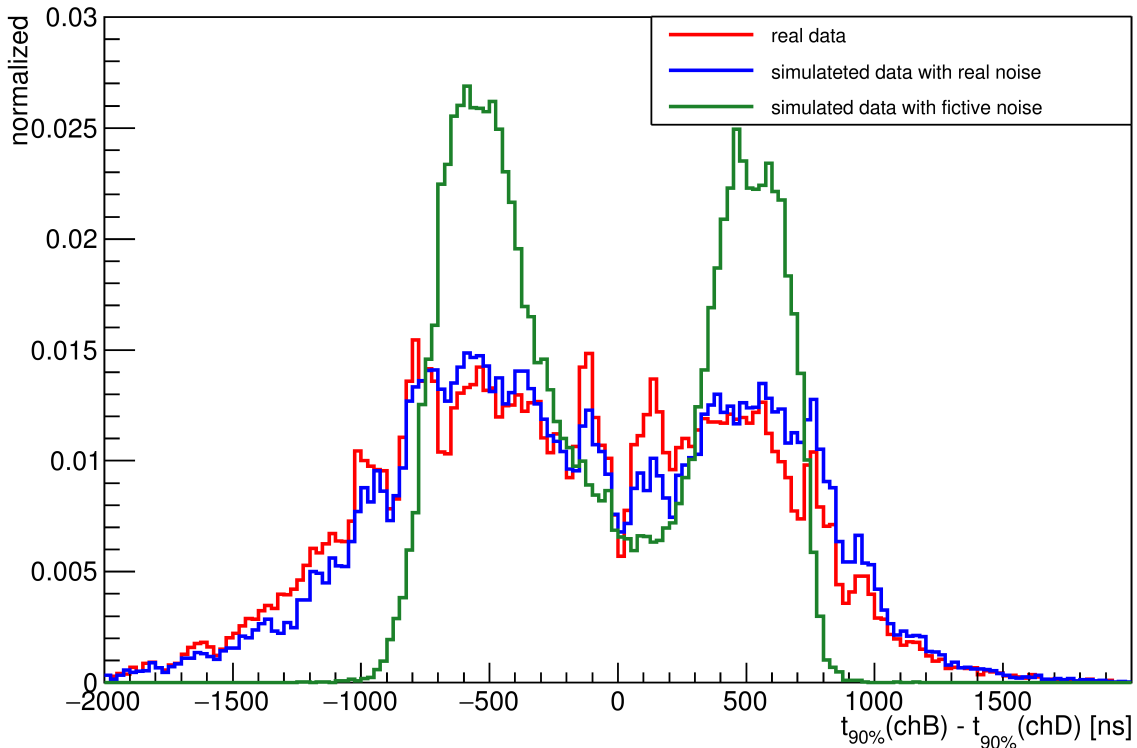
Figure 4.18: Normalized spectra of $\Delta t_{90\%}$. Real data of run 309 for ^{133}Ba (red), simulated events with real noise (blue) and simulated events with fictive noise, i.e. a factor 10 improved (green).

a factor 10.

4.5 Perspectives of time resolved ionization channels in EDEL-WEISS

Based on the obtained results, the time resolved channel represents an additional information which can be of particular interest for some individual events at high ionization energies. For instance the outlaying events in the figures 2.9 or 2.11 and 2.13 with recoil energies above 150 keV would be interesting to see as time resolved ionization pulses. However, these events are very rare. To find them, it is necessary to operate time resolved sampling on all detectors over the complete run time, which is not possible with the two prototype upgrades that exist as of now within EDELWEISS. Furthermore, the efficiency of the time resolved channel readout suffers from the heat modulation frequency. With the present rectangular modulation at a frequency of 500 Hz, 10% of all triggered events have to be discarded because they are too close to the transient region of the cross-talking modulation. This part of the efficiency scales directly with the modulation frequency, 250 Hz would cause a dead time of 5%, instead.

A future version of the hardware for the time resolved channels within the present bolometer box should be equipped with 14 bit or even 12 bit ADCs instead of 16 bit. This simplifies the hardware significantly, since 14 bit ADCs are available with more than two channels per chip. The signal quality would not suffer from a 2 bit reduction because the present noise level is in the order of 3-4 bit. Furthermore, the reduction of ADC resolution significantly reduces the power consumption and subsequently, the temperature inside the bolometer box. The saved power can be reinvested in a higher sampling frequency, for instance 60 MHz or even 100 MHz. We can see in fig. 4.10 that the EDELWEISS detectors register

fiducial events with rise times below 500 ns. With the current bandwidth of 40 MHz is one sample point represents 25 ns. A higher sampling rate would allow a finer binning in the rise time spectrum. A higher sampling rate results in a stretched FFT spectrum and allows a selection of single frequencies at a higher precision.

The number of channels is another point to rethink. For the analysis of charge migration and surface event rejection it would be much more efficient to have 4 channels instead of two. For instance the presented calibration in section 4.3.1 and especially visible in fig. 4.9 would benefit from a 4 channel readout which enables to correct the channel-to-channel cross talk. Nevertheless, applying surface event rejection based on the 100 kHz channels, a hardware with 2 time resolved channels, connected to the fiducial electrodes, is sufficient to acquire additional information on the discussed events with high energies close to the nuclear recoil band.

In the case of more outlaying events in the coming EDELWEISS results, it may be considered to install time resolved ionization channels on the full detector array. The additional work load by doing this is relatively small, since the new FPGA based DAQ supports the hardware trigger for all detectors. Within the framework of this thesis, scripts are existing to automatically set the trigger parameters for a moderate event rate. It was shown that the time resolved channels are not reliable for energies below ~ 100 keV, therefore an application with a trigger threshold of ~ 50 keV would reduce the number of events enormously but not affect the usability of the recorded data for the timing analysis. Since the energy resolution of the time resolved channels is far below the conventional EDELWEISS analysis, it would be sufficient to just record the time resolved pulses and analyze them only for particular interesting events, such as the outlaying events in the discussed plots. Even a calibration of the time resolved channels could be skipped, because the interesting parameters are the rise time and the pulse shape, whereas the true value of the amplitude is better extracted in the 100 kHz and 1 kHz channels. However, for this thesis the calibration was an important step to analyze the possible scope of the time resolved channel.

5. Conclusions and Outlook

This thesis was performed within the third phase of the EDELWEISS dark matter search experiment. The first experimental goal of EDELWEISS-III was to probe the parameter space for a spin-independent WIMP-nucleon scattering down to a cross-section of $\mathcal{O}(10^{-43}$ cm$^2)$ for standard mass WIMPs ($m_\chi \approx 50$ GeV) and $\mathcal{O}(10^{-41}$ cm$^2)$ for low-mass WIMPs ($m_\chi \approx 10$ GeV). To achieve this goal, up to 36 detectors were installed and simultaneously read out. Each detector is equipped with two heat channels for a calorimetric measurement of the total event energy, and four ionization channels for a measurement of the energy quenching between heat and ionization. This quenching measurement enables the discrimination of nuclear recoils and electron recoils. Furthermore, the geometrical setup of four groups of electrodes with different voltages enable the selection of fiducial events in the bulk volume of the crystal and a rejection of surface events for which the ionization charge collection may be incomplete and thus the energy measurement incorrect. All 216 channels are digitized in specifically developed boxes with a resolution of 16 bit and a sampling frequency of 100 kHz.

The enlarged EDELWEISS-III detector array requires a modern, scalable and reliable data acquisition system. This was not possible with the existing DAQ system from the EDELWEISS-II phase. Within the framework of this thesis, a new DAQ system was installed. It was developed at the institute IPE at the KIT and is based on a similar DAQ which is successfully used at the HEAT enhancement of the Piere Auger observatory and at the focal plane detector of the KATRIN neutrino mass experiment. This integrated DAQ was modified with dedicated input/output cards for the EDELWEISS requirements and is in use since January 2014. It features the integrated readout of external detectors such as the muon veto system. A stable time stamp is provided to synchronize all EDELWEISS components and external detectors to one global reference clock.

It was shown in experiments with EDELWEISS-type detectors that the pulse shape of ionization signals, especially the rise time, can be used to discriminate bulk and surface events. Typical rise times of ionization signals have values of < 3000 ns which can not be resolved with the conventional 100 kHz sampling rate. Therefore, a hardware upgrade with a prototype of two time resolved ionization channels sampling at 40 MHz was initiated for the EDELWEISS front end electronics. The FPGA design for this card was developed within the frame of this thesis, and one detector at the experimental site was equipped with these fast channels. A continuous data stream, as it is realized for all 100 kHz channels, is not a practicable option because the data rate of these cards (1280 MBit/s) exceeds the maximal performance of EDELWEISS-specific detector hardware (12 Mbit/s). Therefore,

an event based readout was introduced. FPGA based trigger units in the input/output cards of the new DAQ system detect ionization pulses and then initialize a readout procedure of a defined record length around the event. With typical event rates of < 50 mHz, the expected amount of triggered data is small and can be transmitted within the conventional readout stream. The event based readout is implemented in a way that works completely in parallel to the continuous stream of 100 kHz data of the conventional EDELWEISS readout. The trigger decision within the FPGA must be fast because of the limitations of memory in the digitization unit. In addition it must be precise in time, to cover the complete pulse trace. Furthermore, the trigger algorithm has to detect pulses with the shape of a Heavyside function, embedded into a rectangular pattern with a frequency of 500 Hz. Which arises from crosstalk of the heat channel modulation. The edges of the rectangular pattern look very similar to a physical pulse. Therefore, the FPGA has to recognize and reject the pattern to find the physical pulse. A cascaded trapezoidal filter performs both tasks (detailed in section 3.3.3 and figure 3.12). In a first stage, the pattern is subtracted and the channel integrated. We exploit the fact that the crosstalk pattern is originating from the electronics itself, thus having a precisely known phase and a very stable and known frequency. The shaping length of the filter is adopted to the length of the heat channel modulation, i.e. to the period of the crosstalk pattern. The filter response to a Heavy-side function is a triangular shaped pulse. A second stage of the same type of filter is applied to the output of the first stage. The triangular pulse is again integrated, transforming it into two parabola (almost sinusoidal). The FPGA detects therein the zero-crossing, which is systematically related to the time stamp of the event.

The trigger quality was extensively analyzed and compared to the conventional EDELWEISS analysis system. The results for event time stamps is shown in fig. 4.1, showing that the new DAQ system detects events systematically 32 μs later than the standard analysis. A fine tuning for the readout of the time resolved channel compensates this offset. The efficiency of the FPGA based trigger algorithm and its sensitivity is analyzed and compared with the EDELWEISS standard acquisition. The results are shown in fig. 4.2. The FPGA based trigger has a threshold at an ionization energy of 1.7 keV and it reaches a 50% efficiency at 3.1 keV. The efficiency between $\sim 7 - 20$ keV has a plateau of 94 % and is at 100 % for energies above 20 keV. The FPGA based trigger has never been optimized for reaching low thresholds. Therefore, a 50% efficiency at 3.1 keV is an excellent achievement as first implementation.

This low threshold is fully sufficient for recording of time-resolved channels: The peak to peak baseline noise of the time resolved ionization channels is ~ 400 keV. This could be improved to ~ 100 keV applying various filters. Nevertheless, due to this rather high noise level of ~ 100 keV, events with an ionization energy < 100 keV are ignored in the following analysis of time resolved pulses.

Since this is the first time within EDELWEISS that a second and independent readout path exists, it was possible to check the trigger efficiency of the conventional DAQ. This cross-check is described in section 4.1.2. The relative low efficiency derived for the standard readout system can be explained by the nature of the heat pulses. These pulses have a rise time of ~ 10 μs and a following decay of several 100 μs. The readout window for these pulses has a length of 2 s. Therefore, the low trigger efficiency has to be interpreted as a dead time effect of the readout, and not as a systematic non-recognition of events. When EDELWEISS results are presented, the exposure given in units of kg · days is corrected for this dead time.

In section 4.2, a detailed discussion of the data processing of the time resolved ionization channel is given. Systematic artifacts such as technically necessary FET resets of the analog readout part are detected and removed. This is performed with several python

based scripts that have been developed within this work. The time resolved ionization channels are calibrated to the 356 keV photopeak of a ^{133}Ba source. The calibration is crosschecked with the EDELWEISS standard analysis by comparing coincident events of the time resolved channel and the 100 kHz channel. The linearity of this calibration is presented in fig. 4.9. The small mismatch for fiducial events with energies above 1000 keV arises from the extrapolation of the 356 keV ^{133}Ba energy, which is about 6 times smaller. The clear difference of the calibration scale for surface events is explained by the fact that the (prototype) time resolved channel card supports only two channels, but the detector has four ionization channels. The so called veto channels are therefore not recorded. However, for surface events a large part of the signal is recorded on these electrodes. All electrodes of the detector have crosstalk with the others. A set of 12 parameters enables the correction which is possible if the amplitude of 4 electrodes is known. Since only two electrodes on the time resolved channels are available, such a cross-talk correction was not feasible. Despite having no veto electrode information in the fast channels it is possible to detect surface events with the time resolved channel by their asymmetric energy deposit on both collecting channels and on the time information.

We have defined the rise time of the time resolved ionization channels as the time in which the signal increases from 10% to 90% of the event amplitude. It is computed individually for both channels, and additionally for a combined signal taking the difference of both channels. In fact, since the pulses are bipolar, their norm adds up. The noise, originating from the power supply of the readout electronics is symmetrical and consequently it is significantly reduced. Thereby, the combined channel offers a much better signal to noise ratio and it refers to the complete event rise time. These complete event rise times are analyzed in a spectrum shown in fig. 4.10. A cut on the event rise time rejecting events in the Barium calibration with 425 ns removes 95% of all surface events while accepting 94.25% of fiducial events. The rejection is even better in the WIMP search mode, where a rise time cut of 450 ns leads to a rejection factor of surface events of

$$S_{\text{rejection}^{\text{surface}}} = 20 \tag{5.1}$$

while keeping an acceptance of 95.6% for fiducial events. However, this analysis is performed by accepting events with an ionization energy above 100 keV only. This very high energy regime resulted from the fact that the FWHM level in the time resolved ionization channel baseline is ~ 50 keV, whereas the conventional EDELWEISS ionization channels (with down sampling from 100 kHz to 1 kHz) have a FWHM of typically less than 1 keV.

A validation of the analysis of the time resolved channel was presented in section 4.4 by comparing the results with a charge migration simulation. Therefore, an FID800 type detector is modeled and 100.000 events are randomly started within the simulated electric potential. The electric field is computed by a finite element method following the Ramo theorem. The simulation computes the drifting of charge carriers within the electric field and the resulting induced charges in the ionization channel electrodes as a function of time. The time steps were selected equal to the sampling rate of the time resolved channel on the experimental site. The simulated events are then enhanced by adding noise as shown in fig. 4.13. Furthermore, a data set with an optimistic noise for a next generation hardware was computed. The data sets were then processed by the same algorithms and functions that have been applied to the experimental data. Since the start coordinates of the event within the detector are known for the simulations, spatial dependences, such as the discrimination into fiducial and surface events can be derived as shown in fig. 4.12. From particular interest is the potential to detect the z-coordinate of an energy deposit by analyzing and comparing the rise time of the charge collecting electrodes from both detector sides. This is shown in fig. 4.15 for the real noise and the fictive noise simulated

data. A spatial resolution of

$$\Delta z = 0.28 \text{ cm} \tag{5.2}$$

can be achieved with the given noise situation, whereas a z resolution of

$$\Delta z = 0.05 \text{ cm} \tag{5.3}$$

was derived for a potential next generation readout hardware with a signal to noise ratio increased by a factor 10. A comparison with the data recorded at the experiment shows an agreement between simulated data with real noise and real data (fig. 4.18).

During the detailed work with the EDELWEISS detector electronics, an upgrade of the bolometer boxes was developed to supply the detector electrodes with higher voltages of up to ± 70 V per electrode. This enables a total detector bias of up to 140 V. Within the work of this thesis we constructed a first prototype and after succesfully testing it, we upgraded 10 detectors to the higher voltages. The motivation for increasing the electrode voltage is the Neganov Trofimov Luke effect. Charges drifting in an electric field obtain energy of the field. Normally, EDELWEISS used small voltages of 8 V to reduce the influence of the Neganov-Luke effect. But newer approaches towards a low-mass WIMP sector require a reduced energy threshold. The Neganov-Luke effect is used as an amplification inside the detector. The heat energy is increased by adding energy during the drifting process with the increased electric field. The electronic upgrade and first results were presented in section 2.4. All EDELWEISS detectors were found to be capable of holding biases of 20 V in total, which is more than twice the usual voltage. Some detectors accept the full 140 V. The limiting effect for high bias operation seems to be a surface leakage current which strongly depends on the surface treatment of the detector. Multiple detectors with different electrode geometry, so called planar electrodes, are currently tested with the higher voltages. Furthermore, a passivated layer of silicon instead of germanium beneath the electrodes is under current investigation. First preliminary results with the higher voltages show a lowering of the online threshold down to ~ 50 eV (see fig. 2.24) which is more than ten times better than the value of 620 eV [128] in the most recent EDELWEISS publication. The heat FWHM improves to a value of < 100 eV which is three times better than the published values [128]. This is all preliminary and the current ongoing run is dedicated to further test the NTL amplified mode with different detectors. The detector operation at higher voltages will play a central role in germanium based searches for low-mass WIMPs.

For future detector readout electronics with a time resolved ionization channel, the entire readout electronics has to be optimized to avoid crosstalk and high frequency noise. In this work, the most disturbing component of noise is a 1.1 MHz (and all harmonics up to 20 MHz) oscillation caused by DC-DC voltage converters inside the detector readout units. These converters could be replaced by an external power supply system, placed far away from the detectors. This would also allow to have more space for the application of massive filters and less restrictions for the selection of materials. Another issue is the power dissipation of voltage converters. Currently, the detector readout units are cooled by a water cooling, because ventilators would induce to much vibrations. The bolometer boxes are mechanically connected to the cryostat, thus to the detectors where vibrations are a source of background. However, circulating water can be a source of vibrations as well. Without the DC-DC converters, the bolometer boxes could be operated without an active cooling.

Another optimization could be a lower energy resolution of the digitization unit in a time resolved ionization channel. With the situation found in this analysis, the noise level of the 16 bit channel was in the order of 100 keV i.e. the 4 LSB of the ADCs are just recording noise. Therefore, a downgrade to 14 bit or even 12 bit ADCs for a future time resolved channel can be considered. Such microchips are available with a lower power

consumption (less heat in the readout units) and the advantage of two or four channels integrated in one IC. In addition, higher sampling frequencies are as well possible with 14 bit ADCs. Especially for the pulse shape comparison as shown in figures 4.15 and 4.18 a higher sampling rate could bring a significant improvement.

The trend to use germanium detectors for probing the low-mass WIMP sector by increasing the detector voltages motivates a future front end electronic with the built in functionality of providing higher detector voltages. The upgrade that we presented in section 2.4 is limited to ± 70 V. Currently no operational amplifier is available with a wider output dynamic (rail-to-rail) than this. Here, the same argument counts as for the DC-DC converters: there is no reason to control the detector biasing voltage inside the readout units. It could be outsourced to a larger and better device, whereas the bolometer box would fulfill only digitization tasks and the controlling of low-voltage signals, such as relays and FET baseline corrections.

Bibliography

[1] Planck Collaboration, et al., "Planck 2015 results. XIII. Cosmological parameters", arXiv, 1502.01589 (2015) `10.1007/s13398-014-0173-7.2` (cit. on pp. 1, 3, 10, 11).

[2] F. Zwicky, "Die Rotverschiebung von extragalaktischen Nebeln", Helvetica Physica Acta **6**, 110–127 (1933) `10.5169/seals-110267` (cit. on p. 8).

[3] F. Zwicky, "On the Masses of Nebulae and of Clusters of Nebulae", The Astrophysical Journal **86**, 217 (1937) `10.1086/143864` (cit. on p. 8).

[4] G. Bertone, and D. Hooper, "A History of Dark Matter", 1–88 (2016) (cit. on pp. 8, 9).

[5] D. Clowe, et al., "A Direct Empirical Proof of the Existence of Dark Matter", The Astrophysical Journal **648**, 109–113 (2006) `10.1086/508162` (cit. on pp. 8, 9).

[6] S. W. Randall, et al., "Constraints on the Self-Interaction Cross Section of Dark Matter from Numerical Simulations of the Merging Galaxy Cluster 1E $0657 - 56$", The Astrophysical Journal **679**, 1173–1180 (2008) `10.1086/587859` (cit. on p. 9).

[7] M. Bradac, et al., "Revealing the Properties of Dark Matter in the Merging Cluster MACS $J00254 - 1222$", The Astrophysical Journal **687**, 959–967 (2008) `10.1086/591246` (cit. on p. 9).

[8] M. J. Jee, et al., "HUBBLE SPACE TELESCOPE /ADVANCED CAMERA FOR SURVEYS CONFIRMATION OF THE DARK SUBSTRUCTURE IN A520", The Astrophysical Journal **783**, 78 (2014) `10.1088/0004-637X/783/2/78` (cit. on p. 9).

[9] Y. Sofue, and V. Rubin, "Rotation Curves of Spiral Galaxies", Annual Review of Astronomy and Astrophysics **39**, 137–174 (2001) `10.1146/annurev.astro.39.1.137` (cit. on p. 9).

[10] E. Corbelli, and P. Salucci, "The Extended Rotation Curve and the Dark Matter Halo of M33", **447** (1999) `10.1046/j.1365-8711.2000.03075.x` (cit. on p. 9).

[11] V. C. Rubin, and J. Ford, W. Kent, "Rotation of the Andromeda Nebula from a Spectroscopic Survey of Emission Regions", The Astrophysical Journal **159**, 379 (1970) `10.1086/150317` (cit. on p. 9).

[12] J. F. Navarro, C. S. Frenk, and S. D. M. White, "The Structure of Cold Dark Matter Halos", The Astrophysical Journal **462**, 563 (1996) `10.1086/177173` (cit. on p. 9).

[13] J. Einasto, "Kinematics and dynamics of stellar systems", Astrofiz. Alma-Ata **51**, 87 (1965) (cit. on p. 10).

[14] D. Merritt, et al., "Empirical Models for Dark Matter Halos. I. Nonparametric Construction of Density Profiles and Comparison with Parametric Models", The Astronomical Journal **132**, 2685–2700 (2006) `10.1086/508988` (cit. on p. 10).

[15] Y. Sofue, "Grand Rotation Curve and Dark-Matter Halo in the Milky Way Galaxy", Publications of the Astronomical Society of Japan **64**, 75 (2012) `10.1093/pasj/64.4.75` (cit. on p. 10).

[16] F. Iocco, M. Pato, and G. Bertone, "Evidence for dark matter in the inner Milky Way", Nature Physics **11**, 245–248 (2015) `10.1038/nphys3237` (cit. on p. 10).

[17] J. I. Read, "The local dark matter density", Journal of Physics G: Nuclear and Particle Physics **41**, 063101 (2014) `10.1088/0954-3899/41/6/063101` (cit. on p. 10).

[18] R. A. Alpher, H. Bethe, and G. Gamow, "On the origin of the chemical elements", Physical Review **73**, 803–804 (1948) `10.1007/BF01005949` (cit. on p. 10).

[19] A. A. Penzias, and R. W. Wilson, "A Measurement of Excess Antenna Temperature at 4080 Mc/s.", The Astrophysical Journal **142**, 419 (1965) `10.1086/148307` (cit. on p. 10).

[20] D. J. Fixsen, "THE TEMPERATURE OF THE COSMIC MICROWAVE BACK-GROUND", The Astrophysical Journal **707**, 916–920 (2009) `10.1088/0004-637X/707/2/916` (cit. on p. 10).

[21] A. Benoît, et al., "Archeops: A high resolution, large sky coverage balloon experiment for mapping cosmic microwave background anisotropies", Astroparticle Physics **17**, 101–124 (2002) `10.1016/S0927-6505(01)00141-4` (cit. on pp. 10, 37).

[22] P. de Bernardis, et al., "A flat Universe from high-resolution maps of the cosmic microwave background radiation", Nature **404**, 955–9 (2000) `10.1038/35010035` (cit. on p. 10).

[23] E. L. Wright, et al., "Angular Power Spectrum of the Cosmic Microwave Background Anisotropy seen by the COBE DMR", Astrophysical Journal Letters v.464 **464**, L21 (1996) (cit. on p. 10).

[24] D. Larson, et al., "SEVEN-YEAR WILKINSON MICROWAVE ANISOTROPY PROBE (WMAP) OBSERVATIONS: POWER SPECTRA AND WMAP -DERIVED PARAM-ETERS", The Astrophysical Journal Supplement Series **192**, 16 (2011) `10.1088/0067-0049/192/2/16` (cit. on p. 10).

[25] Planck Collaboration, et al., "Planck 2015 results. I. Overview of products and scientific results", Astronomy & Astrophysics (2015) `10.1051/0004-6361/201321529` (cit. on p. 10).

[26] X. Huang, G. Vertongen, and C. Weniger, "Probing dark matter decay and annihilation with Fermi LAT observations of nearby galaxy clusters", Journal of Cosmology and Astroparticle Physics **2012**, 042–042 (2012) `10.1088/1475-7516/2012/01/042` (cit. on p. 11).

[27] M. G. Baring, et al., "New limits on the dark matter lifetime from dwarf spheroidal galaxies using Fermi-LAT", Physical Review D **93**, 103009 (2016) `10.1103/PhysRevD.93.103009` (cit. on p. 11).

[28] L. Chuzhoy, and E. W. Kolb, "Reopening the window on charged dark matter", Journal of Cosmology and Astroparticle Physics **2009**, 014–014 (2008) `10.1088/1475-7516/2009/07/014` (cit. on p. 11).

[29] A. Kamada, et al., "Effects of electrically charged dark matter on cosmic microwave background anisotropies", (2016) (cit. on p. 11).

[30] C. Frenk, and S. White, "Dark matter and cosmic structure", Annalen der Physik **524**, 507–534 (2012) `10.1002/andp.201200212` (cit. on p. 12).

[31] H. Baer, et al., "Dark matter production in the early Universe: Beyond the thermal WIMP paradigm", Physics Reports **555**, 1–60 (2015) `10.1016/j.physrep.2014.10.002` (cit. on p. 12).

[32] D. Boncioli, et al., "Surprises from extragalactic propagation of UHECRs", Nuclear Physics B - Proceedings Supplements **00**, 1–5 (2015) (cit. on pp. 12, 20).

[33] M. A. Shifman, A. I. Vainshtein, and V. I. Zakharov, "Can confinement ensure natural CP invariance of strong interactions?", Nuclear Physics, Section B **166**, 493–506 (1980) `10.1016/0550-3213(80)90209-6` (cit. on p. 12).

[34] M. Dine, W. Fischler, and M. Srednicki, "A simple solution to the strong CP problem with a harmless axion", Physics Letters B **104**, 199–202 (1981) `10.1016/0370-2693(81)90590-6` (cit. on p. 12).

[35] K. Abazajian, G. M. Fuller, and M. Patel, "Sterile neutrino hot, warm, and cold dark matter", Physical Review D **64** (2001) `10.1103/PhysRevD.64.023501` (cit. on p. 13).

[36] F. P. An, et al., "Search for a Light Sterile Neutrino at Daya Bay", Physical Review Letters **113**, 141802 (2014) `10.1103/PhysRevLett.113.141802` (cit. on p. 13).

[37] P. B. Pal, and L. Wolfenstein, "Radiative decays of massive neutrinos", Physical Review D **25**, 766–773 (1982) `10.1103/PhysRevD.25.766` (cit. on p. 13).

[38] A. Boyarsky, et al., "Unidentified line in X-ray spectra of the andromeda galaxy and perseus galaxy cluster", Physical Review Letters **113**, 1–6 (2014) `10.1103/PhysRevLett.113.251301` (cit. on p. 13).

[39] P. Bareyre, et al., "Limits on the Macho Content of the Galactic Halo from the EROS-2 Survey of the Magellanic Clouds", Astronomy & Astrophysics (2011) (cit. on p. 13).

[40] C. Alcock, R. Allsman, and D. Alves, "The MACHO project: microlensing results from 5.7 years of large magellanic cloud observations", The Astrophysical Journal (2000) (cit. on p. 13).

[41] J. L. Feng, "Dark Matter Candidates from Particle Physics and Methods of Detection", Annual Review of Astronomy and Astrophysics **48**, 495–545 (2010) `10.1146/annurev-astro-082708-101659` (cit. on p. 13).

[42] H. Nishino, et al., "Search for proton decay via p→e+π0 and p→μ+π0 in a large water cherenkov detector", Physical Review Letters **102**, 2–6 (2009) `10.1103/PhysRevLett.102.141801` (cit. on p. 13).

[43] S. P. Martin, "A Supersymmetry Primer", arXiv, 152 (1997) `10.1142/9789814307505_0001` (cit. on p. 14).

[44] M. Klasen, M. Pohl, and G. Sigl, "Indirect and direct search for dark matter", Progress in Particle and Nuclear Physics **85**, 1–32 (2015) `10.1016/j.ppnp.2015.07.001` (cit. on p. 14).

[45] D. Williams, "Earth Fact Sheet", NASA Goddard Space Flight Center (2016) (cit. on p. 14).

[46] K. Freese, and J. Frieman, "Signal modulation in cold-dark-matter detection", Physical Review D **37**, 3388–3405 (1988) `10.1103/PhysRevD.37.3388` (cit. on p. 14).

[47] T. Piffl, et al., "The RAVE survey: the Galactic escape speed and the mass of the Milky Way", Astronomy & Astrophysics **562**, A91 (2014) `10.1051/0004-6361/201322531` (cit. on p. 15).

[48] T. M. Undagoitia, and L. Rauch, "Dark matter direct-detection experiments", Journal of Physics G: Nuclear and Particle Physics **43**, 013001 (2016) `10.1088/0954-3899/43/1/013001` (cit. on p. 16).

[49] K. Abe, et al., "XMASS detector", Nuclear Instruments and Methods in Physics Research, Section A: Accelerators, Spectrometers, Detectors and Associated Equipment **716**, 78–85 (2013) `10.1016/j.nima.2013.03.059` (cit. on p. 16).

[50] M. Batygov, et al., "DEAP-3600 Dark Matter Search", **00**, 1–7 (2015) (cit. on p. 16).

[51]P. Agnes, et al., "Results from the first use of low radioactivity argon in a dark matter search", Physical Review D - Particles, Fields, Gravitation and Cosmology **93**, 1–7 (2016) `10.1103/PhysRevD.93.081101` (cit. on p. 16).

[52]E. Aprile, et al., "The XENON100 dark matter experiment", Astroparticle Physics **35**, 573–590 (2012) `10.1016/j.astropartphys.2012.01.003` (cit. on p. 16).

[53] XENON Collaboration, et al., "Lowering the radioactivity of the photomultiplier tubes for the XENON1T dark matter experiment", European Physical Journal C **75**, 1–10 (2015) `10.1140/epjc/s10052-015-3657-5` (cit. on p. 16).

[54]D. N. McKinsey, et al., "The LUX dark matter search", Journal of Physics: Conference Series **203**, 012026 (2010) `10.1088/1742-6596/203/1/012026` (cit. on p. 16).

[55] The LZ Collaboration, et al., "LUX-ZEPLIN (LZ) Conceptual Design Report", (2015) (cit. on p. 16).

[56]C. Amole, et al., "Dark Matter Search Results from the PICO-2L C3 F8 Bubble Chamber", Physical Review Letters **114**, 1–14 (2015) `10.1103/PhysRevLett.114.231302` (cit. on p. 17).

[57]R. Agnese, et al., "Search for Low-Mass Weakly Interacting Massive Particles with SuperCDMS", Physical Review Letters **112**, 241302 (2014) `10.1103/PhysRevLett.112.241302` (cit. on pp. 17, 50).

[58]G. Angloher, et al., "Results on light dark matter particles with a low-threshold CRESST-II detector", The European Physical Journal C **76**, 25 (2016) `10.1140/epjc/s10052-016-3877-3` (cit. on pp. 17, 50).

[59]G. Angloher, et al., "Commissioning run of the CRESST-II dark matter search", Astroparticle Physics **31**, 270–276 (2009) `10.1016/j.astropartphys.2009.02.007` (cit. on p. 17).

[60]K. E. Schneck, "Search for Low-Mass Dark Matter With Supercdms Soudan and Study of Shorted Electric Field Configurations in CDMS Detectors", PhD (STANFORD UNIVERSITY, 2015) (cit. on p. 17).

[61]V. Khachatryan, et al., "Search for dark matter, extra dimensions, and unparticles in monojet events in proton–proton collisions at $\sqrt{s} = 8$ TeV", European Physical Journal C **75** (2015) `10.1140/epjc/s10052-015-3451-4` (cit. on p. 19).

[62]M. De Naurois, "The Galactic Sky seen by H.E.S.S.", Advances in Space Research **51**, 258–267 (2013) `10.1016/j.asr.2011.04.009` (cit. on p. 19).

[63]M. Doro, et al., "Dark matter and fundamental physics with the Cherenkov Telescope Array", Astroparticle Physics **43**, 189–214 (2013) `10.1016/j.astropartphys.2012.08.002` (cit. on p. 19).

[64]R. G. Wagner, and f. t. V. Collaboration, "Indirect Dark Matter Searches with VERITAS", eprint arXiv **0910**, 4563 (2009) (cit. on p. 19).

[65]B. Kyae, and J. C. Park, "130 GeV Fermi gamma-ray line from dark matter decay", Physics Letters, Section B: Nuclear, Elementary Particle and High-Energy Physics **718**, 1425–1429 (2013) `10.1016/j.physletb.2012.12.041` (cit. on p. 19).

[66]A. Hektor, M. Raidal, and E. Tempel, "Fermi-LAT gamma-ray signal from Earth limb, systematic detector effects and their implications for the 130 GeV gamma-ray excess", European Physical Journal C **73**, 1–9 (2013) `10.1140/epjc/s10052-013-2578-4` (cit. on p. 19).

[67]V. Barger, et al., "PAMELA and dark matter", Physics Letters, Section B: Nuclear, Elementary Particle and High-Energy Physics **672**, 141–146 (2009) `10.1016/j.physletb.2009.01.016` (cit. on p. 19).

[68] G. Giesen, "AMS-02 antiprotons, at last! Secondary astrophysical component and immediate implications for Dark Matter", Journal of Cosmology and Astroparticle Physics **2015**, 12 (2015) `10.1088/1475-7516/2015/09/023` (cit. on p. 19).

[69] M. G. Aartsen, et al., "Search for dark matter annihilations in the sun with the 79-string icecube detector", Physical Review Letters **110**, 1–7 (2013) `10.1103/PhysRevLett.110.131302` (cit. on p. 20).

[70] A. Broniatowski, et al., "A new high-background-rejection dark matter Ge cryogenic detector", Physics Letters, Section B: Nuclear, Elementary Particle and High-Energy Physics **681**, 305–309 (2009) `10.1016/j.physletb.2009.10.036` (cit. on pp. 21, 58, 74, 106).

[71] C. Berger, and E. al., "Experimental study of muon bundles observed in the Frejus detector", Physical Review D - Particles, Fields, Gravitation and Cosmology **40**, 2163 (1989) `10.1119/1.1975329` (cit. on p. 21).

[72] D.-M. Mei, and A. Hime, "Muon-induced background study for underground laboratories", Physical Review D **73**, 053004 (2006) `10.1103/PhysRevD.73.053004` (cit. on p. 21).

[73] B. Schmidt, et al., "Muon-induced background in the EDELWEISS dark matter search", Astroparticle Physics **44**, 28–39 (2013) `10.1016/j.astropartphys.2013.01.014` (cit. on pp. 21, 23).

[74] E. Armengaud, et al., "Background studies for the EDELWEISS dark matter experiment", Astroparticle Physics **47**, 1–9 (2013) `10.1016/j.astropartphys.2013.05.004` (cit. on pp. 22, 24, 25, 44).

[75] J. Reichenbacher, "Untersuchung der optischen Eigenschaften grossflächiger Plastikszintillatoren für den KARMEN-Upgrade", Ph.D. (Forschungszentrum Karlsruhe GmbH, 1998) (cit. on p. 23).

[76] C. Kéfélian, "Search for dark matter with EDELWEISS-III excluding background from muon-induced neutrons", PhD (Université Claude Bernard Lyon and Karlsruher Institut für Technologie, 2016), p. 184 (cit. on pp. 23, 45, 48, 66, 83).

[77] H. M. Kluck, "Measurement of the cosmic-induced neutron yield at the Modane underground laboratory", PhD thesis (2013) (cit. on pp. 24, 32, 66).

[78] V. Kozlov, et al., "A detection system to measure muon-induced neutrons for direct dark matter searches", Astroparticle Physics **34**, 97–105 (2010) `10.1016/j.astropartphys.2010.06.001` (cit. on pp. 24, 32).

[79] V. Chazal, et al., "Neutron background measurements in the Underground Laboratory of Modane", Astroparticle Physics **9**, 163–172 (1998) `10.1016/S0927-6505(98)00012-7` (cit. on p. 24).

[80] S. Rozov, et al., "Monitoring of the thermal neutron flux in the LSM underground laboratory", Arxiv preprint arXiv:1001.4383 (2010) (cit. on p. 24).

[81] AURUBIS, *NOSV copper www.aurubis.com*, 2016 (cit. on p. 25).

[82] M. Laubenstein, et al., "Underground measurements of radioactivity", Applied Radiation and Isotopes **61**, 167–172 (2004) `10.1016/j.apradiso.2004.03.039` (cit. on p. 25).

[83] EDELWEISS Collaboration, "Performance of the EDELWEISS-III array for the direct search of dark matter", Article in preparation (2016) (cit. on pp. 26, 43, 48, 103).

[84] E. Haller, "Physics and design of advanced IR bolometers and photoconductors", Infrared Physics **25**, 257–266 (1985) `10.1016/0020-0891(85)90088-0` (cit. on p. 26).

[85] S. Mathimalar, et al., "Characterization of Neutron Transmutation Doped (NTD) Ge for low temperature sensor development", Nuclear Instruments and Methods in Physics Research Section B: Beam Interactions with Materials and Atoms **345**, 33–36 (2015) `10.1016/j.nimb.2014.12.020` (cit. on p. 26).

[86] C. Nones, "Characterization of EDW thermistors from wafer 38B", Internal Presentation (2012) (cit. on p. 26).

[87] J. Billard, et al., "Characterization and optimization of EDELWEISS-III FID800 heat signals", Journal of Low Temperature Physics, 1–8 (2016) `10.1007/s10909-016-1500-5` (cit. on pp. 27, 36).

[88] P. Flubacher, a. J. Leadbetter, and J. a. Morrison, "The heat capacity of pure silicon and germanium and properties of their vibrational frequency spectra", Philosophical Magazine **4**, 273–294 (1959) `10.1080/14786435908233340` (cit. on p. 27).

[89] M. Piat, et al., "Modelling and Optimizing of High Sensitivity Semiconducting Thermistors at Low Temperature", Journal of Low Temperature Physics **125**, 189–203 (2001) `10.1023/A:1012911722522` (cit. on p. 27).

[90] M. Unrau, "Kalibration eines EDELWEISS Ge-Bolometers mit unterschiedlichen Filtermethoden zur Extraktion von Signalpulsen", Diploma Thesis (Karlsruhe Institute of Technology, 2012) (cit. on p. 27).

[91] R. Pehl, et al., "Accurate Determination of the Ionization Energy in Semiconductor Detectors", Nuclear Instruments and Methods **59**, 45–55 (1968) (cit. on p. 28).

[92] P. N. Luke, "Voltage-assisted calorimetric ionization detector", Journal of Applied Physics **64**, 6858–6860 (1988) `10.1063/1.341976` (cit. on pp. 28, 51).

[93] R. C. Alig, "Scattering by ionization and phonon emission in semiconductors", Physical Review B **27**, 968–977 (1983) `10.1103/PhysRevB.27.968` (cit. on p. 28).

[94] K. W. Jones, and H. W. Kraner, "Stopping of 1- to 1.8-kev 73Ge Atoms in Germanium", Physical Review C **4**, 125–129 (1971) `10.1103/PhysRevC.4.125` (cit. on p. 29).

[95] Y. Messous, et al., "Calibration of a Ge crystal with nuclear recoils for the development of a dark matter detector", Astroparticle Physics **3**, 361–366 (1995) `10.1016/0927-6505(95)00007-4` (cit. on p. 29).

[96] X. Ruan, "Nuclear recoil quenching factor measurement for HPGe detector", Presentation at conference **Peking** (2011) (cit. on p. 29).

[97] C. E. Aalseth, et al., "CoGeNT: A search for low-mass dark matter using p-type point contact germanium detectors", Physical Review D - Particles, Fields, Gravitation and Cosmology **88**, 1–20 (2013) `10.1103/PhysRevD.88.012002` (cit. on pp. 29, 30).

[98] J. Lindhard, V. Nielsen, and M. Scharff, "Approximation Metho D in Classical Scattering B Y", Matematisk-fysiske Meddelelser **36** (1968) (cit. on p. 29).

[99] O. Martineau, et al., "Calibration of the EDELWEISS cryogenic heat-and-ionization germanium detectors for dark matter search", Nuclear Instruments and Methods in Physics Research, Section A: Accelerators, Spectrometers, Detectors and Associated Equipment **530**, 426–439 (2004) `10.1016/j.nima.2004.04.218` (cit. on pp. 29, 31).

[100] T. Shutt, et al., "A solution to the dead-layer problem in ionization and phonon-based dark matter detectors", Nuclear Instruments and Methods in Physics Research Section A: Accelerators, Spectrometers, Detectors and Associated Equipment **444**, 340–344 (2000) `10.1016/S0168-9002(99)01379-0` (cit. on p. 30).

[101] V. Mandic, et al., "Study of the dead layer in germanium for the CDMS detectors", Nuclear Instruments and Methods in Physics Research Section A: Accelerators, Spectrometers, Detectors and Associated Equipment **520**, 171–174 (2004) `10.1016/j.nima.2003.11.285` (cit. on p. 30).

[102]S. Marnieros, et al., "Controlling the Leakage-Current of Low Temperature Germanium Detectors Using XeF2 Dry Etching", Journal of Low Temperature Physics **176**, 182–187 (2014) `10.1007/s10909-013-0997-0` (cit. on p. 30).

[103]W. Shockley, "Currents to Conductors by a Moving Point Charge", Journal of Applied Physics **9**, 635–636 (1938) (cit. on pp. 30, 102).

[104]S. Ramo, "Currents Induced by Electron Motion", Proceedings of the IRE **27**, 584–585 (1939) `10.1109/JRPROC.1939.228757` (cit. on pp. 30, 102).

[105]Z. He, "Review of the Shockley–Ramo theorem and its application in semiconductor gamma-ray detectors", Nuclear Instruments and Methods in Physics Research Section A: Accelerators, Spectrometers, Detectors and Associated Equipment **463**, 250–267 (2001) `10.1016/S0168-9002(01)00223-6` (cit. on p. 31).

[106]E. Armengaud, et al., "Final results of the EDELWEISS-II WIMP search using a 4-kg array of cryogenic germanium detectors with interleaved electrodes", Physics Letters B **702**, 329–335 (2011) `10.1016/j.physletb.2011.07.034` (cit. on pp. 31, 32).

[107]Z. Ahmed, et al., "Combined limits on WIMPs from the CDMS and EDELWEISS experiments", Physical Review D **84**, 011102 (2011) `10.1103/PhysRevD.84.011102` (cit. on p. 32).

[108]E. Armengaud, et al., "Axion searches in the EDELWEISS-II experiment", Journal of Cosmology and Astroparticle Physics **2013**, 067–067 (2013) `10.1088/1475-7516/2013/11/067` (cit. on p. 32).

[109]A. Juillard, "Status and Prospects of the EDELWEISS Direct WIMP Search Experiment", Journal of Low Temperature Physics **167**, 1056–1062 (2012) `10.1007/s10909-012-0512-z` (cit. on pp. 33, 36).

[110]J. Gascon, and N. Bastidon, "The EDELWEISS-III Project and the Rejection Performance of Its Cryogenic Germanium Detectors", Journal of Low Temperature Physics **176**, 870–875 (2014) `10.1007/s10909-014-1096-6` (cit. on pp. 34, 35).

[111] EDELWEISS, "Synoptique_BBv3", internal document (2013) (cit. on pp. 37, 38).

[112]S. Gaertner, et al., "A new readout system for bolometers with improved low frequency stability", Astronomy and Astrophysics Supplement Series **126**, 151–160 (1997) `10.1051/aas:1997256` (cit. on p. 37).

[113]J. M. Lamarre, et al., "The Planck High Frequency Instrument, a third generation CMB experiment, and a full sky submillimeter survey", New Astronomy Reviews **47**, 1017–1024 (2003) `10.1016/j.newar.2003.09.006` (cit. on p. 37).

[114] InterFET Corporation, *IF860 Dual N-Channel Silicon Junction Field-Effect Transistor*, 1999 (cit. on pp. 37, 39).

[115] InterFET Corporation, *IF1320 N-Channel Silicon Junction Field-Effect Transistor*, 2004 (cit. on p. 38).

[116]A. Gullasch, "Charakterisierung des Rauschspektrums der Ausleseelektronik für das EDELWEISS-III Experiment", Bachelor Thesis (Karlsruhe Institute of Technology, 2015) (cit. on p. 39).

[117]X. Zhang, "Cold Cabling Developments", Internal Presentation (2013) (cit. on p. 40).

[118]X. Zhang, "Laminated Cabling – A Status Report", internal Presentation (2014) (cit. on p. 40).

[119] LinearTechnology, *LT1941 - Triple Monolithic Switching Regulator*, tech. rep. (), pp. 1–24 (cit. on p. 41).

[120] A. S. Barabash, et al., "Enriched Zn100MoO4 scintillating bolometers to search for $0\nu2\beta$ decay of 100Mo with the LUMINEU experiment", The European Physical Journal C **74**, 3133 (2014) `10.1140/epjc/s10052-014-3133-7` (cit. on pp. 43, 60).

[121] W. B. Wilson, et al., "Sources: A code for calculating (alpha, n), spontaneous fission, and delayed neutron sources and spectra", Progress in Nuclear Energy **51**, 608–613 (2009) `10.1016/j.pnucene.2008.11.007` (cit. on p. 44).

[122] S. Agostinelli, et al., "GEANT4 - A simulation toolkit", Nuclear Instruments and Methods in Physics Research, Section A: Accelerators, Spectrometers, Detectors and Associated Equipment **506**, 250–303 (2003) `10.1016/S0168-9002(03)01368-8` (cit. on p. 44).

[123] J. Allison, et al., "Geant4 developments and applications", IEEE Transactions on Nuclear Science **53**, 270–278 (2006) `10.1109/TNS.2006.869826` (cit. on p. 44).

[124] S. Scorza, "Background investigation in EDELWEISS-III", in Aip conf. proc. (2015), p. 100002, `10.1063/1.4928002` (cit. on pp. 44, 45).

[125] B. Schmidt, "Background discrimination of EDELWEISS-III cryogenic Ge-detectors for dark matter search", PhD thesis (Karlsruhe Institut of Technology, 2015) (cit. on pp. 47, 95).

[126] Y. Khazov, A. Rodionov, and F. Kondev, "Nuclear Data Sheets for A = 133", Nuclear Data Sheets **112**, 855–1113 (2011) `10.1016/j.nds.2011.03.001` (cit. on p. 48).

[127] T. de Boissière, "Low mass WIMPs and axion searches with the EDELWEISS experiment", PhD (Université Paris-Sud, 2015) (cit. on p. 49).

[128] E. Armengaud, et al., "Constraints on low-mass WIMPs from the EDELWEISS-III dark matter search", Journal of Cosmology and Astroparticle Physics **2016**, 019–019 (2016) `10.1088/1475-7516/2016/05/019` (cit. on pp. 49, 50, 55, 116).

[129] C. E. Aalseth, et al., "Results from a search for light-mass dark matter with a p-type point contact Germanium detector", Physical Review Letters **106**, 1–4 (2011) `10.1103/PhysRevLett.106.131301` (cit. on p. 50).

[130] R. Agnese, et al., "Silicon detector dark matter results from the final exposure of CDMS II", Physical Review Letters **111**, 1–6 (2013) `10.1103/PhysRevLett.111.251301` (cit. on p. 50).

[131] G. Angloher, et al., "Results from 730 kg days of the CRESST-II Dark Matter search", European Physical Journal C **72**, 1–22 (2012) `10.1140/epjc/s10052-012-1971-8` (cit. on p. 50).

[132] R. Bernabei, et al., "Final model independent result of DAMA/LIBRA-phase1", European Physical Journal C **73**, 1–11 (2013) `10.1140/epjc/s10052-013-2648-7` (cit. on p. 50).

[133] E. Armengaud, et al., "Search for low-mass WIMPs with EDELWEISS-II heat-and-ionization detectors", Physical Review D - Particles, Fields, Gravitation and Cosmology **86**, 1–6 (2012) `10.1103/PhysRevD.86.051701` (cit. on p. 50).

[134] D. S. Akerib, et al., "First Results from the LUX Dark Matter Experiment at the Sanford Underground Research Facility", Physical Review Letters **112**, 091303 (2014) `10.1103/PhysRevLett.112.091303` (cit. on p. 50).

[135] J. Barreto, et al., "Direct search for low mass dark matter particles with CCDs", Physics Letters B **711**, 264–269 (2012) `10.1016/j.physletb.2012.04.006` (cit. on p. 50).

[136] R. Agnese, et al., "New Results from the Search for Low-Mass Weakly Interacting Massive Particles with the CDMS Low Ionization Threshold Experiment", Physical Review Letters **116**, 071301 (2016) `10.1103/PhysRevLett.116.071301` (cit. on pp. 50, 51).

[137]L. Hehn, et al., "Improved EDELWEISS-III sensitivity for low mass WIMPs using a profile likelihood approach (in preparation)", European Physical Journal C, 1–10 (2016) (cit. on pp. 49, 50).

[138]L. Hehn, "Search for Dark Matter signals in EDELWEISS-III with a multidimensional maximum likelihood method (in preparation)", PhD (Karlsruhe Institute of Technology, 2016) (cit. on p. 49).

[139]X. de la Broïse, and A. Bounab, "Cryogenic ultra-low noise HEMT amplifiers board", Nuclear Instruments and Methods in Physics Research Section A: Accelerators, Spectrometers, Detectors and Associated Equipment **787**, 51–54 (2015) `10.1016/j.nima.2014.11.016` (cit. on p. 50).

[140]A. Phipps, et al., "An HEMT-Based Cryogenic Charge Amplifier for Sub-kelvin Semiconductor Radiation Detectors", Journal of Low Temperature Physics **184**, 505–511 (2016) `10.1007/s10909-016-1475-2` (cit. on p. 50).

[141]Q. ARNAUD, et al., "Optimizing cryogenic detectors for low-mass WIMP searches", Journal of Low Temperature Physics (2015) (cit. on p. 51).

[142]J. Gascon, *Searches for Low-Mass WIMPs with EDELWEISS*, Munich, 2015 (cit. on p. 51).

[143]V. Neganov, B.; Trofimov, *Otkrytia i Izobret.* 1985 (cit. on p. 51).

[144]R. Agnese, et al., "Search for low-mass weakly interacting massive particles using voltage-assisted calorimetric ionization detection in the SuperCDMS experiment", Physical Review Letters **112**, 1–6 (2014) `10.1103/PhysRevLett.112.041302` (cit. on p. 51).

[145]L. T. Corporation, *LTC6090/LTC6090-5 - 140V CMOS Rail-to-Rail Output, Picoamp Input Current Op Amp*, tech. rep. (2012), pp. 1–26 (cit. on p. 52).

[146] EA-Elektro-Automatik, *PS 2000 B Triple*, tech. rep. (2000) (cit. on p. 53).

[147] CSNSM, *Centre de Sciences Nucléaires et de Sciences de la Matière*, 2016 (cit. on p. 54).

[148] BSI, *Baltic Scientific Instruments*, 2016 (cit. on p. 54).

[149]V. Sanglard, et al., "Final results of the EDELWEISS-I dark matter search with cryogenic heat-and-ionization Ge detectors", Physical Review D **71**, 122002 (2005) `10.1103/PhysRevD.71.122002` (cit. on p. 56).

[150]S. Scorza, "EDELWEISS-II , direct Dark Matter search experiment: first data analysis and results", Ph.D thesis (2009) (cit. on p. 56).

[151]J. Gascon, "Run 309: Results so far", Internal Document, 1–38 (2016) (cit. on p. 57).

[152]T. Bergmann, et al., "FPGA-based multi-channel DAQ systems with external PCI express link to GPU compute servers", in 2012 18th ieee-npss real time conference, rt 2012 (June 2012), pp. 1–5, `10.1109/RTC.2012.6418197` (cit. on p. 61).

[153]A. Aab, et al., "The Pierre Auger Cosmic Ray Observatory", Nuclear Instruments and Methods in Physics Research, Section A: Accelerators, Spectrometers, Detectors and Associated Equipment **798**, 172–213 (2015) `10.1016/j.nima.2015.06.058` (cit. on p. 61).

[154]Z. Fodor, S. D. Katz, and A. Ringwald, "Possible detection of relic neutrinos and determination of their mass: Quantitative analysis", ICRC, 769–772 (2001) (cit. on p. 61).

[155]C. Meurer, and N. Scharf, "HEAT - A low energy enhancement of the Pierre Auger Observatory", Astrophysics and Space Sciences Transactions **7**, 183–186 (2011) `10.5194/astra-7-183-2011` (cit. on p. 61).

[156] A. BEGLARIAN, et al., "KATRIN design report 2004", Wissenschaftliche Berichte FZKA (2005) (cit. on p. 61).

[157] J. F. Amsbaugh, et al., "Focal-plane detector system for the KATRIN experiment", Nuclear Instruments and Methods in Physics Research, Section A: Accelerators, Spectrometers, Detectors and Associated Equipment **778**, 40–60 (2015) `10.1016/j.nima.2014.12.116` (cit. on p. 61).

[158] M. Erhard, et al., "High-voltage monitoring with a solenoid retarding spectrometer at the KATRIN experiment", Journal of Instrumentation **9**, P06022–P06022 (2014) `10.1088/1748-0221/9/06/P06022` (cit. on p. 61).

[159] H. Gemmeke, et al., "An improved 3D ultrasound computer tomography system", IEEE International Ultrasonics Symposium, IUS, 1009–1012 (2014) `10.1109/ULTSYM.2014.0247` (cit. on p. 61).

[160] TexasInstruments, *GTL/BTL: A Low-Swing Solution for High-Speed Digital Logic*, tech. rep. (Texas Instruments, 1997) (cit. on p. 62).

[161] F. Habermehl, "Entwicklung der Datenaufnahme und Tests der Vetomodule für das EDELWEISS II muon-Vetozählersystem", PhD thesis (2004) (cit. on p. 66).

[162] Nvidia, *Cuda Toolkit Documentation*, 2015 (cit. on p. 69).

[163] Nvidia, *Cufft Library User ' S Guide*, July (2013) (cit. on p. 69).

[164] T. Bergmann, et al., "A Scalable DAQ System with High-Rate Channels and FPGA- and G GPU-Trigger for the Dar rk Matter Experi iment EDELWEISS-III", in Ieee nuclear science symposium (2015), pp. 2–4 (cit. on p. 69).

[165] M. Gros, *SAMBA acquisition software* (cit. on p. 70).

[166] M. Howe, et al., "Sudbury neutrino observatory neutral current detector acquisition software overview", IEEE Transactions on Nuclear Science **51**, 878–883 (2004) `10.1109/TNS.2004.829527` (cit. on p. 73).

[167] B. Aharmim, et al., "Combined analysis of all three phases of solar neutrino data from the Sudbury Neutrino Observatory", Physical Review C - Nuclear Physics **88**, 1–27 (2013) `10.1103/PhysRevC.88.025501` (cit. on p. 73).

[168] R. Brun, and F. Rademakers, "ROOT — An object oriented data analysis framework", Nuclear Instruments and Methods in Physics Research Section A: Accelerators, Spectrometers, Detectors and Associated Equipment **389**, 81–86 (1997) `10.1016/S0168-9002(97)00048-X` (cit. on p. 73).

[169] N. Foerster, et al., "Pulse-Shape Analysis of Ionization Signals in Cryogenic Ge Detectors for Dark Matter", Journal of Low Temperature Physics (2016) `10.1007/s10909-016-1532-x` (cit. on pp. 74, 75, 101).

[170] LinearTechnology, "LT6600-10 Very Low Noise, Differential Amplifier and 10MHz Lowpass Filter", Datasheet, 1–8 (2002) (cit. on p. 75).

[171] NumPy Developers, *NumPy* (cit. on p. 88).

[172] SciPy.org, *SciPy library*, 2015 (cit. on p. 88).

[173] J. D. Hunter, "Matplotlib: A 2D Graphics Environment, Computing in Science & Engineering", Computing In Science & Engineering **9**, 90–95 (2007) `10.1109/MCSE.2007.55` (cit. on p. 88).

[174] R. H. Byrd, R. B. Schnabel, and G. A. Shultz, "Approximate solution of the trust region problem by minimization over two-dimensional subspaces", Mathematical Programming **40**, 247–263 (1988) `10.1007/BF01580735` (cit. on p. 91).

[175]D. C. Sorensen, "Newton's Method with a Model Trust Region Modification", SIAM Journal on Numerical Analysis **19**, 409–426 (1982) `10.1137/0719026` (cit. on p. 91).

[176]A. Broniatowski, "Carrier anisotropy and impurity scattering in Ge at mK temperatures: Modeling and comparison to experiment", Journal of Low Temperature Physics **167**, 1069–1074 (2012) `10.1007/s10909-012-0543-5` (cit. on p. 95).

[177]E. Browne, et al., "Nuclear Data Sheets for A", Nuclear Data Sheets **82**, 347–449 (1992) `10.1016/j.nds.2013.11.002` (cit. on p. 97).

[178]N. Foerster, "Characterization of the charge transport in the FID800 Germanium single crystals of the EDELWEISS experiment", PhD thesis (Karlsruhe Institute of Technology, 2016) (cit. on p. 101).

[179]M. I. Nathan, "Anisotropy of the conductivity of n-type germanium at high electric fields", Physical Review **130**, 2201–2204 (1963) `10.1103/PhysRev.130.2201` (cit. on p. 102).

[180]A. Broniatowski, "Intervalley scattering of hot electrons in germanium at millikelvin temperatures", Journal of Low Temperature Physics **176**, 860–869 (2014) `10.1007/s10909-014-1091-y` (cit. on p. 102).

[181]M.-C. Piro, et al., "Hot Carrier Trapping in High-Purity and Doped Germanium Crystals at Millikelvin Temperatures", Journal of Low Temperature Physics **176**, 796–801 (2014) `10.1007/s10909-014-1088-6` (cit. on pp. 102, 107).

Danksagung

Ich bedanke mich für die Unterstützung und die Mithilfe von vielen Menschen, ohne die diese Arbeit nicht möglich gewesen wäre.

Mein besonderer Dank gilt Professor Dr. Dr. h.c. Johannes Blümer, der diese Arbeit als Doktorvater ermöglicht hat. Ebenso danke ich dem Korreferenten Professor Dr. Marc Weber für die intensive Zusammenarbeit und die Unterstützung durch das IPE.

Meinem Betreuer Dr. Klaus Eitel danke ich für die hervorragende Betreuung und Unterstützung, für die täglichen Möglichkeiten zur Diskussion und die Chance durch eine Vielzahl an Besuchen, das Experiment vor Ort mitzugestalten und an dessen Betrieb teilzuhaben.

Für tägliche Diskussionen über Elektronik, FPGAs und Auslesesysteme danke ich Denis Tcherniakhovski. Ich habe viele Methoden und Techniken lernen können, die zur Umsetzung der Messungen für diese Arbeit essentiell waren. Ebenso haben Dr. Matthias Kleifges, Dr. Till Bergmann und Alexander Menshikov regelmäßig mit mir über die Ausleseelektronik diskutiert und zu einer Vielzahl von Problemlösungen beigetragen.

Ich bedanke mich bei meinen Kollegen der EDELWEISS-Gruppe in Karlsruhe, insbesondere bei Dr. Valentin Kozlov, Dr. Benjamin Schmidt und Nadine Foerster, deren Arbeiten mit meiner Doktorarbeit einige Überschneidungen aufweisen und deren Kooperation und Hilfsbereitschaft besonders wertvoll für mich waren. Ebenso gilt mein Dank den Kollegen in Frankreich, besonders Professor Dr. Jules Gascon, Dr. Michel Gros, Dr. Bernard Paul und Dr. habil. Stefanos Marnieros, mit denen zusammen ich die Gelegenheit hatte, am Experiment arbeiten zu dürfen. Die Arbeitseinsätze in Modane waren auch dank ihnen immer ein faszinierendes Ereignis.

Meiner ganzen Familie bin ich dankbar für jede Form der Hilfestellung und des Beistands: Von der Finanzierung des Studiums bis zu den Besuchen in Karlsruhe. Ich danke meiner Freundin Ann-Katrin für ihre tägliche Unterstützung. Der familiäre Rückhalt und Zuspruch hat mir sehr viel bedeutet.

Ich widme diese Doktorarbeit meiner Mutter Jutta Siebenborn, die den Abschluss meines Studiums leider nicht mehr erleben durfte.